Aqueous Solution Synthesis of Nanocrystalline TiO_2 Powders: Kinetics, Characterization and Application to Fabrication of Dye-Sensitized Solar Cell Photoanodes

Cécile Charbonneau

Department of Mining and Materials Engineering

McGill University

Montréal, Québec

Canada

February 2011

A thesis submitted to McGill University in partial fulfillment of the requirements of the degree of Doctor of Philosophy

To my parents, and to Anne, Antoine and Hélène

Abstract

The scope of this thesis is the aqueous synthesis and characterization of TiO_2 nanostructured powders for the fabrication of thin film photoanodes used in DSC devices. The development and study of this novel process is approached from the standpoint of determining the relationship between the hydrolytic behaviour of isothermally treated $TiCl_4$ aqueous solutions (speciation and kinetics of conversion of Ti(IV) into TiO_2(s)) and the properties of the resultant TiO_2 products. From an application standpoint, the aqueous synthesized nanocrystalline TiO_2 material is studied for the formulation of screen-printing pastes used in the fabrication of mesoporous photoanodes and resultant dye-sensitized solar cell (DSC) performance.

The synthesis of TiO_2 nanostructured powders by forced hydrolysis of aqueous Ti(IV) chloride solutions is described in terms of precipitation kinetics and nucleation and growth mechanism over the temperature range 70-90 °C and Ti(IV) concentration 0.2-1.5 M. Several techniques are used to characterize the resultant solid products, among which are XRD, FEG-SEM/FEG-TEM, BET surface area, TGA, FT-IR, and EDS analyses. Via appropriate selection of conditions, the aqueous synthesis process is shown that can lead to the preferential production of nanostructured rutile powder with unique self-assembled nanofibre (100 nm – 3 µm) spheroidal particles or colloids made of well dispersed 4-8 nm crystallites with anatase as the major crystalline phase (85 wt.%). These results are explained and discussed based on the effect of various process parameters (T, agitation), but most importantly based on the pronounced effect of the initial concentration of the $TiCl_4$ aqueous solution on the speciation of the solution and related kinetics of the hydrolysis reaction.

When compared to benchmark products such as the P25 TiO_2 from Degussa (50 m^2/g, 30 nm average crystallite size, very little to no surface $-OH/-OH_2$, and 3.15 eV band gap), the two types of aqueous-synthesized materials are found to possess a high specific surface area, with 80-120 m^2/g for the rutile powders and 250-350 m^2/g for the anatase powders, enhanced surface hydroxylation, and larger band gap (3.37 eV) in the

case of the anatase nanopowder. These materials are shown that can be used for the fabrication of thin film photoanodes prepared by the screen-printing method either separately (i.e. anatase) or as hybrid (anatase-rutile) with the latter being superior in terms of photovoltaic performance. Finally, the direct preparation of paste without drying of the nanocolloids is demonstrated.

Résumé

Cette étude porte sur la synthèse en milieu aqueux de particules nano-structurées de TiO_2 utilisées pour la fabrication de photoanodes, une composante des cellules photovoltaïques à pigments colorés (DSCs). Le développement et l'étude de ce nouveau procédé de synthèse est abordé de façon à déterminer la relation existante entre le comportement hydrolytique de solutions aqueuses de $TiCl_4$ traitées de manière isothermique (spéciation et cinétique de conversion de Ti(IV) en TiO_2(s)) et les propriétés des produits de TiO_2 résultant. D'un point de vue pratique, le produit de TiO_2 nanocristallin synthétisé en milieu aqueux est examiné pour la formulation de pâtes à imprimer utilisées dans le procédé de fabrication de photoanodes mésoporeuses; l'impact de ce matériau sur l'efficacité des cellules photovoltaïques à colorant est également considéré.

La synthèse de poudres de TiO_2 nano-structurées, effectuée par hydrolyse de solutions aqueuses de $TiCl_4$, est décrite d'un point de vue de la cinétique de précipitation et des mécanismes de nucléation et de croissance des particules de TiO_2, sur des intervalles de température et de concentration variant respectivement de 70 à 90 °C et de 0.2 à 1.5 M. Plusieurs techniques sont utilisées afin de caractériser les produits solides, parmi lesquels la DRX, le MEB et le MET, les spectroscopies FT-IR et EDS, et des mesures d'aire de surface BET et de thermogravimétrie. Il est montré qu'en choisissant les conditions expérimentales de manière appropriée, le procédé de synthèse en milieu aqueux mène à la production de poudres nano-structurées de rutile composées de particules sphéroïdales dont la forme résulte de la croissance radiale de nanofibres (de 100 nm à 3 µm) ou bien de colloïdes contenant des nano-cristaux de 4 à 8 nm dont la principale phase cristalline est l'anatase (85 % m/m). Ces résultats sont expliqués et commentés sur la base des effets induits par les paramètres expérimentaux (T, agitation) et plus particulièrement l'effet prononcé de la concentration de la solution aqueuse de $TiCl_4$ sur la nature des espèces en solution et la cinétique associée à la réaction d'hydrolyse.

Si l’on compare les matériaux synthétisés en milieu aqueux avec des produits standards commerciaux tels que la poudre de TiO_2 P25 de Degussa (50 m^2/g, 30 nm de taille moyenne de particules, présence faible voire nulle de groupes de surface -OH/-OH_2 et un band gap de 3.15 eV), ceux-ci sont caractérisés avec une aire de surface plus importante, 80-120 m^2/g pour les poudres de rutile et 250-350 m^2/g pour les poudres d’anatase, un taux d’hydroxylation de surface plus élevé et un band gap plus large dans le cas de l’anatase (3.37 eV). Il est montré que ces matériaux, plus précisément la poudre d’anatase seule ou bien une poudre hybride d’anatase et de rutile, peuvent être utilisés afin de fabriquer des photoanodes préparées par méthode d’impression, la deuxième poudre ayant montré une qualité supérieure en termes de performance photovoltaïque. Enfin, la préparation de pâtes à imprimer directement à partir de nanocolloides de TiO_2, sans avoir à recourir à l’extraction et au séchage des poudres, est décrite.

Remerciements

Pour commencer, je tiens à exprimer mes plus sincères remerciements à mon superviseur, Professeur George P. Demopoulos, pour m'avoir donné l'immense opportunité d'effectuer mon doctorat sous sa supervision. Je lui suis extrêmement reconnaissante pour l'aide, le support et les conseils qu'il m'a apporté tout au long de mes études supérieures. J'aimerais également exprimer ma gratitude à son égard pour m'avoir permis d'explorer un sujet d'étude portant sur des domaines diversifiés et offrant de nombreux débouchés de carrière. Enfin, je tiens à le remercier pour avoir encouragé ma participation à de nombreuses conférences scientifiques d'étendue internationale qui ont grandement contribuées à stimuler ma curiosité, mon enthousiasme et ma passion pour la recherche.

Mes remerciements vont également à la société Werner Graupe pour m'avoir généreusement offert une bourse d'étude (Werner Graupe International Fellowship) et au Département de Génie des Mines et des Matériaux de l'université McGill pour m'avoir honorée d'une bourse d'excellence.

Je souhaite également remercier les techniciens de laboratoire qui m'ont apporté une aide précieuse dans mes travaux de recherche, en particulier Monique Riendeau (XRD et mesures d'aire de surface BET), Petr Fiurasek (TGA), Ranjan Roy (ICP-AES), Helen Campbell (FEG-SEM) et Xue-Dong Liu (FEG-TEM). Je vous suis très reconnaissante pour m'avoir offert votre expertise et tout particulièrement pour m'avoir formée à l'utilisation de techniques d'analyses scientifiques variées.

Je remercie tous les membres de mon équipe de recherche, les Hydromets, pour leur soutien et leurs collaborations. Vera, Jeff, Vincent, Levente, Karl, Nicolas, Sebastian, Renaud, Derek, Guobin et Nima, merci pour avoir été de si bons amis et collègues de travail. Un grand merci également à Barbara Hanley pour son aide précieuse dans toutes mes démarches administratives à McGill. A tous mes amis du Département de Génie des Mines et des Matériaux et de Montréal, merci infiniment, vous avez fait de mon séjour à McGill et à Montréal une expérience absolument inoubliable. Je remercie également tous mes amis de France et d'ailleurs pour avoir gardé contact et m'avoir apporté leur soutien.

Enfin, je tiens tout particulièrement à remercier ma famille. D'abord mes parents, à qui je dois tant et suis infiniment reconnaissante pour m'avoir toujours soutenue dans mes choix universitaires et pour n'avoir jamais cessé de m'encourager durant mon doctorat. A tous les cinq, merci pour vos innombrables appels d'outre-Atlantique et vos fréquentes visites à Montréal qui ont tant compté pour moi. Papa, Maman, Anne, Antoine et Hélène, je vous remercie du fond du cœur et vous dédie cette thèse.

Table of Contents

List of Figures

List of Tables

Chapter 1: Introduction

Background

Nanopowders of TiO_2 possess remarkable photo-catalytic and semiconductor properties that make them suitable candidates for various advanced technology fields of application. Among the applications, dye-sensitized solar cells (DSCs), the latest generation of electrical power generation photovoltaic devices that mimic natural photosynthesis [1,2] have recently attracted a lot of attention in the world of scientific research due to the pressing need for the development of new energy sources.

As an answer to the increasing interest and demand for the fabrication of TiO_2 nanopowders with suitable properties (crystalline phase [3,4], size distribution, surface area, and shape [5,6], band gap [7] etc…) for the fabrication of mesoporous TiO_2 DSC photoanodes, a variety of synthesis techniques has been advanced [8-14]. The two step sol-gel/hydrothermal synthesis process is currently the most widely employed synthesis method [15-17]: a titanium alkoxide-based solution is first hydrolysed to form amorphous TiO_2 powders; crystallization is then induced in an autoclave at high pressure and temperature (typically 250 °C). This method has been successfully developed for the preparation of anatase TiO_2 nanoparticles (10-30 nm) with large surface area (80-150 m^2/g) [18]. However, sol-gel processing is chemical and energy intensive, multi-step, and time consuming that does not render itself to easy scale-up and cost-effective operation. The P25 TiO_2 powder from Degussa (20 wt. % rutile, 80 wt. % anatase, 50 m^2/g, 30 nm average particle size), which is considered a reference material among the commercially available nanostructured TiO_2 powders, is produced by flame synthesis [19]. This process, although efficient in terms of production, suffers from the difficulty to control the size distribution of the particles, a key factor in optimizing the efficiency of TiO_2-based DSC devices.

For DSC devices to be able to enter the market of power supply photovoltaics as a competitor of already well established products such as silicon-based solar panels (~ 88 % of the market share) and thin film CIGS and CdTe photovoltaic technologies (~ 12 %

of the market share), it is imperative that its manufacturing cost is lowered. In particular, one of the challenges consists in decreasing the production cost of TiO_2 nanopowders by a factor of 4 within the next 2-3 years (according to recent numbers, sol-gel/hydrothermal processed TiO_2 nanopowders used for the fabrication of DSC photoanodes is currently produced at ~ 1000 $/kg [20]).

For this reason, it has been chosen to investigate the synthesis of TiO_2 nanopowders via aqueous solution processing that may provide a simpler, less costly and cleaner alternative to the sol-gel/hydrothermal route. Several investigations have dealt with this approach in the past. These studies involved either precipitation of TiO_2 with the aid of neutralizing agents or via hydrolysis forced by heating below or above the boiling point of water. For example, as a preliminary work on the synthesis of TiO_2 neutralization of $TiCl_4$ solutions with MgO at 95 °C was recently completed in our laboratory [21]. Direct or forced hydrolysis of $TiCl_4$ aqueous solutions without resorting to the use of a neutralizing agent was investigated by other researchers [22-27] who reported on the synthesis of crystalline nanosized TiO_2 particles with the rutile, mixed rutile/anatase or the anatase phase. However, none of the methods described in these studies were further tailored specifically for the synthesis of TiO_2 nanopowders and fabrication of DSC devices.

Objectives

The main objective of this thesis is to study the synthesis of TiO_2 nanopowders with controlled properties via forced hydrolysis ($T < 100$ °C, P_{atm}) of $TiCl_4$ aqueous solutions and their evaluation as paste material in fabricating mesoporous thin film electrodes for DSC devices. More specifically, one important goal of this project is to define the effect of processing parameters such as the Ti(IV) concentration of the precursor $TiCl_4$ aqueous solution, the temperature and agitation, and the use of additives, on the kinetics of the hydrolysis reaction and the properties of the obtained solid products. By optimizing such solution synthesis route and understanding and controlling the governing chemical phenomena, it is eventually aimed to define processing windows for reproducible, green, scalable, and low-cost production of diverse nanostructured TiO_2 material suitable for the fabrication of photoanodes in DSC devices. Finally, it is intended to use and adapt the aqueous synthesis process for direct and simple formulation of TiO_2-based screen-printable pastes developed for the fabrication DSC photoanodes.

Thesis layout

This work has been divided in several chapters. In this chapter, an introduction is provided that presents the background, justification, and objectives of this research. The second chapter of the thesis consists of an extensive literature survey of the properties, applications and synthesis techniques of TiO_2 powders, and the TiO_2-based dye-sensitized solar cells. Chapter 3 provides all details on the materials and equipment used, and the experimental procedures and characterization techniques employed for the synthesis and characterization of the various materials and devices studied. Chapter 4 investigates the speciation of Ti(IV) in Ti(IV)-Cl(-I)-H_2O aqueous solutions. Chapter 5 presents a study on the synthesis of self-assembled nanofibre rutile (TiO_2) particles via forced hydrolysis of 0.5-1.5 M $TiCl_4$ aqueous solutions while Chapter 6 focuses on the synthesis and characterization of anatase nanocolloids produced by isothermal treatment at 80 °C of a 0.2 M aqueous $TiCl_4$ solution. In Chapter 7, the properties of TiO_2 thin film photoanodes prepared with the aqueous synthesized TiO_2 nanostructured powders are investigated and compared to films prepared with the reference powder P25, via extensive characterization and DSC device performance evaluation. The final chapter is a synopsis that contains the main conclusions and claims to originality of the present work, and recommendations for future work. Finally, in an Appendix, some additional results that investigate the effect of sulfate additives or pre-neutralization of a 1 M $TiCl_4$ aqueous solution on the properties of isothermally produced TiO_2 powders are summarized.

Publications

Parts of this led to the publication of three papers. The first one, entitled "*Nucleation and growth of self-assembled nanofibre-structured rutile (TiO_2) particles via controlled forced hydrolysis of titanium tetrachloride solution*" [28], encompasses most of the results reported in Chapter 5 of this thesis. The second one, entitled "*Aqueous solution synthesis of crystalline anatase nanocolloids for the fabrication of dye-sensitized solar cell (DSC) photoanodes*" [29], reports on most results presented in Chapter 6 and sections 2 and 3 of Chapter 7 of this thesis. Finally, the paper entitled "*Preparation and DSSC performance of mesoporous film photoanodes based on aqueous-synthesized anatase nanocrystallites*" [30], gathers results issued from a collective experimental and data interpretation work performed by Cecile Charbonneau, Guobin Shan, and Kee Eun Lee, some of which have been reported in the section 2 of Chapter 7 (namely Figures 7.5 and 7.6).

References

[1] http://www.dyesol.com/conference_files/Light_and_Energy,_Electric_Power_Generation_by_Dye.pdf

[2] B. O’Regan and M. Grätzel, *Nature*, **353** (1991), 737.

[3] A.G. Vega Poot, D. Reyes Coronado, and G. Oskam, *ECS Trans.*, **3** (2006), 233.

[4] G. Li, C. P. Richter, R. L. Milot, L. Cai, C. A. Schmuttenmaer, R. H. Crabtree, G. W. Brudvig, and V. S. Batista, *Dalton Trans.*, **45** (2009), 10078.

[5] S. Chuangchote, T. Sagawa, and S. Yoshikawa, *ECS Trans.*, **16** (2009), 21.

[6] C. Baek, M. Vithal, J. A. Chang, J. H. Yum, M. K. Nazeeruddin, M. Grätzel, Y. C. Chung, and S. Seok, *Electrochem. Commun.,* **11** (2009)**,** 909.

[7] Y. Lei, H. Liu, and W. Xiao, *Modelling Simul. Mater. Sci. Eng.,* **18** (2010), 025004.

[8] T. Ishigaki and J.-G. Li, *Sci. Tech. Adv. Mater.*, **8** (2007), 617.

[9] P.V.A. Padmanabhan, K.P. Sreekumar, T.K. Thiyagarajan, R.U. Satpute, K. Bhanumurthy, P. Sengupta, G.K. Dey and K.G.K. Warrier, *Vacuum*, **80** (2006), 1252.

[10] S.-M. Oh and T. Ishigaki, *Thin Sol. Films*, **457** (2004), 186.

[11] W. P. C. Duyvesteyn, T. M. Spitler, B. J. Sabacky, J. Prochazka, US Patent # 6,440,383.

[12] M. Graetzel, *J. Sol-Gel Sci. Technol.*, **22** (2001), 7.

[13] S. Gablenz, D. Voltske, H. P. Abicht, and J. Neumann-Zoralek, *J. Mater. Sci. Lett.*, **17** (1998), 537.

[14] Degussa technical information brochure n°1243.

[15] S. Lee, I.-S. Cho, J. H. Lee, D. H. Kim, D. W. Kim, J. Y. Kim, H. Shin, J.-K. Lee, H. S. Jung, N.-G. Park, K. Kim, M. J. Ko, and K. S. Hong, *Chem. Mater.*, **22** (2010), 1958.

[16] M. Grätzel, *J. Sol-gel Sci. Technol.*, **22** (2001), 7.

[17] S. Kambe, K. Murakoshi, T. Kitamura, Y. Wada, S. Yanagida, H. Kominami, and Y. Kera, *Sol. Energy Mat. Sol. Cells*, **61** (2000), 427.

[18] C. J. Barbe, F. Arendse, P. Compte, M. Jirousek, F. Lenzmann, V. Shklover, and M. Grätzel, *J. Am. Ceram. Soc.*, **80** (1997), 3157.

[19] J. Liu, Y. J. Hu, F. Gu, and C. Z. Li, *Ind. Eng. Chem. Res.*, **48** (2009), 735.

[20] http://www.dyesol.com/download/DSCIC10/DesilvestroHans_Dyesol.pdf

[21] Y. Li and G. P. Demopoulos, *Hydrometallurgy*, **90** (2008), 26.

[22] M. Addamo, M. Bellardita, A. Di Paola, and L. Palmisano, *Chem. Comm.*, **47** (2006), 4943.

[23] S. R. Dhage, V. D. Choube, V. Samuel, and V. Ravi, *Mater. Lett.* **58** (2004), 2310.

[24] Y. Zheng, E. Shi, Z. Chen, W. Li, and X. Hu, *J. Mater. Chem.*, **11** (2001), 1547.

[25] S.-J. Kim, S. D. Park, Y. H. Cho, W. W. Kim., *J. Sol. Stat. Chem.*, **146** (1999), 230.

[26] Q.-H. Zhang, L. Gao and J.-K Guo, *Nanostruct. Mater.* **11** (1999), 1293.

[27] S. Cassaignon, M. Koelsch, and J.-P. Jolivet, *J. Mater. Sci.*, **42** (2007), 6689.

[28] C. Charbonneau, R. Gauvin, and G. P. Demopoulos, *J. Cryst. Growth*, **312** (2009), 86**.**

[29] C. Charbonneau, R. Gauvin, and G. P. Demopoulos, *J. Electrochem. Soc.***, 158** (2011), H224.

[30] C. Charbonneau, K. E. Lee, G. B. Shan, M. A. Gomez, R. Gauvin, and G. P. Demopoulos, *Electrochem. Solid-State Lett.*, **13** (2010)**,** H257**.**

Chapter 2: Literature Survey

2.1. Introduction

In this chapter, an extensive literature survey is presented starting with an introduction to the TiO_2 material itself. This first part contains a description of the various crystalline forms of natural and synthetic TiO_2 and their associated thermodynamic (stability, phase transition phenomena), optical and electronic properties and a non-extensive overview of the application fields that make use of TiO_2 nanomaterials. In the second part, the methods so far developed for the synthesis of TiO_2 nanomaterials, their advantages and drawbacks, are presented with an emphasis given to solution processes of which the aqueous synthesis, the method investigated in this study. The third part of this survey starts with the general theory associated to forced hydrolysis of aqueous solutions and a complete description of the mechanisms involved in particle nucleation and growth. These theoretical concepts are further applied to the particular case of TiO_2 precipitation via forced hydrolysis of a $TiCl_4$ aqueous solution: possible pathways for the formation of TiO_2 rutile, anatase and brookite crystal unit cells are proposed based on the gathering of data on the speciation and hydrolytic behavior of Ti-Cl-H_2O systems; a discussion on the advances reported in literature regarding the development of aqueous synthesis experimental routes (involving $TiCl_4$ as a precursor), in terms of process design and control of the product properties, concludes this part of the survey. Finally, a non-extensive review on TiO_2-based dye-sensitized solar cells (DSC) is presented which provides an introduction to the structure, operational mode, performance parameters and testing of these devices. The photoanode characteristics, which are known to bear a significant impact on the overall efficiency of DSCs, are listed and discussed based on published results.

2.2. About TiO_2

2.2.1. Natural and synthetic crystalline forms

In nature, Ti is generally associated with Fe in a mineral oxide called ilmenite, of formula $FeTiO_3$. The latter is extensively processed as a raw material in the mineral industry for the recovery of Ti and for the production of TiO_2 white pigments. Titanium also occurs naturally as titanium dioxide with a number of crystalline phases. The most common natural and synthetic crystalline forms of TiO_2 are rutile, anatase and brookite. These belong to the "low-pressure" group of crystalline forms, where the less common naturally occurring TiO_2 (B, Banfield), and synthetic TiO_2 (R, Ramsdellite) and TiO_2 (H, Hollandite) structures are also found. All these "low-pressure" TiO_2 crystalline forms are based on the arrangement of distorted TiO_6 octahedra, where Ti is located at the centre of the octahedron. Figure 2.1 shows the sequential arrangement of the octahedra in the rutile, anatase and brookite TiO_2 crystalline structures [1,2]. In the rutile structure, each octahedron has ten neighboring octahedra, two of them sharing edges and the other eight sharing corners. In the anatase and brookite structure, each octahedron has eight neighboring octahedra, four of them sharing edges and the other four sharing corners. Anatase and brookite are polytypic forms of TiO_2, i.e. they only differ in the way their atomic layers are stacked, whereas anatase (or brookite) and rutile are polymorphic crystalline forms of TiO_2, i.e. they only share the same chemical composition.

In all previously mentioned TiO_2 polymorphs, the nature of the bonding between Ti and O atoms is mixed ionic-covalent. The ratio between the ionicity and covalency of the bonding depends on the crystalline structure and may also vary with the crystal size. For instance *Li et al.* [3] reported that the Ti-O bonding of rutile, which is 63 % ionic in bulk crystals, undergoes a covalency enhancement at the scale of nanocrystals.

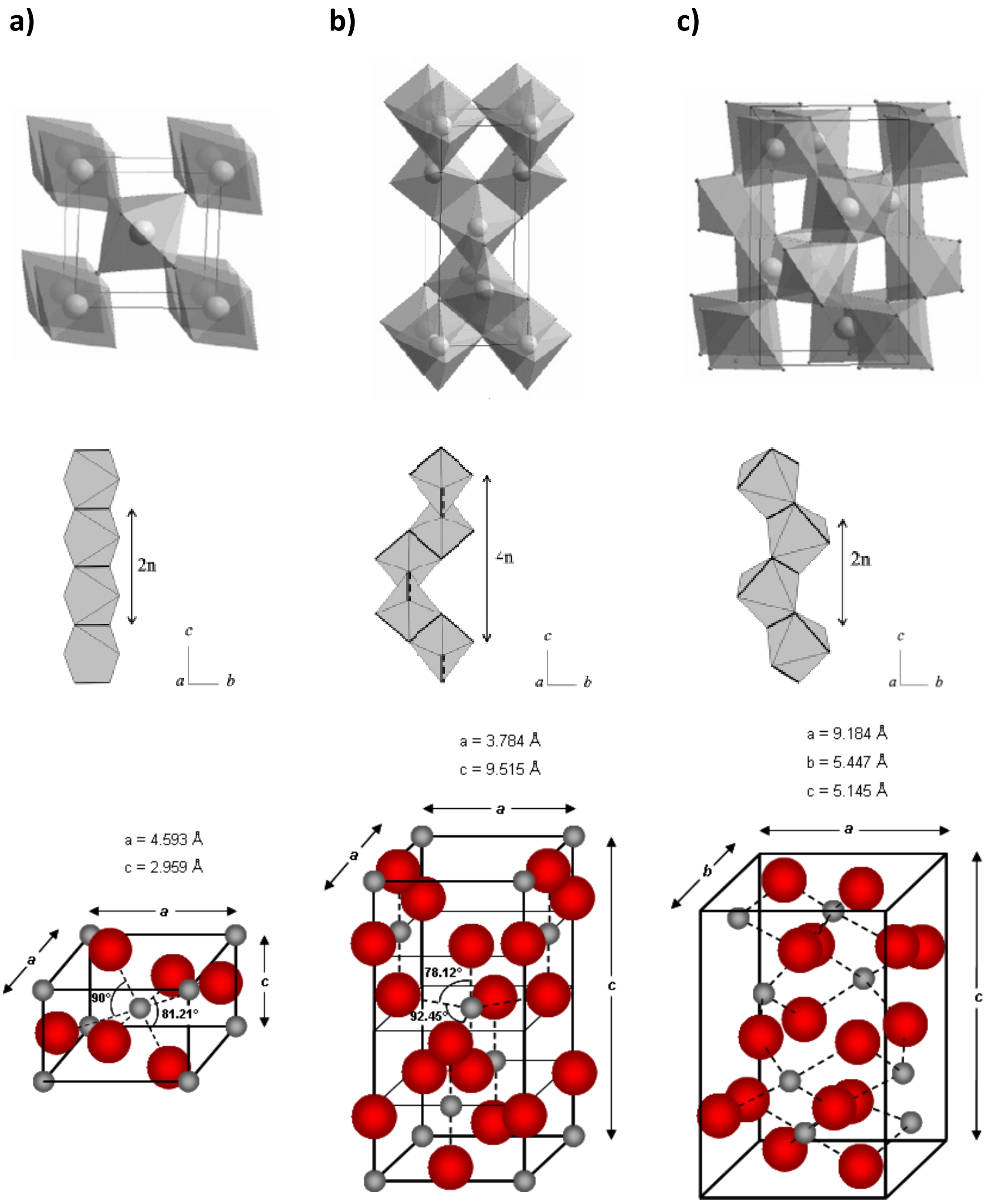

Figure 2.1. Crystalline structures of rutile (a), anatase (b) and brookite (c). Upper part: Ti atoms are symbolized by spheres in octahedral coordination with O atoms. Middle part: shared edges are marked by bold lines, taken from ref. [1,2]. Lower part: crystal unit cells and parameters (Ti atoms are in grey and O atoms in red).

2.2.2. Thermodynamic properties

Mathematical modelling based on lattice energy minimization was developed by *Swamy et al.* [4] to simulate low and high-pressure TiO_2 crystal structures and further used to establish the relative order of stability of TiO_2 crystalline structures under atmospheric conditions. By only considering the rutile, anatase and brookite crystalline forms, it was established that rutile was the most stable form and anatase the least stable among the three. This finding is however counter intuitive with the low occurrence of brookite in nature as compared to anatase, an indication that multiple factors may affect the relative stability of TiO_2 crystalline forms. For instance, *Zhang and Banfield* [5,6] established that the crystal size, in the nanoscale range, has an impact on the order of stability of the TiO_2 crystalline forms. At the nanometric scale, anatase, respectively brookite, and rutile were found to be the most stable phases among the three for crystal size < 11 nm, 11-35 nm, and > 35 nm, respectively (Figure 2.2.a). Other researchers [7] compared the stability of anatase, brookite and rutile TiO_2 powders with different surface area, this way integrating the crystalline density (for which theoretical values are provided in Table 2.1) as an additional factor to the crystal size. They found that rutile, brookite, and anatase were energetically the most stable of the three when their surface area is < 592 m^2/mol (7 m^2/g or > 200 nm), 592 to 3174 m^2/mol (7-40 m^2/g or 200-40 nm), and > 3174 m^2/mol (< 40 nm), respectively (Figure 2.2.b).

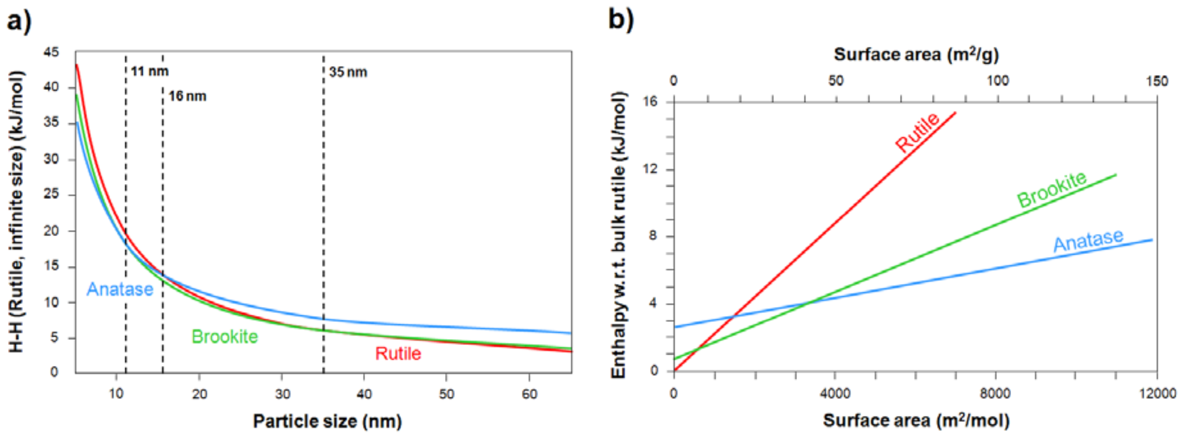

Figure 2.2. Thermodynamic stability of the rutile, anatase, and brookite crystalline structure: effect of the crystal size (a), reproduced from ref. [5]; effect of the surface area (b), reproduced from ref. [7].

Table 2.1. Physical properties of the rutile, anatase and brookite crystalline structures of TiO_2.

Physical properties	**Rutile**	**Anatase**	**Brookite**
Density (theoretical)	4.25 g/cm^3	3.89 g/cm^3	4.13 g/cm^3
Refractive indices (experimental)	n_ω = 2.605 - 2.613 n_ε = 2.899 - 2.901	n_ω = 2.561 n_ε = 2.488	n_α = 2.583 n_β = 2.584 n_γ = 2.700
Band gap (experimental)	3.00-3.06 eV	3.18-3.40 eV	3.11-3.13 eV

Polymorphic phase transformations of TiO_2 crystalline particles (rutile, anatase and brookite) were investigated in varied contexts, namely under hydrothermal or dry high temperature heat treatments [5,8-10]. The phase transition mechanisms so far reported in literature are summarized in Equations 2.1.a-c, which show that the anatase-to-brookite and inversely brookite-to-anatase, but also brookite-to-rutile and anatase-to-rutile are possible direct phase transition mechanisms under the appropriate set of conditions.

$$\begin{aligned} &\text{a) } A \longrightarrow B \longrightarrow R \text{ [5]} \\ &\text{b) } A \longrightarrow R \text{ [5,8]} \\ &\text{c) } B \longrightarrow A \text{ [10]} \end{aligned} \qquad (2.1)$$

The occurrence of these transformations has been observed under different experimental conditions of pressure and temperature [5,10], and are known to depend on a number of parameters such as the size, shape (spherical as opposed to faceted particles [11]), and surface chemical characteristics (concentration of H-terminated Ti or O surface atoms) [11] of the crystalline particles.

Kinetics models using the classical Smoluchowski theory [12] were developed by several research groups to simulate the phase transitions described in Equations 2.1.a and 2.1.b [5,9]. These are usually based on the following assumptions: the overall reaction is first-ordered, coalescence is the dominating mechanism of coarsening, and phase transformations are particle size independent. The anatase-to-rutile phase transition was investigated under various experimental conditions and observed to be accelerated under hydrothermal conditions as opposed to dry high temperature environment, as shown in Figure 2.3. This phenomenon is an important issue for the control of the crystalline properties of TiO_2 powders when precipitated from $TiCl_4$ aqueous solutions.

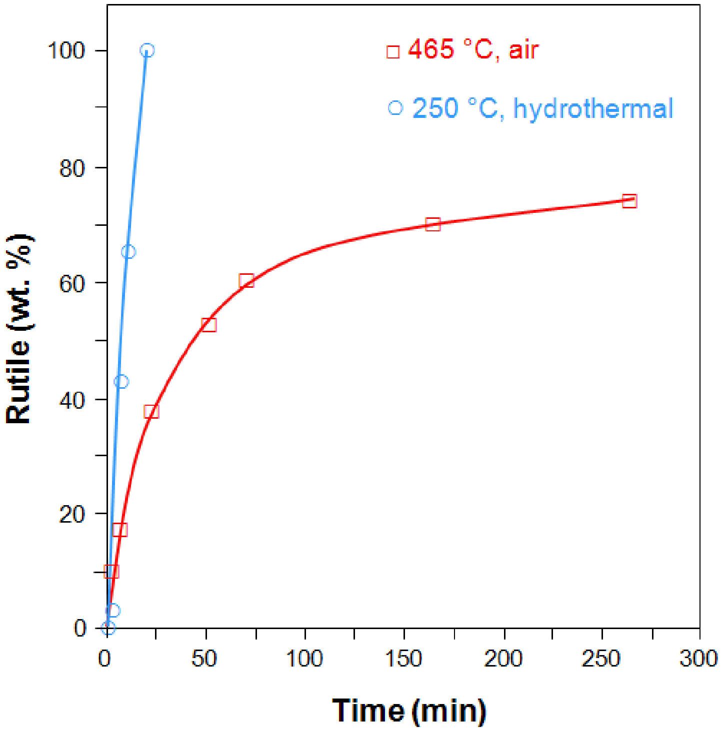

Figure 2.3. Effect of ageing conditions on the kinetics of the anatase-to-rutile phase transition. Reproduced from [8].

Polymorphic transformations of TiO_2 particles under hydrothermal or dry high temperature treatment are usually associated with grain growth or particle coarsening via coalescence at the contact zones of the particles [9,13]. The driving force of these mechanisms is the reduction in surface energy. However, polymorphic phase transformations were also observed to happen within single crystals: the analyses of HR-TEM (High Resolution-Transmission Electron Microscopy) images and SAED (Selected Area Electron Diffraction) patterns of hydrothermally treated nanocrystalline anatase made it possible to locate the nucleation of rutile planes at anatase {112} twin surfaces

[8]. The atomic displacement mechanism that was proposed to explain the growth of rutile within the anatase crystalline lattice involves the movement of both Ti and O planes. This mechanism is very similar and usually compared to the atomic displacements mechanism at the origin of the brookite-to-rutile phase transformation because of the polytypic relation between anatase and brookite. The same researchers also found the occurrence of brookite at anatase {112} twin surfaces and suggested a displacement mechanism based on the translation of Ti atoms for the inter-conversion of anatase and brookite [14].

2.2.3. Optical and electronic properties

Titanium dioxide has been extensively studied for its electrical and optical properties. These are closely linked to one another and directly depend on the crystalline structure of TiO_2 and hence vary slightly among its polymorphs. Table 2.1 presents a comparison between the density, refractive indices and band gap properties of the rutile, anatase and brookite forms of TiO_2. It may be observed from these data that the refractive indices increase with increasing density, whereas the band gap values follow the opposite trend. Rutile has the highest and anatase the lowest density and refractive indices respectively. A study by *Otterman and Bange* shows a linear dependence between the density and the refractive index of TiO_2 thin films, which corroborates the latter observations [15]. However, the band gap properties of TiO_2 polymorphs tend to follow the inverse trend with anatase having the largest and rutile the smallest band gap values respectively.

With the development of photovoltaic device applications, such as dye-sensitized solar cells, TiO_2 semiconductor properties have been widely investigated. Titanium dioxide is known to be an n-type semiconductor, e.g. it can provide extra electrons from its conduction band and allow the circulation of electrons at the same energy level. Numerous studies investigated the electronic band structure of the rutile and anatase TiO_2 polymorphs. However, reports on the brookite crystalline form are less common. Anatase electrical properties have been extensively studied due to its higher band gap properties (when compared to rutile), an attractive feature in the application field of photovoltaics. The band gap of bulk anatase (particles with diameter, *d* ≥ 10 nm) has been reported in several studies to be ~ 3.20 eV [16-18]. However, for nanoparticles with decreasing diameter in the range 2-10 nm, experimental values of anatase band gap were found to increase up to 3.35-3.40 eV [16,19]. One explanation for this phenomenon is the manifestation of quantum size effects [19-21], although dissenting opinions about this phenomenon exist [18,22]. Quantum size effects may be described as the unusual behaviour of small crystals (typically with *d* ≤ 10 nm) due to the confinement of electrons in small regions of space. In relation with this theory, *Swamy et al.* [23] recently reported on the non-linear variation of anatase lattice parameters for particles with decreasing diameter from 65 to 2 nm. The mean lattice strain of these particles was found to increase drastically for particles with decreasing diameter in the range 2 nm ≤ *d* ≤ 10 nm. Other researchers suggested that the stress resulting from lattice strains along with the possible creation of Ti^{4+} vacancies may be responsible for the increase of the band gap, a manifestation of quantum size effects in anatase nanoparticles and other nanostructured materials. In the case of rutile, the values reported for experimental band gap measurements are in the range 3.00-3.06 [17,24]. Because of the complexity of the brookite crystalline structure, conflicting results have been reported regarding its band gap value. However, most studies report that brookite has a lower band gap than anatase with a value of ~ 3.11-3.13 eV [17,25,26].

To calculate the band gap of semiconductor thin films, one of the most common experimental methods is diffuse reflectance spectroscopy in the UV-Vis range (200-800 nm): a reflectance spectrum collected by the apparatus (R_∞ vs. λ with R_∞, the reflectance of an infinitely thick film with respect to a reference for each wavelength of the light source, and λ the wavelength of the light source) is converted into the equivalent absorption coefficient α_{KM} by using the Kubelka Munk function [27,28], shown in Equation 2.2:

$$\alpha_{KM} = \frac{(1-R_\infty)^2}{2R_\infty} \tag{2.2}$$

The next step consists in drawing the Tauc plots by plotting α_{KM}^{2} (for direct semiconductors) or $\alpha_{KM}^{1/2}$ (for indirect semiconductors) vs. E_{phot}, the photon energy, as shown in Figure 2.4. The relation between the photon energy and its wavelength are provided in Equation 2.3 where E_{phot} and λ are expressed in eV and nm respectively.

$$E_{phot} = \frac{1239}{\lambda} \tag{2.3}$$

On Figure 2.4, the dash lines illustrate the linear relationship existing at the absorption edge between α_{KM}^{2} (or $\alpha_{KM}^{1/2}$) and the photon energy. A good approximation of the band gap, E_g, corresponds to the value of E_{phot} at the intersection of the linear extrapolation of the absorption edge with the “x” abscise of the diagram.

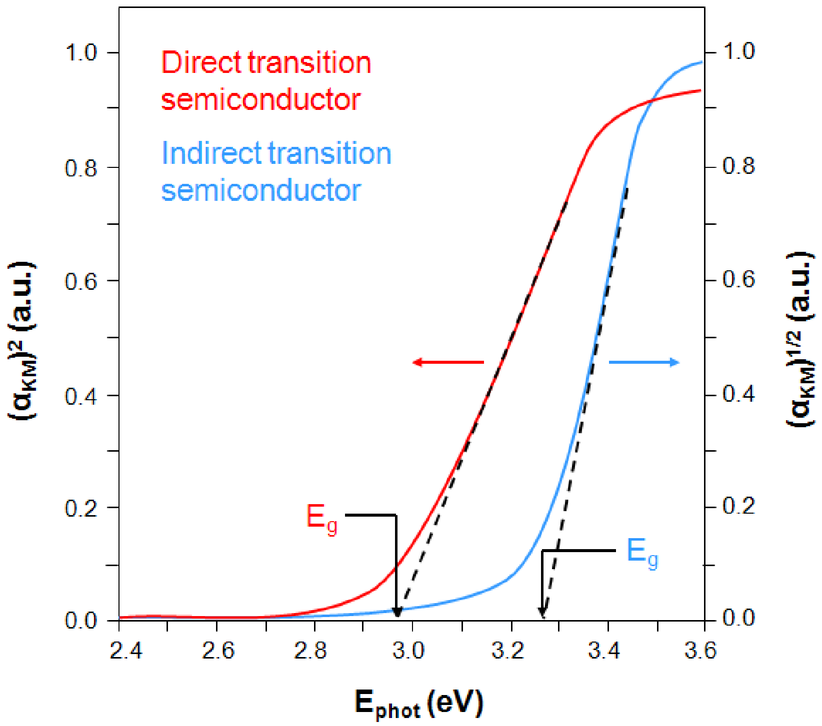

Figure 2.4. Tauc plots for direct and indirect transition semiconductors and calculation of their band gaps, E_g (explained in ref. [16]).

For rutile and brookite the transition of the electrons from the valence band (VB) to the conduction band (CB) is usually reported to be direct (Figures 2.5.a and 2.5.c) but for anatase is indirect (Figure 2.5.b) [26]. A direct transition is characterized by the conservation of the momentum of the electrons from the VB to the CB, e.g. the energy provided by a photon is sufficient to achieve the transition. In the case of an indirect transition, the momentum of the electron is shifted with the assistance of a phonon.

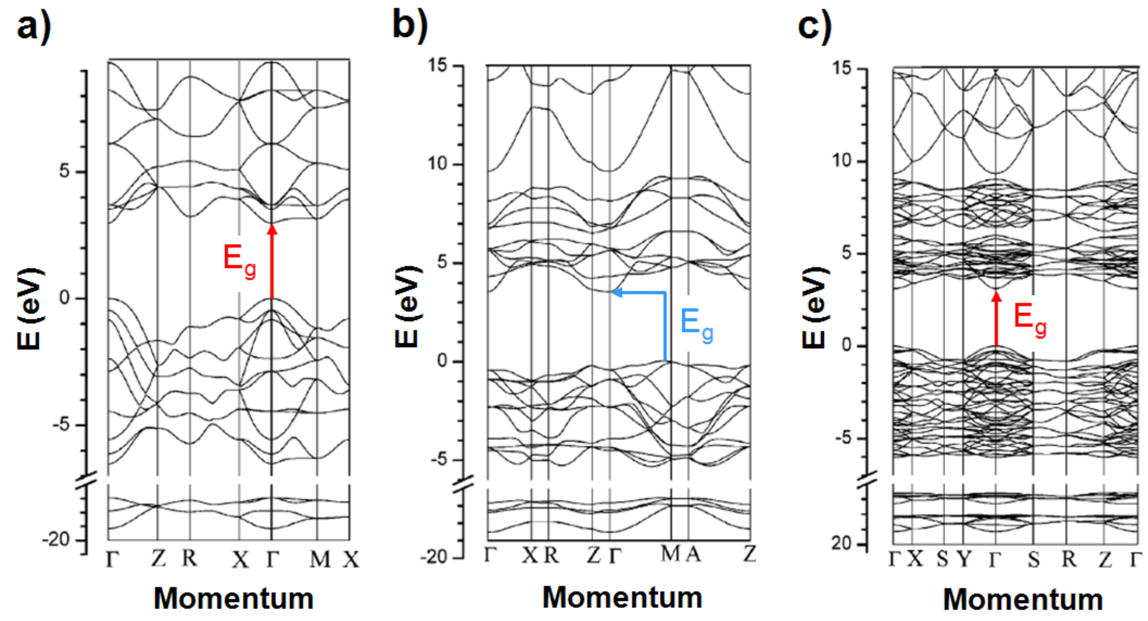

Figure 2.5. Band structure of the rutile (a), anatase (b) and brookite (c) crystalline forms of TiO_2. The valence band maximum is taken as E = 0 eV. Taken from ref. [26].

Optical properties of TiO_2 are closely related to the electronic properties and refractive indices of its crystalline forms. It can be noticed from Table 2.1 that all polymorphs of TiO_2 are characterized with very high refractive indices (higher than the refractive index of diamond, n_α = 2.435), especially the rutile crystalline form. This property makes TiO_2 a very good light-scattering material when synthesized in the form of submicron size powders. Titanium dioxide is also well known for its UV absorbance properties whereas in the visible range it is characterized with very low absorbance properties. As for most semiconductor materials, the main mechanism of light absorption in TiO_2 is the inter-band (VB to CB) electron transition. For indirect semiconductors such as anatase though, this phenomenon is very limited since the direct transition of electrons from the valence to the conduction band is prohibited by the crystal symmetry. For crystallites with an average size < 20 nm, as well as for mesoporous materials, interface absorption becomes the predominant mechanism and absorption is expected to improve due to the higher proportion of interface as opposed to inner atoms.

2.2.4. Application fields of TiO_2 powders

Over the last couple of decades, TiO_2 powders have been extensively used in the industry and investigated as a material presenting very attractive features in a variety of application fields. At the submicron scale, e.g. for powders with average particle size in the range 100-1000 nm, TiO_2 is a white pigment with very good light-scattering, opacifying, UV resistance and bio-compatibility (non-toxicity) properties, especially when synthesized in the rutile crystalline form. For this reason, submicron size rutile TiO_2 powders are world widely produced (4 million tones per year) and exploited in the paint, ink, coatings, paper, and plastic industries. At the nanometric scale, e.g. for powders with average particle size < 100 nm, the combination of TiO_2 high surface area and enhanced semiconductor properties (especially within the anatase crystalline form) makes it an ideal candidate for a variety of innovative application fields. The most promising of these include photovoltaic devices [29,30], photocatalytic applications (water splitting [31-34], waste-water treatment [31,35,36] and antimicrobial agents [37-39]), electrochromic devices [40,41], energy storage [42,43], etc…

Among these applications, dye-sensitized solar cells have attracted a lot of attention after the seminal publication in 1991 of the first light-to-electric energy conversion yield results (7.1-7.9 %) by M. Graetzel [29], the inventor of the DSC. Since then, extensive research has been concentrated on the optimization of various parameters which are known to bear a significant impact on the overall efficiency of the device, such as the TiO_2 photoanode (morphology, structure, crystalline composition, etc…), the organic dye and electrolyte chemical composition. These efforts have led to greatly improved performance of DSC devices, up to 11.18 % [44] and opened great opportunities for the development of new low-cost, well controlled and reproducible processes for the synthesis of nanostructured TiO_2 powders with tailored properties [45], such as the aqueous synthesis-based process investigated in this study. More details are provided in the last section of this literature survey, which are related to the structure, working principles and optimization of TiO_2-based DSC fabrication methods and performance.

2.3. Synthesis of TiO_2 particles

2.3.1. From the manufacture of pigments to the synthesis of nanomaterials

The manufacture of TiO_2 powders has been widely accomplished (for several decades) through hydro- or pyrometallurgical processes, namely the "sulfate process" and "chloride process" with the latter being currently the dominant process. Their flow charts are presented and compared in Figure 2.6. The resulting products are TiO_2 white pigments with broad particle size distribution in the micron and submicron size range. These are provided with very good light scattering, opacity, stability, and non-toxicity properties.

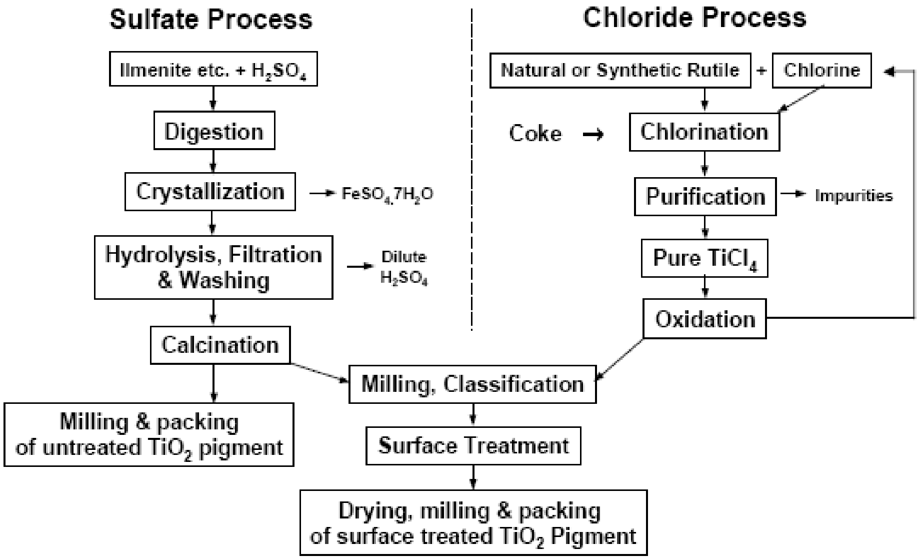

Figure 2.6. Schematic description and comparison of the sulfate and chloride processes for the synthesis of TiO_2 pigments, taken from ref. [46].

With the increasing demand for nanostructured TiO_2-based materials (powders, thin films, porous membranes, textile fibres, etc…), a range of synthesis techniques have been developed that may provide solutions to advanced fields of technology. Among the exhaustive list of investigated techniques (sol-gel, micelle and inverse micelle, sol, hydrothermal, solvothermal, direct oxidation, chemical vapour deposition, physical vapour deposition, electrodeposition, and sonochemical and microwave methods) some have attracted more attention based on the reported experimental results or their practical and cost-effective advantages. The following sections provide some insights on the methods specifically developed for the synthesis of TiO_2 nanoparticles with controlled properties.

2.3.2. High temperature (vapour) methods

2.3.2.1. Chemical and physical vapour deposition (CVD and PVD)

The CVD and PVD techniques are based on the use of a liquid or solid precursor which is first vaporized at high temperature under vacuum conditions and further condensed into a solid-phase material at the surface of a substrate. The condensation is driven by the temperature difference between the flame or the plasma used to vaporize the precursor and the substrate. In the case of PVD, unlike CVD, no chemical reaction occurs. Both techniques have been successfully used for the deposition of nanostructured TiO_2 thin films on a variety of substrates. For instance, *Wu et al.* [47] obtained homogeneous thin films of well aligned and perpendicularly oriented TiO_2 nanorods (200-300 nm) by condensation on a silica substrate of a titanium acetylacetonate precursor vaporized at 500-700 °C in an N_2/O_2 gas flow. Other researchers developed PVD methods involving the use of Ti powders as precursor. Typically, vaporization of the powders was conducted in a vacuum chamber under ~ 300 Torr at 850 °C in an argon gas flow and condensation led to direct deposition of a layer of TiO_2 powders or nanowires depending on the experimental parameters [48]. In both CVD and PVD methods, it is usually possible to vary the experimental conditions in order to control the shape and the phase of the deposited TiO_2 nanomaterials as well as the thickness of the resulting film. However, the high production costs associated to the temperature conditions, and the complexity of the equipment used, constitute significant drawbacks.

2.3.2.2. Flame hydrolysis

A derivative of the CVD method is flame hydrolysis that was successfully developed and used for the industrial production of highly crystalline TiO_2 nanopowders. This process is currently used to produce the P25 powder from Degussa (Evonik) [49] which is considered the main reference material among other commercially available TiO_2 nanopowders. Unlike CVD and PVD, flame oxidation/hydrolysis is run under atmospheric pressure conditions, and condensation of the vapor phase into a solid-phase material is driven by the temperature difference between the flame and the ambient temperature. The precursor, usually a solution of $TiCl_4$ or titanium tetraisopropoxide, is vaporized using argon as a carrier gas into a reactor chamber heated at high temperature $T > 1000$ °C under a pre-mixed O_2/H_2/air or O_2-CH_4/air gas flow (or flame). The temperature of the flame, the composition the of precursor, and the gas composition and flow rates may be adjusted to control to some extent the properties of the TiO_2 powdered material [50,51]. However, the obtained powders are often characterized with broad particle size distribution and the phase and impurity contents are difficult to control. Recently, a lower temperature variation of this process has been developed by Altair Nano [52] that involves spray hydrolysis under atmospheric pressure at temperatures just over 200 °C.

2.3.3. Solution methods

2.3.3.1. Sol-gel

Sol-gel synthesis has been widely investigated as a possible route to produce TiO_2 nanostructured materials with controlled properties. This method consists in forming a colloidal suspension of very fine particles by hydrolysis and polymerization of an inorganic metal salt or metal organic compound (typically alkoxide). Once polymerization is completed, a liquid gel composed of an amorphous polymeric network of titanium oxides and hydroxides is obtained that can be further employed either as is or after hydrothermal treatment (more on the latter in section 2.3.3.2) to fabricate thin films (by spin-coating or dip-coating), aerogels (under supercritical conditions), complex 3D structures (by using templates) or nanopowders.

Hydrolysis of the precursor, typically a Ti(IV) alkoxide of formula $Ti(OR)_x$, is achieved by addition of water. Generation of Ti-O-Ti bonds and further polymerization of the precursor into primary particles is induced by addition of a catalytic agent, usually an inorganic acid solution aimed at controlling the peptization of the colloidal suspension. A fine tuning of the experimental parameters such as the pH, temperature and water content makes it possible to favor the formation of long polymeric Ti-O-Ti chains or 3-dimentional structures within a narrow size distribution range.

Among the exhaustive list of investigated precursors, titanium tetraisopropoxide (TTIP) has been used by many research groups to synthesize pure anatase nanoparticles with controlled diameter. For instance, the production of TiO_2 nanopowders with an average size distribution of 10-15 nm dedicated to the fabrication of mesoporous films in the early DSC devices [45] was realized based on a multi-step sol-gel/hydrothermal process: a mixed TTIP/acetic acid precursor was hydrolyzed by addition of water and peptization was controlled using nitric acid at ambient temperature; the hydrothermal treatment was carried out in an autoclave at 230 °C for 12 hrs. *Cordero-Cabrera et al.* [53] realized a systematic study showing the effect of the precursor (TTIP)/water molar ratio, temperature (50-90 °C) and concentration of the peptizing agent (HNO_3). They found that temperature had the greatest impact on the size uniformity of the particles and reported conditions for the synthesis of monomodal sols with average particle size from 6 to 40 nm in the temperature range 50 - 70 °C. The use of additives such as amines, which act as surfactants and shape controllers, was also explored. For instance, *Chemseddine and Moritz* [54] found that a fine control of the initial concentrations of the titanium alkoxide precursor and the additive, tertramethylammonium hydroxide, led to the formation of triangular, ellipsoidal or hexagonal nanocrystals with very narrow size distribution.

A derivate method of the sol-gel route has been developed that makes use of organic surfactants for controlling the particles size and shape properties, namely the micelle and inverse micelle method. *Kim et al.* [55] conducted a study based on the use of a micelle route involving the hydrolysis of an organic solution of titanium tetraethylorthotitanate in cyclohexane with an oil/water microemulsion in the presence of a non-ionic surfactant, polyoxyethylene-5-nonylphenyl ether. By controlling the molar ratios of the precursor, water and surfactant, they obtained TiO_2 nanoparticles with different sizes and narrow size distribution. A non-hydrolytic approach, namely the sol method, was also developed which employs titanium tetrachloride as a precursor while the oxygen donor may be chosen from a wide range of chemicals from titanium alkoxides to organic ethers. This method proved effective for the fabrication of short nanorods or nanoparticles with high homogeneity in size and shape, as reported by *Zhang et al.* [56].

According to this review, it is clear that the sol-gel and its derived method offer a relatively easy and low capital cost way to synthesize TiO_2 nanomaterials with well adjusted morphological properties. However, these methods suffer from some significant inconveniences: 1) Results with low reproduction yield are often associated with these techniques due to the great dependence of the products properties on the experimental parameters; 2) the resulting products are characterized with very poor crystallinity. Supplemental heat treatments, such as annealing or hydrothermal and solvothermal processing, which are introduced in the next section, most often need to be employed in order to remediate the latter issue. The latter adds to the cost and complexity of the process that makes it less suited for large scale production. Finally, the sol-gel process involves the use of many organic chemicals that impose environmental pressures if large scale operation is employed on one hand while on the other the used TTIP precursor is significantly more expensive than $TiCl_4$ - the latter produced in million tones each year as part of the chloride pigment manufacturing process.

2.3.3.2. Hydrothermal and solvothermal processing

Hydrothermal and solvothermal processes in general rely on the use of an autoclave. The difference between the hydrothermal and solvothermal routes lies in the nature of the solvent: the process is said to be hydrothermal or solvothermal depending if the solvent used to carry the reaction is aqueous or organic, respectively. An advantage of both techniques is the elevated range of processing temperature, usually passed the boiling point of the solvent. Also, the hydrothermal and solvothermal routes are very often employed for improving the crystallinity of particles initially synthesized via the sol-gel route. *Yanagizawa and Ovenstone* [57] studied the impact of hydrothermal treatment (at 250 °C, in the presence of various inorganic salts and under acidic and basic conditions) on the crystallinity and phase composition of TiO_2 amorphous powders which had been prepared via three different sol-gel routes involving the use of TTIP or $TiCl_4$ as precursors. The results showed that 1 hr of hydrothermal processing at 250 °C was sufficient to drastically improve the crystallinity of the powders. In the same study, it was found that basic conditions and/or the presence of sulfate ions favor the crystallization of pure anatase phase. *Shan and Demopoulos* [58] recently reported on the synthesis of well-dispersed and phase-pure anatase TiO_2 nanoplatelets via hydrolysis of a $TiCl_4$ solution carried out at 240 °C with ethylene glycol as a solvent.

2.3.4. Aqueous synthesis method

Aqueous synthesis in the context of the present work involves the preparation of oxide particulate materials by forced hydrolysis of aqueous inorganic metal salt solutions. As such, therefore it belongs to the category of solution synthesis methods. However, what makes this process particularly interesting is that unlike the popular multi-steps sol-gel/hydrothermal or solvothermal processes, aqueous synthesis is run under atmospheric pressure conditions. Thus, it does not require the use of expensive autoclaves and makes it low-cost and easily scalable. Moreover, aqueous synthesis is by far more environmentally friendly than the sol-gel and solvothermal processes, which are organic chemical-intensive. Several studies already provided proof that aqueous synthesis may be considered for the elaboration of high production yield methods for the synthesis of ceramic nanomaterials with tailored properties. For instance, *Vayssieres* [59] reported on the growth of semiconductor nanostructured zinc, iron, and manganese oxides on different types of substrates by heterogeneous precipitation of aqueous inorganic metal salt solutions at low temperature < 100 °C. Other researchers explored the aqueous synthesis of TiO_2 nanomaterials based on the hydrolysis of $TiCl_4$, $TiOSO_4$, and TiF_4 solutions and tested the obtained materials for a variety of application domains ranging from the fabrication of photoanodes for DSC devices to photocatalytic applications [60-64]. However, precursors such as TiF_4 aqueous solutions are not desirable for obvious safety and environmental reasons, especially when designing large-scale production processes. Section 2.4.2 of this literature review provides an overview on the underlying theory and advances related to the aqueous synthesis of TiO_2 nanomaterials based on forced hydrolysis of $TiCl_4$ solutions.

2.3.5. Discussion

The above review described briefly the various methods which have been commonly reported for the synthesis of TiO_2 nanomaterials. Although several studies related to the development and improvement of these methods at the laboratory scale already provided very promising experimental results, scaling-up of these processes for industrial production of nanomaterials with identical properties remains a challenge. For instance, the sol-gel route, although very popular among researchers, makes use of organic precursors or solvents, which are often not compatible with the environment and rather expensive. Besides they require the use of supplemental post heat treatment, which increase the duration, complexity (use of autoclaves) and cost of the process. Energy intensive techniques such as chemical and physical vapor deposition are fast and efficient processes. However, the complexity of the associated set-up (high temperature vacuum chambers, plasma, etc…) represents a real obstacle to the scaling-up of these techniques. The flame hydrolysis process seems to have successfully overcome the latter issues, nonetheless bringing along limited control of the product properties (most notably the phase composition and particle size distribution). In view of these issues, there exists a need for developing low cost, easily scalable, high production yield and environmentally friendly processes, such as the aqueous synthesis based on forced hydrolysis, the method investigated in this study.

2.4. Aqueous synthesis of TiO_2 nanoparticles

2.4.1. Forced hydrolysis - General Theory

Forced hydrolysis is a process aimed at synthesizing metallic oxide particles by homogeneous precipitation in aqueous solutions. It is carried out by heating or diluting a metal salt solution in order to force the hydrolysis of the hydrated metal ions in solution. From a chemical point of view, the formation of metal oxide particles happens through progressive deprotonation of the hydrated metal ion complexes in solution, as shown in Equation 2.4 [65]:

$$xM(H_2O)_n^{z+} \Rightarrow M_x(OH)_y(H_2O)_{(nx-y)}^{(xz-y)+} + yH^+ \tag{2.4}$$

Formation of colloidal particles by homogeneous precipitation in solution is described in Figure 2.7. Particle nucleation starts with the formation of hydrated metal complexes in the dilute solution. These monomers in turn get bonded to each other and give rise to longer polymeric chains which cluster into embryos. The progressive organization of the embryos leads to the formation of nuclei. Growth of the nuclei into nanosized primary particles or crystallites takes place via diffusional growth until the crystallites have reached their critical size. These further get aggregated into bigger amorphous or crystalline particles. If the resulting particle-suspension solution mixture is allowed to age, the crystalline character of the particles may change due to further particle growth and associated phase transitions as explained in section 2.2.2 of the review. The nature of the final products is strongly influenced by the precursor aqueous species initially present in the solution. This in turn signifies that the initial concentration and speciation of the solution are crucial parameters. The kinetics of the hydrolysis reaction is also critical to the characteristics of the particles produced. Forced hydrolysis is controlled by selecting and maintaining an appropriate temperature.

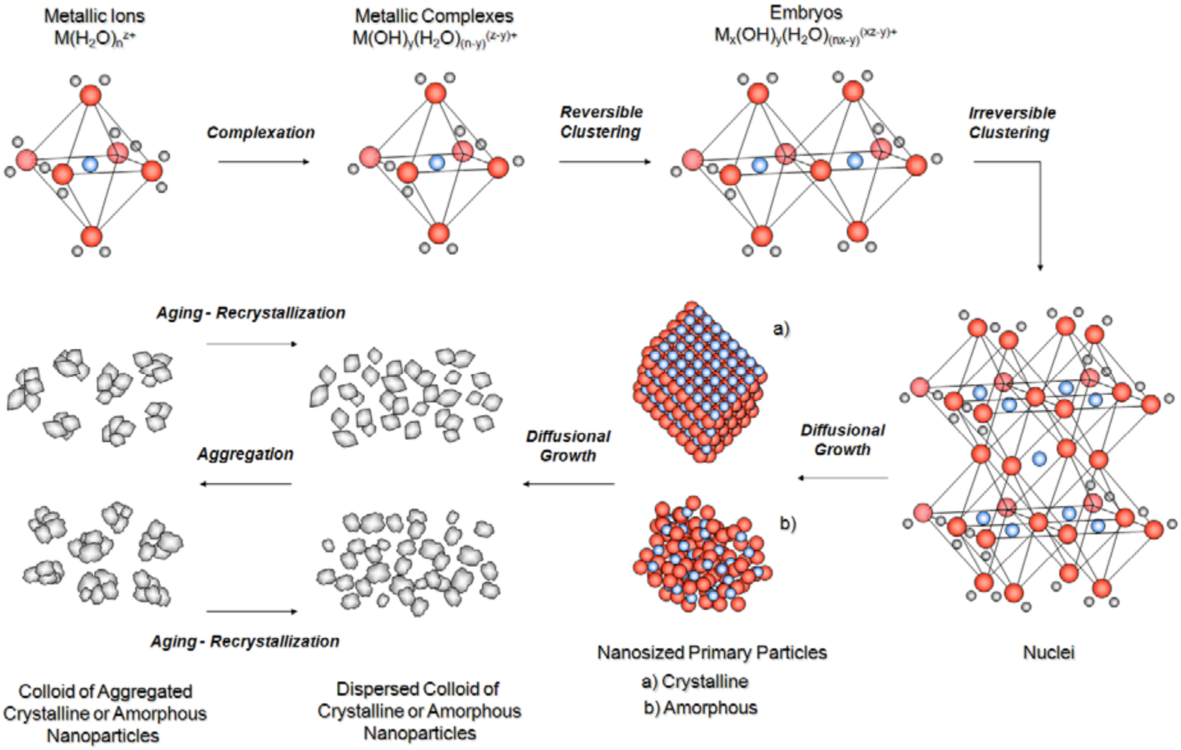

Figure 2.7. Stages in the formation of colloidal particles by precipitation in homogeneous solutions. Adapted from [65].

2.4.2. Synthesis of TiO_2 via forced hydrolysis of $TiCl_4$ solutions

2.4.2.1. Speciation of Ti-Cl-H_2O aqueous systems

In Ti-Cl-H_2O aqueous systems, Ti(IV) may be present in different forms from simple hydrated cations to more complex ones depending on the pH and Cl^- concentration of the solution, as presented in Figure 2.8. At ambient temperature, dilution of pure liquid $TiCl_4$ with water favors the formation of intermediate 6-coordinated octahedral aqueous species, namely hydrated oxy- or hydroxy-chloro-titanium complexes of general formulae $[TiO_yCl_n.(H_2O)_{6-y-n}]^{4-(n+2y)}$ or $[Ti(OH)_xCl_n.(H_2O)_{6-x-n}]^{4-(n+x)}$, among those presented in Figure 2.8.

However, the qualitative and quantitative determination of such species by employment of spectroscopic methods remains limited. Only very few species such as $TiOCl_2$(aq), which is commonly referenced as the major product of the reaction of pure liquid $TiCl_4$ with water at ambient temperature [66-71], were encountered both in spectroscopic and thermodynamic studies (Figure 2.8). According to resin ion exchange studies [72,73], as the concentration of Cl^- ions in a Ti-Cl-H_2O aqueous solution is increased, the population of chlorine ions coordinated to Ti(IV) central cations becomes denser. On the other hand, according to thermodynamic studies [72,74,75], when the pH of such aqueous solutions increases, chlorine anions progressively get replaced by hydroxyl groups (-OH), as suggested in Figure 2.8. The same phenomenon was also reported under the effect of dilution or temperature increase [76], e.g. when forced hydrolysis is promoted.

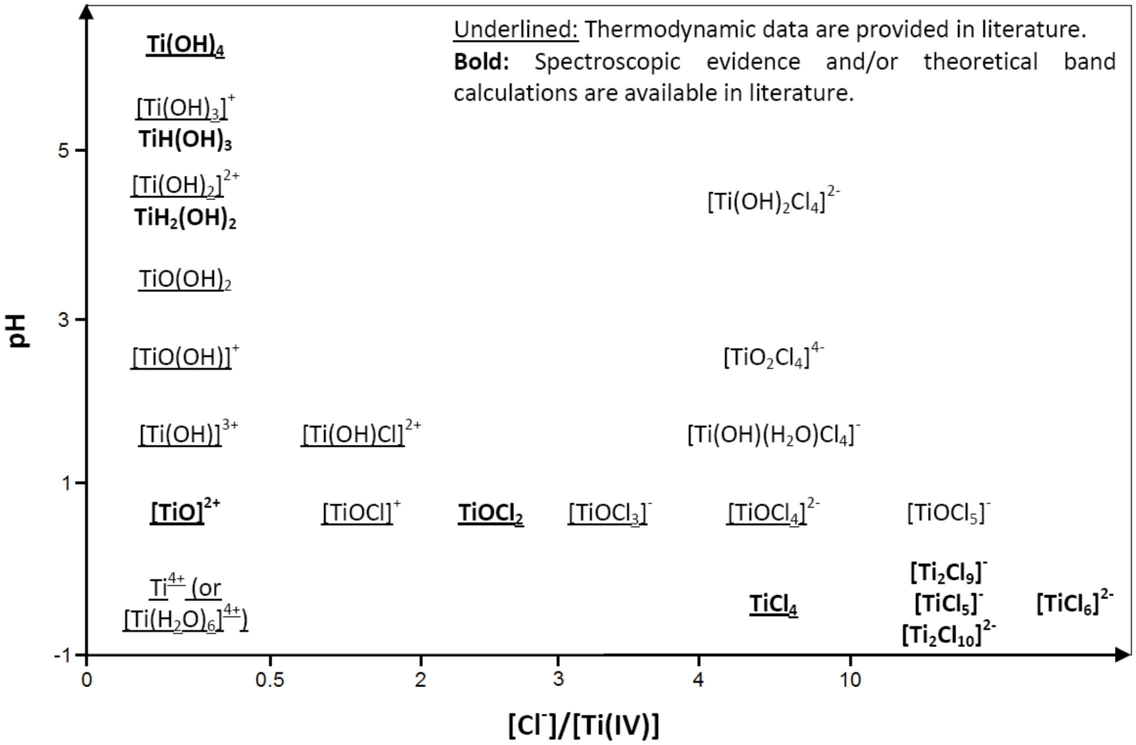

Figure 2.8. Composite speciation diagram of the species present in Ti-Cl-H_2O aqueous systems based on data from various spectroscopic and thermodynamic studies [66, 69-75,77-90].

2.4.2.2. *Nucleation and growth of TiO_2 particles*

Nucleation of TiO_2 particles starts with the progressive assembling of octahedral solvated complexes, or monomers, described in the previous section. In solution, these get bonded to form polynuclear chains or clusters via polycondensation of the -OH/-OH_2 groups. The chemical reactions involved in this transformation, the olation and oxolation reactions [91,92], lead to the formation of oxo and hydroxo bridges along with elimination of water. They proceed via one- and two-step nucleophilic substitution as described in Figure 2.9.

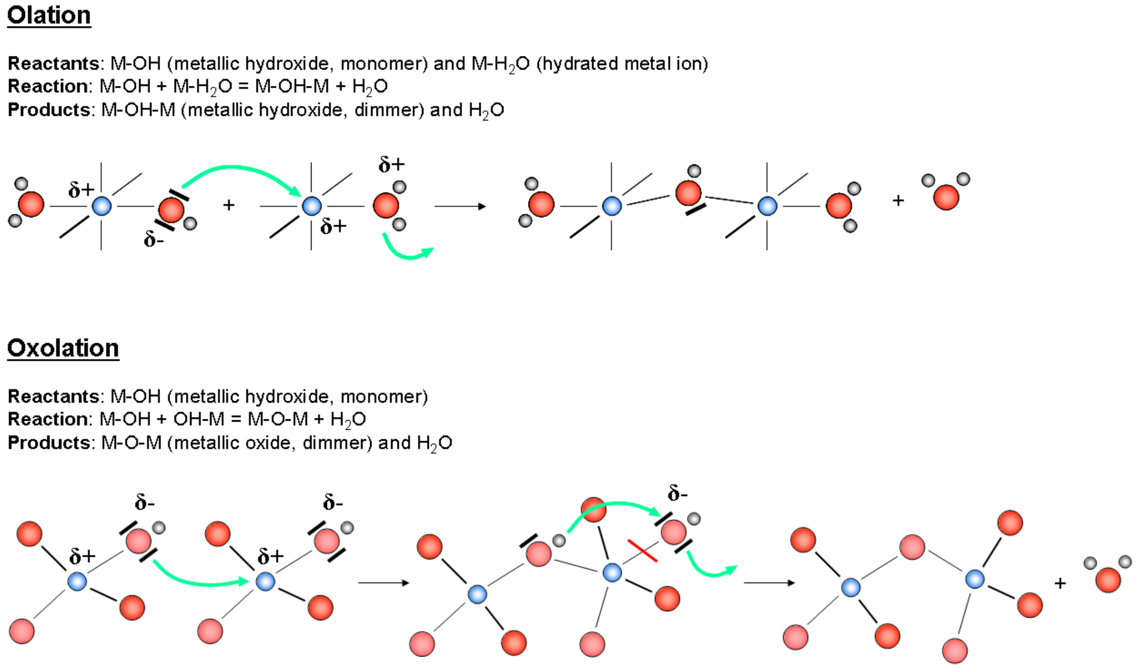

Olation

Reactants: M-OH (metallic hydroxide, monomer) and M-H_2O (hydrated metal ion)
Reaction: M-OH + M-H_2O = M-OH-M + H_2O
Products: M-OH-M (metallic hydroxide, dimmer) and H_2O

Oxolation

Reactants: M-OH (metallic hydroxide, monomer)
Reaction: M-OH + OH-M = M-O-M + H_2O
Products: M-O-M (metallic oxide, dimmer) and H_2O

Figure 2.9. Olation and oxolation theoretical mechanisms, adapted from [91-93].

Depending on the nature of the present complexes, e.g. configuration of the -O, -OH, -OH_2 and -Cl groups coordinated to the Ti(IV) cation, the growth of TiO_2 unit cells is driven by sharing of corners, equatorial and/or apical edges of the octahedral monomers, as suggested in a few studies [76,94,95]. Consequently, the formation of nuclei can be oriented towards the crystallization of rutile, brookite or anatase phases.

Theoretical mechanisms have been proposed [94,95], such as those shown in Figure 2.10 which illustrate the selective formation of rutile and anatase or brookite nuclei via sharing of the equatorial and apical edges of $[Ti(OH)_2(OH_2)_4]^{2+}$ octahedral monomers, respectively.

Once primary nuclei are formed, their growth takes place through a diffusion process until equilibrium, in terms of particle surface tension, has been reached. While crystallites get bigger, they may undergo phase transitions as explained in more detail in section 2.2.2 of this review. Growth of TiO_2 particles also takes place via aggregation [96]. Once the crystallites have reached their stable size, either they remain in the form of a stable dispersed colloid or they tend to aggregate into larger particles. Both diffusional growth and aggregation phenomena strongly depend on the temperature at which forced hydrolysis is run and on the concentration of the solution. High temperature ($T > 200$ °C) and low concentration ($[TiCl_4] < 0.5$ M) were reported by *Cheng et al*. [76] to favor small particle size and moderate aggregation of particles. On the contrary, at lower temperature ($T < 100$ °C) and/or higher concentration ($[TiCl_4] > 1$ M), micron-size aggregates were reported to be obtained. The same phenomena were observed elsewhere [97,98]. Although the effect of concentration and temperature on particle size, aggregation and shape were described in a few isolated case studies, no fundamental kinetic study concerning the precipitation of TiO_2 via forced hydrolysis of $TiCl_4$ solutions has yet been reported. Modelling of the precipitation yield vs. time curves with the Avrami precipitation kinetics model may be proposed as a new way to characterize the kinetics of TiO_2 particle nucleation, growth and aggregation. Correlation of the modelling results with a complete characterization of the products obtained in varied experimental conditions may provide explanations for the effect of temperature and $TiCl_4$ concentration on the TiO_2 particles final size, shape and aggregation stage. Such type of study was for instance performed by *Sarraf-Mamoory et al.* [99,100] in the case of preparation of fine copper powders from organic media.

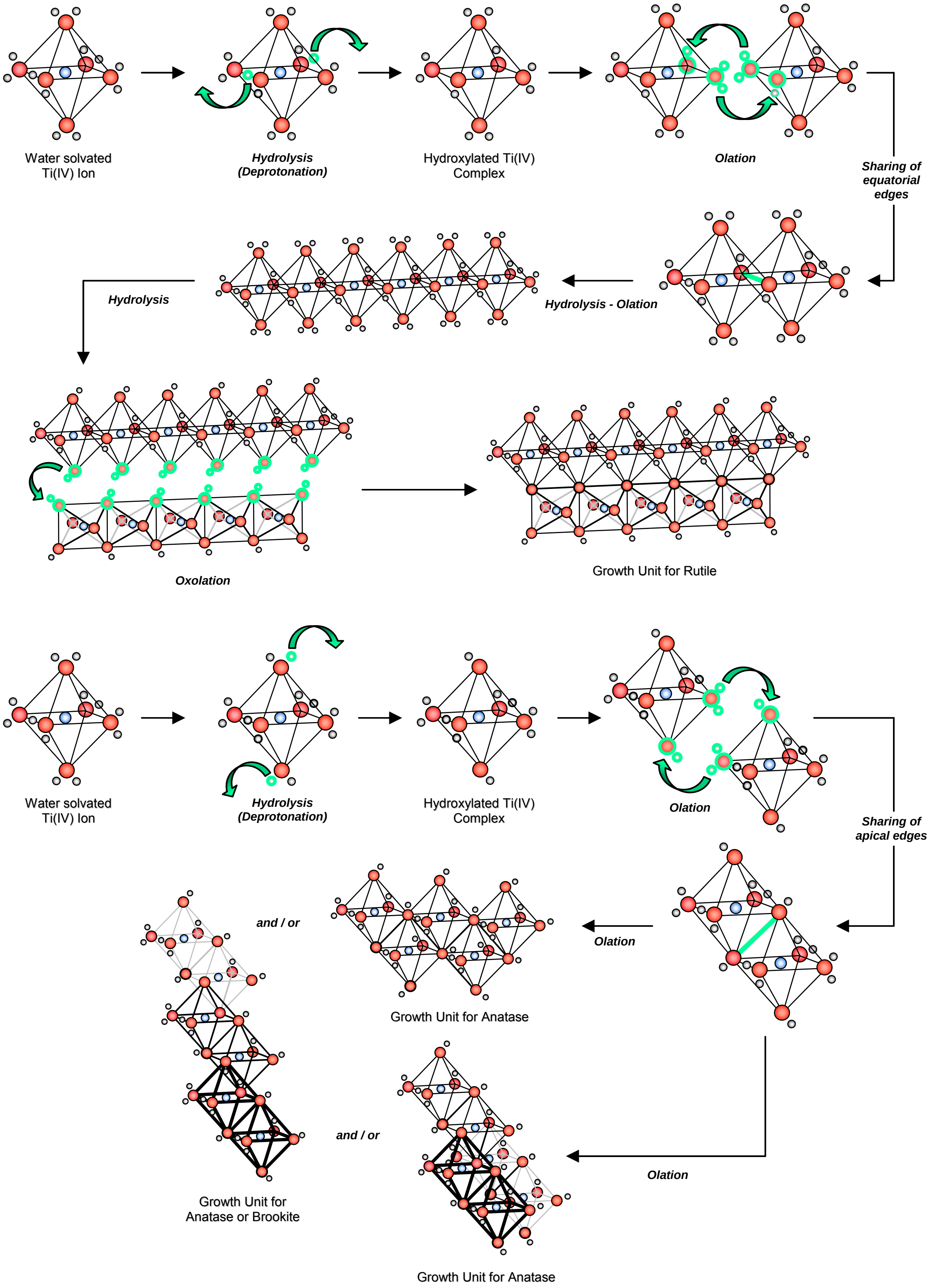

Figure 2.10. Possible condensation pathways for TiO_2 nuclei of rutile (a), and anatase and brookite (b) nuclei starting from octahedral cations $[Ti(OH)_2(OH_2)_4]^{2+}$, adapted from ref. [93].

2.4.3. Advances on the synthesis of TiO_2 nanoparticles from $TiCl_4$ solution

2.4.3.1. Via forced hydrolysis

Synthesis of TiO_2 nanoparticles with the rutile, anatase, brookite or mixed phase by forced hydrolysis (isothermal treatment) of $TiCl_4$ aqueous solutions has been the subject of a number of investigations. *Kim et al*. [67] studied the precipitation of TiO_2 nanostructured powders, with the use of an autoclave, from an aqueous 0.67 M $TiCl_4$ solution at various temperatures. Drying of the powders was performed at 150 °C for 2 hours. Powders with different compositions were reported: pure rutile powders at $T < 65$ °C and $T > 155$ °C, pure anatase powders at 70 °C $< T <$ 95 °C, and mixed powders of rutile and anatase in the temperature range 95 °C $< T <$ 155 °C. However, *Addamo et al.* [98] reported the production of poorly crystalline anatase nanosized particles at the boiling temperature ($T > 100$ °C) from a 0.9 M $TiCl_4$ aqueous solution and only at higher concentration (4.5 M $TiCl_4$) a mixture of poorly crystalline mixed phase of rutile and anatase was obtained. In this case, drying of the powders was performed at 60 °C over two days. By comparing the characteristics of the powders obtained in the temperature range $T > 100$ °C in these two studies [67,98] it may be observed that: a) concentration has an effect on the crystalline phase of the powders; and b) drying temperature improves the degree of crystallinity of the products. *Zheng et al.* [93] studied separately the influence of concentration and temperature on the composition of the obtained mixed crystalline anatase and rutile phase powders. At 200 °C and in the concentration range 0.1-1 M $TiCl_4$, they reported that the higher the concentration, the higher the content of rutile phase becomes. Similarly, for a 0.3 M $TiCl_4$ solution isothermally treated in the temperature range 100-300 °C, they found that an increase of the crystallizing temperature was accompanied with a raise of the rutile phase. Finally, *Li and Demopoulos* [101], as part of their study on nanosized TiO_2 precipitation from $TiCl_4$ aqueous solution by neutralization with MgO, observed the production of nanostructured rutile particles by forced hydrolysis at 95 °C. In particular, rutile TiO_2 powders with different crystallite sizes between 11 and 18 nm were obtained from aqueous $TiCl_4$ solutions with Ti(IV) concentration ranging from 0.5 to 2 M.

2.4.3.2. With the use of additives

The use of additives for the control of the shape, size or crystalline phase of TiO_2 powders formed via hydrolysis of $TiCl_4$ solution has been examined to some extent in the past. Hydrolysis of a $TiCl_4$ aqueous solution by addition of a base (neutralization) with further ageing of the suspension under controlled conditions of temperature, ionic strength, and pH has been reported for the selective production of anatase, brookite, and rutile nanoparticles [68, 102-104]. In general, the addition of a base into an acid metal salt aqueous solution at ambient temperature leads to the precipitation of small metastable and amorphous metal oxyhydroxide nanoparticles [91,105]. However, the size and crystalline degree of these primary particles may be improved upon ageing under specific conditions. For instance, a fine control of the pH, hence the protonation/electrostatic charge density of the particles surface, may be used to control the final particle size by lowering the interfacial tension between the particles. The ionic strength of the solution may be adjusted in order to orient the crystallization of the nanoparticles into a targeted phase by controlling the speciation of the suspension. *Pottier et al.* [103] reported on the synthesis of TiO_2 nanoparticles by addition of 3 M NaOH to 0.7M $TiCl_4$ aqueous solution in the pH range $2 \leq pH \leq 6$ followed by ageing at 60 °C. They found that base addition first led to precipitation of 2-3 nm size amorphous $TiO_{0.5}(OH)_{1.5}\cdot 0.2H_2O$. These were further transformed into larger crystalline anatase, brookite or rutile nanoparticles upon ageing, depending on the pH and ionic strength (imposed by the addition of NaCl) conditions of the suspension. *Li and Demopoulos* [101] reported on the synthesis of mixed phase (rutile-anatase) TiO_2 nanoparticles by neutralization of 1.0 M $TiCl_4$ solution with MgO at 95 °C. The anatase fraction (ranging from 0 to 70 wt. %) increased with pH elevation (from 2.5 to 6). The magnesium content in the TiO_2 products was found to increase with a rise of the final pH due to partial hydrolysis of magnesium. It was less than 0.1 % when the final pH was kept at or below 3.

Sulfate ions are known for their ability to orient the hydrolysis reaction of $TiCl_4$ towards the selective production of anatase crystalline phase [102,106]. *Zhang et al.*

[107] also reported that the use of sulfate ion traces in $TiCl_4$ solutions inhibited the anatase-to-rutile phase transition and improved the uniformity of the powders. On the other hand researchers found that $TiCl_4$ aqueous solutions with high HCl or chloride salt content seem to favor the formation of brookite typically for $17 \leq [Cl_{total}]/[Ti] \leq 35$ and/or rutile for $[Cl_{total}]/[Ti] \geq 35$ [76,94,108,109]. The hydrolysis of $TiCl_4$ aqueous solution in the presence of concentrated HNO_3 was also reported by *Lee et al.* [110] to favor the formation of pure brookite TiO_2 nanoparticles. According to *Hwang et al*. [111] TiO_2 powders precipitated from solutions of $TiCl_4$ containing $AlCl_3$ or $ZrOCl_2$ were mainly crystallized in the anatase phase. Finally, *Yin et al.* [104] found that the use of HF and HCl as cooperative catalysts favored the production of anatase cubic nanoparticles.

The above review provides evidence that upon proper control, forced hydrolysis of $TiCl_4$ aqueous solutions can lead to the production of TiO_2 nanoparticles with tailored properties. Interesting enough, such aqueous-synthesized TiO_2 nanopowders have not been considered for the fabrication of DSC photoanodes. This is done in the present work.

2.5. TiO_2-based dye-sensitized solar cells (DSCs)

2.5.1. What makes DSCs part of our future

According to the latest estimations on global energy consumption [112], if we consider all energy sources together, an equivalent amount of 3 cubic miles (CMO), or 3.3 trillion gallons of oil is being used per year. To illustrate this number, 3 CMOs would put Manhattan under 150 feet of oil. The pie chart presented in Figure 2.11 shows the repartition of our global energy consumption with 87 % of it based on oil, coal and natural gas which are “inherited”, e.g. non-renewable energy sources and only 13 % relying on “income”, e.g. renewable energy sources such as hydroelectricity, biomass, geothermal, wind, photovoltaic, and solar thermal energy.

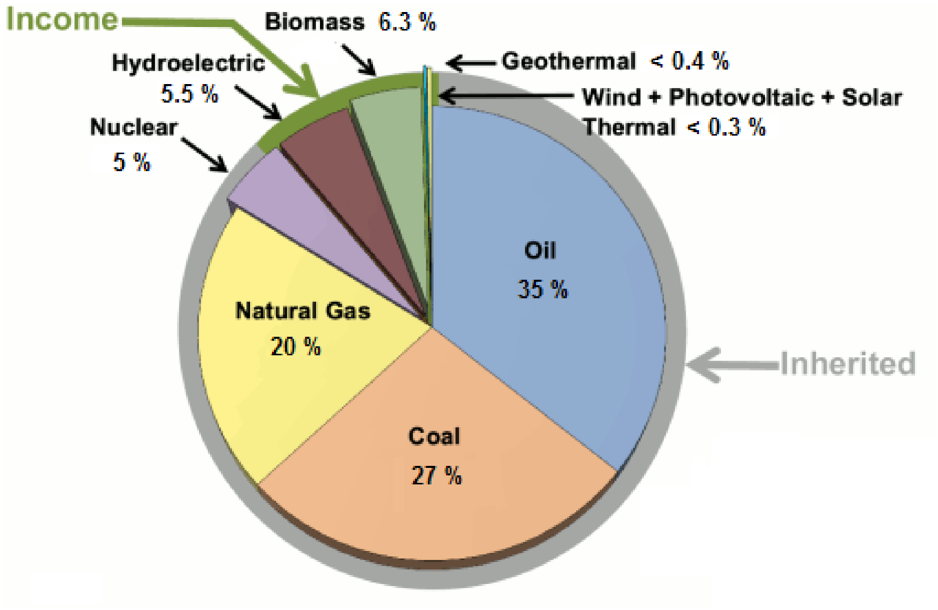

Figure 2.11. Pie chart representing global energy usage. Adapted from [113].

Estimations based on the consumption trend observed in the last decades predict that we will have progressively to rely more and more on the use of renewable energy sources over the next 40 years if we want to face the combined challenge of decreasing oil reserves, increased energy demand and mitigation of threatening climate change effects. This alarming situation justifies the urgent need for the development of new, clean and renewable energy sources as well as the scaling-up of the technologies already developed in laboratories.

Dye sensitized solar cells is one among the newly developed solar energy conversion technologies. Since the invention of DSC devices in the 90s by *O'Regan and Graetzel* [29], great improvements made at the laboratory scale have brought their light-to-electrical yield efficiency up to ~ 11-12 %, and facilitated their fabrication. These results encouraged the creation of several companies: Dyesol (Australia), G24i (United Kingdom), and Solaronix (Switzerland) have already started the commercialization of the diverse components necessary for DSC fabrication and are about to launch the first generation of derived products accessible to public consumers. Among these innovations are portable battery charging items (bag packs, blankets, etc…), embedded applications (cell phones, computer and TV screens, etc…) and fully building-integrated structures (roofs, blinds, stained windows, etc…). With their numerous advantages such as lost cost, light weight, thin, flexible (when prepared on plastic substrates or metal foils), customizable, performing under low light irradiance, DSC devices offer an infinite number of possibilities for the development of low scale applications.

2.5.2. Device structure, working principle and performance parameters

Dye-sensitized solar cells are photovoltaic devices engineered for generating electricity under light irradiation, in a certain way mimicking the photosynthesis phenomenon achieved by plants in nature. DSC devices differ from the conventional semiconductor devices in the sense that the light absorption function is separated from the charge carrier transport. As illustrated in Figure 2.12, DSCs are sandwich-like type of cells composed of a photoanode, a counter electrode, and a redox electrolyte mediator in between the two electrodes.

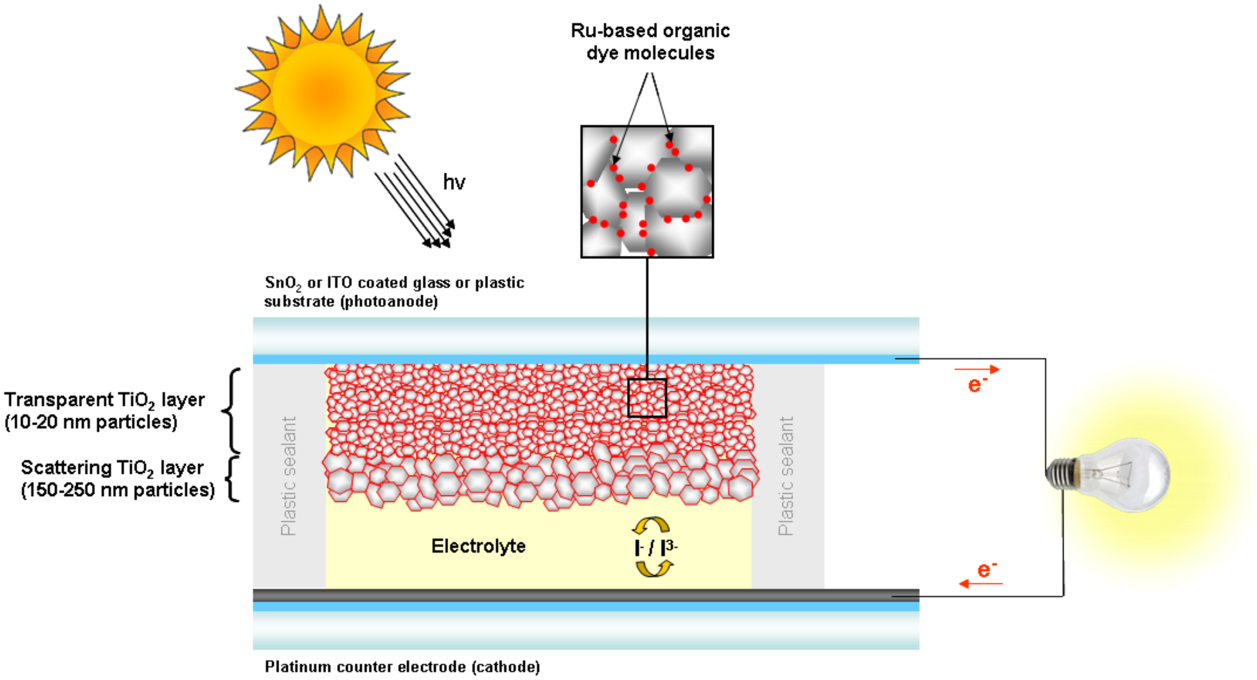

Figure 2.12. Diagram representing the structure of a DSC.

The photoanode, the focus of this research, consists of a thin mesoporous film of TiO_2 nanoparticles deposited on a conductive transparent substrate and sensitized with an organometallic dye. When the photoanode is irradiated by a light source, the dye is oxidized (Dye*, (1)) and electrons are injected into the conduction band of the semiconductor TiO_2 thin film (2), as shown in Figure 2.13. These generated electrons are further transported through the network of TiO_2 particles until they reach the conductive surface of the anode (3) and are further driven towards the platinum counter electrode through the external load. The electrolyte regenerates the ground state of the dye (Dye) by injecting electrons into its valence band: the dye accepts electrons from I^- ions of the I^-/I_3^- redox couple electrolyte (4), the latter get oxidized into I_3^-, which diffuses towards the counter electrode where it is reduced back to I^- ions (5). The maximum voltage generated by the device corresponds to the difference between the Fermi level of TiO_2 and the redox potential of the electrolyte. Overall, a DSC produces electrical power under illumination without suffering any significant permanent chemical damage.

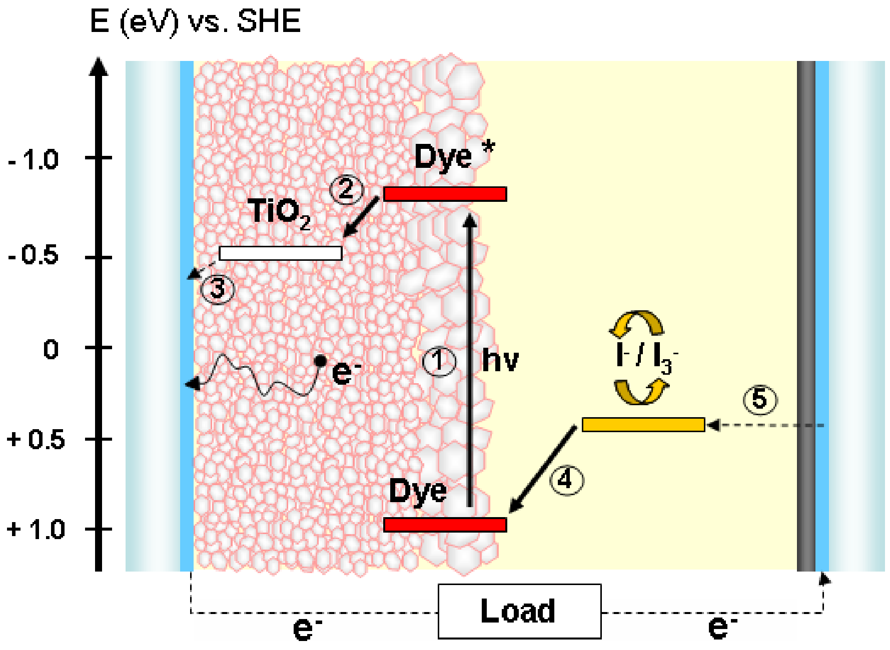

Figure 2.13. Diagram representing the working principle of a DSC, adapted from [114].

The following information provides more details about some major components of DSC devices:

- In this study, FTO (fluorine-doped tin oxide)-coated glass substrates were used for the assembly of DSC devices. However, one of the great advantages of DSCs is that flexible and light substrates such as ITO (indium-doped tin oxide)-coated plastic sheets or thin metal foils may also be used as electrode substrates.
- The TiO_2 semiconductor film is usually composed of a "transparent layer" and a "scattering layer" on top with particle size in the range 10-20 nm and 150-250 nm, respectively. On one hand, the transparent layer optimizes the quantity of adsorbed dye molecules, hence is characterized with a high surface area provided by the small TiO_2 nanoparticles. On the other hand, the "scattering layer" made of larger particles scatters/reflects the photons, which haven't been absorbed by the dye while crossing the transparent layer. Optimization of TiO_2 films is the subject of the next section.
- Typically, the dye or photosensitizer used is a ruthenium (II) complex, such as *cis*-(di-thiocyano)bis(2,2_-bipyridil-4,4_-dicarboxylic acid), commercially known as N719 (Figure 2.14) which was developed by Graetzel's group [114]. The absorption properties of the dye in the visible (450-600 nm) and near IR region (920 nm) are attributed to the metal (Ru) to ligand (NCS, thiocianato) charge transfer transition. Since this breakthrough, other ruthenium (II) sensitizers have been developed [115,116], namely the black dye, which made it possible to achieve overall DSC conversion efficiency of 10.4 %.
- The binding mechanism for the dye adsorption on the TiO_2 particle surface has been studied to some extent. *Leon et al.* [117], among others, proposed as the main binding mechanism the chemisorption of the dye via the covalent-like bonding of carboxyl groups from the dye to TiO_2 surface. More recently, *Lee et al.* [118] suggested a new mechanism involving mixed bidentate bridging and H-bonding between the carboxylic acid/carboxylate (-COOH, $-COO^-$) groups and Ti-OH surface groups.

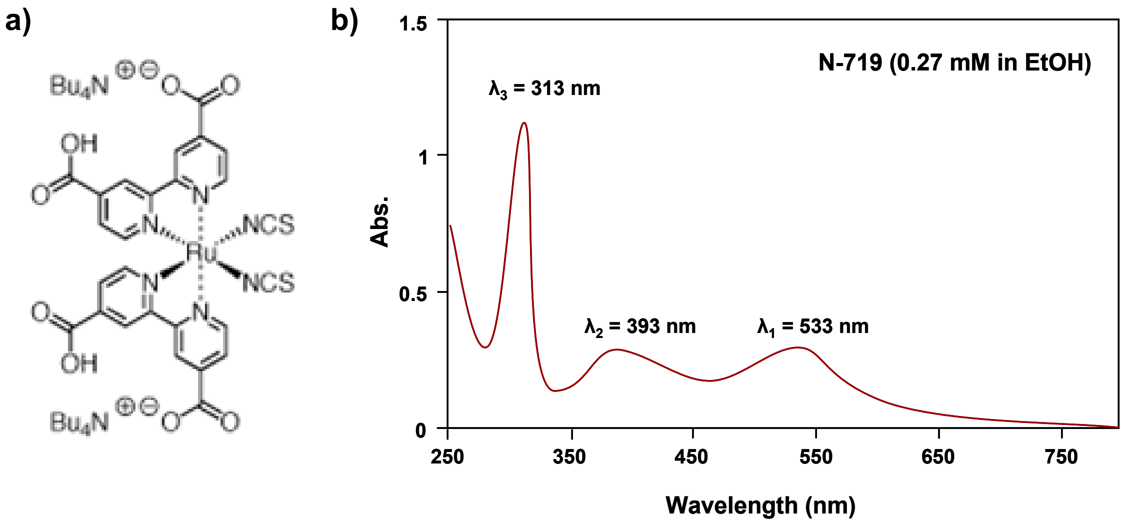

Figure 2.14. Molecular structure (a) and UV-Vis absorption spectrum (b) of the N719 ruthenium complex in solution, reproduced from [119,120].

- The electrolyte usually consists of an organic solvent containing a redox mediator system such as the iodide/triiodide couple. Lately, more extensive research has been devoted to improving the properties of the electrolyte as is the collaborative work of Marsan and Graetzel groups, which led to the development of a non-corrosive disulfide/thiolate redox couple [121].

The performance of a dye-sensitized solar cell is characterized by:

- Its short-circuit current density (I_{SC}), the maximum current density that can flow between the two electrodes.
- Its open-circuit voltage (V_{OC}), a measure of the maximum potential difference that can be provided by the cell (at $I_{sc} = 0$). Theoretically, the V_{OC} corresponds to the difference between the Fermi level of the TiO_2 nanoparticles and the redox potential of the electrolyte.
- The voltage and current density yielding maximum power, respectively V_{MP} and I_{MP}, as illustrated in Figure 2.15.

- Its fill factor (FF), is defined as the ratio of the maximum achievable power to the theoretical power, such as expressed in Equation 2.5:

$$FF = \frac{V_{MP} * I_{MP}}{V_{OC} * I_{SC}} = \frac{P_{\max}}{P_{theoretical}} \quad (2.5)$$

- Its overall light-to-current conversion efficiency, η, which corresponds to the ratio of the maximum achievable power of the cell to the power of the incident light irradiation, such as expressed in Equation 2.6:

$$\eta = \frac{P_{\max}}{P_{light}} \quad (2.6)$$

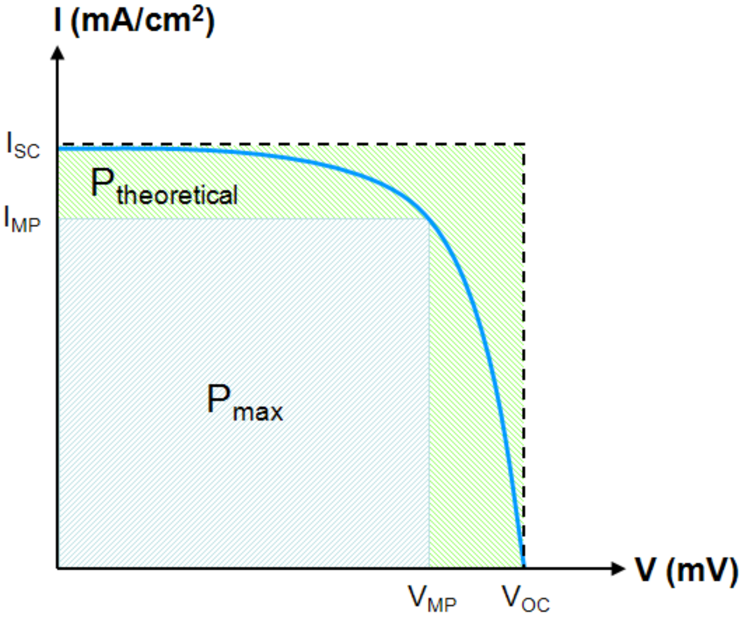

Figure 2.15. Diagram representing a typical DSC performance plot of I vs. V curve.

The performance of DSC devices is tested by determining the I vs. V curve (Figure 2.15) while the cell is irradiated by a calibrated light source simulating the sun light. Conventionally, the lamp is calibrated so that the incident light is characterized with a power of 1000 W/m^2 and AM 1.5 (Air Mass 1.5). Outside of atmosphere the power of the sun light reaches 1360 W/m^2 but at the sea level it is approximately 1000 W/m^2 due to light absorption by the atmosphere. The air mass index relates to the spectral energy distribution of the light (Figure 2.16). Air Mass 1 is associated to the light with the sun directly overhead whereas Air Mass 1.5 is associated to the light received by locations at latitudes between 30° and 60°, as illustrated in Figure 2.16.

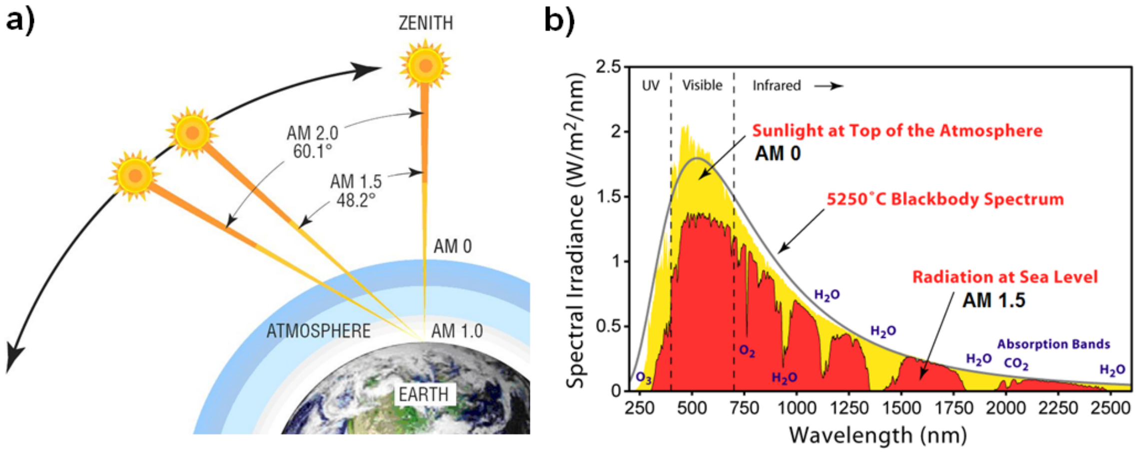

Figure 2.16. Representation of the atmospheric sun light absorption related to various air mass indices (a) and associated solar radiation spectrum (b), taken from [122,123].

2.5.3. Fabrication of TiO_2 photoanodes

The performance of DSC devices depends on a number of parameters related to the properties of the dye, the mesoporous semiconductor TiO_2 film, and the electrolyte. However, the scope of this research is restricted to improving the properties and fabrication method of the semiconductor film. This section provides an overview on the advances reported in literature regarding the latter aspects.

2.5.3.1. Fabrication techniques – Screen-printing

In the last decade, a variety of techniques has been developed for the fabrication of TiO_2 photoanodes used in DSC devices, such as doctor blade coating/screen-printing [124], hydrothermal crystallization [125], electrophoretic deposition [126], spray pyrolysis deposition [127], UV-assisted chemical vapour deposition [128], and lift-off/transfer [129]. Screen-printing, an easy technique already employed in a broad range of industrial applications (plastics, adhesives, glass and ceramics, electronics, etc…) has also become popular among research groups in the field of DSCs [130]. The technique consists in coating a water- or an organic-based paste onto a substrate by motion of a doctor-blade under precise conditions of pressure, speed, and angle, this way ensuring a good control of the thickness of the film as well as the reproducibility of high quality films. For the fabrication of TiO_2 photoanodes, a paste typically assuming ~ 10-15 wt. % TiO_2 nanoparticles loading is prepared for screen-printing. Screen printing is directly followed by sintering of the film at elevated temperature (450-500 °C) aimed at evaporating/burning off the supporting organic or mixed aqueous/organic medium and achieving necking/sintering of the particles network (Figure 2.17).

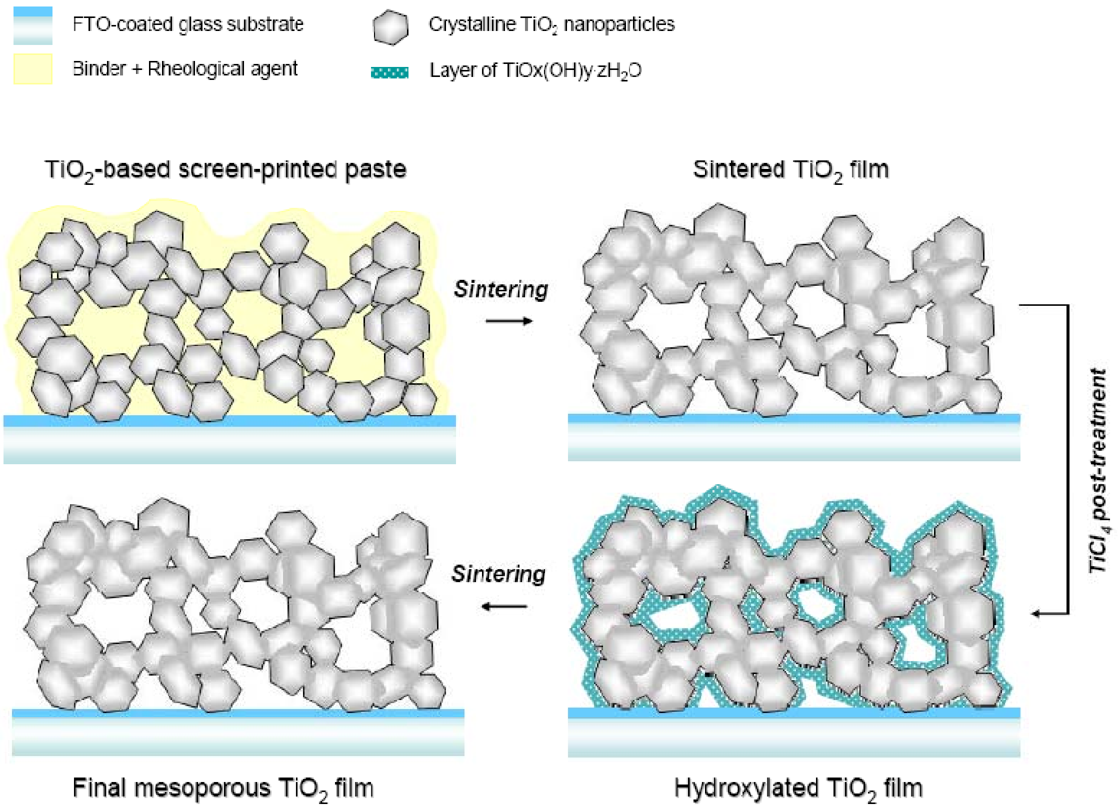

Figure 2.17. Schematic diagram illustrating the sintering and $TiCl_4$ post-treatment of a TiO_2 film.

A chemical post-treatment of the sintered film is often applied which consists in dipping the film in a low concentration (40-50 mM) aqueous solution of $TiCl_4$, followed by another sintering cycle. Optimization of screen-printed TiO_2 photoanode in DSC devices depends on a number of parameters among which the properties of the TiO_2 powders, the formulation of the paste, the thickness and structure (single vs. double layer) of the film, the sintering parameters, and the chemical $TiCl_4$ post-treatment, as discussed below.

2.5.3.2. Effect of TiO_2 nanoparticle characteristics

In addition to the light absorption and chemical stability of the dye, the performance of TiO_2 photoanodes primarily relies on the properties of the TiO_2 nanopowders. Among these properties, particle size and morphology [131-133], crystallinity, phase content [134,135], band gap [133], chemical composition (doping) [136] and surface groups [118,137] have been extensively studied and shown to have a significant bearing on the overall efficiency of DSC devices. First, the average particle size and particle size distribution need to be balanced so that the semiconductor film is characterized with a high surface area (to maximize the dye loading) and an average porosity in the mesoporous range (2-50 nm average pore size), to allow the diffusion of the dye and the electrolyte within the film. With respect to this issue, *Miranda et al.* [138] reported that the overall performance of DSC devices was optimized with photoanodes fabricated from powders with bimodal crystal size distribution consisting of two classes of nanocrystals, 5 and 50-100 nm in size, as compared to photoanodes based on powders with unimodal crystal size distribution. Moreover, the particles size should be considered carefully for its direct impact on the band gap of the film [133] and the electron diffusion length [139]. On one hand, the band gap of TiO_2 nanocrystals is known to increase with decreasing average crystal size, providing potential for the enhancement of the open circuit voltage in DSC devices. But on the other hand, *Nakade et al.* [139] found that the use of small nanoparticles is also known to have a detrimental effect on the electrons diffusion length and associated recombination life time. Second, the crystalline degree and phase content are important aspects of TiO_2 powders properties known to affect the efficiency of DSCs. High crystallinity of the TiO_2 powders favors electron transport with minimum charge recombination losses. Pure crystalline anatase nanoparticles are usually preferred for DSC applications due to their larger band gap. However, *Li et al.* [135] recently found that the introduction of 10-15 % rutile nanoparticles significantly improved light harvesting and the overall solar conversion efficiency of anatase nanoparticles in DSCs. Finally, the effects of bulk and surface chemical composition of TiO_2 nanoparticles were investigated to some extent. Enhanced performance of DSCs assembled with W- and/or Al-doped TiO_2 nanoparticles due to electrical surface-state modifications induced by the metal-ion dopants was reported by *Ko et al.* [136]. The presence of hydroxyl surface groups (Ti-OH) was recently suggested to contribute to a better photocurrent due to improved adsorption mechanism of the dye on the TiO_2 nanoparticles [118,137].

2.5.3.3. Effect of the paste formulation

The formulation of the paste plays an important role in the fabrication of TiO_2 mesoporous thin films with good uniformity, porosity, and mechanical properties [124,140,141]. Typically, the screen-printing paste is prepared by mixing TiO_2 nanopowders (pre-dispersed in a solvent) with a binder and a rheological agent. The obtained mixture is further condensed by evaporation until an appropriate viscosity and TiO_2 content has been reached. Each component of the paste has a specific functionality. The binder is used to create the voids in between the particles. It plays an important role during sintering as it affects the viscoelastic properties of the film and subsequently the final strength, porosity (density), and topological structure of the sintered film [142,143]. Typically, an excess of binder will result in poor adhesion of the film on the substrate whereas low binder content will induce the formation of cracks in the film. The rheological agent controls the dispersion of the particles and the viscosity of the paste [141]. Improved dispersion of the particles may be achieved by using additional surfactants, providing the paste with better steric stabilization and avoiding the aggregation of particles [144,145]. So far, most studies have reported on the use of polyethylene glycol (PEG) or ethylcellulose as binders, α-terpineol as a rheological agent, and ethanol as a solvent [124,141,143,144]. Only very few studies focused on the preparation of aqueous-based pastes even though these are less chemical intensive, hence more environmentally friendly and better suited for large scale production [140,146].

2.5.3.4. Effect of the structure of the film

Optimization of the thickness and structure of the film has also been investigated by a few research groups [145,147,148]. Ideally, the thickness of the film should be smaller than the electron diffusion length so that a maximum number of electrons injected to the CB of TiO_2 can reach the conductive surface of the anode. Given that the electrons life time or diffusion length depends on such parameters as the TiO_2 particle size and shape, there is no absolute optimal film thickness. For instance, *Ito et al.* [147] reported that the best light-to-current conversion efficiency results were obtained for 12-14 µm TiO_2 films prepared with 20 nm average particle size, whereas *Lao et al.* [146] found that 6 µm was the best film thickness for photoanodes prepared with 10 nm mean particle size. The structure of the film also plays an important role in the performance of DSCs. The addition of a scattering overlayer containing TiO_2 particles with larger diameter (150-500 nm), on top of the transparent layer, was found to enhance the photocurrent of DSCs [147,149]. The function of the scattering layer is to scatter back the incident photons that were not absorbed by the dye while travelling across the transparent layer, this way enhancing the light collection properties of the photoanode. The scattering effects may also be achieved by adding an overlayer containing submicron size cavities acting as scattering centres, for instance characterized with an inverse opal structure, such as suggested by *Tao et al.* [150].

2.5.3.5. Effect of sintering temperature profile and $TiCl_4$ post-treatment

Finally, other fabrication parameters such as the sintering temperature profile and the application of an additional $TiCl_4$ post-treatment of the film were found to strongly affect the performance of DSCs. Sintering of the film is usually achieved by step-wise gradual increase of the temperature [151]. *Lee et al.* [152] studied the effect of sintering temperature in the range 400-600 °C and found that the overall cell efficiency was optimized for films sintered at 500 °C due to necking of the particles. Above 500 °C, crystal growth occurred leading to a decrease of the surface area of film, hence of the amount of dye adsorbed, which translated into lower photocurrent. Post-treatment of the film with an aqueous solution of $TiCl_4$ is often applied to enhance the photocurrent of the cell [146,152,153]. However, the root cause of this enhancement remains quite unclear. At first it was suggested that $TiCl_4$ post-treatment improved particle necking via chemical sintering (formation of a thin layer of Ti-oxo/-hydroxo species at the surface of the particles, further transformed into crystalline TiO_2 during sintering), hence improving the electrons transport within the network of particles [147]. However, this assumption is contradictory with the observations made by *Yip et al.* [153] who reported that the $TiCl_4$ post-treatment was responsible for an increase in the surface area of the film. Besides, *Sommeling et al.* suggested that the $TiCl_4$ post-treatment resulted in a shift in the conduction band edge of the TiO_2, which in turn led to improved injection of the electrons from the dye to the TiO_2 [154].

2.6. References

[1] S. Filatov, N. Bendeliani, B. Albert, J. Kopf, T. Dyuzeva, L. Lityagina, *Sol. Stat. Sci.*, **7** (2005), 1363.

[2] A. Beltran, L. Gracia, J. Andres, *J. Phys. Chem. B*, **110** (2006), 23417.

[3] G. Li, J. Boerio-Goates, B. F. Woodfield, *Appl. Phys. Lett.*, **85** (2004), 11.

[4] V. Swamy, J. D. Gale, L.S. Dubrovinsky, *J. Phys. Chem. Sol.*, **62** (2001), 887.

[5] H. Zhang, J. F. Banfield, *J. Phys. Chem. B*, **104** (2000), 3481.

[6] H. Zhang, J. F. Banfield, Materials Research Society Symposium, in Proceedings: Phase Transformations and Systems Driven Far from Equilibrium, **481** (1998), 619.

[7], M. R. Ranade, A. Navrotsky, H. Z. Zhang, J. F. Banfield, S. H. Elder, A. Zaban, P. H. Borse, S. K. Kulkarni, G. S. Doran, H. J. Whitfield, *Proc. Natl. Acad. Sci. USA*, **99** (2002), 6476.

[8] R. L. Penn, J. F. Banfield, *Am. Miner.*, **84** (1999), 871.

[9] I. L. Cooper, T. A. Egerton, F. Qiu, *J. Eur. Ceram. Soc.*, **29** (2009), 637.

[10] X. Ye, J. Sha, Z. Jiao, L. Zhang, *Nanostruct. Mater.* **8** (1998), 919.

[11] A. S. Barnard, P. Zapol, *Phys. Rev. B*, **70** (2004), 235403.

[12] H. Gedan, H. Lichtenfeld, H. Sonntag, *Colloid & Polymer Sci.,* **260** (1982), 1151.

[13] O. Kurakevych, *Mater. Chem. Phys.*, **105** (2007), 401.

[14] R. L. Penn, J. F. Banfield, *Am. Miner.*, **83** (1998), 1077.

[15] C.R. Ottermann, K. Bange, *Thin Sol. Films*, **286** (1996), 32.

[16] K. M. Reddy, S. V. Manorama, A. R. Reddy, *Mater. Chem. Phys.*, **78** (2002), 239.

[17] D. Reyes-Coronado, G. Rodriguez-Gattorno, M. E. Espinosa-Pesqueira, C. Cab, R. de Coss, G. Oskam, *Nanotech.*, **19** (2008), 145605.

[18] N. Serpone, D. Lawless, R. Khairutdinovt, *J. Phys. Chem.*, **99** (1995), 16646.

[19] C. Kormann, D. W. Bahnemann, M. R. Hoffmann, *J. Phys. Chem.*, **92** (1988), 5196.

[20] A. Kumar, R. Jose, K. Fujihara, J. Wang, S. Ramakrishna, *Chem. Mater.*, **19** (2007), 6536.

[21] A. N. Enyashin, G. Seifert, *Phys. Stat. Sol. B*, **242** (2005), 1361.

[22] S. Monticone, R. Tufeu, A.V. Kanaev, E. Scolan, C. Sanchez, *Appl. Surf. Sci.*, **162–163** (2000), 565.

[23] V. Swamy, D. Menzies, B. C. Muddle, A. Kuznetsov, L. S. Dubrovinsky, Q. Dai, V. Dmitriev, *Appl. Phys. Lett.*, **88** (2006), 243103.

[24] J. Pascual, J. Camassel, H. Mathieu, *J. Phys. Rev.*, **18** (11) (1978), 5606.

[25] M. Posternak, A. Baldereschi, E. J. Walter, H. Krakauer, *Phys. Rev. B*, **74** (2006), 125113.

[26] Y.-F. Zhang,W. Lin, Y. Li, K.-N. Ding, J.-Q. Li, *J. Phys. Chem. B*, **109** (2005), 19270.

[27] L. Yang, S. J. Miklavcic, *J. Opt. Soc. Am.*, **22** (9) (2005), 1866.

[28] P. Kubelka, *J. Opt. Soc. Am.*, **38** (1948), 448.

[29] B. O'Regan, M. Grätzel, *Nature*, **353** (1991), 737.

[30] E. W. McFarland, J. Tang, *Nature*, **421** (2003), 616.

[31] Y. Liu, B. Zhou, J. Bai, J. Li, J. Zhang, Q. Zheng, X. Zhu, W. Cai, *Appl. Catal. B*, **89** (2009), 142.

[32] R. Dholam, N. Patel, M. Adami, A. Miotello, *Int. J. Hydrogen Energy*, **33** (2008), 6896.

[33] M. Ni, M. K. H. Leung, D. Y.C. Leung, K. Sumathy, *Renew. Sust. Energy Rev.*, **11** (2007), 401.

[34] A. Fujishima, K. Honda, *Nature*, **37** (1972), 238.

[35] S. B. Kim, H. T. Hwang, S. C. Hong, *Chemosphere*, **48** (2002), 437.

[36] J. Krysa, G. Waldner, H. Mestankovac, J. Jirkovskyc, G. Grabner, *Appl. Catal. B*, **64** (2006), 290.

[37] R. Dastjerdi, M. Montazer, *Coll. Surf. B*, **79** (2010), 5.

[38] H. Choia, E. Stathatosb, D. D. Dionysioua, *Desalination*, **202** (2007), 199.

[39] Y. Kikuchi, K. Sunada, T. Iyoda, K. Hashimoto, A. Fujishima, *J. Photochem. Photobiol. A*, **106** (1997), 51.

[40] P. Bonhote, E. Gogniat, F. Campus, L. Walder, M. Graetzel, *Displays*, **20** (1999), 137.

[41], M. Ottaviani, S. Panero, S. Morzilli, B. Scrosati, M. Lazzari, *Sol. Stat. Ionics*, **20** (1986), 197.

[42] P. Pillai, K.S. Raja, M. Misra, *J. Pow. Sour.*, **161** (2006), 524.

[43] S. H. Lim, J. Luo, Z. Zhong, W. Ji, *J. Lin, Inorg. Chem.*, **44** (12) (2005), 4124.

[44] M. Graetzel, *J. Photochem. Photobiol. A*, **164** (2004), 3.

[45] M. Graetzel, *J. Sol-Gel Sci. Technol.*, **22** (2001), 7.

[46] http://www.millenniumchem.com/NR/rdonlyres/B753C492-F08B-4DB1-BBC6-88058279FBFF/0/Figure101TiO2F.pdf

[47] J. J. Wu, C. C. Yu, *J. Phys. Chem. B*, **108** (2004), 3377.

[48] J. M. Wu, H. C. Shih, W.T. Wu, *Chem. Phys. Lett.*, **413** (2005), 490.

[49] Degussa technical information brochure n°1243.

[50] S. Vemury, S. E. Pratsinis, *Appl. Phys. Lett.*, **66** (1995), 3275.

[51] G. W. Lee, S. M. Choi, *J. Mater. Sci.*, **43** (2008), 715.

[52] W. P. C. Duyvesteyn, T. M. Spitler, B. J. Sabacky, J. Prochazka, US Patent # 6,440,383.

[53] M. C. Cordero-Cabrera, G. S. Walker, D. M. Grant, *J. Mater. Sci.*, **40** (2005), 3709.

[54] A. Chemseddine, T. Moritz., *Eur. J. Inorg. Chem.*, **2** (1999), 235.

[55] K. D. Kim, S. H. Kim, H. T. Kim, *Coll. Surf. A*, **254** (2005), 99.

[56] Z. Zhang, X. Zhong, S. Liu, D. Li, M. Han, *Angew. Chem. Int. Ed.*, **44** (2005), 3466.

[57] K. Yanagisawa, J. Ovenstone, *J. Phys. Chem. B*, **103** (1999), 7781.

[58] G. Shan, G.P. Demopoulos, *Nanotech.*, **21** (2010), 025604.

[59] L. Vayssieres, *C. R. Chimie*, **9** (2006), 691.

[60] C. Lao, Y. Chuai, L. Su, X. Liu, L. Huang, H. Cheng, D. Zou, *Sol. Energy Mater. Sol. Cells*, **85** (2005), 457.

[61] M.C. Hidalgo, D. Bahnemann, *Appl. Catal. B*, **61** (2005) 259.

[62] H. G. Yang, C. H. Sun, S. Z. Qiao, J. Zou, G. Liu, S. C. Smith, H. M. Cheng, G. Q. Lu, *Nature*, **453** (2008), 638.

[63] Q. Zhang, L. Gao, J. Guo, *Appl. Catal. B*, **26** (2000), 207.

[64] K.-J. Kim, K. D. Benkstein, J. Van de Lagemaat, A. J. Frank, *Chem. Mater.*, **14** (2002), 1042.

[65] E. Matijevic, R. S. Sapiesko, in: Forced hydrolysis in homogeneous solutions, Fine Particles: Synthesis, Characterization, and Mechanisms of Growth, Ed. Sugimoto T., CRC Press, (2000), p. 2-3.

[66] T. C. De Vore, T. N. Gallaher, *High Temp. Sci.*, **16** (1983), 269.

[67] S.-J. Kim, S. D. Park, Y. H. Cho, W. W. Kim., *J. Sol. Stat. Chem.*, **146** (1999), 230.

[68] S. R. Dhage, V. D. Choube, V. Samuel, V. Ravi, *Mater. Lett.*, **58** (2004), 2310.

[69] T. Kapias, R. F. Griffiths, *J. Haz. Mater.*, **119** (2005), 41.

[70] L. A. Bruno, B. C. Beard, *J. Appl. Spectros.*, **51** (1997), 131.

[71] S. Raoot, N. R. Desikan, R. Shekhar, J. Arunachalam, *J. Appl. Spectros.*, **54** (2000), 1412.

[72] B. I. Nabivanets, *Russ. J. Inorg. Chem.*, **7** (1962), 212.

[73] B. I. Nabivanets, L. N. Kudritskaya, *Russ. J. Inorg. Chem.*, **12** (1967), 789.

[74] M. Madekufamba, L. N. Trevani, P. R. Tremaine, *J. Chem. Thermodyn.*, **38** (2006), 1563.

[75] C. F. Baes, R. E. Mesmer. The Hydrolysis of Cations. Ed. J. Wiley & Sons, New York, (1976), p. 147-152.

[76] H. Cheng, J. Ma, Z. Zhao,L. Qi, *Chem. Mater.*, **7** (1995), 663.

[77] I. Cservenyak, G. H. Kelsall, W. Wang, *Electrochim. Acta*, **41** (1996), 563.

[78] P. Comba, A. Merbach, *Inorg. Chem.*, **26** (1986), 1315.

[79] J. D. Ellis, G. A. K. Thompson, *Inorg. Chem.*, **15** (1976), 3172.

[80] L. Ciavatta, D. Ferri, G. Riccio, *Polyhedron*, **4** (1985), 15.

[81] G. H. Kelsall, D. J. Robbins, *J. Electroanal. Chem.*, **283** (1990), 135.

[82] J. E. D. Davies, D. A. Long, *J. Chem. Soc. A*, (1968), 2560.

[83] V. D. Hildenbrand, H. Fuess, G. Pfaff, P. Reynders, *J. Phys. Chem.*, **194** (1996), 139.

[84] C. S. Creaser, J. A. Creighton, *Dalton Trans.*, (1975), 1402.

[85] R. J. H. Clark, C. J. Willis, *Inorg. Chem.*, **10** (1971), 1118.

[86] I. S. Ignatyev, M. Montejo, J. J. Lopez Gonzalez, *J. Phys. Chem. A*, **111** (2007), 7973.

[87] M. M. Knocka, R. E. Riman, *Chem. Mater.*, **5** (1993), 61.

[88] X. Wang, L. Andrews, *J. Phys. Chem.*, **109** (2005), 10689.

[89] M. Gratzel, F. P. Rotzinger, *Inorg. Chem.*, **24** (1985), 2320.

[90] K. Nakamoto, in: Infrared and Raman Spectra of Inorganic and Coordination Compounds, Part A: Theory and Applications in Inorganic Chemistry, 5th edition, Ed. Wiley-Interscience Pub, New York, (1997), p. 153-321.

[91] J.-P. Jolivet, S. Cassaignon, C. Chaneac, D. Chiche, E. Tronc, *J. Sol-Gel Sci. Technol.*, **46** (2008), 299.

[92] M. Henry, J.-P. Jolivet, J. Livage, *Struct. Bond.*, **77** (1992), 155.

[93] Z. L. Wang, Z. C. Kang, Functional and Smart Materials - Structural Evolution and Structure Analysis, New York, Plenum Publishing Corporation, (1998), p. 231.

[94] Y. Zheng, E. Shi, Z. Chen, W. Li, X. Hu X, *J. Mater. Chem.*, **11** (2001), 1547.

[95] A. Pottier, C. Chaneac, E. Tronc, L. Mazerolles, J.-P. Jolivet, *J. Mater. Chem.*, **11** (2001), 1116.

[96] P. Jongsoon, V. Privman, *Recent Res. Dev. Stat. Phys.*, **1** (2000), 1.

[97] S.-J. Kim, S.-D. Park, Y. H. Jeong, S. Park, *J. Am. Ceram. Soc.*, **82** (1999), 927.

[98] M. Addamo, M. Bellardita, A. Di Paola, L. Palmisano, *Chem. Comm.*, **47** (2006), 4943.

[99] R. Sarraf-Mamoory, G. P. Demopoulos, R. A. L. Drew, *Metall. Mater. Trans. B*, **27** (1996), 557.

[100] R. Sarraf-Mamoory, G. P. Demopoulos, R. A. L. Drew, *Metall. Mater. Trans. B*, **27** (1996), 585.

[101] Y. Li, G.P. Demopoulos, *Hydrometallurgy*, **90** (2008), 26.

[102] Q. H. Zhang, L. Gao, J. K. Guo, *Nanostruct. Mater.*, **11** (1999), 1293.

[103] A. Pottier, S. Cassaignon, C. Chaneac, F. Villain, E. Tronc, J.-P. Jolivet, *J. Mater. Chem.*, **13** (2003), 877.

[104] H. Yin, Y. Wada, T. Kitamura, S. Kambe, S. Murasawa, H. Mori, T. Sakata, S. Yanagida, *J. Mater. Chem,* **11** (2001) 1694.

[105] G. P. Demopoulos, *Hydrometallurgy*, **96** (2009), 199.

[106] G. Lian, Z. Qinghong, *Mater. Trans.*, **42** (2001), 1676.

[107] Q. Zhang, L. Gao, J. Guo, *J. Eur. Ceram. Soc.*, **20** (2000), 2153.

[108] J. H. Lee, Y. S. Yang, *J. Eur. Ceram. Soc.*, **25** (2005), 3573.

[109] A. Di Paola, G. Cufalo, M. Addamoa, M. Bellardita, R. Campostrini, M. Ischia, R. Ceccato, L. Palmisano, *Coll. Surf. A*, **317** (2008), 366.

[110] J. H. Lee, Y. S. Yang, *J. Mater. Sci.*, **41** (2006), 557.

[111] D. S. Hwang, N. H. Lee, D. Y. Lee, J. S. Song, S. H. Shin, S. J. Kim, *Smart Mater. Struct.*, **15** (2006), S74.

[112] K. Hara and H. Arakawa, Handbook of Photovoltaic Science and Engineering, Ed. A. Luque and S. Hegedus, John Wileys & Sons, New York, (2003), p. 663-700.

[113] http://www.energyandcapital.com/articles/future-sources-energy/787

[114] A. Hagfeldt, M. Gratzel, *Chem. Rev.*, **95** (1995), 49.

[115] M. K. Nazeeruddin, P. Pechy, T. Renouard, S. M. Zakeeruddin, R. Humphry-Baker, P. Comte, P. Liska, L. Cevey, E. Costa, V. Shklover, L. Spiccia, G. B. Deacon, C. A. Bignozzi, M. Graetzel, *J. Am. Chem. Soc.*, **123** (2001), 1613.

[116] M. Graetzel, *Acc. Chem. Res.*, **42** (2009), 1788.

[117] C. Perez Leon, L. Kador, B. Peng, M. Thelakkat, *J. Phys. Chem. B*, **110** (2006), 8723.

[118] K. E. Lee, M. A. Gomez, S. Elouatik, G. P. Demopoulos, *Langmuir*, **26** (2010), 9575.

[119] http://www.solaronix.com/products/rutheniumdyes/ruthenizer535bistba/

[120] http://www.sigmaaldrich.com/materials-science/organic-electronics/dye-solar-cells.html

[121] M. Wang, N. Chamberland, L. Breau, J.-E. Moser, R. Humphry-Baker, B. Marsan, S. M. Zakeeruddin, M. Graetzel, *Nature Chemistry*, 2 (2010), 385.

[122] http://www.optoiq.com/index/photonics-technologies-applications/lfw-display/lfw-article-display/361941/articles/laser-focus-world/features/photovoltaics-measuring-the-sun.html

[123] http://org.ntnu.no/solarcells/pages/Chap.2.php

[124] S. Ito, P. Chen, P. Comte, M. K. Nazeeruddin, P. Liska, P. Pechy, M. Gratzel, *Prog. Photovolt.: Res. Appl.*, **15** (2007), 603.

[125] D. Zhang, T. Yoshida, K. Furuta, H. Minoura, *J. Photochem. Photobiol. A*, 164 (2004) 159.

[126] L. Grinis, S. Dor, A. Ofir, A. Zaban, *J. Photochem. Photobiol. A*, **198** (2008), 52.

[127] M. Okuya, K. Nakade, D. Osa, T. Nakano, G. R. A. Kumara, S. Kaneko, *J. Photochem. Photobiol. A*, **164** (2004), 167.

[128] T. N. Murakami, Y. Kijitori, N. Kawashima, T. Miyasaka, *J. Photochem. Photobiol. A*, **164** (2004), 187.

[129] M. Durr, A. Schmid, M. Obermaier, S. Rosselli, A. Yasuda, G. Nelles, *Nature Mater.*, **4** (2005), 607.

[130] E. Koenig, M. Hilpert, K. Messmer, US Patent Application # 20090165661 (USPC Class: 101129, IPC8 Class: AB41M112FI).

[131] C.-Y. Huang, Y.-C. Hsu, J.-G. Chen, V. Suryanarayanan, K.-M. Lee, K.-Ch. Ho, *Sol. Energy Mater. Sol. Cells*, **90** (2006), 2391.

[132] C. Baek, M. Vithal, J. A. Chang, J. H. Yum, M. K. Nazeeruddin, M. Grätzel, Y. C. Chung, S. Seok, *Electrochem. Commun.*, **11** (2009), 909.

[133] Y. Lei, H. Liu, W. Xiao, *Modelling Simul. Mater. Sci. Eng.*, **18** (2010), 025004.

[134] N.-G. Park, J. van de Lagemaat, A. J. Frank, *J. Phys. Chem. B*, **104** (2000), 8989.

[135] G. Li, C. P. Richter, R. L. Milot, L. Cai, C. A. Schmuttenmaer, R. H. Crabtree, G. W. Brudvig, V. S. Batista, *Dalton Trans.*, **45** (2009), 10078.

[136] K. H. Ko, Y. C. Lee, Y. J. Jung, Enhanced efficiency of dye-sensitized TiO_2 solar cells (DSSC) by doping of metal ions, *J. Coll. Int. Sci.*, **283** (2005) 482.

[137] F. Hirose, K. Kuribayashi, T. Suzuki, Y. Narita, Y. Kimura, M. Niwanob, *Electrochem. Sol. Stat. Lett.*, **11** (2008) A109.

[138] L. Miranda, A. Chianese, *Chem. Eng. Trans.*, **17** (2009), 975.

[139] S. Nakade, Y. Saito, W. Kubo, T. Kitamura, Y. Wada, S. Yanagida, *J. Phys. Chem. B*, **107** (2003), 8609.

[140] T. Ma, T. Kida, M. Akiyama, K. Inoue K, S. Tsunematsu, K. Yao, H. Noma, E. Abe, *Electrochem. Commun.*, **5** (2003), 369.

[141] K. Fan, M. Liu, T. Peng, L. Ma, K. Dai, *Renewable Energy*, **35** (2010), 555.

[142] K.-M. Lee, V. Suryanarayanan, K.-C. Ho, *Sol. Energy Mater. Sol. Cells*, **90** (2006), 2398.

[143] S. K. Dhungel, J. G. Park, *Renewable Energy*, **35** (2010), 2776.

[144] J.-G. Nam, E.-S. Lee, W.-C. Jung, Y.-J. Park, B.-H. Sohn, S.-C. Park, J. S. Kim, J.-Y. Bae, *Mater. Chem. Phys.*, **116** (2009), 46.

[145] K. H. Park, C. K. Hong, *Electrochem. Commun.*, **10** (2008), 1187.

[146] C. Lao, Y. Chuai, L. Su, X. Liu, L. Huang, H. Cheng, D. Zou, *Sol. Energy Mater. Sol. Cells*, **85** (2005), 457.

[147] S. Ito, T. N. Murakami, P. Comte, P. Liska, C. Graetzel, M. K. Nazeeruddin, M. Gratzel, *Thin Sol. Films*, **516** (2008), 4613.

[148] C.-Y. Huang, Y.-C. Hsu, J.-G. Chen, V. Suryanarayanan, K.-M. Lee, K.-C. Ho, *Sol. Energy Mater. Sol. Cells*, **90** (2006), 2391.

[149] H.-J. Koo, J. Park, B. Yoo, K. Yoo, K. Kim, N.-G. Park, *Inorg. Chim. Acta*, **361** (2008), 677.

[150] C.-A. Tao, W. Zhu, Q. An, G. Li, *J. Phys. Chem. C*, **114** (2010), 10641.

[151] L. N. Lewis, J. L. Spivack, S. Gasaway, E. D. Williams, J. Y. Gui, V. Manivannan, O. P. Siclovan, *Sol. Energy Mater. Sol. Cells*, **90** (2006), 1041.

[152] W. J. Lee, D. Y. Lee, J. S. Song, B. K., *Met. Mater. Int.*, **11** (2005), 465.

[153] C. T. Yip, C. S. K. Mak, A.B. Djurisic, Y. F. Hsu, W. K. Chan, *Appl. Phys. A*, **92** (2008), 589.

[154] P. M. Sommeling, B. C. O'Regan, R. R. Haswell, H. J. P. Smit, N. J. Bakker, J. J. T. Smits, J. M. Kroon, J. A. M. van Roosmalen, *J. Phys. Chem. B*, **110** (2006), 19191.

Chapter 3: Experimental

3.1. Introduction

In this chapter, all experimental details relating to the chemicals and materials, the laboratory equipment, the methods and procedures, and the analytical equipment used are provided. In the first section, all chemicals and materials involved in the preparation of dilute $TiCl_4$ aqueous solutions or the fabrication and assembly of DSC devices are described. Second, the procedures applied for the synthesis and recovery of various TiO_2 nanostructured materials, the TiO_2-based paste and film preparation, and the DSC assembly are described and explained in details. Finally, the various analytical tools employed to characterize the powders, films, and DSC devices are provided and for each characterization method, the conditions for sample preparation and analyses are explained.

3.2. Chemicals and materials

3.2.1. Synthesis and product recovery

The preparation of $TiCl_4$ aqueous solutions was done by dilution of concentrated liquid titanium tetrachloride (99.9 % $TiCl_4$, Fisher Scientific). In the Appendix, the use of chemical additives is investigated, namely sulfuric acid (concentrated, 95-98 % assay, Fisher Scientific), sodium sulfate anhydrous (Na_2SO_4(s), ACS certified, Fisher Scientific), magnesium sulfate hydrate ($MgSO_4 \cdot 5\ H_2O$ (s), ACS certified, Fisher Scientific), aluminium sulfate hydrate ($Al_2(SO_4)_3 \cdot 18\ H_2O$(s), ACS certified, Fisher Scientific), and liquid sodium hydroxide (10 N, ACS certified, Fisher Scientific). All these reagents were used without further purification. Finally, the use of concentrated ammonium hydroxide (29 % assay, certified ACS plus, Fisher Scientific) was employed in certain cases to facilitate the recovery (solid/liquid separation) of TiO_2 nanoparticles.

3.2.2. Paste and film preparation

The preparation of TiO_2-based pastes involved the use of various organic solvents and chemical reagents such as ethanol (Anhydrous ethyl alcohol, Commercial alcohols, Brampton, Ontario), acetic acid (acetic acid glacial, 99.7 % assay, ACS reagent, Fisher scientific), ethyl cellulose (ethoxy content 48 %, 100 cps, Acros Organics), α-terpineol (97+ %, Acros Organics), polyethylene glycol (PEG 20,000, Avocado Research Chemicals Ltd), and glycerol (99.5 %, certified ACS, ACP Chemicals Inc.). The formulation of certain pastes involved the use of the reference material AEROXIDE® TiO_2 P25 powder provided by Degussa (Evonik) [1].

3.2.3. DSC assembly

FTO-coated conductive glass (Fluorine-doped Tin Oxide-coated glass, 10 Ω/cm^2, Nippon Sheet Glass, Japan) was used as a substrate for the preparation of the photoanode and counter electrode. Cleaning of the substrates involved the use of a specifically formulated concentrated cleaning solution Micro-90 (International Products Corporation, USA) and acetone (ACS certified, Fisher Scientific). Sensitization of the photoanode was carried out by dipping into an ethanolic solution of commercial N-719 dye (B2, Dyesol, Australia), used without any further purification. Rinsing of the excess dye after sensitization was done with ethanol. The platinum counter electrode was prepared by deposition of a solution of H_2PtCl_6 (certified ACS, Sigma Aldrich) dissolved in 2-propanol (99.9 %, certified ACS Plus, Fisher Scientific). Sealing of the sensitized photoanode and Pt-counter electrode was achieved with a plastic sealant Surlyn©-30 purchased from Dyesol. Finally, the electrolyte was prepared by mixing N-methybenzimidazole, iodine (I_2), guanidinium thiocyanate, and 4-tertbutylpyridine in a mixed organic solvent of acetonitrile-valeronitrile 85/15 vol. %. In this case, all the chemicals and solvents were purchased from Sigma Aldrich and used without further purification.

3.3. Procedures and equipment

3.3.1. Preparation of 2 M $TiCl_4$ aqueous stock solution

Liquid titanium tetrachloride reagent was drop-wise added under magnetic stirring to an approximate volume of 200 mL deionised water, maintained below 10 °C, in an ice-water bath (Figure 3.1). The drop-wise addition of $TiCl_4$ was controlled by using a glass separatory funnel, which was regularly fed through a plastic funnel by addition of 10-20 mL of concentrated $TiCl_4$(l). Care was taken to clean and thoroughly dry both glass separatory and plastic funnels prior to use in order to avoid the premature precipitation of $TiCl_4$(l) by contact with water droplets or surface moisture. Additional cold water was eventually added in order to reach a final concentration of 2 M $TiCl_4$. The concentration of Ti(IV) in the so prepared stock solution was measured by Inductively Coupled Plasma Atomic Emission Spectrometry (ICP-AES) analyses (more details are provided in section 3.4.1.2) and readjusted to 2 M if necessary by supplemental addition of reagent-grade $TiCl_4$ or water. The stock solution was stored in a cold bath at 3 °C. No changes in the solution appearance were observed for storage duration as long as 6 months. The preparation of dilute $TiCl_4$ aqueous solutions was performed by addition of the stock solution to deionised water at ambient temperature. Characterization of dilute $TiCl_4$ aqueous solutions involved pH measurements, titration of the Ti(IV) concentration in solution by using ICP-AES, and Raman spectroscopic analyses.

3.3.2. Forced hydrolysis of $TiCl_4$ aqueous solutions

3.3.2.1. Starting set-up

During the early course of the work, $TiCl_4$ aqueous solutions were processed in magnetically stirred conical flasks at controlled temperature. The flasks were immersed into a hot water bath consisting of a transparent Plexiglass tank equipped with a circulating heater (Figure 3.2). The bath was placed over a stirring plate, allowing the simultaneous processing of up to 5 flasks. This set-up was used in order to study the effect of the initial concentration of $TiCl_4$ solution on the induction-nucleation phenomena during step-wise linear temperature increase (Chapter 5). It was noticed with these tests that minor changes applied to the agitation conditions affected the kinetics of precipitation. Thus it was decided to standardize the reactor to ensure reproducibility during the subsequent bulk synthesis work.

Figure 3.1. Pictures of the experimental set-up used to prepare 1 L of 2 M $TiCl_4$ aqueous solution. Overview (left) and close view (right).

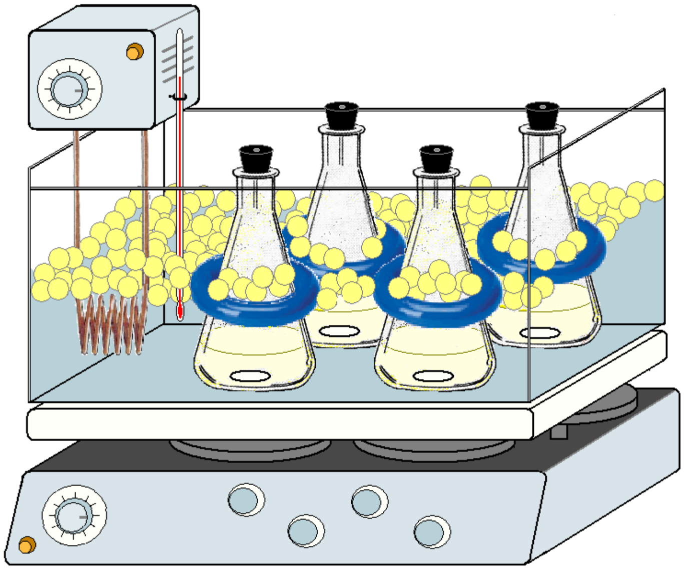

Figure 3.2. Illustration of the preliminary set-up used to thermally process $TiCl_4$ aqueous solutions.

3.3.2.2. Main synthesis stirred reactor

The reactor, a 400 mL beaker equipped with custom made Teflon lid and baffles, was designed to process a volume of 200 mL of $TiCl_4$ aqueous solution (Figure 3.3). Magnetic stirring was replaced by mechanical stirring with adjustable rotation speed provided with a 3-blade axial flow polyethylene coated impeller. All the dimensions of the reactor and internal elements are described in Table 3.1. A hot water bath into which the reactor was immersed to ¾ of its height was used for heating. For each test, a volume of 200 mL of an aqueous solution with the desired concentration, at ambient temperature, was poured into the reactor placed already in the preheated water bath and mechanical stirring was started (1000 rpm). This instance signified the start of the synthesis experiment (t = 0). Typically the solution attained the target temperature within 10 min after the start of the experiment.

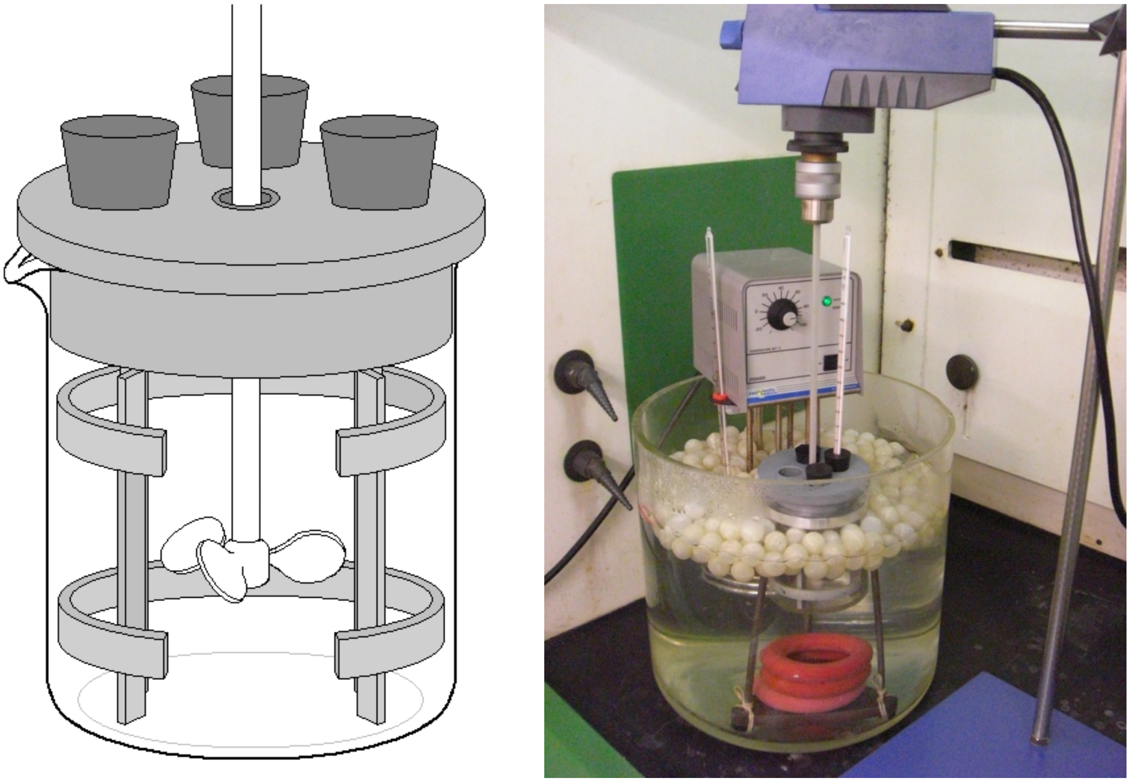

Figure 3.3. Technical drawing of the reactor (left) and overview picture of whole set-up (right).

Table 3.1. Technical description of the reactor and internal parts.

Part	Material	Parameters, Dimensions
Reactor	Glass beaker	400 mL standard beaker
Lid	Teflon	Smaller diameter: 7 cm; fits tight inside the beaker in order to minimise evaporation losses. Larger diameter: 9 cm; four holes on the lid to allow the use of sensing probes, sample collector or rubber stoppers.
Baffles	Teflon	Number of baffles: 4 Width: 0.9 cm Height: 8 cm
Impeller	Wings: Polyethylene Arm: Polyethylene coated steel	Number of wings: 3 Wings length: 2 cm Distance to bottom of reactor: 2.5 cm

3.3.2.3. Recovery of TiO_2 powders

Two different solid recovery (S/L separation) routes were designed for the TiO_2 nanopowders, which are compared in the flow chart presented in Figure 3.4. Pressure filtration (A) using compressed air and membrane filters with 0.1 µm pore size was the first method used. Washing of the powders was performed by pouring deionised water at ambient temperature directly inside the pressure filtration vessel and re-filtering. This operation was repeated 3 times before collecting a wet cake or an aqueous gel of TiO_2 powders. The use of pressure filtration, although clean and facile, was found to be associated with some technical difficulties when processing very fine TiO_2 nanoparticles: when the synthesized particles had an average diameter < 100 nm, some were lost through the pores of the filters and subsequent clogging led to long filtration periods (typically ~ 1-2 days per 500 mL of TiO_2 colloidal suspension); corrosion of the pressure filtration vessel (made of stainless steel) due to the strong acidic nature of the synthesized TiO_2 colloids presented another challenge of using this route.

An alternative nanoparticle (with average size < 100 nm) recovery route (N) was developed to avoid the technical issues related to the use of pressure filtration: concentrated ammonium hydroxide (29 % assay) was added to the synthesized TiO_2 colloidal suspension and the pH was raised to 3, a pH at which fast settling of the nanoparticles was visually observed, in order to suppress peptization via mild aggregation of the nanoparticles [2,3]. This was followed by centrifugation and washing with deionised water at ambient temperature. After repeating this operation 3 times (the duration of the entire operation was ~ 1 hour) an aqueous gel of TiO_2 nanoparticles was collected. The TiO_2-containing gels obtained by using route A and N were dried over night in an oven at 60 °C and manually ground (dry) in a glass mortar. The effect of solid recovery route is addressed most specifically in Chapter 6, where both routes were tried and tested for optimizing the recovery of small 3-5 nm anatase nanocrystallites.

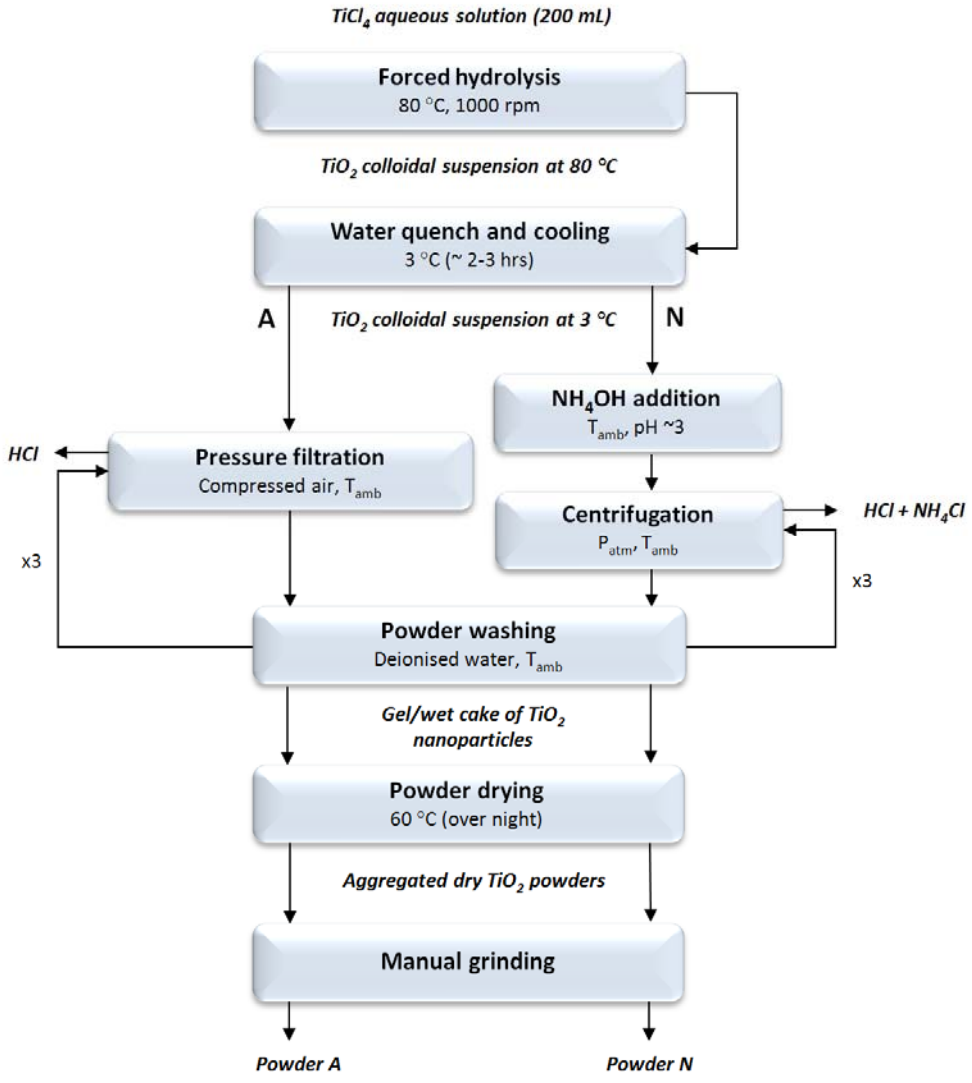

Figure 3.4. Process flow chart: isothermal synthesis and recovery of TiO_2 nanostructured powders.

3.3.2.4. Kinetics - Experimental procedure

When studying the kinetics of $TiCl_4$ hydrolysis, samples of approximately 3 mL in volume were withdrawn at various times with using plastic disposable pipettes. These were directly flushed into sample collectors (~ 10 cm^3) immersed into ice-water in order to freeze/stop the reaction. After the samples were collected, they were kept overnight in a cold bath (at 3 °C) to let the particles settle. If settling was not effective, the solid products were separated from the solution by filtration using 0.025 µm pore size Millipore filters. A volume of 50 µL of clear solution was pipetted and diluted into 10 mL volumetric flasks with a solution of ~ 5 wt. % hydrochloric acid. The concentration of Ti(IV) in the diluted samples was determined by ICP-AES measurements.

3.3.3. Fabrication of TiO_2 photoanodes

3.3.3.1. Paste formulation

Film deposition of the TiO_2 nanoparticles was performed by using the screen-printing method. The recipe for preparing the screen-printing paste was first adapted from a standard method described in literature [4]. Later on, variations were tried involving the use of wet TiO_2 gel as a starting material (as opposed to dry powders) and new organic solvents. In total, 9 different paste recipes were formulated, the preparation of which is explained and compared in Table 3.2.

a) Standard method

A 200 mL 5 wt. % ethanolic solution of ethyl cellulose was prepared at room temperature under magnetic stirring. 1 g of dry TiO_2 nanopowder were manually ground in an alumina mortar for 1 min after adding 0.5 mL of acetic acid and 1 mL of deionised water (Figure 3.5.a). Grinding was continued upon addition of ~ 50 mL of pure ethanol (~ 5 mL every 5 min) alternating with 10 g of the cellulose ethanolic solution (~ 5 mL every 5 min). Another 50 mL of ethanol was used to transfer the mixture into a beaker.

Table 3.2. Chemical composition and preparation of the pastes.

Paste	1. Starting TiO_2 material	2. Particles dispersion	3. Spacer incorporation	4. Dilution /Transfer	5. Rheological agent addition
A	1 g Powder A	0.5 mL acetic acid + 1mL DIW (grinding)	10 g of ethyl cellulose (5wt. % in ethanol) (grinding)	ethanol, 10*5 mL (grinding) /ethanol	3 g of α-terpineol (magnetic stirring)
N	1g Powder N	0.5 mL acetic acid + 1mL DIW (grinding)	10 g of ethyl cellulose (5wt. % in ethanol) (grinding)	ethanol, 10*5 mL (grinding) /ethanol	3 g of α-terpineol (magnetic stirring)
P25	1 g P25	0.5 mL acetic acid + 1mL DIW (grinding)	10 g of ethyl cellulose (5wt. % in ethanol) (grinding)	ethanol, 10*5 mL (grinding) /ethanol	3 g of α-terpineol (magnetic stirring)
$H_{A/R}$	1 g Powder A + 1 g Powder R	0.5 mL acetic acid + 1mL DIW (grinding)	20 g of ethyl cellulose (5wt. % in ethanol) (grinding)	ethanol, 10*10 mL (grinding) /ethanol	6 g of α-terpineol (magnetic stirring)
N'	10 g Gel N-Eth	0.5 mL acetic acid + 1mL DIW (grinding)	10 g of ethyl cellulose (5wt. % in ethanol) (grinding)	Ethanol, 10*5 mL (grinding) /Ethanol	3 g of α-terpineol (magnetic stirring)
N''	10 g Gel N-Eth	0.5 mL acetic acid + 1mL DIW (grinding)	1 g of PEG (dissolved in 10mL DIW) (magnetic stirring)		
$H'_{N/P25}$	10 g Gel N-Eth + 1 g P25	0.5 mL acetic acid + 1mL DIW (grinding)	20 g of ethyl cellulose (5wt. % in ethanol) (grinding)	ethanol, 10*10 mL (grinding) /ethanol	6 g of α-terpineol (magnetic stirring)
$H'_{N/R}$	10 g Gel N-Eth + 1 g Powder R	0.5 mL acetic acid + 1mL DIW (grinding)	20 g of ethyl cellulose (5wt. % in ethanol) (grinding)	ethanol, 10*10 mL (grinding) /ethanol	6 g of α-terpineol (magnetic stirring)
N-Aq	10 g Gel N-Aq	0.5 mL acetic acid (magnetic stirring)	1 g of PEG (dissolved in 10mL DIW) (magnetic stirring)		3g of glycerol (magnetic stirring)

Legend:

⋯ Steps 3 and 4 were alternatively applied
∼∼∼ Sonication
🟫 Dry TiO_2 powders were used as a starting material
🟦 Wet TiO_2 gels were used as a starting material
🟩 Ethanol was used as a solvent
🟥 Water was used as a solvent

Sonication (illustrated by the blue waving lines in Table 3.2 and shown in Figure 3.5.b) was performed using an ultrasound horn in order to break the remaining aggregates and disperse the TiO_2 nanoparticles (2 s work at 40 %, 2 s off, for 2 min). 3 g of α-terpineol were added to the preparation and magnetically stirred for 1 min. The final preparation was sonicated again and then condensed at 37 °C using a rotary evaporator until the paste had reached an appropriate viscous consistency (Figure 3.5.c). This recipe was applied for the preparation of pastes A, N and P25.

b) Variations of the standard method

A hybrid paste, paste $H_{A/R}$ was prepared based on the mixture of two different aqueous-synthesized TiO_2 powders (dried and ground) with different particle size distributions: 50 wt. % powder A and 50 wt. % powder R. Powder R was produced via forced hydrolysis of a 0.3 M $TiCl_4$ aqueous solution at 80 °C for 2 hrs (solid recovery was issued according to route A). More details on the characteristics of this powder are provided in Chapter 7.

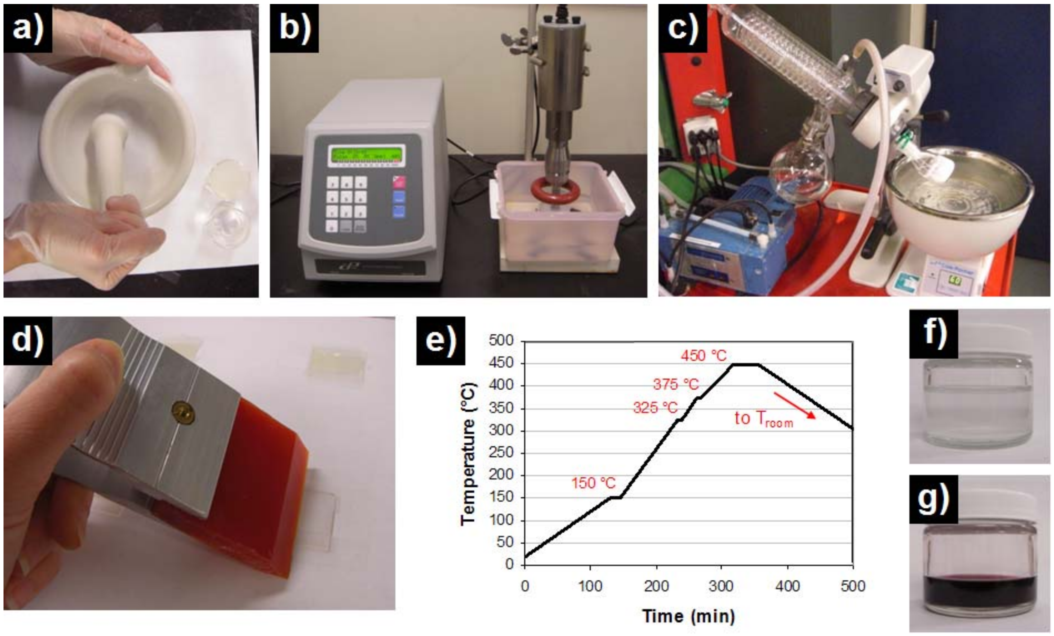

Figure 3.5. Diagram illustrating the step-wise procedure used for the fabrication of a dye sensitized TiO_2-based photoanode: grinding of agglomerated dry powder (a), ultrasound dispersion in ethanol (b), thickening of the paste via evaporation (c), screen-printing (d), annealing (e), $TiCl_4$ post-treatment (f), dye sensitization (g).

Other pastes, namely pastes N', N'', $H'_{N/P25}$, $H'_{N/R}$, and N-Aq were prepared with a wet TiO_2 gel as a starting material. Gel N-Eth, used for the preparation of pastes N', N'', $H'_{N/P25}$ and $H'_{N/R}$, was prepared as per following: a TiO_2 colloid was synthesized via isothermal treatment of 0.2 M $TiCl_4$ aqueous solution at 80 °C for 30 min. After fast cooling down to T_{amb}, concentrated NH_4OH was added to the colloid until its pH is raised to pH 3 and then centrifugation (in 50 mL plastic centrifugation tubes) was applied to complete initial solid/liquid separation a first time. The particles were further washed twice with deionized water (2 x ~ 50 mL) and once with ethanol (~ 50 mL). Centrifugation was applied between each washing cycle. Gel N-Aq was used as a starting material to make paste N-Aq and prepared using the same procedure as gel N-Eth with the exception that only deionized water was used to wash the particles (as opposed to using ethanol in the third washing cycle). The two kinds of gels were found to contain approximately 10 wt. % solids.

In the case of pastes N', N'', $H'_{N/P25}$, and $H'_{N/R}$, ethanol was used as solvent to carry out the transfer of the gel from the conical centrifuge tubes to the alumina mortar (Table 3.2, green cells) or to a magnetically stirred beaker (Table 3.2, red cells), depending on the method used to incorporate the binder to theTiO_2 gel. Instead of ethanol, deionised water was used as a solvent in the case of paste N-Aq. Furthermore, in pastes N'' and N-Aq, the binder used was polyethylene glycol instead of ethyl cellulose. In the case of paste N-Aq, glycerol, a water soluble rheological agent was used instead of α-terpineol.

Once all the components of a paste were mixed together, it was condensed with a rotary evaporator at 37 °C or 50 °C depending if the paste was ethanolic (N', N'', $H'_{N/P25}$, and $H'_{N/R}$), or aqueous (N-Aq). Condensation of the pastes was continued until their TiO_2 content was approximately 10-15 wt. %.

3.3.3.2. Fabrication of the photoanode

The TiO_2 film was prepared on pre-cleaned rectangle pieces of approximately 2 cm*3 cm FTO-coated glass. Cleaning was done by using ultrasounds in a specifically formulated glass cleaning aqueous solution (Micro-90, International Products Corporation, USA), followed by rinsing with deionized water and ethanol, drying, and UV-ozone treatment (30 min). Care was taken that all the tools, used to handle either the glass substrate or to screen print the TiO_2-based paste, were previously cleaned with deionised water and alcohol. The total surface of the screen printed film was delimited to a 1 x 1 cm^2 square with 2 parallel bands of scotch tape applied on the conductive side of the glass substrate (Figures 3.6.a and 3.6.b). A small volume of paste was then deposited to one end of the delimited area and spread evenly by using a soft plastic spatula (Figures 3.5.d and 3.6.a). The bands of scotch tape were removed and the excess of paste was cleaned with a sharp blade (Figures 3.6.c and 3.6.d). The surrounding of the square of screen printed paste was carefully cleaned using alcohol.

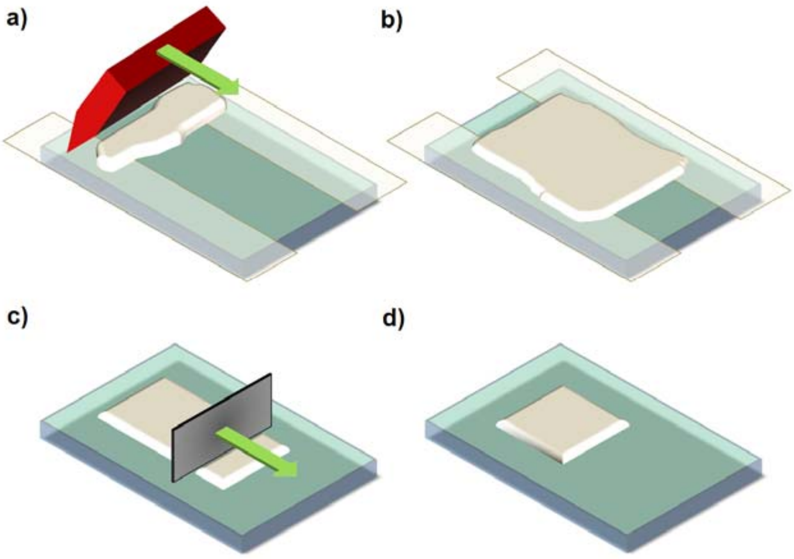

Figure 3.6. Screen printing of a TiO_2 film on a conductive glass substrate: screen printing of the TiO_2-based paste (a,b); removal of paste excess (c); resultant TiO_2 wet film.

Annealing of the film (Figure 3.5.e) was conducted via gradual stepwise heating at 150 °C for 15 min (120 ^oC/hr from room temperature to 150 °C), 325 °C for 5 min (240 ^oC/hr from 150 °C to 325 °C), 375 °C for 5 min (120 ^oC/hr from 325 °C to 375 °C), and at 450 °C for 30 min (60 ^oC/hr from 375 °C to 450 °C) followed by cooling down to room temperature with a cooling rate of 60 ^{o}C/hr. During the annealing treatment, a glass tray was used to cover the hot plate in order to avoid any air flow-related temperature variation between the bottom of the glass substrate and the top of the film, and also to prevent the deposition of impurities (dust) on the films.

After annealing, chemical bonding of the TiO_2 film (Figure 3.5.f) was achieved by application of a treatment in a 50 mM $TiCl_4$ aqueous solution at 80 ^{o}C for 30 min. The film was then slightly rinsed with water and ethanol, and annealed one more time. Once at room temperature, the TiO_2 electrode was sensitized (Figure 3.5.g) by immersion into a 0.5 mM N-719 dye (B2, Dyesol, Australia) solution in ethanol at room temperature for 24 hrs. After sensitization, the excess amount of non-adsorbed dye was carefully rinsed using ethanol.

3.3.3.3. DSC assembly

The platinum counter electrode was prepared as per following: two diagonally opposite holes were drilled through a glass substrate at a distance of 5 mm from each other as shown on Figure 3.7.a. Drill bits with 1 mm diameter were used on a Dremel drillpress. The pierced glass substrates were cleaned according to the cleaning procedure described above (no UV-ozone treatment was applied in the case of the counter electrode) and one drop of 50 mM H_2PtCl_6 (in 2-propanol) solution was deposited and spread on the conductive side of the substrate. Deposition of metallic platinum on the surface of the glass was achieved by annealing the substrates at 450 °C for 3 hrs.

The plastic sealant (Surlyn©-30, Dyesol) was cut with a sharp blade into a square shape that fits around the film and avoids electrolyte leakage (Figure 3.7.b). Sealing of the TiO_2 photoanode and Pt-counter electrode was performed at 120 °C for 4 min by using a programmable Starlight hot press. With this method, hermetic sealing was systematically obtained. The electrolyte (0.6 M N-methybenzimidazole, 0.03 M I_2, 0.10 M guanidinium thiocyanate, and 0.5 M 4-tertbutylpyridine in a mixture of acetonitrile-valeronitrile 85/15 vol. % was back inserted through the two holes of the Pt-counter electrode (Figure 3.7.c) and the holes were sealed using a square piece of sealant covered by a small square piece of thin microscopic observation slide of silica glass (Figure 3.7.d). Sealing was again performed by using the hot press at 120 °C for 4 min.

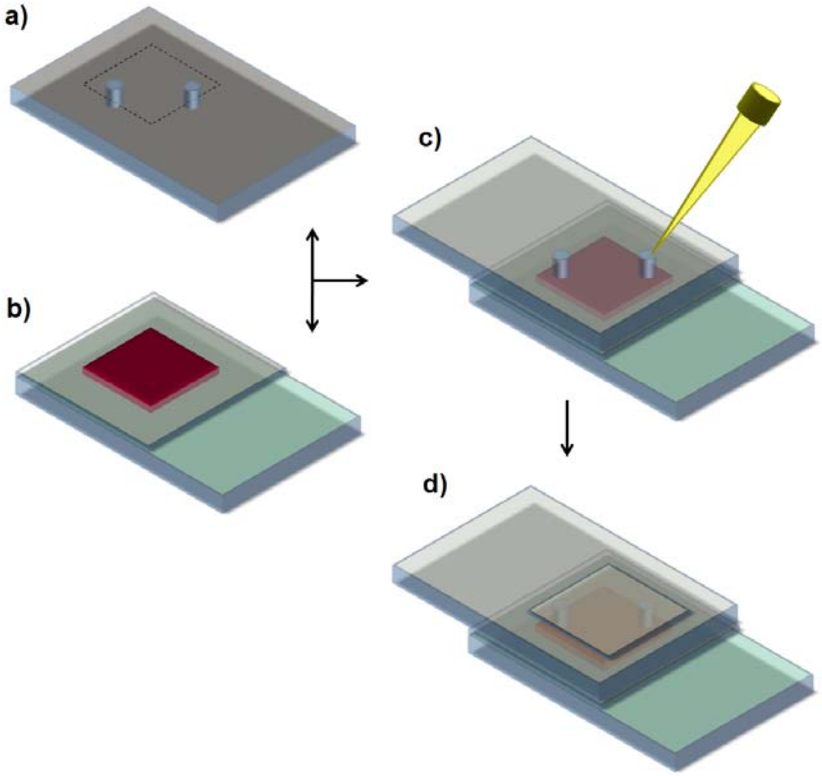

Figure 3.7. Diagram illustrating the assembling of a DSC: Pt-counter electrode (a), sensitized photoanode and plastic sealant (b), electrolyte back injection (c), assembled DSC (d).

3.4. Characterization methods

3.4.1. Ti(IV) chloride solutions

3.4.1.1. pH measurements

The measurements were performed at ambient temperature, under magnetic stirring, with a general-purpose double-junction pH electrode from Cole Parmer, which accuracy is approximately 0.01 pH units for the pH range 0-13. The electrode was systematically calibrated with two buffer solutions at pH 2 and 7 (purchased from Fisher Scientific) prior to performing any pH analyses.

3.4.1.2. Inductive Coupled Plasma-Atomic Emission Spectroscopy (ICP-AES)

The measurements were performed with a Thermo Jarrel Ash Trace Scan Machine. Standards of 50, 100, and 300 ppm of titanium prepared by dilution of a 1000 ppm ICP grade standard, and a blank (4 vol. % HNO_3) were used for the calibration.

3.4.1.3. Micro-Raman spectroscopy

Micro-Raman spectra were collected using an InVia Raman microscope from Renishaw. The laser excitation was provided by a polarized He-Ne laser operating at 514 nm. The laser beam produced a spot size of approximately 1 µm in diameter using the 50x short distance objective. The position of the solution container underneath the laser beam was adjusted so that its focus point was located at ~ 1 cm below the meniscus of the solution. All the spectra were collected over 180 s acquisition time, in the wavelength range 100-4000 cm^{-1}, using 100 % beam energy. The energy resolution was 4 cm^{-1} at the full width half max (FWHM) of the internal Si reference peak.

3.4.2. TiO_2 colloids

3.4.2.1. Turbidity

The turbidity measurements were performed with a Micro 1000 IR Turbidimeter from HF Scientific Inc.. The apparatus was calibrated with 0.02, 10, 100, and 1750 NTU turbidimetry standards.

3.4.2.2. Field Emission Gun-Transmission Electron Microscopy (FEG-TEM)

Field Emission Gun-Transmission Electron Microscopy observations were performed on a Philips CM-200 microscope operated with an accelerating voltage of 200 kV. For sample preparation, a small volume of approximately 0.5 mL of colloid was withdrawn with a plastic pipette and flushed into a glass vial containing ethanol. Ultrasounds were applied in order to de-agglomerate the particles and the resulting ethanolic dispersion was deposited and left to dry at T_{amb} on a Cu grid with an amorphous carbon film.

3.4.3. TiO$_2$ powders and films

3.4.3.1. X-Ray Diffraction (XRD)

X-Ray Powder Diffraction analysis was performed using a Rigaku Rotaflex D-Max diffractometer equipped with a rotating anode, a copper target ($\lambda(CuK_{\alpha1}) = 1.5406$ Å), a monochromator composed of a graphite crystal, and a scintillator detector. The diffractometer used 40 kV and 20 mA. Scanning took place between 20° and 70° (2θ) with a 0.05° step and an acquisition time of 4 s per step. In the case of TiO$_2$ powders, the samples were ground in an alumina mortar and prepared for analyses in the sample holders specifically designed for powder XRD analyses. In the case of TiO$_2$ films, these were prepared on microscopic observation glass slides and characterized as prepared.

The patterns obtained for samples of TiO$_2$ powders and films were compared to the JCPDS reference data of the anatase (#00-021-1272), rutile (#00-001-1292), and brookite (#00-029-1360), which patterns and crystal parameters are provided in Figure 3.8 and Table 3.3, respectively.

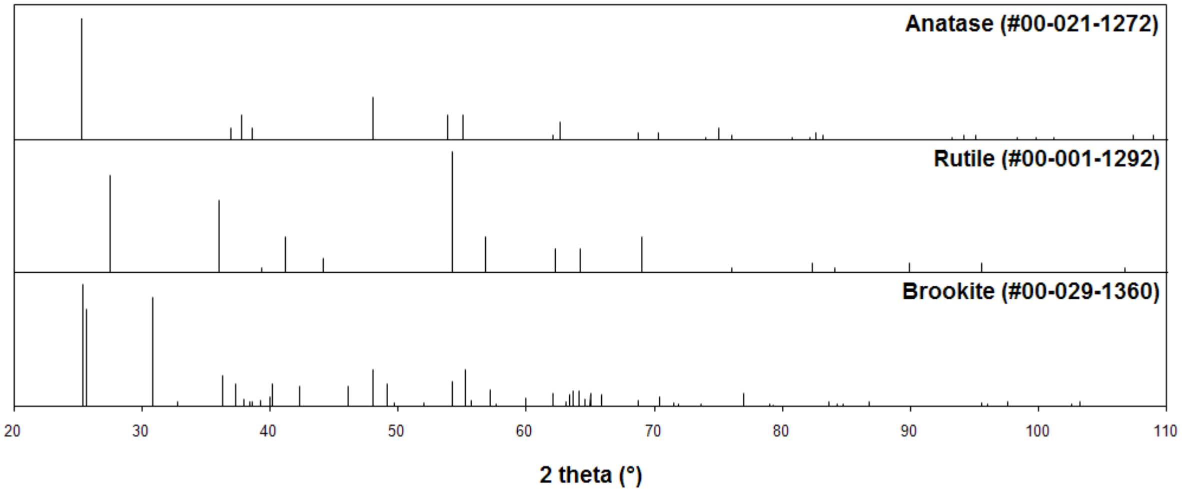

Figure 3.8. JCPDS XRD patterns of the brookite (#00-029-1360), rutile (#00-001-1292), and anatase (#00-021-1272) crystalline phases of TiO$_2$.

Table 3.3. JCPDS crystal phase parameters of the brookite (#00-029-1360), rutile (#00-001-1292), and anatase (#00-021-1272) crystalline phases of TiO_2.

Anatase (#00-021-1272)						Rutile (#00-001-1292)						Brookite (#00-029-1360)					
h	k	l	d (A)	2 theta (°)	I (%)	h	k	l	d (A)	2 theta (°)	I (%)	h	k	l	d (A)	2 theta (°)	I (%)
1	0	1	3.520	25.281	100	1	1	0	3.24	27.507	80	1	2	0	3.512	25.340	100
1	0	3	2.431	36.947	10	1	0	1	2.49	36.041	60	1	1	1	3.465	25.689	80
0	0	4	2.378	37.801	20	2	0	0	2.29	39.312	4	1	2	1	2.900	30.808	90
1	1	2	2.332	38.576	10	1	1	1	2.19	41.187	30	2	0	0	2.729	32.791	4
2	0	0	1.892	48.050	35	2	1	0	2.05	44.142	12	0	1	2	2.476	36.252	25
1	0	5	1.700	53.891	20	2	1	1	1.69	54.233	100	2	0	1	2.409	37.297	18
2	1	1	1.667	55.062	20	2	2	0	1.62	56.783	30	1	3	1	2.370	37.934	6
2	1	3	1.493	62.121	4	0	0	2	1.49	62.26	20	2	2	0	2.344	38.371	4
2	0	4	1.481	62.690	14	3	1	0	1.45	64.179	20	2	1	1	2.332	38.576	4
1	1	6	1.364	68.762	6	3	0	1	1.36	68.999	30	0	4	0	2.296	39.205	5
2	2	0	1.338	70.311	6	2	0	2	1.25	76.084	4	1	1	2	2.254	39.967	8
1	0	7	1.280	74.031	2	3	2	1	1.17	82.352	8	0	2	2	2.244	40.153	18
2	1	5	1.265	75.032	10	4	0	0	1.15	84.107	4	2	2	1	2.133	42.340	16
3	0	1	1.251	76.020	4	2	2	2	1.09	89.934	8	0	3	2	1.969	46.072	16
0	0	8	1.189	80.727	2	4	1	1	1.04	95.578	8	2	3	1	1.893	48.012	30
3	0	3	1.173	82.139	2	1	0	3	0.96	106.719	4	1	3	2	1.851	49.173	18
2	2	4	1.166	82.662	6	5	1	0	0.9	117.716	2	2	1	2	1.833	49.694	3
3	1	2	1.161	83.149	4	4	1	2	0.89	119.881	8	2	4	0	1.757	52.012	3
2	1	7	1.060	93.221	2	5	0	1	0.88	122.171	4	3	2	0	1.691	54.205	20
3	0	5	1.052	94.182	4	2	2	3	0.84	132.99	2	2	4	1	1.662	55.234	30
3	2	1	1.044	95.143	4	3	0	3	0.83	136.273	4	1	5	1	1.649	55.711	5
1	0	9	1.018	98.319	2	5	2	1	0.82	139.899	4	1	1	3	1.610	57.176	13
2	0	8	1.007	99.804	2							2	3	2	1.597	57.685	2
3	2	3	0.997	101.221	2							1	2	3	1.541	59.991	7
3	1	6	0.956	107.448	4							0	5	2	1.494	62.065	10
4	0	0	0.946	108.963	4							1	6	0	1.473	63.065	4
3	0	7	0.925	112.841	2							3	1	2	1.466	63.416	9
3	2	5	0.919	113.861	2							2	5	1	1.461	63.643	12
4	1	1	0.914	114.909	2							2	0	3	1.452	64.104	12
2	1	9	0.897	118.439	4							1	3	3	1.442	64.603	6
2	2	8	0.889	120.104	2							2	1	3	1.434	65.003	10
4	1	3	0.882	121.725	2							1	6	1	1.417	65.876	9
4	0	4	0.879	122.336	2							4	0	0	1.364	68.768	5
4	2	0	0.846	131.036	2							3	3	2	1.336	70.432	8
3	2	7	0.831	135.998	2							4	0	1	1.319	71.490	3
4	1	5	0.827	137.391	4							2	3	3	1.312	71.931	2
3	0	9	0.810	143.888	2							0	0	4	1.285	73.648	2
4	2	4	0.797	150.039	4							0	2	4	1.238	76.949	10
0	0	12	0.793	152.634	2							4	3	1	1.211	79.025	2
												1	2	4	1.207	79.283	1
												3	3	3	1.155	83.643	4
												0	8	0	1.148	84.288	2
												4	4	1	1.143	84.724	2
												0	4	4	1.122	86.743	4
												5	2	1	1.040	95.590	3
												2	8	1	1.037	95.993	2
												3	2	4	1.024	97.609	4
												1	2	5	0.987	102.559	2
												3	7	2	0.983	103.201	4

3.4.3.2. BET surface area analyses (BET)

The analyses of powders and films were performed on a Micromeritics TriStar 3000 apparatus under nitrogen controlled atmosphere. A multiple point specific surface area type of analysis was carried out. Each sample weighed approximately 200 mg and had been degassed for 4 hrs at 80 °C prior to nitrogen physisorption. Powders were analysed as prepared (dried and ground) but the films were carefully scratched off their glass substrate in order to minimize the impact of sample preparation on the analytical results.

3.4.3.3. Fourrier Transformed Infra-Red spectroscopy (FT-IR)

The spectra were collected over the range 4000 to 650 cm^{-1} with 16 sample scans and 4 cm^{-1} resolution using a Perkin Elmer Spectrum 400. The powders and films were previously ground.

3.4.3.4. Thermogravimetric Analysis (TGA)

The analyses were performed with a TA Instruments Q500 TGA, starting at ambient temperature up to 700 °C with a heating rate of 10 °C/min in N_2 atmosphere. All powder and film (previously scratched off the glass substrate) samples were previously dried at 60 °C, but no further grinding was applied

3.4.4. DSC performance

The performance of the assembled devices was characterized by taking photovoltaic measurements under Xenon lamp illumination-equipped ORIEL Model 68820 Solar Simulator. The power of the simulated light was calibrated to 1000 W/m^2. The illuminated area was limited to 0.16 cm^2 by applying an external photo-mask (0.4 × 0.4 cm^2) on the surface of the cell. The Intensity vs. Voltage (I vs. V) curves were obtained with a Keithley 2400 Sourcemeter at 5 mV voltage step.

3.5. References

[1] Degussa technical information brochure n°1243.

[2] R. A. French, A. R. Jacobson, B. Kim, S. Isley, R. L. Penn, and P. C. Baveye, *Environ. Sci. Technol.*, **43** (2009), 1354.

[3] S. Hore, E. Palomares, H. Smit, N. J. Bakker, P. Comte, P. Liska, K. Ravindranathan Thampi, J. M. Kroon, A. Hinsch, and J. R. Durrant, *J. Mater. Chem.*, **15** (2005), 412.

[4] S. Ito, P. Chen, P. Comte, M. K. Nazeeruddin, P. Liska, P. Péchy, and M. Grätzel, *Prog. Photovolt.: Res. Appl.*, **15** (2007), 603.

[5] R. Gauvin, K. Robertson, P. Horny, A.M .Elwazri and S. Yue, *JOM*, **3** (2006), 20.

Chapter 4: On the Speciation of $TiCl_4$ Aqueous Solutions

4.1. Introduction

In this chapter, the preparation of aqueous solutions of $TiCl_4$ with concentrations ranging from 0.01 to 2 M starting from concentrated pure liquid $TiCl_4$ (99,9 %, ρ=1.72 g/cm^3, 9.06 M) is described and the solutions are characterized at room temperature (22 °C). In particular, the effect of dilution on the speciation of $TiCl_4$ solutions is investigated based on the combined results of acid-base titrations, Raman spectroscopy analyses, and thermodynamic modelling of $TiCl_4$ solutions realized by using the OLI software package. The purpose of this chapter is to provide some insights on the nature of aqueous solutions (precursor complexes) of $TiCl_4$, a first necessary step towards the understanding of the chemical mechanisms involved in the synthesis of TiO_2 colloids by forced hydrolysis of $TiCl_4$ aqueous solutions.

4.2. Background information

Concentrated $TiCl_4(l)$ is a colourless liquid, which mostly contains $TiCl_4$ tetrahedral molecules characterized with highly covalent (as opposed to ionic) chemical bonds. It is notorious for its violent exothermic reaction with water at ambient temperature [1], often reported to occur according to the spontaneous reaction described in Equation 4.1:

$$TiCl_4(l) + 2\ H_2O(l/g) = TiO_2(s) + 4\ HCl(g) + \Delta H\ (\Delta H < 0) \tag{4.1}$$

However, at low temperature (typically below 5 °C), liquid $TiCl_4$ can be diluted in water by slow addition of concentrated $TiCl_4(l)$ in water without the occurrence of the above irreversible formation of TiO_2 precipitates. In other words, the complete hydrolysis of $TiCl_4(l)$ is suppressed although partial hydrolysis is suspected to occur, leading to the formation of Ti(IV)-Cl-OH-OH_2 complexes. The formation of these precursor complexes has been investigated by other researchers who made use of thermodynamic calculations and/or spectroscopic analytical techniques. For instance, *Lorimer* (as mentioned by *Kapias and Griffiths* [1]) suggested that the products of concentrated $TiCl_4(l)$ hydrolysis at low temperature depend on the relative concentrations of liquid $TiCl_4$ and water: Equations 4.2 and 4.3 describe the reactions proposed in water or excess liquid $TiCl_4$ respectively [1]:

$$TiCl_4(l) + 4\ H_2O(l) = Ti(OH)_4(aq) + 4\ HCl(g) \tag{4.2}$$

$$TiCl_4(l) + H_2O(l) = TiOCl_2(aq) + 2\ HCl(g) \tag{4.3}$$

Other researchers suggested that the products of $TiCl_4$ hydrolysis have the form of oxy-chloro and hydroxy-chloro Ti(IV) complexes of general formula $[Ti(OH)_xCl_z{\cdot}a(H_2O)]^{4-(x+z)}$ and $[TiO_yCl_z{\cdot}a(H_2O)]^{4-(2y+z)}$ [2-6]. The formation of these species may be described as in Equations 4.4 and 4.5 respectively:

$$TiCl_4 + a\ H_2O = [Ti(OH)_xCl_z{\cdot}(a-x)(H_2O)]^{4-(x+z)} + (4-z)\ Cl^- + x\ H^+ \tag{4.4}$$

$$TiCl_4 + a\ H_2O = [TiO_yCl_z{\cdot}(a-y)(H_2O)]^{4-(2y+z)} + (4-z)\ Cl^- + 2y\ H^+ \tag{4.5}$$

$TiOCl_2$ is often referred to as the main product of $TiCl_4$ partial hydrolysis in dilute (0.5-5 M) aqueous solutions of $TiCl_4(l)$ [4,7-11], while its quantitative determination was claimed to have been made by FT-IR spectroscopy [12,13].

4.3. Preparation of a 2 M stock $TiCl_4$ aqueous solution

When preparing a 2 M $TiCl_4$ stock solution from concentrated liquid $TiCl_4$ at low temperature (0-3 °C), a series of events were visually observed which are described below, along with the temperature fluctuations that were monitored by using a thermometer inside the solution. As droplets of concentrated $TiCl_4(l)$ were dripped into water, the generation of white fumes was first observed (Figures 4.1.b and 4.1.c). With time, these fumes (apparently HCl(g)) were found to be responsible for the corrosion of stainless steel metallic structures present in the fume-hood. When drops of $TiCl_4(l)$ entered water, two simultaneous phenomena were observed: an unstable white-yellow precipitate instantaneously formed and rapidly dissolved (Figure 4.1.c), while a fast increase-decrease of the temperature inside the solution could be read on the thermometer. These observations were made in particular at the beginning of the preparation, when water was present in excess as compared to $TiCl_4$. As the concentration in $TiCl_4$ was being increased, the appearance of the solution gradually evolved towards a yellow translucent colour (Figures 4.1.a and 4.1.d).(a) The exothermic character of $TiCl_4$ hydrolysis was also found to diminish (the temperature inside the solution became more stable) and less fumes were produced. Upon close observation of the area where $TiCl_4$(l) drops entered the solution, it was possible to notice that the previously observed white-yellow precipitates no longer formed. Instead, a local intensification of the yellow tint of the solution and the formation of small bubbles that rapidly dissolved could be observed (Figure 4.1.d). Finally, when preparing dilute $TiCl_4$ aqueous solutions by mixing the 2 M stock solution with deionised water at ambient temperature, only very light fumes were observed to form and both liquid phases mixed homogeneously without resorting to precipitation.

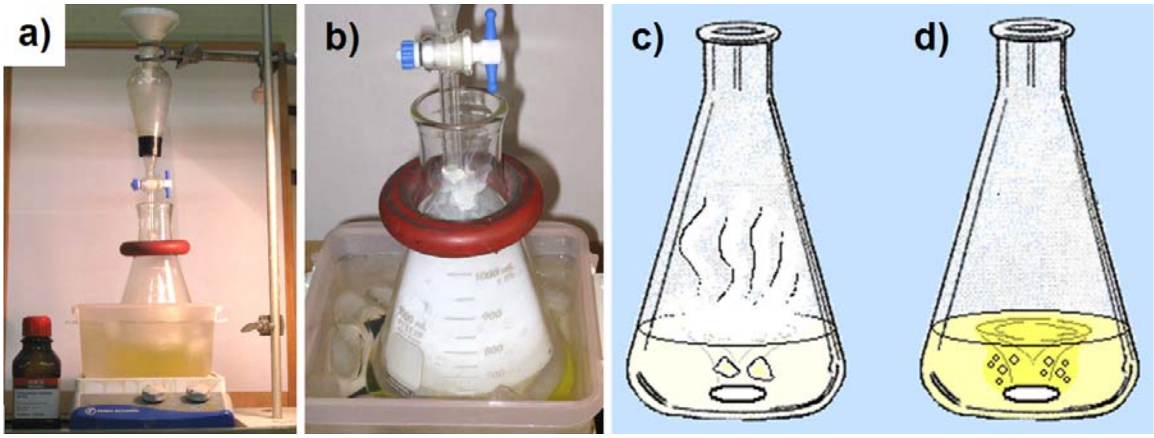

Figure 4.1. Preparation of a 2 M $TiCl_4$ stock solution: front view picture of the set-up (a); closer view of the conical flask while proceeding to the addition of concentrated $TiCl_4$(l) (b); drawing of the system when adding concentrated $TiCl_4$ at the beginning of the preparation (water is in excess) (c), in the middle of the preparation ($TiCl_4$ is in excess) (d).

(a) Footnote: When drops of concentrated $TiCl_4$(l) were dripped on the dry wall of a beaker, the formation of solid compounds with an intense yellow colour occurred apparently by reaction of concentrated $TiCl_4$(l) with the moisture from the environment. Some of the Ti(IV) species present in these solids are thought to be responsible for the colour of aqueous ≥ 1 M $TiCl_4$ solutions. Similar observations were reported by *Davies et Long* [14].

These experimental observations relate to the two reactions described in Equations 4.2 and 4.3. On one hand, the formation of acidic white fumes and bubbles may be associated to the production of HCl(g). On the other hand, the unstable white-yellow precipitates observed to form by introduction of $TiCl_4$(l) in water and the yellow colour characterizing the final stock solution may relate to the presence of condensed polymeric forms of $Ti(OH)_4$, and molecular $TiOCl_2$, respectively, as suggested by other researchers and chemical suppliers [7-10]. These observations represent a first step towards the understanding of $TiCl_4$ partial hydrolysis and the determination of the speciation of dilute aqueous $TiCl_4$ solutions. More extensive characterization of the stock and dilute solutions is described in the following sections.

4.4. Acidic character of $TiCl_4$ aqueous solutions

In order to quantify the amounts of free protons, H^+, generated in dilute $TiCl_4$ solutions prepared with water, acid-base titrations were performed on 0.05, 0.1, 0.5, and 1 M $TiCl_4$ solutions. The solutions were all prepared starting with the same 2 M $TiCl_4$ stock solution. An aqueous solution of NaOH was used as a titrant, of which the concentration was adjusted so that $[NaOH]/[TiCl_4] = 10$. This was done in order to minimize the effect of base volume addition on the profile of the titration curves and as such ensure the full conversion of Ti(IV)(aq) into TiO_2(s). The equivalence point, defined as $[NaOH]\cdot(V_{NaOH,eq.}) = [H^+]_{exp,in.}\cdot(V_{TiCl4,in.})$, was determined by using the tangents method. The titration curves are reported in Figure 4.2. Table 4.1 presents comparative (experimental and thermodynamically simulated) initial pH and $[H^+]$ data, as well as the partial hydrolysis coefficient of the solution prior to titration, $a = [H^+]_{in.}/[TiCl_4]$. Table 4.2 provides pH and $[H^+]$ experimental data related to the point of equivalence, and the final conversion yield, $b = [H^+]_{eq.}/[TiCl_4]$. The simulated data were obtained by using the OLI software package: the MSE (H_3O^+) chemistry model and databank were selected and the assumption was made that no solid phase compounds were present in the initial $TiCl_4$ aqueous solution.

Table 4.1. Acidity of 0.05-1 M $TiCl_4$ solutions: experimental data and thermodynamic simulation (Figure 4.2).

$[TiCl_4]$ (mol/L)	$pH_{initial}$		$[H^+]_{initial}$ (mol/L)		$a = [H^+]_{initial}/[TiCl_4]$	
	Exp	OLI	Exp	OLI	Exp	OLI
0.05	1.12	1.02	0.076	0.124	1.52	2.48
0.10	0.89	0.78	0.129	0.219	1.29	2.19
0.50	0.55	0.56	0.281	0.940	0.56	1.88
1.00	-0.21	-0.38	1.622	1.859	1.62	1.86

Table 4.2. Acid-base titrations of 0.05-1 M $TiCl_4$ solutions: experimental parameters and results.

$[TiCl_4]$ (mol/L)	[NaOH] (mol/L)	$V_{NaOH,\ eq}$ (mL)	$[H^+]_{eq}$ (mol/L)	$b = [H^+]_{eq}/[TiCl_4]$
0.05	0.5	19.3	0.19	3.86
0.10	1	19,5	0.39	3.90
0.50	5	19.7	1.97	3.94
1.00	10	19.5	3.9	3.90

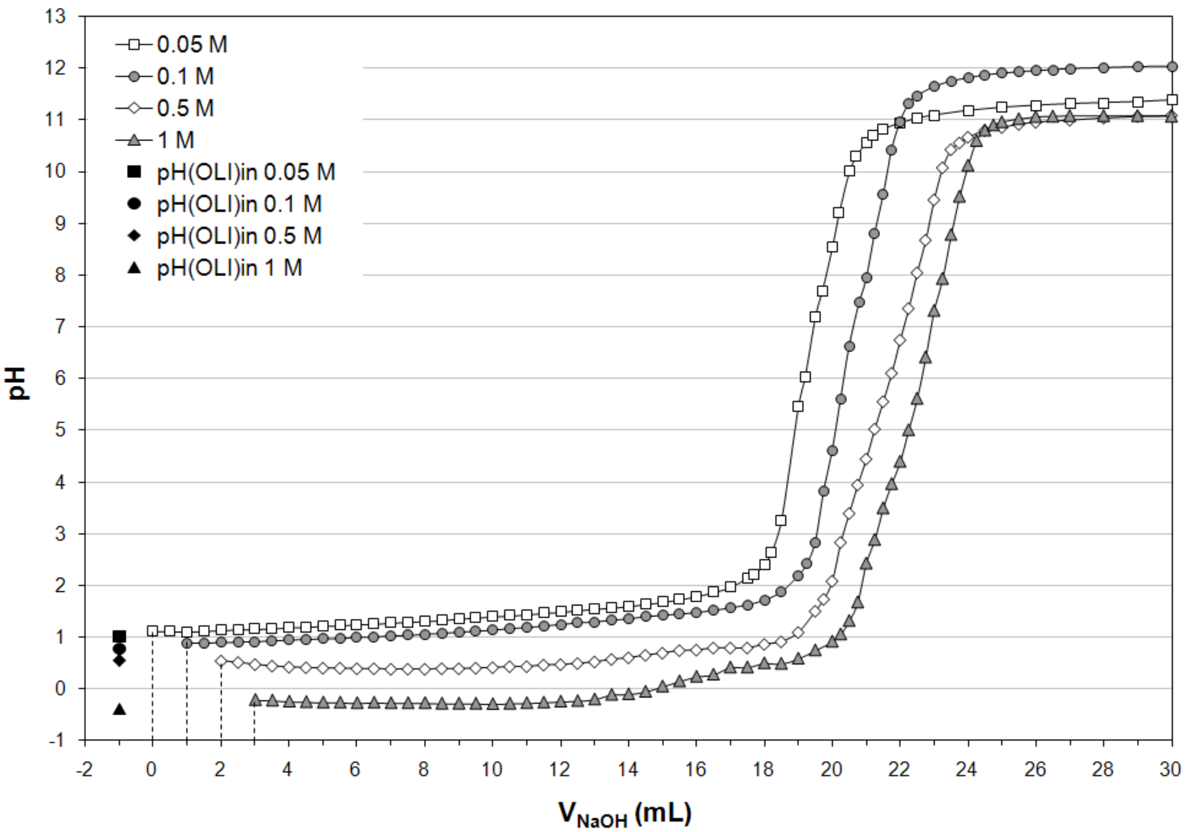

Figure 4.2. Titration curves of 0.05, 0.1, 0.5 and 1 M $TiCl_4$ solutions. The solid black symbols represent the $pH_{OLI,in.}$ computed for each solution and the dash lines the instance V_{NaOH} added = 0 mL for each titration.

The experimental and OLI simulated pH values of 0.05, 0.1, 0.5, and 1 M $TiCl_4$ aqueous solutions reported in Table 4.1 illustrate the strong acidic character of $TiCl_4$ aqueous solutions with $-0.21 < pH_{exp,in.} < 1.12$ and $-0.38 < pH_{OLI,in.} < 1.02$. The acidity of the solutions is seen to increase with the concentration of the solution. The simulated and experimental pH values are in good correlation except for the case of the 1 M $TiCl_4$ solution. The latter may be attributed to the experimental limitations of the pH probe, which is not robust enough for use at very low pH (pH < 0). The experimental pH values were converted to equivalent theoretical concentration in protons, $[H^+]_{exp,in.}$, as in Equation 4.6.

$$[H^+]_{exp,in.} = 10^{-(pHexp,in)} \tag{4.6}$$

The obtained values are compared in Table 4.1 to the OLI values. There exist quite significant discrepencies between the two sets of data. These may be attributed on one hand to the experimental error associated with the pH measurements in very acidic media, and on the other hand to the difference between Equation 4.6 and the theoretical chemistry model used by OLI software that links the hydronium concentration $[H_3O^+]$ to the pH.$^{(b)}$ In fact, in the case of a 0.1 M $TiCl_4$ solution, the values corresponding to the $[H^+]_{exp,in.}$ and $[H_3O^+]_{OLI,in.}$ are observed to differ by a factor of 3 ($[H^+]_{exp,in.} = 0.281$ vs. $[H_3O^+]_{OLI,in.} = 0.940$) although the experimental and simulated pH values were found to be almost identical ($pH_{exp,in.} = 0.55$ vs. $pH_{OLI,in.} = 0.56$). Despite the gap observed between the values obtained for $[H^+]_{exp,in.}$ and $[H_3O^+]_{OLI,in.}$, both are observed to increase with an increasing solution concentration of the solution.

(b) Footnote: In the MSE (H_3O^+) basis of the OLI system, pH is calculated as follows:

$$pH = -\log\left(a^m_{H^+}\right) = -\log\left(\frac{a^x_{H_3O^+}}{a^x_{H_2O}}\frac{1000}{M_{H_2O}}\right) = -\log\left(\frac{\gamma^x_{H_3O^+}\cdot X_{H_3O^+}}{\gamma^x_{H_2O}\cdot X_{H_2O}}\frac{1000}{M_{H_2O}}\right) = -\log\left(\frac{\gamma^x_{H_3O^+}\frac{[H_3O^+]V_t}{n_t}}{\gamma^x_{H_2O}\cdot X_{H_2O}}\frac{1000}{M_{H_2O}}\right)$$

$a^m_{H^+}$: activity of hydrogen ion, on a molality basis

$a^x_{H_3O^+}$: activity of hydronium ion, on a molarity basis

$a^x_{H_2O}$: activity of water, on a molarity basis

M_{H_2O}: molar weight of water

$\gamma^x_{H_3O^+}$: activity coefficient of hydronium ion, on a molarity basis

$\gamma^x_{H_2O}$: activity coefficient of water, on a molarity basis

$X_{H_3O^+}$: molar fraction of hydronium ion

X_{H_2O}: molar fraction of water

$[H_3O^+]$: molar concentration of hydronium ion

V_t: total volume

n_t: total number of moles

All *a* values reported in Table 4.1 are > 0.5, an indication that dilution is consistently associated with partial hydrolysis. If the case of the 1 M $TiCl_4$ solution is excluded, it can be observed that a_{exp} and a_{OLI} decrease with an increasing $TiCl_4$ concentration. In particular, an important drop can be noticed when comparing $a_{0.1M}$ and $a_{0.5M}$ (1.29 vs. 0.56 for $a_{exp.}$ and 2.19 vs. 1.88 for a_{OLI}). From this observation, it may be deduced that the speciation of $TiCl_4$ aqueous solutions depends on their concentration.

The data reported in Table 4.2 show that in all four cases, the values collected for the final conversion yield, *b*, are in the range 3.86-3.94. This result confirms the hypothesis that most of the HCl(g) generated during the preparation of a 2 M $TiCl_4$ stock solution reports into the solution as acid HCl(aq).

Returning to the titration curves in Figure 4.2, it is noticed that all the curves display similar general profiles typical of strong acid-strong base titrations with an initial plateau around $pH_{exp,in.}$, followed by a sharp inflection trend at the equivalence and final plateau. However, when comparing the shape of the titration curves obtained for 0.05 and 0.1 M $TiCl_4$ solutions, some significant differences may be pointed out. First, in the case of the 0.5 and 1 M $TiCl_4$ solutions, it is possible to distinguish the occurrence of a supplemental inflection point prior to the equivalence (at ~ 11-12 mL of added NaOH). Second, at the start of the titration curves, the addition of NaOH is observed to initiate either a slow linear increase of the pH in the case of 0.05 and 0.1 M $TiCl_4$ solutions or a slow decrease-increase event in the case of the 0.5 and 1 M $TiCl_4$ solutions.

The occurrence of multiple inflection points on the titration curves of 0.5 and 1 M $TiCl_4$ solutions suggests that protons are liberated in several steps. These may be related to the sequential and progressive hydrolytic transformation undergone by Ti(IV) species, such as $[Ti(OH)_xCl_z{\cdot}a(H_2O)]^{4-(x+z)}$ or $[TiO_yCl_z{\cdot}a(H_2O)]^{4-(2y+z)}$. It may be assumed, as discussed in section 2.4.2 of Chapter 2 (p. 26) that the chlorides are first replaced by water molecules, which in turn get deprotonated into hydroxyl and/or oxyl groups; these two last steps are expected to generate the release of protons H^+; further on, the hydroxylated and oxylated Ti(IV) complexes combine via olation and oxolation, the latter two reactions also generating protons. On the other hand, the pH decrease-increase event observed at the start of the titration curves of 0.5 and 1 M $TiCl_4$ solutions may be the manifestation of the replacement of chlorides from the first coordination shell of chloro-Ti(IV) complexes with water molecules. In the case of 0.05 and 0.1 M $TiCl_4$ solutions, the occurrence of a single inflection point on the associated titration curves suggests that most Ti(IV) complexes in solution are in the form of already hydroxylated complexes.

4.5. OLI simulation of $TiCl_4$ aqueous solutions

The OLI Stream Analyser is a thermodynamic software used for simulating the speciation and chemical equilibria of multi-component aqueous systems. Several databanks and thermodynamic frameworks are provided within the software and among these the Mixed Solvent Electrolyte model (chemical framework and databank) MSE (H_3O^+ ion) was selected to compute the speciation of $TiCl_4$ aqueous solutions. The assumption was made that no solid phase compounds were present in the system (by deselecting the chemical model option "**So**").

Figure 4.3 is a reproduction of the composite speciation diagram already provided in the literature review of this thesis (Figure 2.8, p. 27). It was modified by adding and/or highlighting the aqueous species listed in the MSE (H_3O^+ ion) chemistry model databank. By comparing both versions of the diagram, four new Ti(IV) species are found to appear, namely $[Ti(OH)_2Cl]^+$, $Ti(OH)_2Cl_2$, $[Ti(OH)_2Cl_3]^-$, and $[Ti(OH)_2Cl_4]^{2-}$. These Ti(IV) hydroxy-chloro complexes may be related to other previously reported Ti(IV) oxy-chloro complexes according to the following hydrolysis reaction:

$$[TiOCl_x]^{(4-2-x)} + H_2O = [Ti(OH)_2Cl_x]^{(4-2-x)} \qquad (4.7)$$

Standard-state properties of these complexes differ by adding/subtracting the standard properties of water. In the MSE (H_3O^+ ion) chemistry model, the assumption is made that all the thermodynamic functions of similar hydrolysis reactions are equal to zero, so that hydroxylated and oxylated complexes of formula $[Ti(OH)_2Cl_x]^{(4-2-x)}$ and $[TiOCl_x]^{(4-2-x)}$, respectively, are considered thermodynamically equivalent in conditions of infinite dilution. In particular, the $Ti(OH)_2Cl_2(aq)$ species figuring in the MSE (H_3O^+ ion) databank may be considered thermodynamically equivalent to the $TiOCl_2(aq)$ species. Nonetheless, several species such as the $[TiCl_x]^{(4-x)}$ complexes, often encountered through spectroscopic investigations in literature, do not appear in the MSE (H_3O^+ ion) databank, apparently due to a lack of "reliable" thermodynamic data [15].

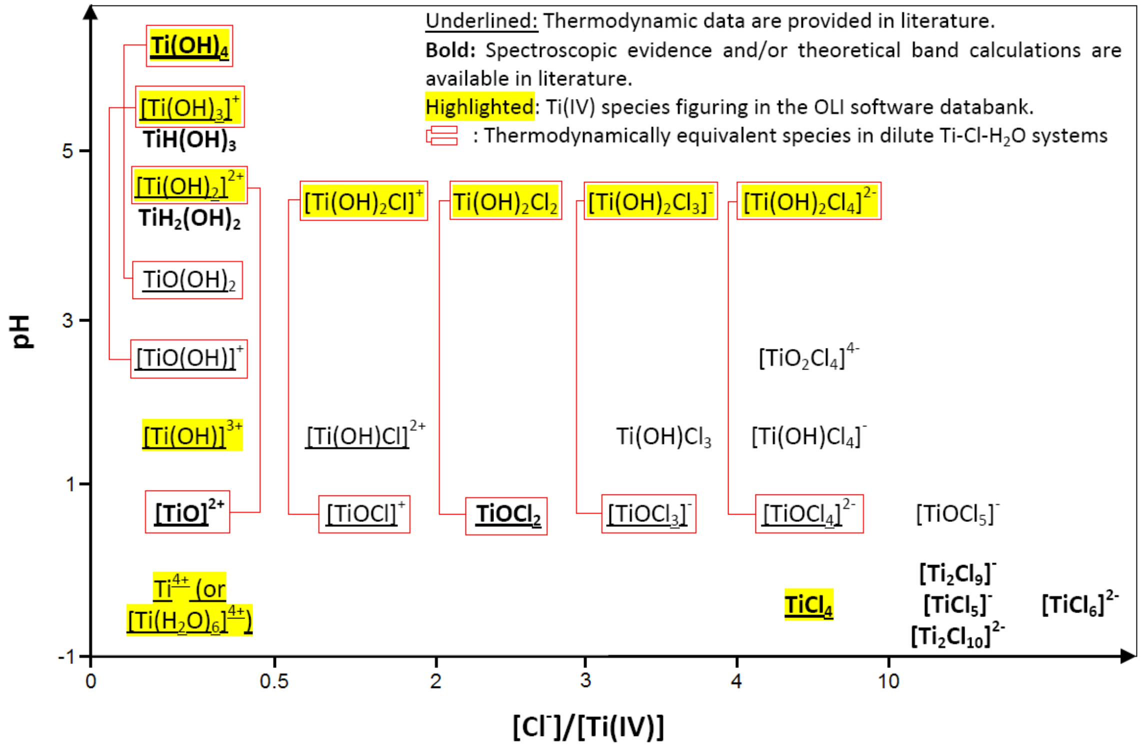

Figure 4.3. Composite speciation diagram of the species present in Ti-Cl-H_2O aqueous systems based on data from various spectroscopic and thermodynamic studies, completed with the Ti(IV) species present in the MSE (H_3O^+ ion) program of the OLI stream analyser software.

A composition survey was performed where Titanium(IV) Chloride and Water were entered as the components of the stream and the concentration of $TiCl_4$ was made to vary in the range 0 – 10 mol/L (Figure 4.4). Figure 4.5 presents the results of this survey: the speciation diagrams obtained for $TiCl_4$ aqueous solutions in the range 0-2 M, 0-5 M, and 0-10 M are shown in Figures 4.5.a, 4.5.b, and 4.5.c, respectively; in addition to the speciation of Ti(IV) species, the concentration of H_3O^+, Cl^- and HCl ions and pH were plotted vs. the $TiCl_4$ concentration in Figure 4.5.c; finally, the percent ratios of Ti(IV) complexes present in 0.05-2 M $TiCl_4$ solutions is illustrated in Figure 4.5.d.

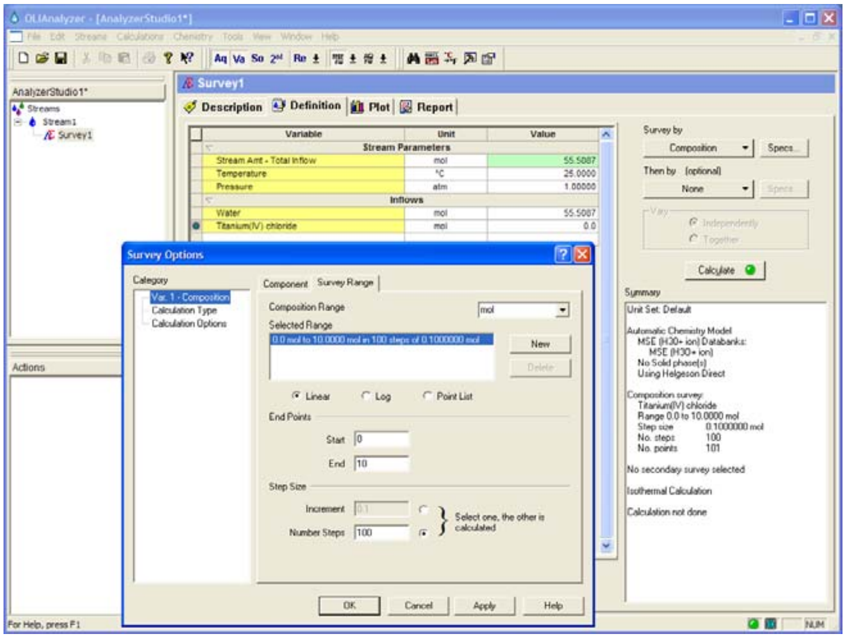

Survey1

Variable	Unit	Value
Stream Parameters		
Stream Amt - Total Inflow	mol	55.5087
Temperature	°C	25.0000
Pressure	atm	1.00000
Inflows		
Water	mol	55.5087
Titanium(IV) chloride	mol	0.0

Survey by: Composition

Then by (optional): None

Vary: ● Independently ○ Together

Composition Range: mol

Selected Range: 0.0 mol to 10.0000 mol in 100 steps of 0.1000000 mol

● Linear ○ Log ○ Point List

End Points

Start: 0

End: 10

Step Size

Increment: 0.1 ○

Number Steps: 100 ●

Select one, the other is calculated

Summary

Unit Set: Default

Automatic Chemistry Model
MSE (H3O+ ion) Databanks:
MSE (H3O+ ion)
No Solid phase(s)
Using Helgeson Direct

Composition survey:
Titanium(IV) chloride
Range 0.0 to 10.0000 mol
Step size 0.1000000 mol
No. steps 100
No. points 101

No secondary survey selected

Isothermal Calculation

Calculation not done

Figure 4.4. Screen view of the survey parameters selected on the interface of the OLI stream analyser software for computing the speciation diagram and pH evolution of 0 - 10 M $TiCl_4$ aqueous solutions.

In the low concentration range (0-2 M $TiCl_4$, Figure 4.5.a) the presence of hydrated and/or hydroxylated complexes can be observed. As the $TiCl_4$ concentration increases, hydroxylated complexes having a decreasing number of hydroxyl groups coordinated to Ti(IV) successively dominate among the chloride-free Ti(IV) complexes. However, for $TiCl_4$ solutions with a concentration > 0.05 M, chloro-Ti(IV) complexes are the dominant species. From Figure 4.5.b, it can be seen that the number of chloride ions coordinated to Ti(IV) complexes increases with the $TiCl_4$ concentration. On Figure 4.5.c, the pH of the solution is observed to drop from 7 to -0.8 for $TiCl_4$ solutions in the concentration range 0-2 M, and further follow a slowly decreasing linear trend for $TiCl_4$ solutions in the concentration range 2-10 M. The concentration of H_3O^+ ions features a linearly increasing trend with a constant molar ratio of ~ 2 mol of H_3O^+ per mol of $TiCl_4$

(Figure 4.5.c). It is also interesting to notice that $[TiCl(OH)_2]^+$ and $TiCl_2(OH)_2$ (Figure 4.5.d), that may be considered as the thermodynamic equivalents of $[TiOCl]^+$ and $TiOCl_2$, respectively, are the two major Ti(IV) species present in solutions with $TiCl_4$ concentrations ranging from 0.05 to 3 M. This is of particular relevance in understanding the nucleation and growth mechanisms involved in the aqueous synthesis of nanostructured TiO_2(s) material via forced hydrolysis of 0.2-1.5 M $TiCl_4$ aqueous solution precursors, as described in the next two chapters.

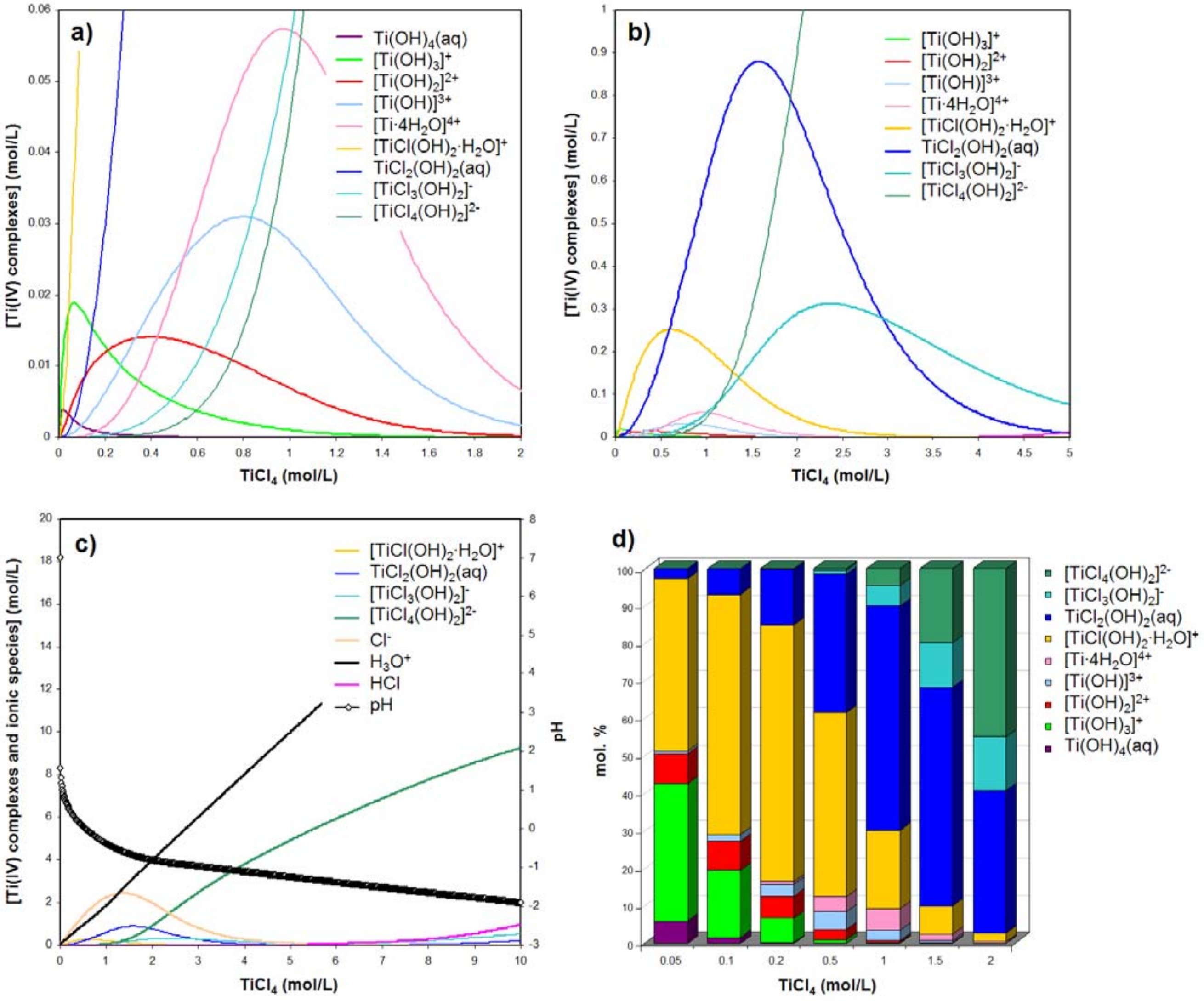

Figure 4.5. Composite speciation diagrams of the species present in $TiCl_4$ aqueous solutions computed with the OLI software at various scales: 0 < $[TiCl_4]$ < 2 M (a), 0 < $[TiCl_4]$ < 5 M (b), and 0 < $[TiCl_4]$ < 10 M (c); molar distribution of the Ti(IV) species present in 0.05-2 M $TiCl_4$ solutions (d).

4.6. Raman spectroscopy of concentrated $TiCl_4$(l) and derived aqueous solutions

Raman spectroscopic analysis was performed on $TiCl_4$ solutions with concentrations in the range 0.05-2 M, pure $TiCl_4$(l) and yellow solid compounds collected during the preparation of the 2 M stock solution ((a) Footnote, p.75). No similar study was found in literature, at least not in the case of dilute (≤ 2 M) $TiCl_4$ aqueous solutions. However, the Raman spectrum of concentrated $TiCl_4$(l) and various other Ti(IV)-Cl(-I)-H_2O systems were found in literature [14,16-20]. The molecular vibration modes reported in these references, whether they were hypothetically assigned or theoretically calculated, were used as background information to interpret the features appearing on the Raman spectra presented in this study. The obtained Raman spectra and a comprehensive list of Raman vibration modes gathered from various literature sources are provided in Figures 4.6.a-c, and Figure 4.6.d, respectively.

In Figure 4.6.a, a series of peaks is observed to successively appear as the concentration of $TiCl_4$ aqueous solutions increases. Starting with the spectrum related to deionised water, one broad band can be observed in the range 100-250 cm^{-1} with a shoulder around 160 cm^{-1}. According to *Carey and Korenovsky* [21] this band is attributed to translational vibration mode of liquid water involving O-O stretching along the O–H···O or hydrogen bond direction. As the concentration of $TiCl_4$ in solution is increased from 0.05 to 0.2 M, the appearance of a peak at ~ 970 cm^{-1} is first noticed. *Graetzel and Rotzinger* [20] observed a peak at 975 cm^{-1} on Raman spectra of aqueous solutions of $TiO(ClO_4)_2$ and $TiOCl_2$ in 2 M HCl, which they attributed to the stretching vibration mode of Ti=O, induced by titanyl $[TiO]^{2+}$ ions. When moving to the Raman spectrum of a 0.5 M $TiCl_4$ solution, an intensification of the peak at 970 cm^{-1} and the broad band in the range 100-150 cm^{-1} can be observed along with the formation of a small shoulder with a maximum around 260 cm^{-1}. On one hand, the increased intensity of the peak at 970 cm^{-1} may be attributed to a higher concentration of $[TiO]^{2+}$ ions or other Ti(IV) species bearing Ti=O types of bonds. On the other hand, the increased intensity of the band in the range 100-150 cm^{-1} and the formation of a shoulder at ~ 260 cm^{-1} may suggest the presence of chloro-Ti(IV) complexes. In fact, it is known from the

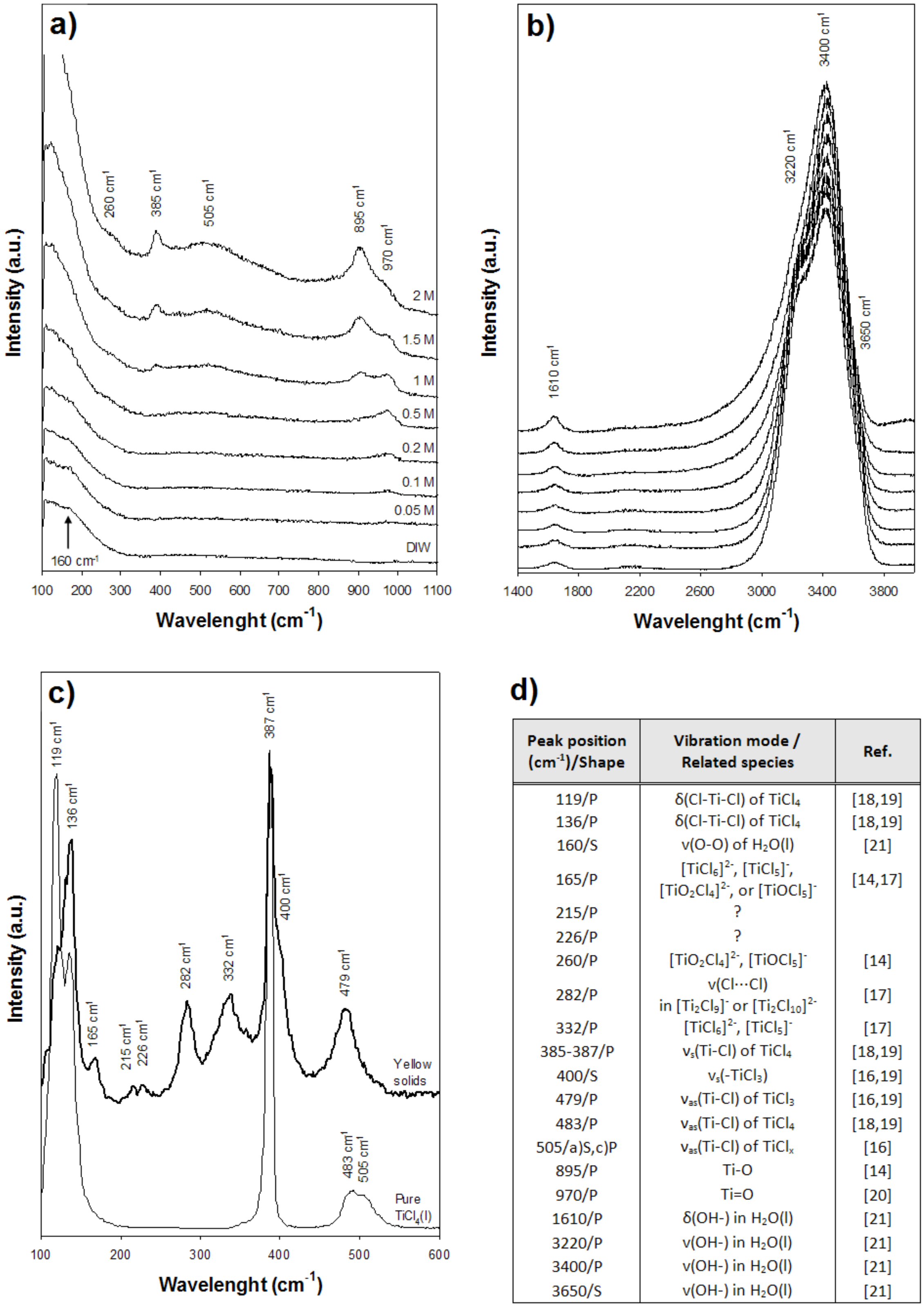

d)

Peak position (cm^{-1})/Shape	Vibration mode / Related species	Ref.
119/P	δ(Cl-Ti-Cl) of $TiCl_4$	[18,19]
136/P	δ(Cl-Ti-Cl) of $TiCl_4$	[18,19]
160/S	ν(O-O) of H_2O(l)	[21]
165/P	$[TiCl_6]^{2-}$, $[TiCl_5]^-$, $[TiO_2Cl_4]^{2-}$, or $[TiOCl_5]^-$	[14,17]
215/P	?	
226/P	?	
260/P	$[TiO_2Cl_4]^{2-}$, $[TiOCl_5]^-$	[14]
282/P	ν(Cl···Cl) in $[Ti_2Cl_9]^-$ or $[Ti_2Cl_{10}]^{2-}$	[17]
332/P	$[TiCl_6]^{2-}$, $[TiCl_5]^-$	[17]
385-387/P	ν_s(Ti-Cl) of $TiCl_4$	[18,19]
400/S	ν_s(-$TiCl_3$)	[16,19]
479/P	ν_{as}(Ti-Cl) of $TiCl_3$	[16,19]
483/P	ν_{as}(Ti-Cl) of $TiCl_4$	[18,19]
505/a)S,c)P	ν_{as}(Ti-Cl) of $TiCl_x$	[16]
895/P	Ti-O	[14]
970/P	Ti=O	[20]
1610/P	δ(OH-) in H_2O(l)	[21]
3220/P	ν(OH-) in H_2O(l)	[21]
3400/P	ν(OH-) in H_2O(l)	[21]
3650/S	ν(OH-) in H_2O(l)	[21]

Figure 4.6. Micro-Raman spectra of 0.05-2 M $TiCl_4$ aqueous solutions in the wavelength range 100-1100 cm^{-1} (a) and 1400-4000 cm^{-1} (b); concentrated $TiCl_4$(l) and yellow solid compounds (c); and list of Raman vibration modes associated to Ti(IV)-Cl(-I)-H_2O systems from literature (d).

Raman spectrum of concentrated $TiCl_4$ that the bending modes δ(Cl-Ti-Cl) of Ti-Cl chemical bonds appear in the wavelength range 110-140 cm^{-1}, namely under the form of two strong peaks at 119 and 136 cm^{-1} in the case of molecular $TiCl_4$ [18,19]. Moreover, *Davies et Long* [14] reported the appearance of two strong Raman peaks in the spectral regions 155-168 cm^{-1} and 255-261 cm^{-1} from the Raman spectra of $TiCl_4$ and $TiOCl_2$ solutions prepared in HCl, which they attributed to the presence of species such as $[TiO_2Cl_4]^{4-}$ or $[TiOCl_5]^{-}$. However, in several studies [14,18,19], the appearance of strong peaks in the spectral range 340-390 cm^{-1} is attributed to the stretching modes of Ti-Cl bonds that do not show on the Raman spectrum of 0.5 M $TiCl_4$ solution. This last observation makes it difficult to draw conclusions on the exact nature of the chloro-Ti(IV) complexes and the features of this spectrum. Nevertheless, the broad band present in the range 100-150 cm^{-1} may be thought to arise from the bending vibration modes δ(Cl-Ti-Cl) of other chloro-Ti(IV) species, such as $TiOCl_2$. Unfortunately, no Raman spectrum associated to the $TiOCl_2$ molecule was found in literature to correlate such hypothesis. For $TiCl_4$ solutions with concentrations in the range 1-2 M, the appearance and increasing intensity of a peak at 385 cm^{-1}, a shoulder with a maximum at ~ 505 cm^{-1}, and another peak at 895 cm^{-1} are observed. The peak at 385 cm^{-1} may be attributed to the symmetric stretching mode of $TiCl_4$ as suggested in various studies [14,18,19] while the broad shoulder at ~ 505 cm^{-1} may be thought to originate from the superimposition of the anti-symmetric vibration mode of $TiCl_4$ and other $TiCl_x$ ($x \neq 4$) species such as suggested by *Schrijnemakers et al.* [16]. The presence of a peak at 895 cm^{-1} may be associated to the vibration modes of Ti-O bonds, generally expected to appear in the wavelength range 800-1100 cm^{-1} [14]. It may be thought to relate to the presence of hydroxyl groups in the first coordination shell of Ti(IV). However, no data were found in literature to corroborate this assumption.

In Figure 4.6.b, a small peak at 1610 cm^{-1}, two large peaks at ~ 3220 and 3400 cm^{-1} and a shoulder at ~ 3650 cm^{-1} can be distinguished. All of these features are associated with the presence of water molecules. More specifically, the small peak at 1610 cm^{-1} is attributed in literature to the -OH bending vibration mode while the other peaks in the range 3000-3700 cm^{-1} relate to of the -OH stretching vibration modes [21]. As the concentration of the solution is increased, it may be observed that the intensity of the peak at 1610 cm^{-1} slightly increases while the intensities of the peaks at 3220 and 3650 cm^{-1} decrease quite significantly. According to *Carey and Korenowski* [21], all these peaks are related to the amount of H-bonding engaged in the solution, so that the significant decrease in intensity of the peaks at 3220 and 3650 cm^{-1} indicates that fewer H-bonds occur in high concentration $TiCl_4$. This observation may also be interpreted as indicative that the quantity of free water molecules, as opposed to water molecules coordinated to Ti(IV) ions, decreases as the concentration of $TiCl_4$ solutions increases.

The spectrum corresponding to concentrated $TiCl_4$(l) (Figure 4.6.c) is very similar to other spectra found in literature. Its main features are two very strong peaks at 119 and 387 cm^{-1}, a strong peak at 136 cm^{-1} and a broad and lower intensity peak in the range 480-510 cm^{-1}. As mentioned earlier, the peaks at 119 and 136 cm^{-1} are attributed to the bending mode δ(Cl-Ti-Cl) of $TiCl_4$ molecules while the peaks at 387 and 483 cm^{-1} correspond to the symmetric ν_s(Ti-Cl) and anti-symmetric ν_{as}(Ti-Cl) stretching modes of $TiCl_4$ [18,19]. Unlike all spectra found in literature, the broad peak at 500 cm^{-1} can be seen to feature two maxima at 483 and 505 cm^{-1}.The shoulder at 505 cm^{-1} was assigned by *Schrijnemakers et al.* [16] to the anti-symmetric vibration mode ν(Ti-Cl) of $TiCl_x$ groups.

The Raman spectrum obtained for the yellow solid compounds is more complex (Figure 4.6.c) to interpret due to the appearance of a multitude of peaks, which are indicative of the presence of various species. Similarities with the spectrum collected for concentrated $TiCl_4$(l) can be noticed, such as the shoulder with a maximum at 120 cm^{-1}, and two peaks at 136 and 387 cm^{-1}, attributed to the presence of $TiCl_4$ molecules. The peak observed at 479 cm^{-1} and the shoulder with a maximum at 400 cm^{-1} may be indicative of the presence of -$TiCl_3$ groups: *Morrow and Hardin* [19] attributed a peak at 400 cm^{-1} to the symmetric stretching mode ν(Ti-Cl) of -$TiCl_3$ groups and suggested that a peak with lower intensity related to the anti-symmetric stretching mode ν_{as}(Ti-Cl) of -$TiCl_3$ groups should appear in the wavelength range 450-500 cm^{-1}. It is also noteworthy to mention that the peaks observed at 165 and 479 cm^{-1} also showed on the spectrum of $TiOCl_2$-HCl solution reported by *Davies and Long* [14]. However, they also reported two strong peaks at 255 and 348 cm^{-1}, which are not present in the spectrum of the yellow solid compounds here investigated. *Mamaevea et al.* [22] also reported that $TiCl_3$ (in the planar D_{3h} symmetry configuration, such as in $[TiCl_3(OH)_2]^-$) is Raman active and should exhibit three peaks at 107±7, 320±30, and 498±16 cm^{-1}. These positions correlate features such as the shoulder with a maximum at 120 cm^{-1} and the peak at 332 cm^{-1}. The latter may also be thought to originate from the superimposition of peaks at 320, 354, and 349 cm^{-1} reported by *Creaser and Creighton* [17], which they attributed to the presence of $[TiCl_6]^{2-}$ and $[TiCl_5]^-$. The same authors also mentioned that in the presence of Ti(IV) chloride dimmers such as $[Ti_2Cl_9]^-$ or $[Ti_2Cl_{10}]^{2-}$, the appearance of peaks in the wavelength range 250-300 cm^{-1} is expected in relation to the stretching mode of chlorine bridges ν(Cl···Cl). This is the case of the Raman spectrum obtained for the yellow solid compounds, which features a peak at 282 cm^{-1}. Besides, the strongest peaks of $[Ti_2Cl_9]^-$ or $[Ti_2Cl_{10}]^{2-}$ are expected in the spectral regions 380-420 and 340-390 cm^{-1}, respectively, correlating the strong peak and shoulder observed in the range 380-410 cm^{-1}. Finally, no similar features were found in literature that explains the appearance of two small peaks at 215 and 226 cm^{-1}. Although these occur in the wavelength range associated with the vibration mode of metal chloride bonds, their interpretation remains inconclusive.

4.7. Discussion

The observations made during the preparation of a 2 M $TiCl_4$ stock solution were in good correlation with literature. First, the exothermic character of $TiCl_4$ hydrolysis [1] was confirmed by monitoring the temperature changes inside the solution. Second, solutions prepared with a concentration ≥ 1 M were found to be characterised with a typical yellow coloration, correlating the observations made by other researchers [14,23]. *Davies and Long* [14] suggested that the colour originates from the formation of $TiOCl_2(s)$. However, *Nabivanets* [23] reported that only solutions containing anionic

Ti(IV) chloride complexes are characterized with a yellow coloration. This last observation is in agreement with the presence of Ti(IV) species such as $[TiCl_6]^{2-}$, $[TiCl_5]^-$, $[Ti_2Cl_9]^-$ and $[Ti_2Cl_{10}]^{2-}$, suggested to appear in ≥ 1 M $TiCl_4$ aqueous solutions based on the appearance of peaks at 282 and 332 cm^{-1} on the Raman spectrum of yellow solid compounds formed by reaction of concentrate $TiCl_4(l)$ with environmental moisture.

The experimental and OLI simulated acidic pH values collected for 0.05-1 M $TiCl_4$ solutions, confirmed the partial hydrolysis of $TiCl_4$ by reaction of $TiCl_4(l)$ with water. The stoechiometric ratio of protons liberated, *a*, was found to vary with the concentration of the solution, an indication that partial hydrolysis leads to the formation of various Ti(IV) species. This assumption was first correlated to features observed on the titration curves of 0.05 to 1 M $TiCl_4$ solutions and particularly to the appearance of multiple inflection points on the titration curves of 0.5 and 1 M solutions. Second, the OLI thermodynamic simulation and Raman spectroscopic investigation of $TiCl_4$ aqueous solutions further confirmed that the speciation of $TiCl_4$ aqueous solutions strongly depends on their concentration.

Identification of some Ti(IV) complexes became possible through the combination of Raman spectroscopic investigation and OLI thermodynamic simulation of 0.05-2 M $TiCl_4$ solutions. First, the appearance and increasing intensity of peaks related to the vibration modes of Ti-Cl bonds on the Raman spectra of 0.5 to 2 M $TiCl_4$ solutions (Figure 4.6.a) was in agreement with the increasing presence of chloro-Ti(IV) complexes suggested by the OLI software (Figure 4.5.a). Second, the occurrence of Raman peaks at 970 cm^{-1} and 895 cm^{-1} related to the vibration modes of Ti=O and Ti-O bonds, respectively, suggested the simultaneous presence of oxylated Ti(IV) aqueous species such as TiOCl, $TiOCl_2$, $TiOCl_3$ and $TiOCl_4$ and hydroxylated thermodynamic equivalents present in the MSE (H_3O^+) chemistry model, namely $[TiCl(OH)_2]^+$, $[TiCl_2(OH)_2]^0$, $[TiCl_3(OH_2)]^-$ and $[TiCl_4(OH)_2]^{2-}$. Besides, both peaks were observed to increase with the concentration of the solution, which phenomenon is corroborated by the increasing concentration of $[TiCl_2(OH)_2]^0$, $[TiCl_3(OH_2)]^-$ and $[TiCl_4(OH)_2]^{2-}$ for $TiCl_4$ aqueous solutions in the concentration range 0-2 M (Figure 4.5.c).

However, some discrepancies appear when comparing results obtained from the Raman spectroscopic and OLI thermodynamic simulation studies of $TiCl_4$ aqueous solutions. For instance, the Ti(IV) chloride aqueous species of formula $[Ti_yCl_x]^{(4y-x)}$, suggested to participate in the speciation of 1-2 M $TiCl_4$ solutions based on the results of Raman spectroscopic analyses, did not figure in the MSE (H_3O^+ ion) databank of the OLI stream analyzer software (apparently due to a lack of reliable thermodynamic data in literature [15]). Moreover, the presence of Ti(IV) hydroxylated complexes of formula $[Ti(OH)_x]^{(4-x)}$ in 0.05-0.1 M $TiCl_4$ solutions, accounting for ~ 30-50 mol. % of the Ti(IV) complexes present in these solutions according to the OLI thermodynamic simulation (Figure 4.5.d), could not be confirmed by using Raman spectroscopy. This, however, may be due to the limited sensitivity of the Micro-Raman apparatus at low $TiCl_4$ concentration. Finally, the Raman spectroscopic analysis of concentrated $TiCl_4$(l) (9.06 M) showed molecular $TiCl_4$ to be the main species present in solution, whereas the OLI thermodynamic simulation of $TiCl_4$ solutions in the concentration range 9-10 M suggested $[TiCl_4(OH)_2]^{2-}$ to be largely predominant.

4.8. Conclusions

Speciation of $TiCl_4$ solutions is a very complex topic. Among the various Ti(IV) aqueous species listed in Figure 4.3, only very few, namely $TiCl_4$, $TiOCl_2$, TiO^{2+}, $Ti(OH)_4$, appear in both thermodynamic and spectroscopic types of studies, so that there is a large gap of information that remains to be filled. Besides, no study was found in literature that systematically investigates the speciation of $TiCl_4$ solutions with concentrations in the range 0-2 M. Finally, it is generally difficult to access detailed information on the speciation of commercially available products such as “$TiOCl_2 \cdot HCl$ aqueous solutions”.

The study reported in this chapter, by combining the results of acid-base titrations, thermodynamic simulations, and Raman spectroscopic analyses, offers some advances and contributes to a better knowledge and understanding of the speciation of $TiCl_4$ aqueous solutions. In particular, the results confirmed that the reaction of $TiCl_4$(l) with water does not necessarily leads to the formation of TiO_2(s) but various partially hydrolyzed Ti(IV)-(Cl) species. Considering the latter, a new general reaction mechanism may be suggested that describes $TiCl_4$ partial hydrolysis (in Equation 4.8, *b* = *x* + *y* and *d* = *a* - *c*):

$$a\ TiCl_4 + b\ H_2O = c\ [Ti(OH)_xCl_{z1}]^{4-(x+z1)} + d\ [TiO_yCl_{z2}]^{4-(2y+z2)} + (4a-cz_1-dz_2)\ Cl^- + (cx+2dy)\ H^+ \quad (4.8)$$

For future work, complementary Infra-Red spectroscopic analyses of 0.05-2 M and concentrated $TiCl_4(l)$ may be performed in order to complete the results obtained with Raman spectroscopy. Improvement of the MSE (H_3O^+ ion) databank by determination of the thermodynamic data related to species of formula $[TiCl_x]^{4-x}$ is necessary to better correlate the results obtained by using OLI thermodynamic simulations and Raman spectroscopic investigation of $TiCl_4$ solutions.

4.9. References

[1] T. Kapias and R. F. Griffiths, *J. Haz. Mater.*, **119** (2005), 41.

[2] B. I. Nabivanets and L. N. Kudritskaya, *Russ. J. Inorg. Chem.*, **12** (1967), 789.

[3] B. I. Nabivanets and L. N. Kudritskaya, *Russ. J. Inorg. Chem.*, **12** (1967), 616.

[4] T. C. DeVore and T. N. Gallaher, *High Temp. Sci.*, **16** (1983), 269.

[5] J. D. Ellis and G. A. K. Thompson, *Inorg. Chem.*, **15** (1976), 3172.

[6] L. Ciavatta, D. Ferri, and G. Riccio, *Polyhedron*, **4** (1985), 15.

[7] S.-J. Kim, S. D. Park, and Y. H. Jeong, *J. Am. Ceram. Soc.*, **82** (1999), 927.

[8] T. G. Kim, H. J. Kim, J. J. Kim, S. W. Kim, S. S. Park, S. S. Hong, and G. D. Lee, *Mater. Sci. Forum*, **544 – 545** (2007), 99.

[9] http://www.lookchem.com/cas-137/13780-39-7.html

[10] http://www.cristalarabia.com/ProductDocuments/TiOCl2%20Technical%20Data%20Sheet%20June%2009.pdf

[11] M. Madekufamba, L. N. Trevani, and P. R. Tremaine, *J. Chem. Thermodyn.*, **38** (2006), 1563.

[12] L. A. Bruno and B. C. Beard, *J. Appl. Spectros.*, **51** (1997), 131.

[13] S. Raoot, N. R. Desikan, R. Shekhar, and J. Arunachalam, *J. Appl. Spectros.*, **54** (2000), 1412.

[14] J. E. D. Davies and D. A. Long, *J. Chem. Soc. A*, (1968), 2560.

[15] Private communication with the technical support staff from OLIsystems.

[16] K. Schrijnemakers, P. Cool, and E. F. Vansant, *J. Phys. Chem. B*, **106** (2002), 6248.

[17] C. S. Creaser and J. A. Creighton, *J. Chem. Soc., Dalton Trans.*, (1975), 1402.

[18] R. J. H. Clark and C. J. Willis, *Inorg. Chem.*, **10** (1971), 1118.

[19] B. A. Morrow and A. H. Hardin, *J. Phys. Chem.*, **83** (1979), 3135.

[20] M. Graetzel, F. P. Rotzinger, *Inorg. Chem.*, **24** (1985), 2320.

[21] D. M. Carey and G. M. Korenowski, *J. Chem. Phys.*, **108** (1998), 2669.

[22] G. I. Mamaeva, G. V. Romanov, V. P. Spiridonov, and S. I. Troyanov, *J. Struct. Chem.*, **28** (1987), 846.

[23] B. I. Nabivanets, *Russ. J. Inorg. Chem.*, **7** (1962), 210.

Chapter 5: Aqueous Synthesis of Self-Assembled Nanofibre-Structured Rutile (TiO_2) Particles

5.1. Introduction

In this chapter, the production of rutile (TiO_2) nanostructured powders by forced hydrolysis of aqueous Ti(IV) chloride solutions is investigated in terms of precipitation kinetics and nucleation and growth mechanism over the temperature range 70-90 °C and Ti(IV) concentration range 0.5-1.5 M. Details on the method used were given in section 3.3.2.4 of Chapter 3. The precipitation kinetics is analysed with the aid of the Avrami model. The effects of experimental parameters such as the type and speed of agitation, the temperature, and the initial concentration of the solution on the kinetics of the hydrolysis reaction and the properties of the obtained TiO_2 products are presented and discussed. Finally, controlled forced hydrolysis is shown that can lead to the production of unique self-assembled nanofibre structured rutile particles with potential for application as scattering centres in the fabrication of DSC photoanodes.

5.2. Induction-nucleation

In the first stage of the present investigation, a study of the induction period of the solution that marks the initiation of the precipitation reaction was conducted. The effect of the initial concentration of the solution was studied: $TiCl_4$ aqueous solutions (100 mL) prepared with 0.5, 0.75, 1, 1.25 and 1.5 M $TiCl_4$ concentration were simultaneously subjected to step-wise heating, starting at ~ 13 °C with an average rate of 1 °C/min, under magnetic stirring (Figure 5.1, more details are provided in section 3.3.2 of Chapter 3). The purpose of this test was to determine the minimum temperature required for the initiation of precipitation by forced hydrolysis.

The initiation of nucleation was visually manifested and monitored. Once nucleation started, the solutions turned white opaque as shown in Figure 5.1. The induction temperature – the temperature at which the milky cloud appeared – was found to vary with the initial $TiCl_4$ concentration. Thus, as it can be seen in Figure 5.1.a and Figure 5.1.b, after 73 min heating (corresponding to 80 °C) nucleation had already occurred in the 0.5 M $TiCl_4$ solution but not in the 1.0 M solution, while it just started in the 0.75 M solution. The heating profile along with the determined induction temperature for the various $TiCl_4$ concentration solutions is presented in Figure 5.1.c. The presented data reveals under the applied heating profile that no nucleation took place below 70 °C. The nucleation temperature increased with increasing concentration, namely 72 °C for 0.5 M; 76 °C for 0.75 M; 82 °C for 1.0 M; 85 °C for 1.25 M and 90 °C for 1.5 M $TiCl_4$ solutions. At the end of the test (95 °C), all solutions were completely white opaque.

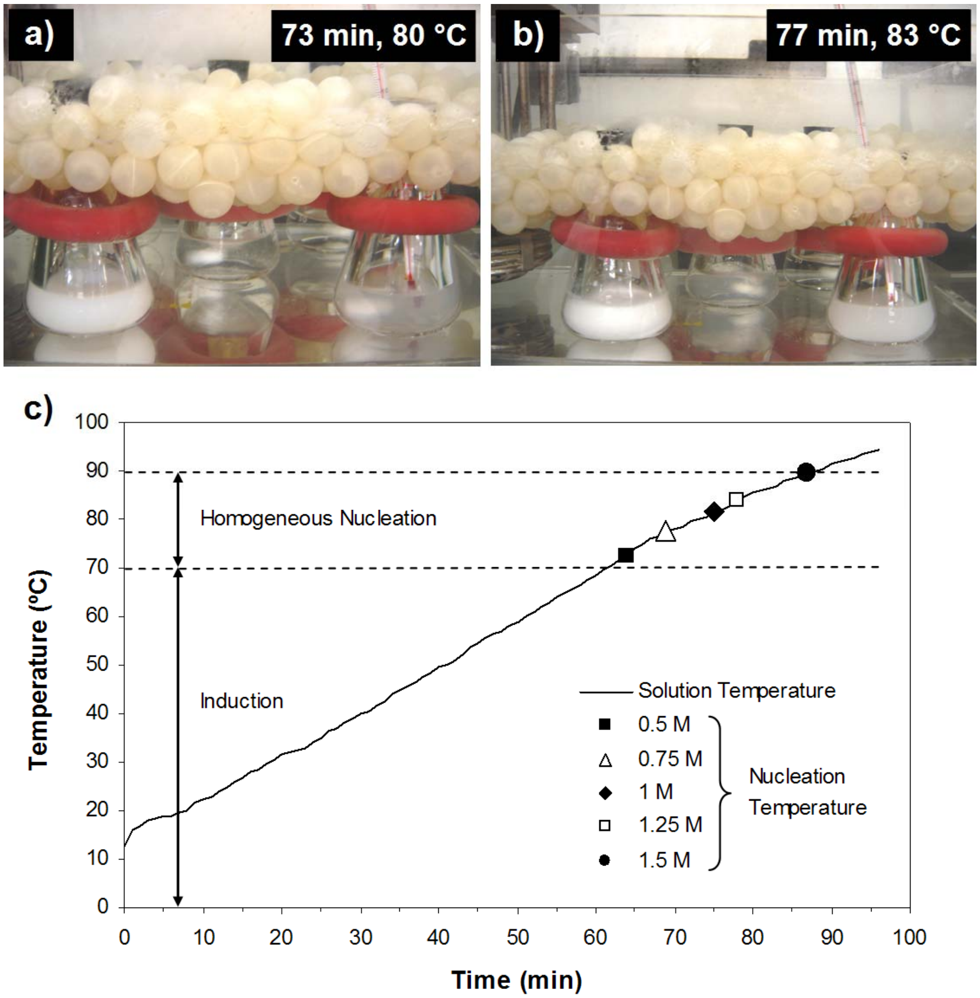

Figure 5.1. Visual monitoring of nucleation onset as a function of time and initial $TiCl_4$ aqueous concentration (a,b): 0.5 M (left corner), 0.75 M (right corner), 1 M (centre); heating profile and nucleation temperature as a function of $TiCl_4$ initial concentration (c).

The question that arises from the obtained data is why the nucleation temperature increases with increasing concentration. The hydrolysis reaction that leads to TiO_2 nucleation-formation is associated with acid generation:

$$TiCl_4(aq) + 2\ H_2O(l) \rightarrow TiO_2(s) + 4\ HCl(aq) \tag{5.1}$$

An increase in $TiCl_4$ initial concentration ($[TiCl_4]_{inital}$) leads to an increase in $[H^+, Cl^-]$, as reported in Chapter 4. Hence, one possible explanation for the observed behaviour may be the increased acidity that hinders the initiation-progress of the hydrolysis reaction (Equation 5.1) in accordance with Le Chatelier's principle. Another possible explanation for the observed behaviour may be the nature of the precursor Ti(IV)-Cl(-I)-H_2O complexes that is known to change with increasing concentration. The investigation on the speciation of $TiCl_4$ aqueous solutions that was presented in Chapter 4 showed that Ti(IV) ions in dilute solution are coordinated either to -OH_2, -OH or -Cl groups. The polymerization of the Ti(IV) complexes leads to the formation of TiO_2 nuclei by interaction of adjacent -OH and/or -OH_2 groups participating in the octahedral structure of the Ti(IV) complex, resulting in the formation of Ti-O-Ti chemical bonds and simultaneous loss of H_2O and protons H^+. The higher the initial concentration of the solution, the less water molecules or hydroxyl groups participate in the octahedral configuration of the Ti(IV) complexes (Figure 4.3 of Chapter 4, p. 81). This leaves Cl^- ions occupying the first coordination shell of Ti(IV), apparently rendering less amenable the latter to hydrolysis.

5.3. Isothermal kinetics

In this part of the study, $TiCl_4$ solutions were isothermically processed in a custom-designed reactor, which is described in Chapter 3. The kinetics of hydrolytic conversion of $TiCl_4(aq)$ to $TiO_2(s)$ was studied at various agitation speeds (500 and 1000 rpm), initial $TiCl_4(aq)$ concentrations (0.5, 0.75, 1, and 1.25 M $TiCl_4$) and temperatures (60, 70, and 80 °C), as presented in Figures 5.2.a, 5.2.b, and 5.2.c, respectively.

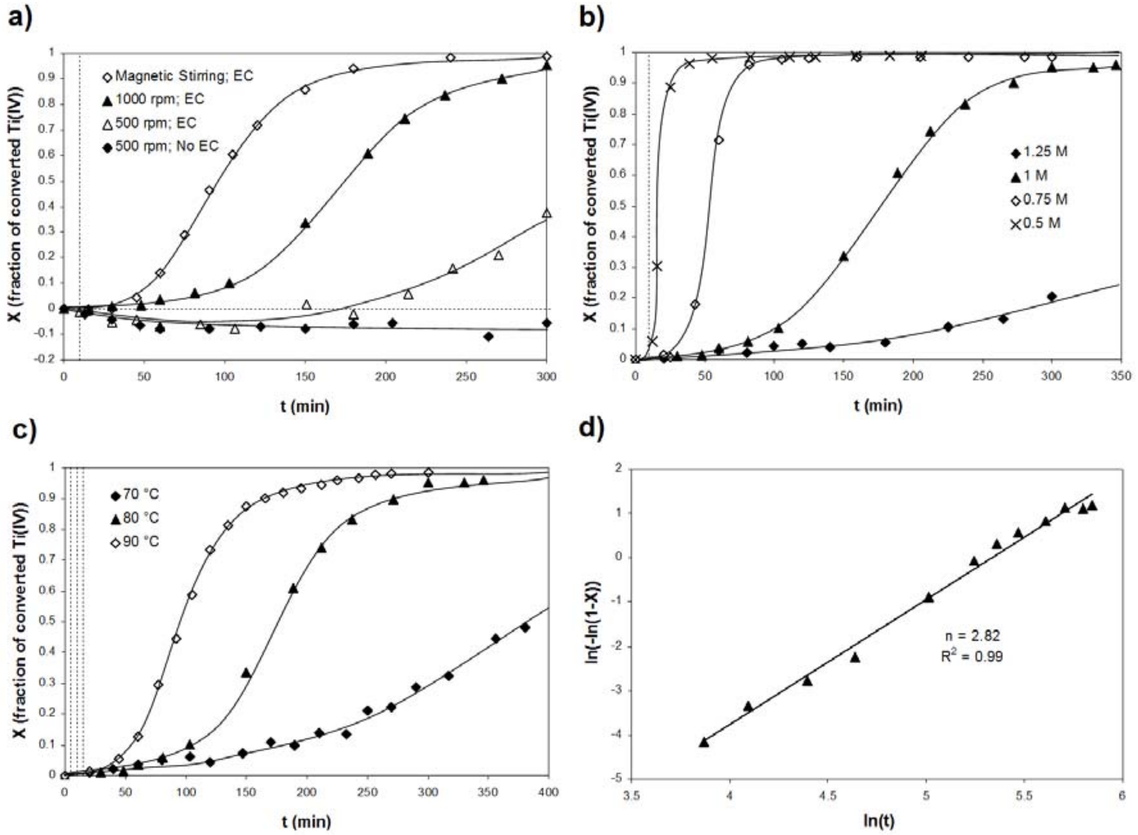

Figure 5.2. Kinetics of TiO_2 precipitation: (a) effect of agitation speed and reactor configuration (evaporation control "EC") on Ti(IV) conversion for $[TiCl_4]_{initial}$ = 1 M and T = 80 °C; (b) effect of $TiCl_4$ concentration on Ti(IV) conversion at T = 80 °C for $[TiCl_4]_{initial}$ = 0.5 M, 0.75 M, 1 M, 1.25 M; (c) effect of temperature on Ti(IV) conversion yield for $[TiCl_4]_{initial}$ = 1 M and T = 70 °C, 80 °C and 90 °C. Dash lines at 10 min (a,b) and at 5, 10 and 15 min (c): end of the heat-up period; (d) ln-ln plot of the Avrami equation for $[TiCl_4]_{initial}$ = 1 M and T = 80 °C.

It is interesting to note that the kinetics of hydrolytic conversion of $TiCl_4$(aq) to TiO_2(s) was greatly affected by the agitation speed as well as the type of agitation (mechanical vs. magnetic) and the use of an open or closed ("evaporation control", EC) vessel.(a) As mentioned in the previous section ("Induction – Nucleation"), the first series of tests involved stoppered conical flasks (Figures 5.1.a and 5.1.b) that were magnetically stirred. Such type of stirring/reactor configuration resulted in shorter indu-

(a) Footnote: On Figure 5.2.a it can be seen that negative conversion values were obtained for two of the tests. These arose from an initial increase of the Ti(IV) concentration in solution as a result of evaporation.

ction period and faster overall kinetics (refer to curve with open diamond symbols in Figure 5.2.a). Upon replacement of magnetic stirring with the mechanically agitated reactor, significantly slower precipitation kinetics was observed. Moreover, the agitation speed was found to generally influence the induction period and overall kinetics (Figure 5.2.a). The kinetics further appeared to slow down, i.e. the induction period was extended, if an open (uncovered) reactor was used. It is tentatively deduced from these results that agitation affects the polymerization process involving the precursor Ti(IV) complex hence the homogenous nucleation of TiO_2 and ultimately the crystal size and morphology of the resultant powder. With the view of controlling the kinetics in a reproducible manner – an issue not addressed in previous studies – the mechanically agitated reactor operated at fixed agitation speed (1000 rpm) was used for the subsequent tests described in Figures 5.2.b and 5.2.c.

By examining Figures 5.2.b and 5.2.c the kinetics of conversion of $TiCl_4$(aq) to TiO_2(s) is observed to slow down with an increase in $TiCl_4$(aq) concentration (or equivalently supersaturation) and to accelerate with an increase in temperature. The former effect is rather counter-intuitive pointing to a non-typical chemical crystallization system. As it can be seen, the reaction curves are S-shaped consisting of an induction period, an accelerating middle part and a final plateau. The induction period corresponding to the formation of the TiO_2 nuclei was found, in addition to agitation speed, to vary according to the $TiCl_4$(aq) concentration and temperature. Thus at 80 °C (Figure 5.2.b) the induction time increased from 10 to 20, 40 and 60 min as the $TiCl_4$(aq) concentration increased from 0.5 to 0.75, 1.0 and 1.25 M respectively. On the other hand at fixed initial concentration 1.0 M Ti(IV) the induction time decreased from 50 min at 70 °C to 40 min at 80 °C and 25 min at 90 °C. (b)

(b) Footnote: Time zero (t=0) in these graphs corresponds to the time heating of the solutions started. Typically it took 5, 10 or 15 min for the solution to reach the target temperature: 70 °C, 80 °C and 90 °C. The end of the heat-up period is indicated on the figures with dash lines.

The S-shaped kinetic curves can be described with the aid of the Avrami nucleation-growth model [1,2], as per Equation 5.2:

$$x(t) = 1 - \exp(-kt^{n}) \qquad (5.2)$$

where x is the conversion of $TiCl_4$(aq) into TiO_2(s), k is the apparent nucleation-growth rate constant and n the particle geometry parameter. As reported in Figure 5.2.d, ln-ln plots of the Avrami equation (Equation 5.3) yielded values of n ~ 3, characteristic of spheroidal particle growth.

$$\ln(-\ln(1 - x)) = \ln(k) + n.\ln(t) \qquad (5.3)$$

Next, the TiO_2 powders are characterized in detail to assess their nucleation-growth mechanism from a microscopic point of view.

5.4. Nanostructured particle characterization

This section provides the results from a characterization study performed on TiO_2 powders obtained via isothermal treatment at 80 °C of 0.5-1.5 M $TiCl_4$ aqueous solutions. In this part of the study, all solid products were recovered by using the solid recovery route A (described in Chapter 3, p. 59-60), involving the use of pressure filtration, drying at 60 °C over night, and manual grinding, prior to characterization. Typically, S/L separation and washing were carried out in a short period of time of approximately 20-30 min, and no significant processing time difference were noticed between the various products.

Figure 5.3 shows the XRD patterns of TiO_2 powders produced from $TiCl_4$(aq) solutions with different initial concentration and different degrees of conversion (x). Patterns (a) to (c) correspond to powders obtained at high degree of conversion ($x \geq 0.9$) while patterns (d) and (e) correspond to low conversion. In particular pattern (e) corresponds to the initially nucleated material ($x = 0.01$). Identification of the peaks

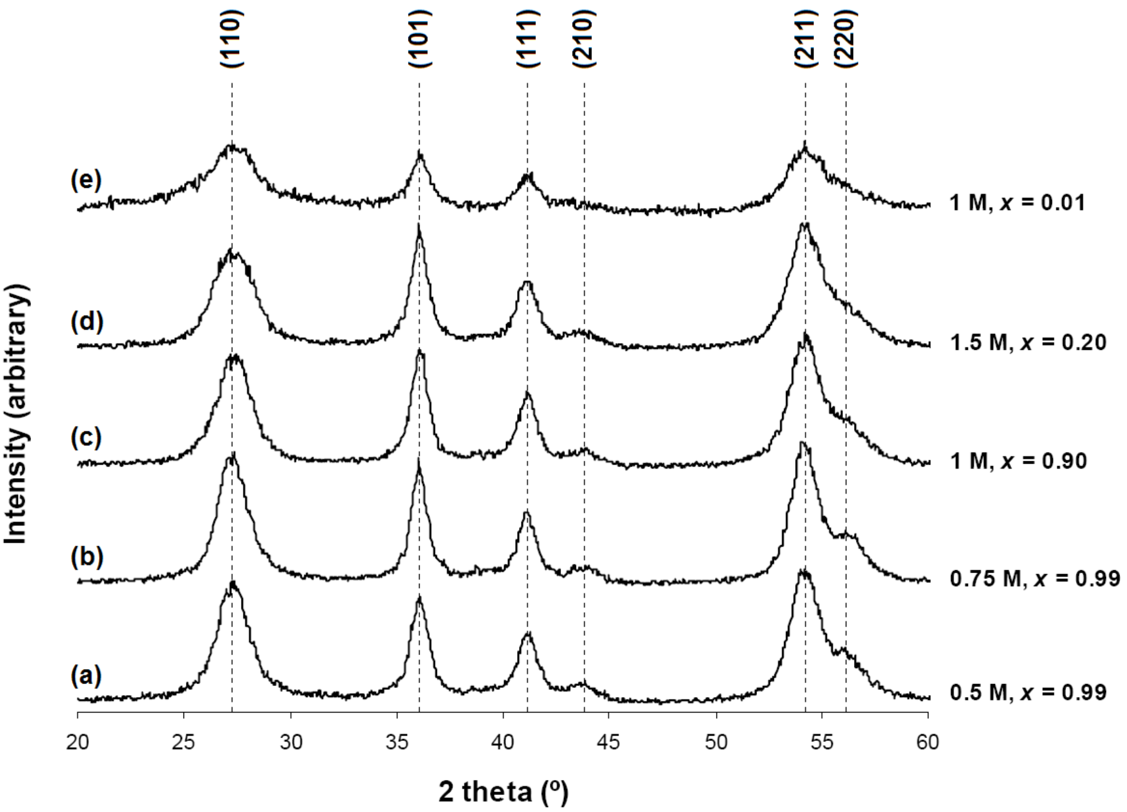

Figure 5.3. XRD patterns of the powders obtained by forced hydrolysis at 80 °C for solutions of various $[TiCl_4]_{initial}$ at different degrees of conversion (*x*).

revealed all the TiO_2 powders to be phase-pure rutile. The patterns exhibited rather broad and low intensity peaks characteristic of partially crystalline powders with nanosized structure. Judging from the shape and intensity of the peaks ((a) to (d)), the crystallinity decreased with an increase in initial $TiCl_4$ concentration. Among the powders produced the one obtained from the 0.5 M $TiCl_4$ solution had the highest degree of crystallinity. This is further exemplified by the appearance of both (201) and (220) peaks at 44.1° and 56.8°. It appears in other words that the higher the initial concentration the lower the crystallinity of the rutile nanostructured powder becomes. By linking this observation to the kinetics of the hydrolytic precipitation reaction (Figure 5.2.b) it is deduced that the faster the kinetics the higher the degree of crystallinity. Such behaviour points again towards significant variation in precursor Ti(IV)-Cl(-I)-OH speciation as a function of $TiCl_4$ concentration that drastically influences the TiO_2

crystallization process. In the case of the 1 M $TiCl_4$ solution processed at 80 °C, samples of TiO_2 powders were collected at the initial stage of the reaction (t = 30 min, $x = 0.01$) and compared to the final product (t = 5 hrs, $x \geq 0.9$). By comparing the XRD patterns of the two samples ((e) vs. (c)) a noticeable increase in peak intensity may be observed with the progress of the reaction. Such an improvement of the crystalline character of the powders may be the result of Ostwald ripening and the growth of the crystals as discussed by *Penn and Banfield* [3].

FEG-SEM examination of the TiO_2 powders showed these to consist of spheroidal particles that were partially fragmented, revealing a unique internal structure (Figure 5.4). The spheroidal particles appeared to have been made of self-assembled nanofibres. The radius of the spheroidal particles was found to increase with the initial concentration of the $TiCl_4$ solution from ~ 300 nm (0.5 M) to ~ 3000 nm (1.5 M) (Figures 5.4.a, 5.4.c and 5.4.e). The interior of the particles was characterized by a nucleation centre from which elongated self-assembled nanofibres had grown isotropically (Figures 5.4.b, 5.4.d, and 5.4.f). The nucleation centre (particle core) appeared to be ~ 50-100 nm in diameter and be made of aggregates of discrete elementary nuclei. The consistency of these nuclei is better appreciated by referring to Figures 5.4.f and 5.4.g that shows SEM images of the initially nucleated material after 30 min treatment of 1M $TiCl_4$ solution at 80 °C corresponding to 1 % conversion ($x = 0.01$) of $TiCl_4$ to TiO_2. This freshly nucleated material is seen to consist of globules of 0.5 µm size (Figure 5.4.f) themselves in turn being aggregates of elementary (~ 10-20 nm) nuclei (Figure 5.4.g).

By TEM imaging analysis (Figures 5.5.a and 5.5.b) further probing of the nucleation-growth mechanism was made. As it can be deduced from Figure 5.5.a the fibres were generated from a common nucleation centre, in agreement with the observations made in Figures 5.4.b, 5.4.d and 5.4.f. At higher magnification (Figure 5.5.b), the fibres seem to grow in 1D direction via discrete building events near the nucleation centre. The SAED (Selective Area Electron Diffraction) pattern provided in Figure 5.5.c displays broad arcs consistent with the preferential orientation of the nanofibres.

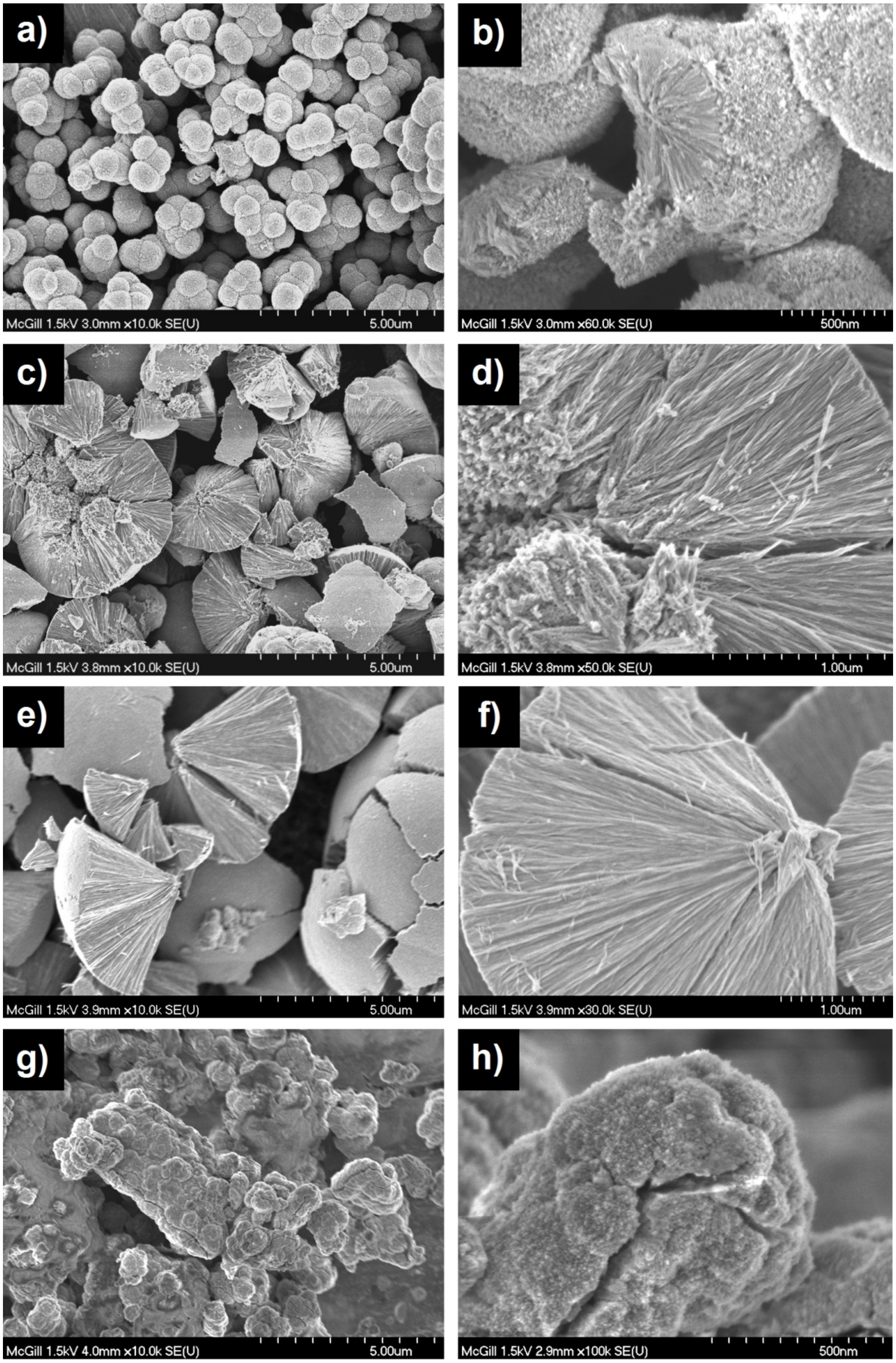

Figure 5.4. FEG-SEM pictures of TiO_2 nanofibre-structured particles produced by forced hydrolysis at 80 °C, effect of $[TiCl_4]_{initial}$: (a,b) 0.5 M $TiCl_4$ (2 hrs, x = 0.95); (c,d) 1 M $TiCl_4$ (5 hrs, x = 0.90); (e,f) 1.5 M $TiCl_4$ (5 hrs, x = 0.20); (g,h) initially nucleated TiO_2 material (80 °C, 1 M $TiCl_4$, 30 min, x = 0.01).

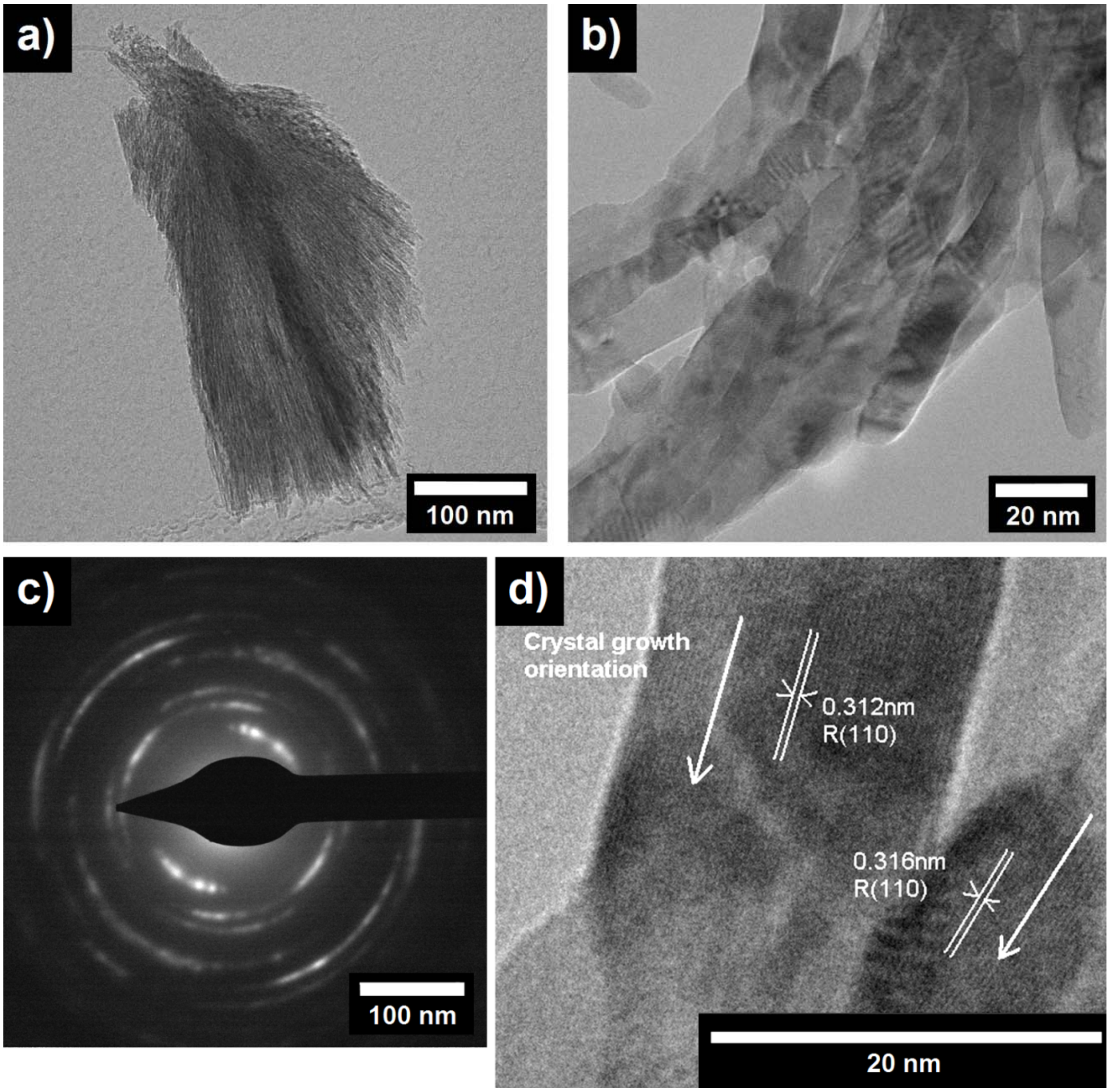

Figure 5.5. TEM pictures (a,b), SAED pattern (c) and HR-TEM picture (d) of the rutile TiO_2 powder produced from 1 M $TiCl_4$ solution (5 hrs, $x \geq 0.9$).

The crystalline structure of the fibres was further investigated with HR-TEM (High Resolution-Transmission Electron Microscope) images (Figure 5.5.d). These images made possible to observe the atomic planes in various locations of the fibres. The d-spacing values were accurately estimated for two fibres and found to be 0.312 nm and 0.316 nm. JCPDS reports the theoretical value for the d-spacing of the (110) plane in the rutile crystalline structure to be 0.322 nm. These measurements provide evidence that the growth of the rutile nanofibres proceeds via preferential elongation of its (110) atomic planes.

The BET surface area of a number of rutile nanostructured powders was measured and was found to be larger than the BET surface area of the commercially available TiO_2 powder P25 from Degussa (Table 5.1). On the same table the equivalent nanocrystallite size from the BET measurements is reported. The latter was found to be ~ 20 nm.

Table 5.1. BET surface area and nanocrystallite size of TiO_2 powders synthesized from aqueous solution compared to P25.

Conversion, *x*	Synthesis conditions	BET surface area ($m^2.g^{-1}$)	d_{BET} (nm)
0.95	0.5 M; 2 hrs; 80 °C	77	20.0
0.90	1 M; 5 hrs; 80 °C	89	17.3
0.20	1.5 M; 5hrs; 80 °C	74	20.8
-	P25	50	30.8

The differential thermal (DT) and thermogravimetric (TGA) curves of a typical nanofibre-structured rutile sample (1 M $TiCl_4$, 80 °C, 5 hrs) are shown in Figure 5.6. Weight loss stages can be identified based on the DT curve, each of them related to the loss of different species. The first two steps were attributed to the loss of physically adsorbed water (3.8 wt. %) and chemically bonded hydroxyl groups (5.1 wt. %), respectively. The presence of these species was confirmed by spectroscopic analysis.

FT-IR spectra obtained for the same product before and after heat treatment are shown in Figure 5.7. In the case of the powder prior to heat treatment, two characteristic bands at 1625 cm^{-1} and ~ 3200 cm^{-1} are present. According to literature [4-6] these bands may be respectively attributed to adsorbed molecular water and -OH stretching vibration of chemically bonded surface and structural hydroxyl groups. Heat treatment (4 hrs) of the rutile powder at 250 °C (spectrum (b) in Figure 5.7) resulted in a reduction in the intensity of these two bands while at 400 °C (4 hrs treatment; spectrum (c)) the two bands disappeared altogether. These observations validate the hypothesis of water and hydroxyl group loss, respectively in the temperature ranges T_{amb}-170 °C and 170-350 °C. The third stage on the DT curve (350-450 °C) associated with 1 wt. % loss may be attributed to the loss of chlorides trapped inside the particles due to incomplete hydrolysis of some Ti(IV) complexes. This was verified via HF digestion of the non heat-treated powder and gravimetric titration of AgCl which yielded ~ 0.7 wt. % chloride content.(c) On the basis of all these analytical data the chemical composition of the non-heat treated nanofibre-structured rutile powder was determined to be: $TiO_{1.86}(OH)_{0.26}(Cl)_{0.02}\cdot 0.18H_2O$.

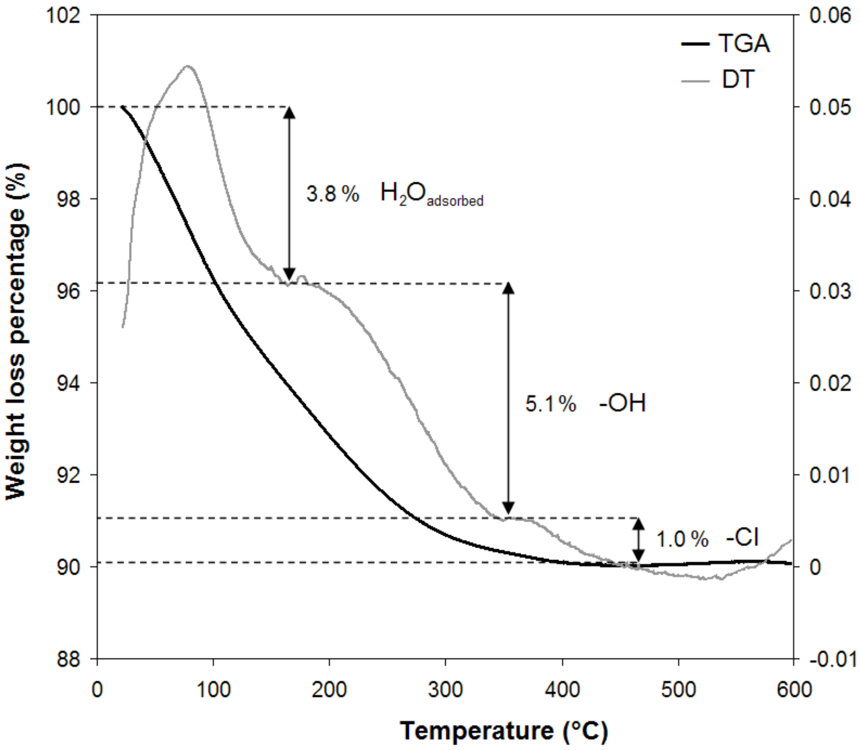

Figure 5.6. DT/TGA analysis of nanofibre-structured rutile powder (1 M $TiCl_4$, 80 °C, 5 hrs).

(c) Footnote: A sample of aqueous-synthesized powder was extensively washed with deionised water in order to largely remove all the surface-adsorbed chlorides from the nanostructured particles. Following thorough washing and drying (at 60 °C for 12 hrs) the solids were digested and analyzed gravimetrically to determine the amount of structural chloride as per following procedure: 1) 10 g of material were digested with ~50 mL of concentrated (49 vol. %) hydrofluoric acid; 2) an excess of 1 N silver nitrate solution was mixed with the digestion solution at T_{amb} for 30 min; 3) the obtained solution was diluted to a volume of 1 L with deionised water; 4) the silver chloride precipitate was separated from the solution via filtration and washed repeatedly; 5) the collected AgCl solids were dried for 3 hrs at 90 °C and weighed.

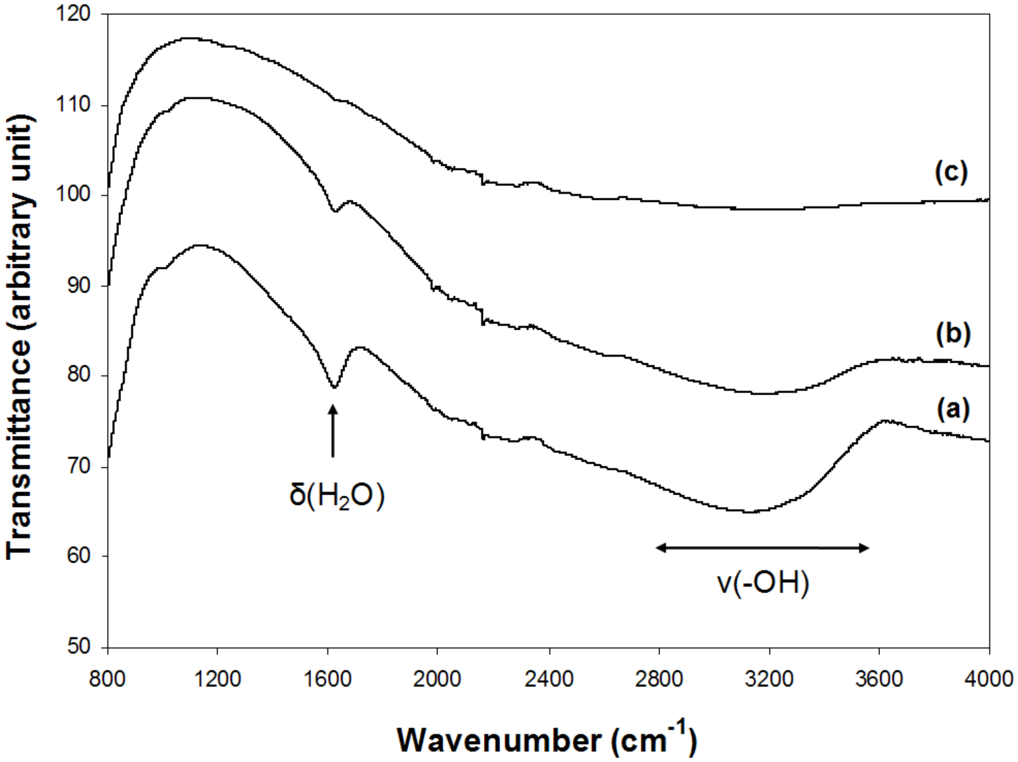

Figure 5.7. FT-IR spectra of the powders before (a) and after 4 hrs heat treatment at 250 °C (b) and 400 °C (c).

5.5. Effect of thermal treatment/annealing

Powders obtained by hydrolysis of 1 M $TiCl_4$ (5 hrs, 80°C, 1000 rpm) were submitted to annealing at various temperatures, namely 250, 400, 550, and 700 °C for 4 hrs. The effect of annealing on the nanostructure of the particles was studied by performing XRD, SEM and BET analyses.

XRD characterization showed the particles after thermal treatment to retain their rutile phase structure but to exhibit sharper and taller peaks indicative of enhanced crystallinity and grain growth (Figure 5.8.a). BET and SEM characterization (Figures 5.8.b and 5.8.c) confirmed that the nanostructure of the material was preserved after heat treatment at 250 °C (surface area equal to 78 m^2/g and nanocrystallite size of ~ 20 nm vs. 89 m^2/g or 17 nm size for the non-heat treated material). The heat treated material at 400 °C was still nanostructured but with less surface area and coarser crystallite size (Figure 5.8.d), namely 32 m^2/g surface area and

49 nm crystallite size. From the SEM characterization of the material heat treated at 550 and 700 °C (Figures 5.8.e and 5.8.f), it can be seen that the nanostructure of the material is lost due to further coarsening and longitudinal assembly of the fibres. The formation of 50-100 nm diameter pores is also observed at the surface and in the inner structure of the particles.

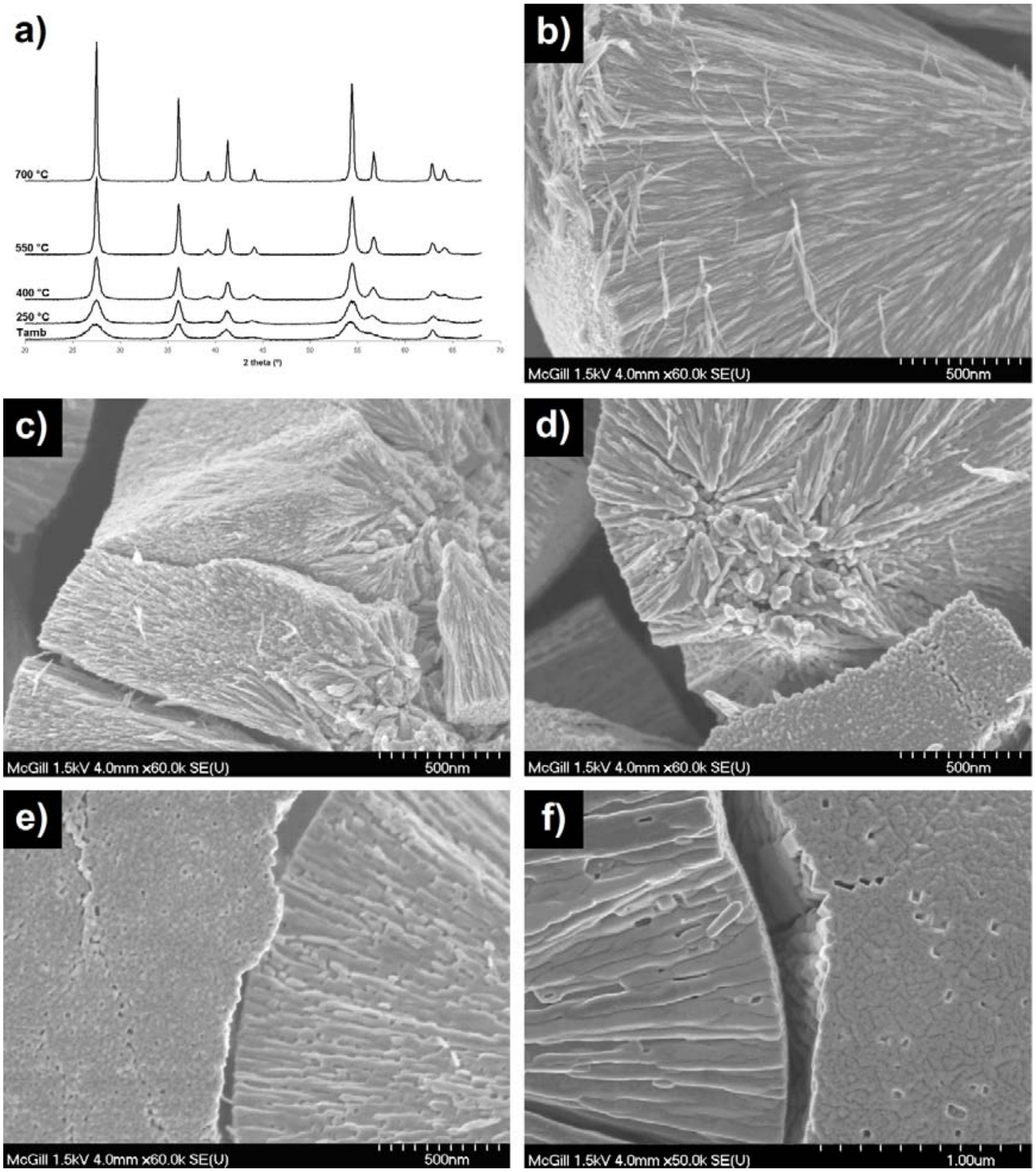

Figure 5.8. Effect of annealing on TiO_2 rutile particle (1 M $TiCl_4$, 80 °C, 5 hrs, 1000 rpm): XRD patterns of the powders as synthesized and annealed for 4 hrs at 250, 400, 550, and 700 °C (a); SEM pictures of powders as synthesized (b), and annealed at 250 °C (c), 400 °C (d), 550 °C (e), and 700 °C (f).

5.6. Conclusions

The kinetics of TiO_2 precipitation via forced hydrolysis of aqueous solutions of $TiCl_4$ was found to exhibit sigmoidal change of Ti(IV) concentration with time, characterized by slow induction-nucleation and accelerated growth stages. The onset of nucleation and length of the induction period were found to depend on the concentration of the solution, temperature and agitation type and speed. Agitation speed and temperature had a positive effect on nucleation and overall kinetics but contrary to normal behaviour an increase in Ti(IV) chloride concentration had the opposite effect. The effects of agitation and Ti(IV) chloride concentration on kinetics were attributed to possible differences in the formation and polymerization of Ti(IV)-Cl(-I)-H_2O precursor complexes.

Forced hydrolysis under the studied conditions ($0.5 \text{ M} \leq [TiCl_4] \leq 1.5 \text{ M}$, $70\ °C \leq T \leq 90\ °C$ and 1000 rpm mechanical agitation) led to the production of self-assembled nanofibre-structured rutile spheroids. The formation of the nanostructured spheroidal particles was observed to proceed via the following steps: 1) nucleation and aggregation of elementary nanocrystallites (~ 10-20 nm); 2) preferential growth of elongated self-assembled nanofibres along the (110) rutile atomic plane. The higher the initial $TiCl_4$ concentration, the longer and thinner the fibres were grown. The nanofibre structured powders exhibited high specific surface area in the order of ~ 80 m^2/g. Coarsening of the fibres and progressive loss of the nanostructure was observed upon annealing.

5.7. References

[1] R. Sarraf-Mamoory, G. P. Demopoulos, and R. A. L. Drew, *Metall. Mater. Trans.* B**,** **27B** (1996), 585-594.

[2] J. Moon, M. L. Carasso, H. G. Krarup, J. A. Kerchner, and J. H. Adair, *J. Mater. Res. Soc.*, **14** (1999), 866-875.

[3] R. L. Penn and J. F. Banfield, *Am. Min.*, **84** (1999), 871–876.

[4] Y. Li and G. P. Demopoulos, *Hydrometallurgy*, **90** (2008), 26-33.

[5] S. Kaewgun, C. A. Nolph, B. I. Lee, and L.-Q. Wang, *Mater. Chem. Phys.*, **114** (2009), 439-445.

[6] K. Nakamoto, Infrared and Raman Spectra of Inorganic and Coordination Compounds, Part A: Theory and Applications in Inorganic Chemistry, 5th edition, Wiley-Interscience, New York, (1997), p. 153-173.

Chapter 6: Aqueous Synthesis of Crystalline Anatase Nanocolloids

6.1. Introduction

In this chapter, the production of anatase (TiO_2) nanostructured material via forced hydrolysis of a 0.2 M $TiCl_4$ aqueous solution is investigated in terms of precipitation kinetics, and nucleation and hydrothermal ageing mechanisms. Two product recovery routes were tried, namely routes A and N, previously described in section 3.3.2.3 of Chapter 3. The products obtained are characterized by FEG-SEM, FEG-TEM, XRD, BET surface area, TGA, EDS, and FT-IR analyses. It is shown that forced hydrolysis of 0.2 M $TiCl_4$ may be used to synthesize TiO_2 nanocolloids containing nanocrystals in the size range 4-5 nm with anatase as the major crystalline phase (~ 85 wt. %).

6.2. Precipitation-Synthesis

Forced hydrolysis of 0.2 M $TiCl_4$ aqueous solution was performed at 80 °C in a mechanically agitated reactor (1000 rpm), under atmospheric pressure conditions (the experimental set-up is described in Chapter 3, p. 58-59). Typically the solution was processed for 30 min, the time required to achieve the maximum $TiCl_4$(aq) to TiO_2(s) conversion rate. However, some tests were run up to 4 hrs in order to study the effect of hydrothermal ageing on the properties of the synthesized material. Because of the technical difficulties encountered when using pressure filtration (route A) to separate the nanoparticles from the liquor, an alternative solid recovery method was tested based on centrifugation following pH adjustment with ammonium hydroxide (route N, described in Chapter 3, p. 59-60). In this section, a kinetics study is first presented, followed by the characterization of the colloid and dry products obtained under various processing conditions. In particular, the effects of hydrothermal ageing and solid recovery on the properties of the synthesized material are investigated. The properties of the aqueous-synthesized powders are compared to the properties of the commercial reference TiO_2 material P25 from Degussa (Evonik).

6.3. Kinetics of nucleation and transformation

Figure 6.1 presents the fraction of converted Ti(IV) to TiO_2 as a function of time for two tests repeated under the same experimental conditions. According to this diagram the conversion of soluble $TiCl_4$ to insoluble TiO_2 follows an “S-shape” kinetic curve (up to 35 min) that can be divided into three parts: an induction period, a fast increase and a short plateau. Similar kinetic profiles were previously observed and described in Chapter 5 when processing 0.5-1.5 M $TiCl_4$ aqueous solutions at 80 °C. The end of the induction period was visually manifested by a change in the appearance of the solution which started to turn white translucent at ~2-3 min. Up to 35 min, gradual color intensification was observed due to the formation of the TiO_2 nanocolloid, as shown in Figure 6.2. At 35 min, both reaction curves indicate a quasi-complete (near 95 %) conversion of the $TiCl_4$ to TiO_2. The fast hydrolysis kinetics upon lowering the $TiCl_4$ concentration down to 0.2 M may be attributed to enhanced water activity as discussed elsewhere [1].

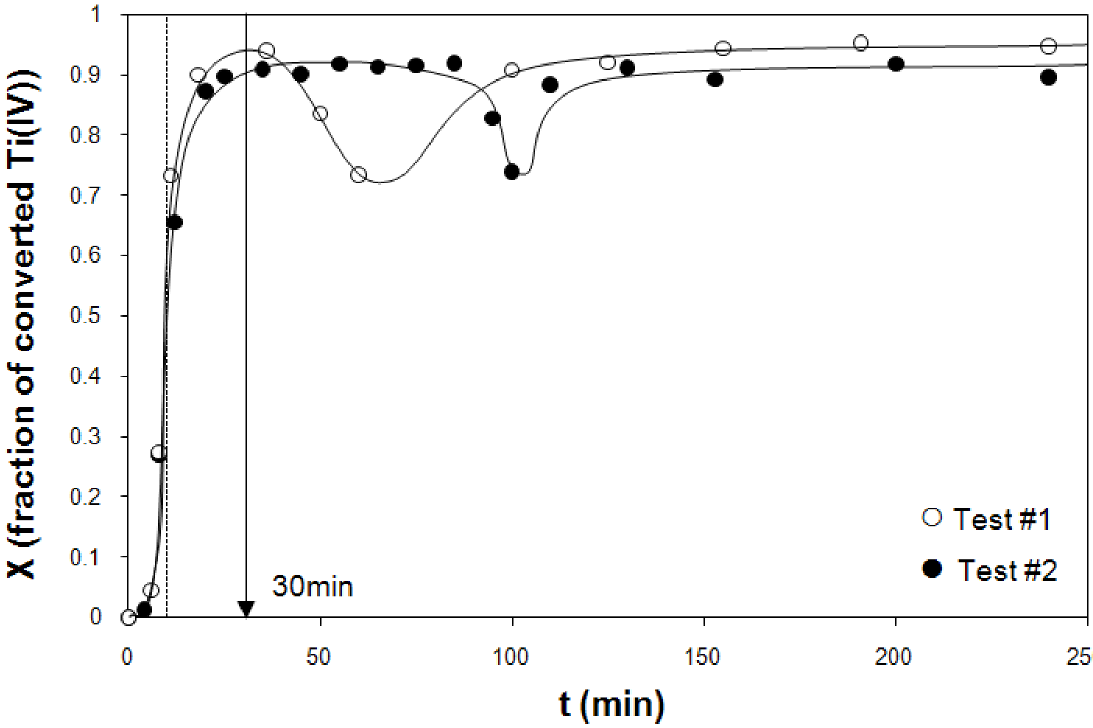

Figure 6.1. Kinetics of TiO_2 production: $[TiCl_4]_{initial}$ = 0.2 M, T = 80 °C and 1000 rpm mechanical agitation; the dash line at 10 min and the arrow at 30 min denote the end of the heat-up period from T_{room} to 80 °C and the end of the standard aqueous synthesis time, respectively.

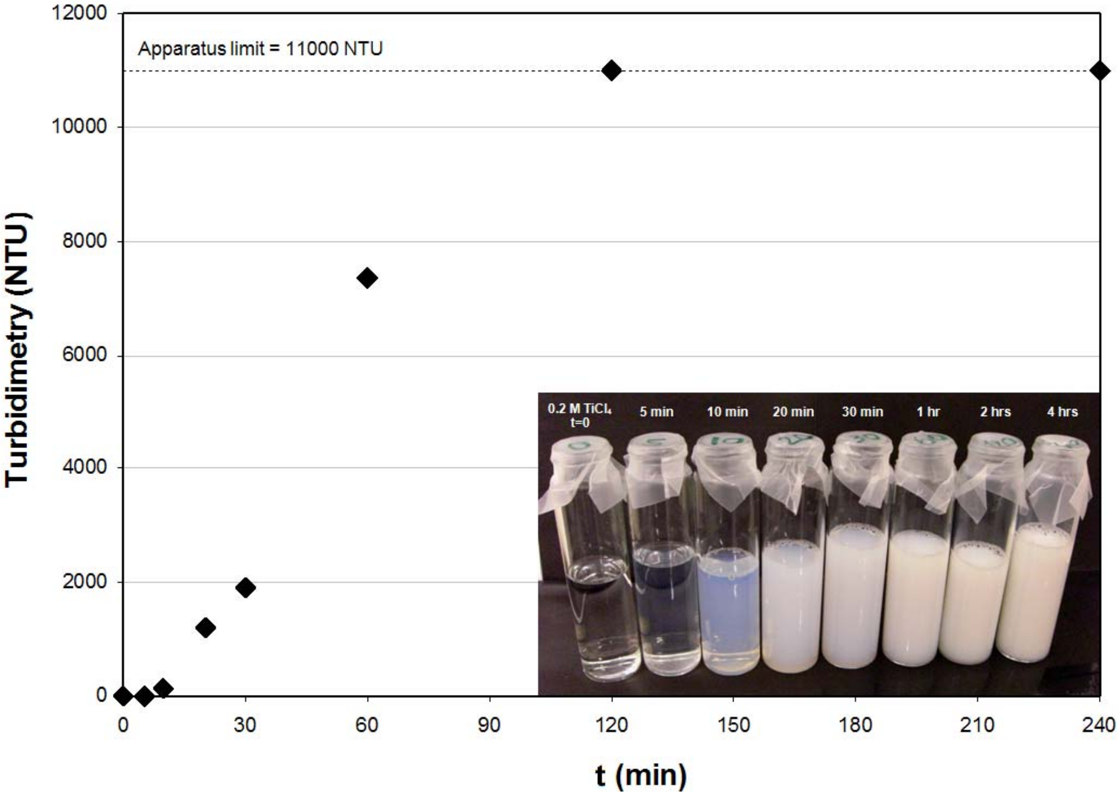

Figure 6.2. Turbidity measurements and picture of colloid samples taken at various times during the isothermal processing of a 0.2 M $TiCl_4$ aqueous solution (80 °C, 1000 rpm).

The second part of the reaction curves, from 35 min to 4 hrs, describes the hydrothermal ageing kinetics of the colloid. At this stage of the process, the color of the solution inside the reactor was observed to progressively change from white translucent to white opaque (Figure 6.2). On Figure 6.1, both reaction curves feature a redissolution event that leads temporarily to lowering of the converted fraction down to ~ 0.73 before its rise again to > 0.90. The decrease of the Ti(IV) conversion fraction down to 0.73 signifies that a fraction (approximately 15 mol. %) of the nanocolloid present at 35 min dissolved back in the solution. The subsequent increase of the Ti(IV) conversion fraction back to > 0.90 suggests that an equivalent amount of Ti(IV) re-appeared as solid phase via hydrolysis. *Reyes-Coronado et al.* [2] recently reported that titania becomes soluble at high hydrochloric acid concentration and is susceptible to transformation via dissolution-recrystallization [3]. In this study, the synthesis of titania based on the hydrolysis of $TiCl_4$ is associated with an increase in the concentration of hydrochloric acid in the solution, up to ~ 0.76 M HCl at 35 min (according to the EDTA-assisted titration of the colloid), corresponding to pH ~ 0.12. The dissolution-recrystallization events are shown to be initiated at different times, 35 min and 85 min for Test #1 and Test #2, respectively. The delay observed between the two curves may be thought to originate from minor variations of the experimental conditions, namely the different sample collection frequency leading to temperature and mixing conditions alteration, as discussed in Chapter 5.

6.4. Characterization of the colloids-Effect of time

6.4.1. TEM analysis

TEM images of colloid samples collected at 30 min and 4 hrs are presented in Figures 6.3.a and 6.3.b, respectively. At 30 min (Figure 6.3.a), the colloid was found to mostly contain very lightly aggregated nanocrystallites with crystallite size of 4-6 nm, hence the broad rings displayed on the associated SAED pattern (Figure 6.3.d). Higher magnification observations of the sample confirmed the nanoparticles to have a rather high degree of crystallinity as it was possible to observe the atomic planes on most particles (Figure 6.3.e). In addition the associated SAED pattern displays broad rings which are characteristic of small nanocrystalline particles. At 4 hrs, the appearance of few large isolated aggregates characterized with dimensions in the range 100-300 nm was observed, as shown in Figure 6.3.b. These aggregates are thought to result from the condensation of small nanocrystals into self-assembled nanorods. The nanorods were found to have an approximate diameter of 10 nm and length in the range 20-50 nm with radial orientation. Such self-assembled nanostructured aggregate morphology was previously observed to be characteristic of rutile TiO_2 nanoparticles obtained by forced hydrolysis of $TiCl_4$ solutions with higher concentration (Chapter 5).

Both aqueous-synthesized nanocolloids recovered by either route A or N following washing were highly hydrated having a gel-like consistency. TEM imaging analysis presented in Figure 6.3.c shows that the gel obtained via route N contains slightly aggregated nanoparticles in the size range 5-10 nm, i.e. somewhat larger than those of the original aqueous colloid (prior to particle recovery, Figure 6.3.a). This may be explained by an increase of the degree of aggregation due to pH elevation and lowering of the surface charge and zeta potential [4].

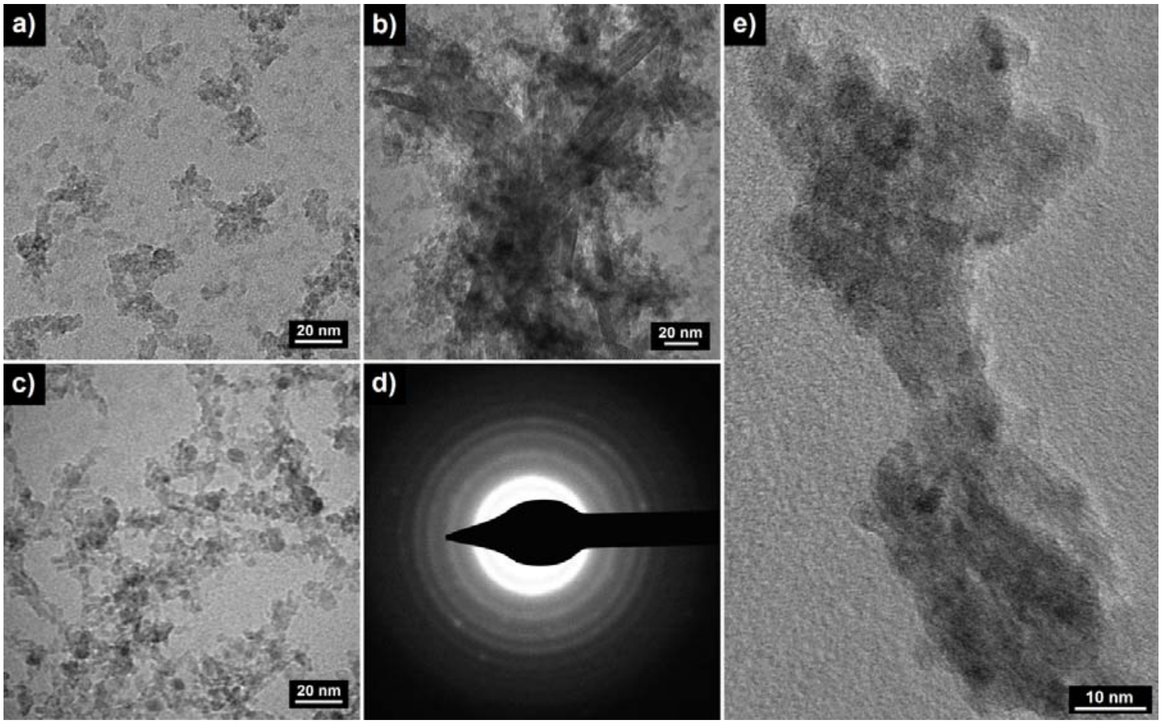

Figure 6.3. TEM pictures of nanocrystallites collected from the reactor at 30 min (a) and at 4 hrs (b), from the centrifuged gel obtained via particle recovery route N (c); HR-TEM picture (e) and associated SAED pattern (d) of nanocrystallites collected from the reactor at 30 min.

6.4.2. <u>XRD analysis</u>

Three batches of aqueous nanocolloids were prepared, one after 30 min and the others after 2 and 4 hrs reaction time in order to subject them to phase identification following their recovery through route A. The resulting TiO_2 powders, named powder A, A’, and A’’, respectively, were submitted to x-ray diffraction analysis as presented in Figure 6.4. The patterns corresponding to the three powders exhibit rather broad- and low-intensity peaks. Such features are usually associated with semi-crystalline powders or crystalline powders composed of very small nanocrystals. In the present case it is rather the latter as evident by the TEM images (Figures 6.3.a and 6.3.b). The different peaks appearing on the XRD patterns related to the three powders were compared with the reference patterns of crystalline TiO_2 anatase (#00-021-1272), rutile (#00-001-1292), and brookite (#00-029-1360). Looking at the relative intensity of the (101) anatase peak at 25.3° and the other peaks appearing on the patterns of powders A, A', and A'', anatase clearly appears to be the major TiO_2 phase present in all powders. The presence of small amounts of rutile and brookite, hardly visible on the pattern of powder A, is more clearly evident on the patterns of powders A' and A'' as revealed by the emergence of low-intensity peaks at 27.3°, 36.1° and 41.2° attributed to rutile (110), (101), and (200) peaks, and a shoulder centered at 30.8° attributed to brookite (121) peak.

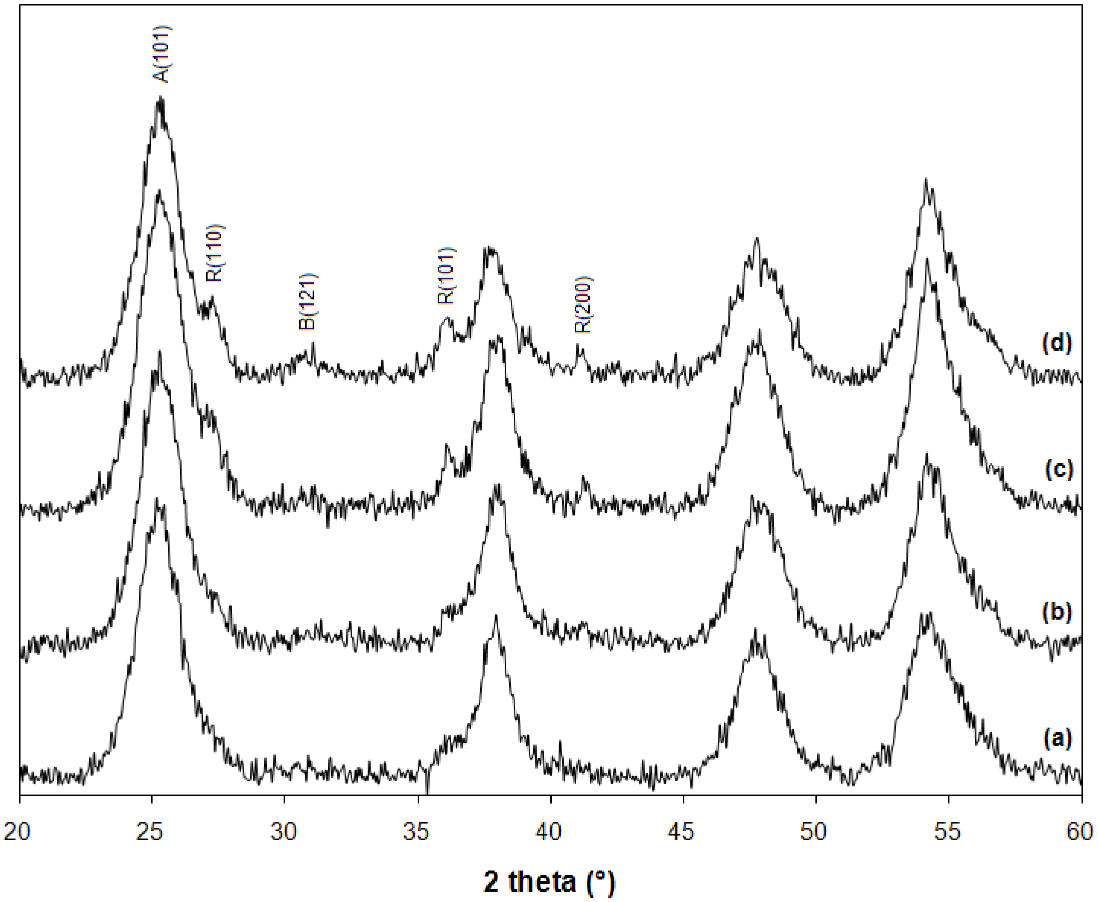

Figure 6.4. XRD patterns of the TiO_2 nanopowders obtained by forced hydrolysis (at 80 °C, 1000 rpm) of a 0.2M $TiCl_4$ aqueous solution for 30 min and recovered via route N (a) and A (b) (powders A and N); hydrothermally aged for 2 hrs (c) and 4 hrs (d) and recovered via route A (powders A' and A'').

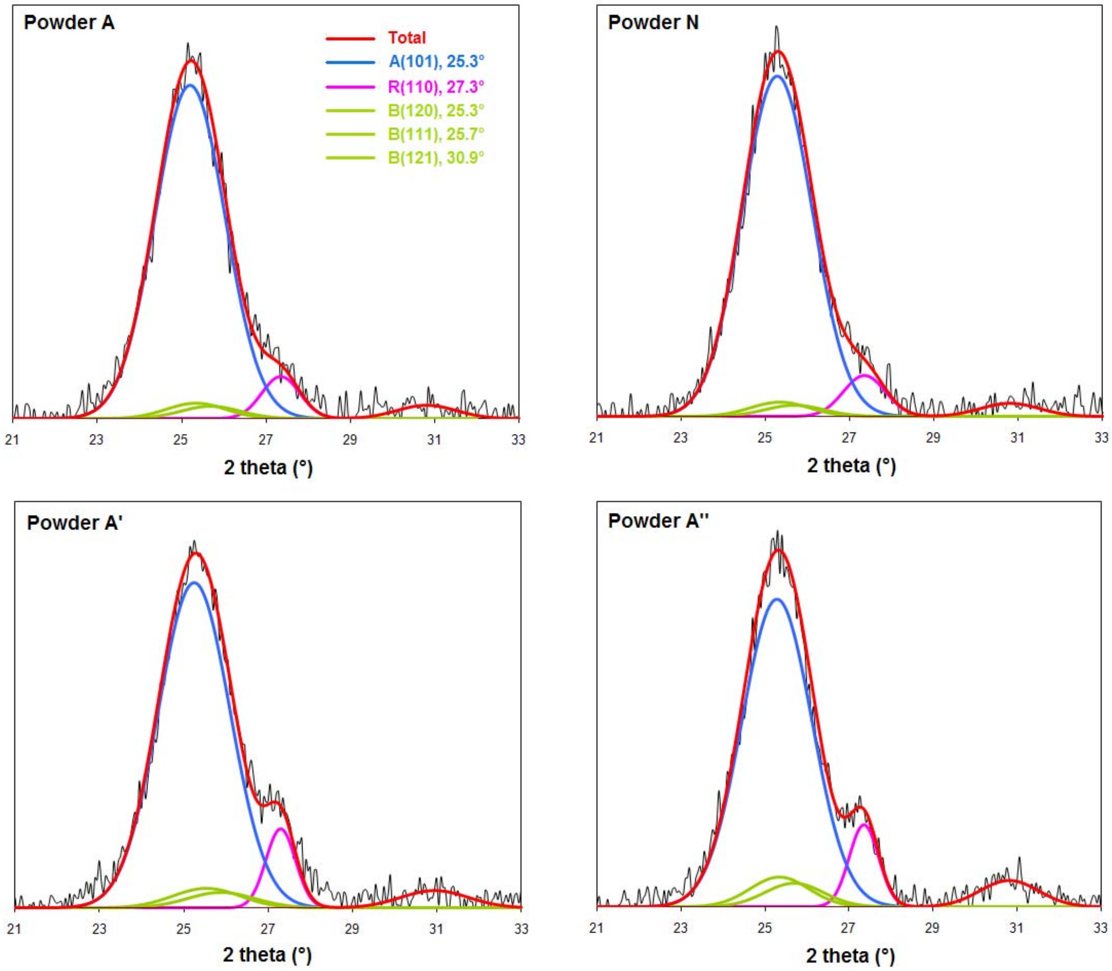

Figure 6.5. Gaussian fit of the XRD patterns obtained for powders N, A, A’, and A’’ in the 21-33° 2θ range.

Table 6.1. Anatase, rutile and brookite phase contents of powders N, A, A’ and A’’.

Sample	Synthesis conditions	Anatase (wt. %)	Rutile (wt. %)	Brookite (wt. %)
Powder N	0.2M; 30 min; 80 °C; N	84.8	6.4	8.8
Powder A	0.2 M; 30 min; 80 °C; A	84.6	6.9	8.5
Powder A’	0.2 M; 2 hrs; 80 °C; A	79.0	8.9	12.1
Powder A’’	0.2 M; 4 hrs; 80 °C; A	74.1	9.5	16.4

A closer analysis of these patterns in the 21-32° 2θ range was performed in order to calculate the content of each phase present in the powders. The XRD patterns of powders A, A’ and A’’ were fitted and deconvoluted using a Gaussian distribution function, as shown in Figure 6.5. *Zhang and Banfield* [5] developed a method to determine the phase content in wt. % of anatase, rutile and brookite in TiO_2 mixed-phase powders. The three equations derived in that method were applied to the Gaussian fits of the anatase (101), rutile (110), and brookite (121) peaks. The results of these calculations are summarized in Table 6.1. They confirm anatase to be the major TiO_2 phase present with 84.6, 79.0 and 74.1 wt. % in powders A, A' and A'', respectively. The results also show that upon hydrothermal ageing the anatase phase content decreased by 5.6 and 4.9 wt. % units between 30 min and 2 hrs and between 2 and 4 hrs, respectively. Within the same time intervals, the rutile and brookite phase contents increased correspondingly by 2.0 and 0.6 wt. % (from 6.9 to 8.9 wt. % and from 8.9 to 9.5 wt. %) and by 3.6 and 4.3 wt. % (from 8.5 to 12.1 wt. % and from 12.1 to 16.4 wt. %) units, respectively. These findings indicate that the particle dissolution-precipitation phenomenon deduced from the kinetics reaction curves (Figure 6.1) is accompanied with phase transition phenomena. The anatase-to-rutile phase transition has been shown to occur either via direct transformation of anatase to rutile, or via a two-step phase transition mechanism involving the formation of brookite as an intermediate phase [5]. In this study, the increasing brookite content upon hydrothermal ageing seems to indicate that the two-step (anatase-to-brookite-to-rutile) phase transition is the leading mechanism. The crystallization of rutile and brookite TiO_2 via hydrothermal treatment of aqueous $TiCl_4$ solutions (with hydrochloric acid present as in this study) was shown in previous studies to highly depend on the initial [Cl]/[Ti] ratio and acidity of the solution [6,7]. This appears to be the underlying factor here triggering the transition from anatase to brookite and rutile. Thus, at the point of maximum redissolution, the concentrations of Ti(IV) and chloride ions in solution were approximately 0.05 M (25 % of $[TiCl_4]_{initial}$) and 0.76 M (95 % of $[Cl^-]_{total,}$ released upon hydrolysis at 35 min) respectively, which give a [Cl]/[Ti] ratio of 15.2. This ratio is close to the one ([Cl]/[Ti] =18) reported by *Di Paola et al.* [7] to favor the crystallization of brookite. In the latter study, the synthesis of pure rutile particles via hydrolysis of dilute $TiCl_4$ aqueous solutions was shown to occur under even higher ratio ([Cl]/[Ti] = 38).

On the basis of these observations, it was selected to produce anatase nanocrystallites (85 wt. % anatase content, 4-5 nm size) at high yield (95 % conversion) by running the aqueous solution (0.2 M $TiCl_4$) synthesis process for 30 min at 80 °C and 1000 rpm followed by either direct filtration (powder A) or neutralization to pH 3 and centrifugation (powder N).

6.5. Characterization of the TiO_2 dry nanopowders

6.5.1. Nanocrystallite properties

Upon drying (at 60 °C, over night), the TiO_2 gels (A and N) lost their water and formed brittle scales that required grinding prior to their characterization and use. The phase composition of powder N was calculated based on the Gaussian fit of its XRD pattern in the 2θ range 22-33°. It was found to contain 84.8, 6.4, and 8.8 wt. % anatase, rutile and brookite, respectively, which is very similar to the composition of powder A (Table 6.1). SEM examination of the ground powders A (Figures 6.6.a and 6.6.b) and N (Figures 6.6.c and 6.6.d) revealed the presence of large aggregates. When compared to powder P25 TiO_2 (Figures 6.6.e and 6.6.f), powders A and N had a more compact structure. These visual features were confirmed by performing BET surface area and porosity analyses of the three powders. The results, presented in Table 6.2, show the three powders to be nanostructured: the aqueous-synthesized powders were found to have a very high surface area, 362 and 250 m^2/g, and inversely small equivalent average crystallite diameter of 4.3 and 6.2 nm for powder A and N respectively, as compared to the P25 powder with BET surface area of 51 m^2/g with and equivalent crystallite diameter of 30.2 nm. The equivalent BET crystallite size diameter calculated for powders A and N are in good agreement with the TEM visual observation of the particles shown in Figures 6.3.a and 6.3.c. The porosity results showed powders A and N to have similar porosity with an average pore size of 27 and 32 Å, respectively. Powder P25 was found to have a much higher porosity with an average pore size of 118 Å.

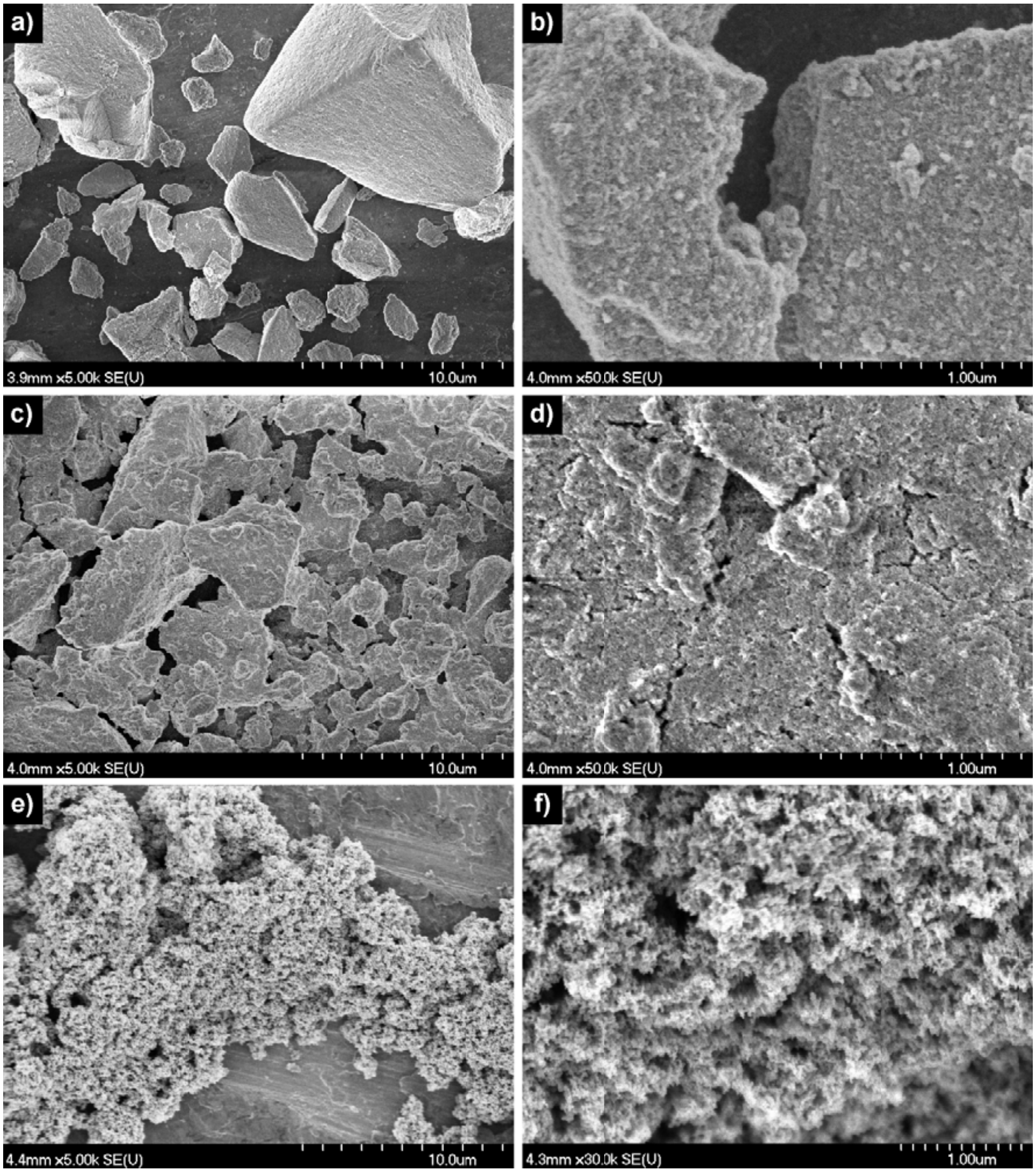

Figure 6.6. SEM pictures of powders A (a,b) and N (c,d) after drying (60 °C overnight) and manual grinding, and powder P25 (e,f).

Table 6.2. BET surface area and porosity analyses of powders and films A, N, and P25.

Sample	**BET surface area ($m^2.g^{-1}$)**	**BET average pore size (Å)**	**d_{BET} (nm)**
Powder A	362 (± 20)	27	4.3
Powder N	250 (± 5)	33	6.2
Powder P25	51 (± 1)	118	30.2

6.5.2. Surface hydroxylation/hydration

Chemical characterization of powders A, N and P25 was made by combining TGA, FT-IR and EDS analyses. TGA analyses of powders A, N and P25 are presented in Figure 6.7. The curves related to powders A and N both display three weight loss stages with inflection points at 100 and 200 °C whereas the curve related to P25 powder only displays two distinct weight loss stages with a transition at 100 °C. These stages have been delimited with dash lines on the graphs. In all cases, the weight loss observed in the temperature range T_{amb}-100 °C is attributed to dehydration of the samples by loss of physically adsorbed water. Surface hydration of powder A and N (9 and 10 wt. % respectively) was found to be 20 times more important as compared to powder P25 (0.5 wt. %), owing on one hand to the synthesis process (aqueous vs. flame synthesis) and on the other hand to the higher surface area of powders A and N (Table 6.2). Between 100 and 200 °C, dehydration continues by loss of chemically bound water. But more importantly, the loss of chemically bound surface -OH and -Cl groups is also expected to occur above 100 °C [8]. In this temperature range, the weight loss (4-5 wt. %) of the aqueous-synthesized powders was 10 times more important than the one of powder P25 (~ 0.4 wt. %). These losses to a large degree reflect the higher presence of surface Ti-OH/-OH_2 groups. The weight losses above 200 °C are believed to be due to structural (internal) chemically bound -Cl (according to another study, P25 contains 0.3 wt. % Cl [9]) and -OH groups or water molecules. For example, it is possible that incomplete hydrolysis of some Ti(IV)-Cl-OH precursor complexes during particle nucleation and growth is at the origin of structural -OH/-OH_2 and -Cl groups. The presence of water in all powders was confirmed with FT-IR analysis (Figure 6.8). This is evident by the peak at 1620 cm^{-1} plus the broad band in the range 2700-3600 cm^{-1} attributed respectively to the δ_{H2O} bending mode and the overlapping of the ν_{OH} stretching vibration modes of adsorbed/structural water and H-bonded -OH groups [10].

6.5.3. Cl and N impurities

In addition to the surface hydroxyl groups and water, evidence of the presence of Cl and N/NH_4 (counting for part of the weight loss above 200 °C) was detected in the case of powders A and N. The EDS results, presented in Figure 6.9 (the curves were normalized on the base of Ti K_α line) show that both aqueous-prepared powders contain Cl, with powder N bearing a higher content than powder A. It is likely that some chloride ions participating in the structure of the Ti(IV) precursor complexes get carried into the nanoparticles during their crystallization and/or remain chemically adsorbed to their surface. In the case of powder N, the FT-IR spectrum displays the appearance of a peak at 1405 cm^{-1} with a shoulder attributed to the presence of a smaller peak at 1440 cm^{-1} and three other small peaks at a higher frequency range with maxima at 2800, 3000 and 3120 cm^{-1} (as featured using downwards arrows on Figure 6.8). The same series of peaks was identified by *Robertson et al.* [11] to relate to the vibration modes of ammonium chloride (NH_4Cl) particles. It is deduced, therefore, from these results that the ammonium chloride formed by neutralization reaction in the case of colloid N may have contaminated the particles. In particular, the additional contamination by NH_4Cl can explain the higher weight loss experienced by powder N above 200 °C. However, it is shown in the next chapter that the Cl and N impurities are easily removed by annealing (450 °C, 30 min) the powders, without causing any phase transformation or loss of their nanostructure.

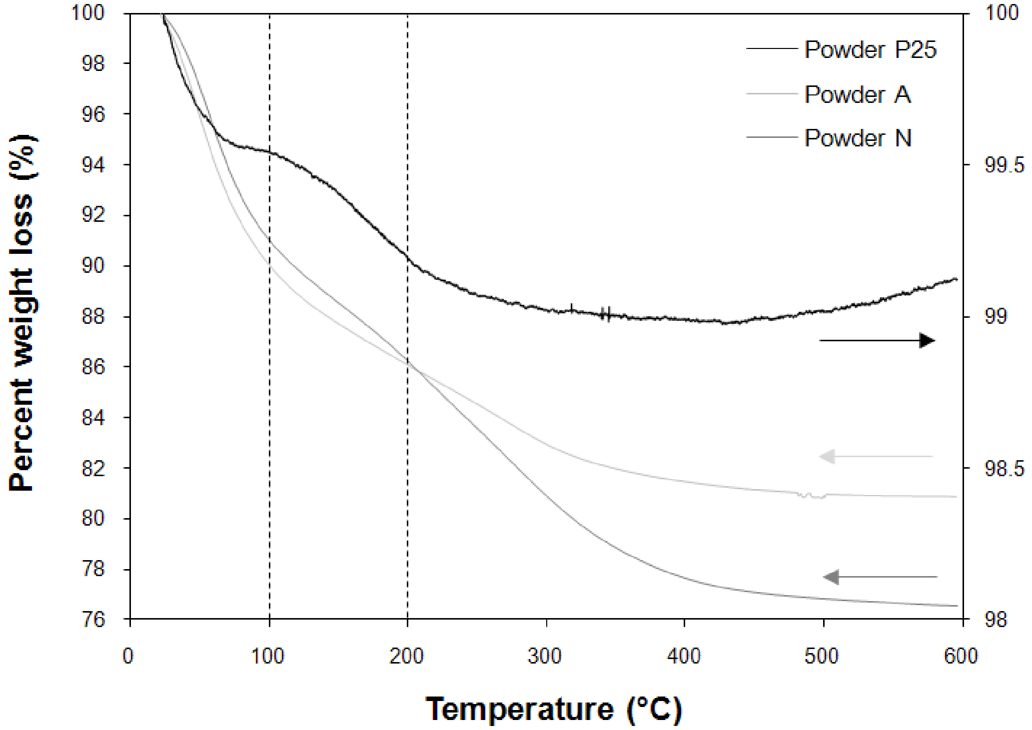

Figure 6.7. TGA curves of powders A, N, and P25.

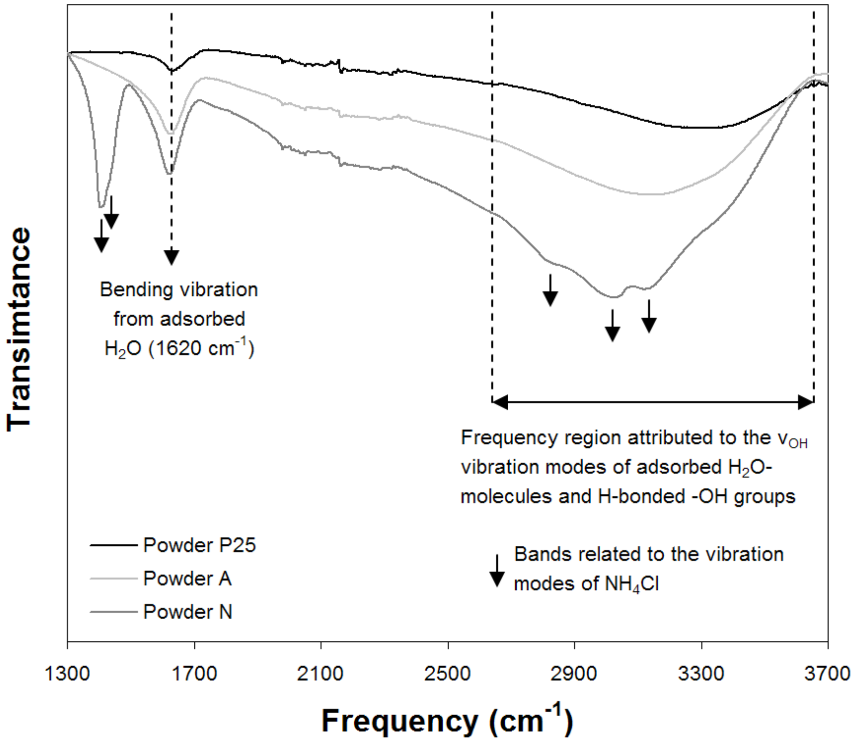

Figure 6.8. FT-IR spectra of powders A, N, and P25.

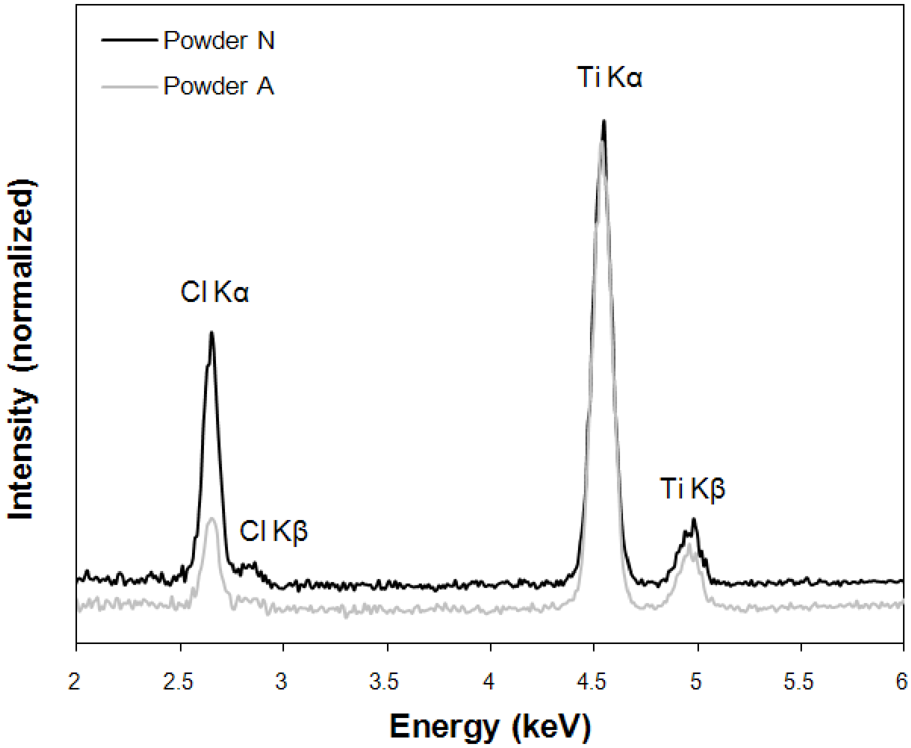

Figure 6.9. EDS spectra of powders A and N.

6.6. Conclusions

An aqueous solution, low-cost, scalable (0.2 M $TiCl_4$, 80 °C, 30 min) and environmentally friendly process was designed for the synthesis of anatase nanocolloids. The recovery of the nanoparticles from the colloid was optimized by adjusting the final pH to 3 with ammonium hydroxide (route N), as opposed to using pressure filtration (route A). This adjustment promotes light aggregation that facilitates particle recovery by fast centrifugation. The isolated dry nanopowders were found to consist predominantly of anatase as the major phase (~ 85 wt. %) along with small amounts of rutile and brookite. They were determined to possess a very high surface area (up to 250-350 m^2/g) and their primary nanocrystallites to be in the order of ~ 5 nm. An interesting feature of the aqueous-synthesized anatase nanocrystallites is their relatively elevated content of surface hydroxyl groups, in comparison to the P25 reference material.

6.7. References

[1] K. Yanagisawa and J. Ovenstone, *J. Phys. Chem. B*, **103** (1999), 7781.

[2] D. Reyes-Coronado, G. Rodriguez-Gattorno, M. E. Espinosa-Pesqueira, C. Cab, R. De Coss, and G. Oskam, *Nanotech.*, **19** (2008), 145605.

[3] G. P. Demopoulos, *Hydrometallurgy*, **96** (2009), 199.

[4] R. A. French, A. R. Jacobson, B. Kim, S. Isley, R. L. Penn, and P. C. Baveye, *Environ. Sci. Technol.*, **43** (2009), 1354.

[5] H. Zhang, J.F. Banfield, *J. Phys. Chem. B*, **104** (2000), 3481.

[6] A. Pottier, C. Chanéac, E. Tronc, L. Mazerolles, and J-P Jolivet, *J. Mater. Chem.*, **11** (2001), 1116.

[7] A. Di Paola, G. Cufalo, M. Addamo, M. Bellardita, R. Campostrini, M. Ischia, R. Ceccato, and L. Palmisano, *Coll. Surf. A*, **317** (2008), 366.

[8] K. I. Gnanasekar, V. Subramanian, and J. Robinson, *J. Mater. Res.*, **17** (2002), 1507.

[9] O. d'Hennezel and D. F. Ollis, Helv. *Chim. Acta*, **84** (2001), 3511.

[10] M. Minella, M. G. Faga, V. Maurino, C. Minero, E. Pelizzetti, S. Coluccia, and G. Martra, *Langmuir*, **26** (2010), 2521.

[11] E. G. Robertson, C. Medcraft, L. Puskar,R. Tuckermann, C. D. Thompson, S. Bauerecker, and D. McNaughton, *Phys. Chem. Chem. Phys.*, **11** (2009), 7853.

Chapter 7: TiO_2-based Single Layer Photoanodes for DSC Applications

7.1. Introduction

In this chapter, the formulation of various screen-printable TiO_2 pastes and their effect on the properties of annealed TiO_2 single layered thin film photoanodes is investigated (all experimental details are provided in Chapter 3, p. 61-67). The first section reports on the properties and associated cell performance of mesoporous thin TiO_2 films fabricated with powders A, N, and P25 that were introduced in Chapter 6. The preparation of the corresponding pastes was made according to a standard protocol provided in literature [1]. In the next two sections, opportunities for improvement of light-to-electron conversion cell efficiency and for simpler, less costly, and more environmentally friendly paste preparation methods are suggested. For instance, the use of mixed powder combining high surface area anatase nanoparticles and larger rutile particles acting as light scattering centres for the preparation of hybrid pastes is introduced and shown to lead to increased cell efficiency. Second, early results on the use of aqueous-synthesized TiO_2 colloidal gels as starting materials for direct (without drying and regrinding) paste formulation are presented. Based on SEM imaging work, this new method is shown that leads to the fabrication of highly uniform TiO_2 thin films, as opposed to fabricating photoanodes from dry TiO_2 powders that suffer from aggregation.

7.2. Pastes A, N, and P25

Powders A, N, and P25 (Chapter 6) were used to prepare three pastes of identical composition, as per procedure described in Chapter 3. As a reminder, powders A and N were prepared by aqueous synthesis with the former collected by pressure filtration from the spent acidic solution while the latter was collected following neutralization (to pH 3 with NH_4OH) and centrifugation. P25 was used for comparison purposes. These were screen printed and annealed on non-conductive silica-based glass substrates and the resultant films were characterized in terms of thickness, surface area, porosity and crystallinity via multiple analytical techniques (profilometry, SEM, TEM, BET surface area, XRD, UV-Vis absorption, Micro-Raman, FT-IR, and TGA).

7.3. Characterization of mesoporous films prepared with pastes A, N, and P25

Typical profiles obtained for films A, N, and P25 are presented in Figure 7.1. According to these profiles, the roughness of films A and N appears to be higher than the roughness of film P25. SEM micrographs of the same films are presented in Figure 7.2 (top views). The presence of submicron size aggregates can be observed on the micrographs of films A and N (mainly this one) whereas film P25 is characterized with a uniformly porous nanostructure, in agreement with the profilometry data. The average pore size calculated from the BET surface area analyses were, 79, 76 and 236 Å for films A, N and P25 respectively (Table 7.1). Pore size and development of an open porous network is vital for full access and coverage of all TiO_2 surface by the dye on one hand and the fast/unhindered diffusion of the electrolyte. It can be concluded from the above results that the paste preparation protocol was not optimum in terms of particle dispersion when using the aqueous-synthesized TiO_2 powders A and N.

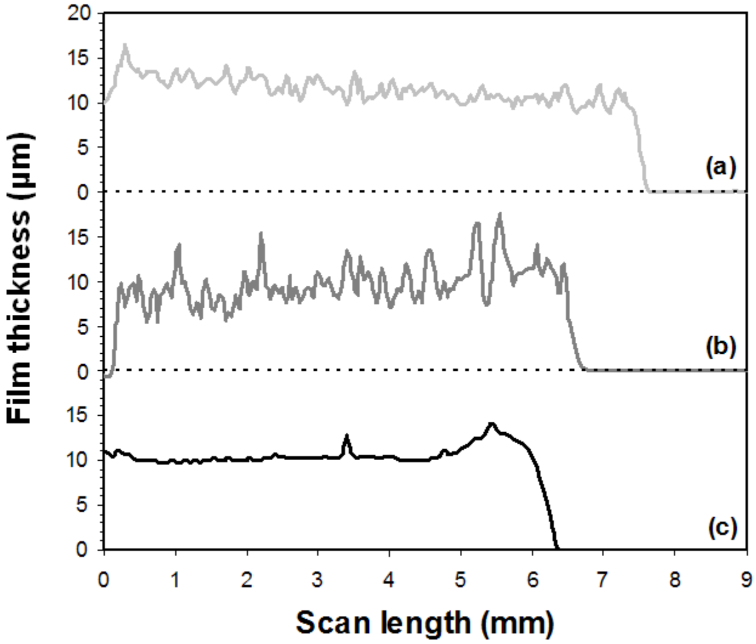

Figure 7.1. Profilometry scans obtained for films A (a), N (b) and P25 (c).

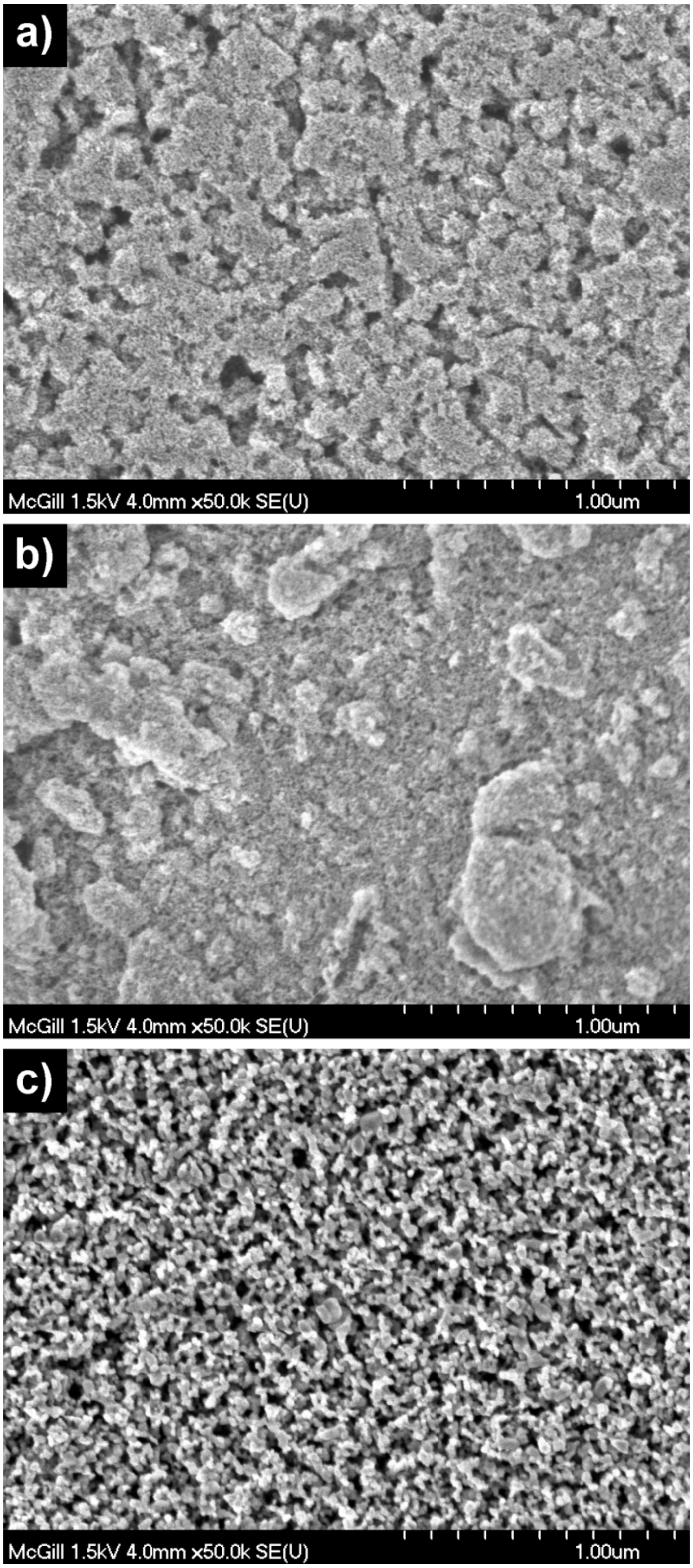

Figure 7.2. FEG-SEM top views of films A (a), N (b) and P25 (c).

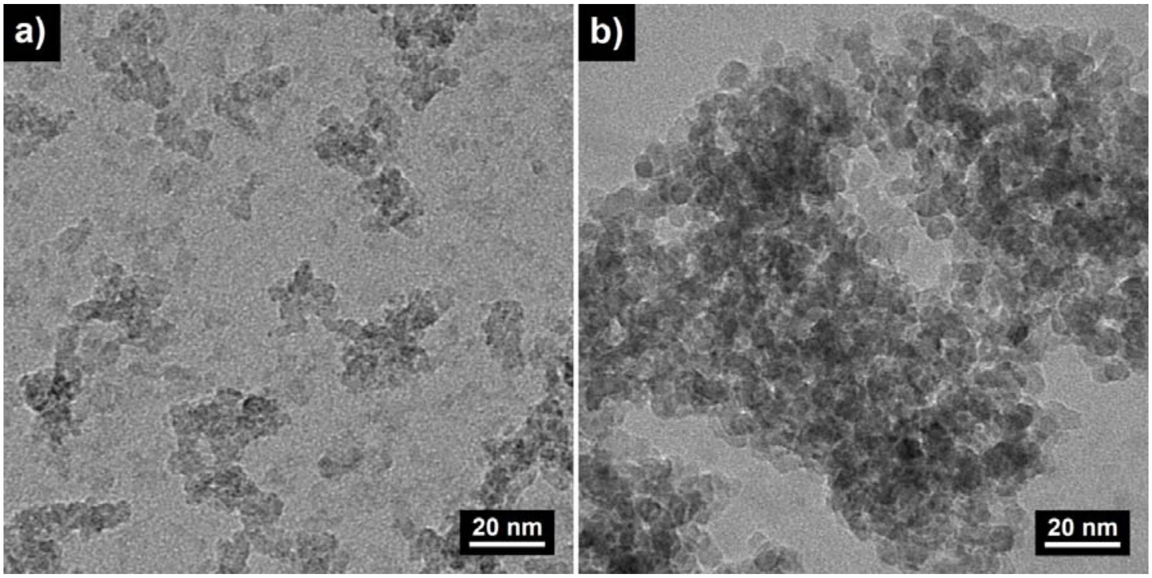

Figure 7.3. TEM pictures of nanocrystallites extracted from colloid A (0.2 M $TiCl_4$, 30 min, 80 °C, 1000 rpm) (a) and film A after annealing (b).

The BET surface area measurements performed on the three different powders and annealed films are presented in Table 7.1. These data show that films A and N are characterized with a much higher surface area (135 and 131 m^2/g respectively) than film P25 (49 m^2/g). The decrease in the surface area observed between the aqueous-synthesized powders and the corresponding films is caused by the growth of the nanoparticles upon annealing (Figure 7.3). This phenomenon was substantiated by performing TEM analysis of powder A after annealing. The corresponding image (Figure 7.3.b) shows aggregated nanoparticles with a narrow size distribution in the range 8-12 nm, agreeing with the equivalent BET particle diameter value (11.9 nm) reported for film A in Table 7.1. Particle growth and improvement of the crystallinity upon film annealing can also be deduced from the X-ray diffraction patterns obtained for films A and N (Figure 7.4), according to which an increase in peak intensity and a slight narrowing of the anatase (101) peak is evident. By comparing the phase compositions reported in Table 7.2 for powder A (84.6 wt. % anatase, 6.9 wt. % rutile, and 8.5 wt. % brookite) and film A (83.5 wt. % anatase, 6.9 wt. % rutile, and 9.6 wt. % brookite), or powder N (84.8 wt. % anatase, 6.4 wt. % rutile, and 8.8 wt. % brookite) and film N (85.7

wt. % anatase, 7.2 wt. % rutile, and 7.1 wt. % brookite), it is deduced that no phase transition occurred upon annealing.

Table 7.1. BET surface area and porosity analyses of powders and films A, N, and P25.

Sample	BET surface area (m^2.g^{-1})	BET average pore size (Å)	d_{BET} (nm)
Powder A	362 (± 20)	27	4.3
Powder N	250 (± 5)	33	6.2
Powder P25	51 (± 1)	118	30.2
Film A	135	79	11.9
Film N	131	76	11.4
Film P25	49	236	31.5

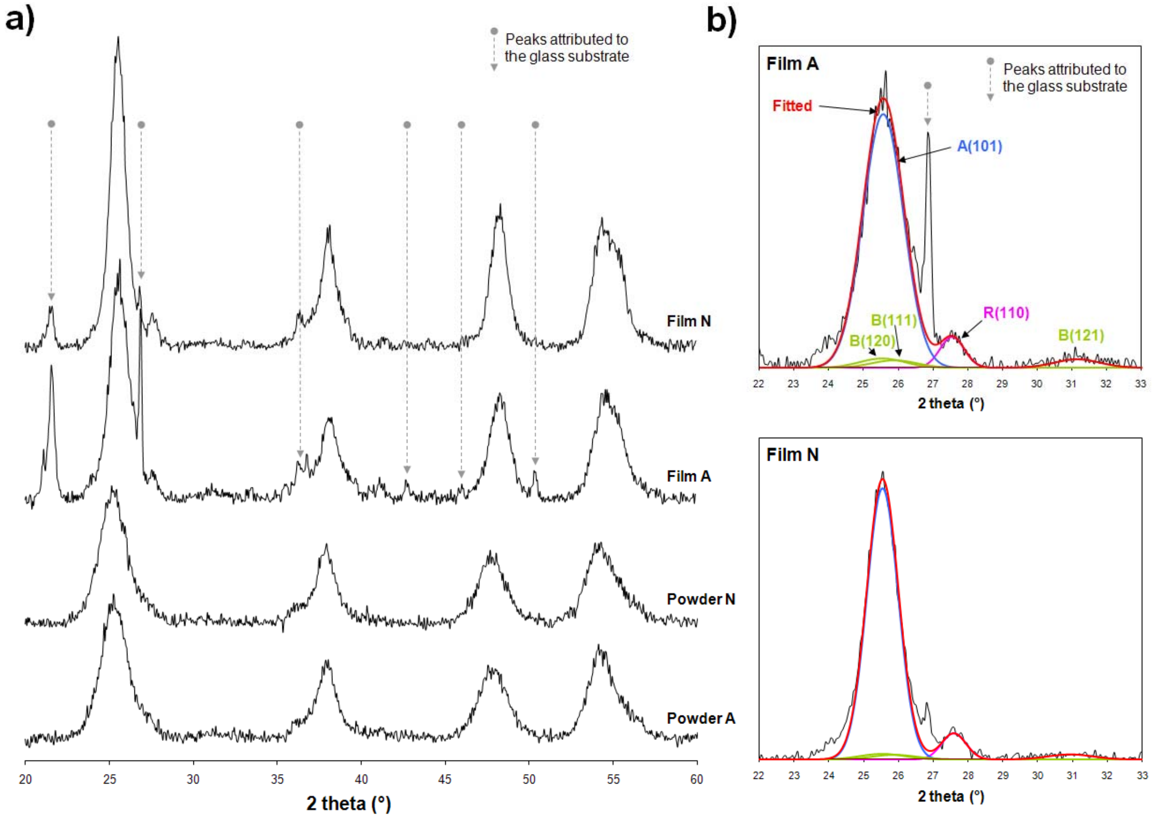

Figure 7.4. XRD patterns of powders A and N, and films A and N (a); Gaussian fits of the XRD patterns of films A and N (b).

Table 7.2. Anatase, rutile, and brookite phase composition of TiO_2 powders and films A and N.

Sample	Synthesis conditions	Anatase (wt. %)	Rutile (wt. %)	Brookite (wt. %)
Powder A	0.2 M; 30 min; 80 °C; (A)	84.6	6.9	8.5
Powder N	0.2 M; 4 hrs; 80 °C; (N)	84.8	6.4	8.8
Film A	0.2 M; 30 min; 80 °C; (A); annealing (450 °C, 30min)	83.5	6.9	9.6
Film N	0.2 M; 30 min; 80 °C; (N); annealing (450 °C, 30min)	85.7	7.2	7.1

Note: The phase composition data associated with powders A and N were already presented in Chapter 6.

UV-visible absorption curves of the TiO_2 films A and P25 supported on FTO glass are shown in Figure 7.5.a. The absorption efficiencies of the bare TiO_2 films were corrected for the FTO-glass background. The absorption curves were computed by converting the measured reflectance spectra (R) with the aid of the Kubelka-Munk function, F(R). By assuming the thickness of the films to be infinite, the simplified version of the Kubelka-Munk function, $F(R_\infty)$ shown in Equation 7.1, was derived and used [2].

$$F(R_\infty) = (1 - R_\infty)^2/(2R_\infty) \tag{7.1}$$

It can be seen on Figure 7.5.a, that as we move from P25 to the aqueous-synthesized TiO_2-derived film, the films become progressively more transparent to visible light. This (blue) shift of the absorption edge may be interpreted as a result of the quantum confinement effect of the TiO_2 nanocrystals. To estimate the band gap of the semiconductor, the linear part of the Tauc plots $(F(R).h\nu)^n$ vs. $h\nu$ to $(F(R).h\nu)^n = 0$, was extrapolated as explained elsewhere [3]. For indirect transition semiconductors such as TiO_2, $n = {}^1/_2$ (section 2.2.3 of Chapter 2, p. 13-17). The Tauc plots are presented in Figure 7.5.b. From the associated linear extrapolations the following band gap values were computed: 3.37 eV (film A) and 3.15 eV (film P25). These results reflect the diminishing crystallite size effect [4]. Furthermore as the crystallite size decreases, the frequency and line-width of the E_g Raman peak (Figure 7.6) increases/blue-shifts, respectively as a result of phonon confinement [5,6].

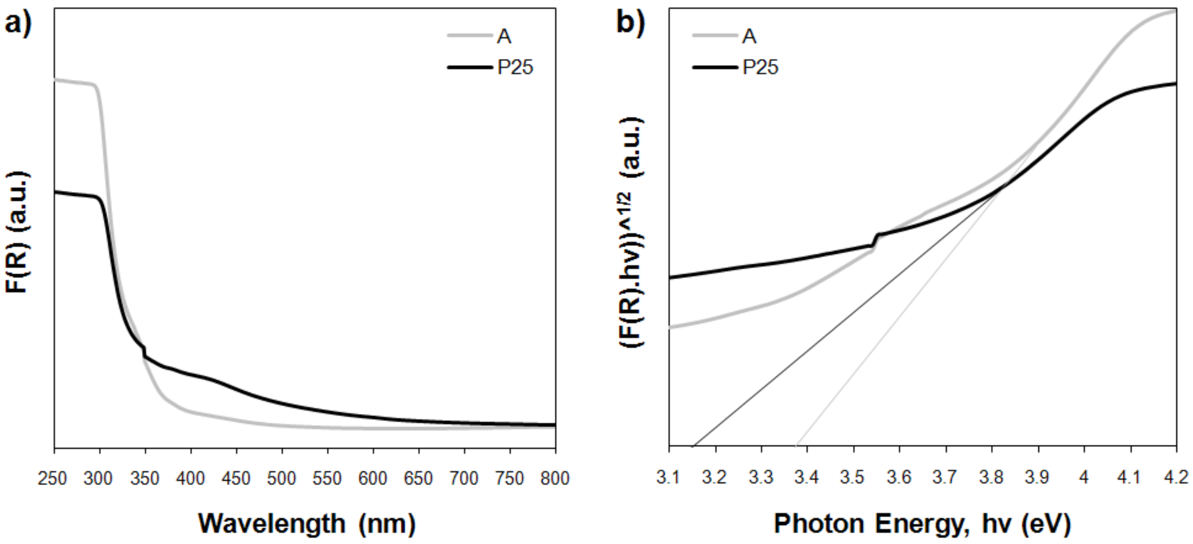

Figure 7.5. UV-vis absorption spectra of films A and P25 (in diffuse reflectance mode) (a) and corresponding Tauc plots (b).

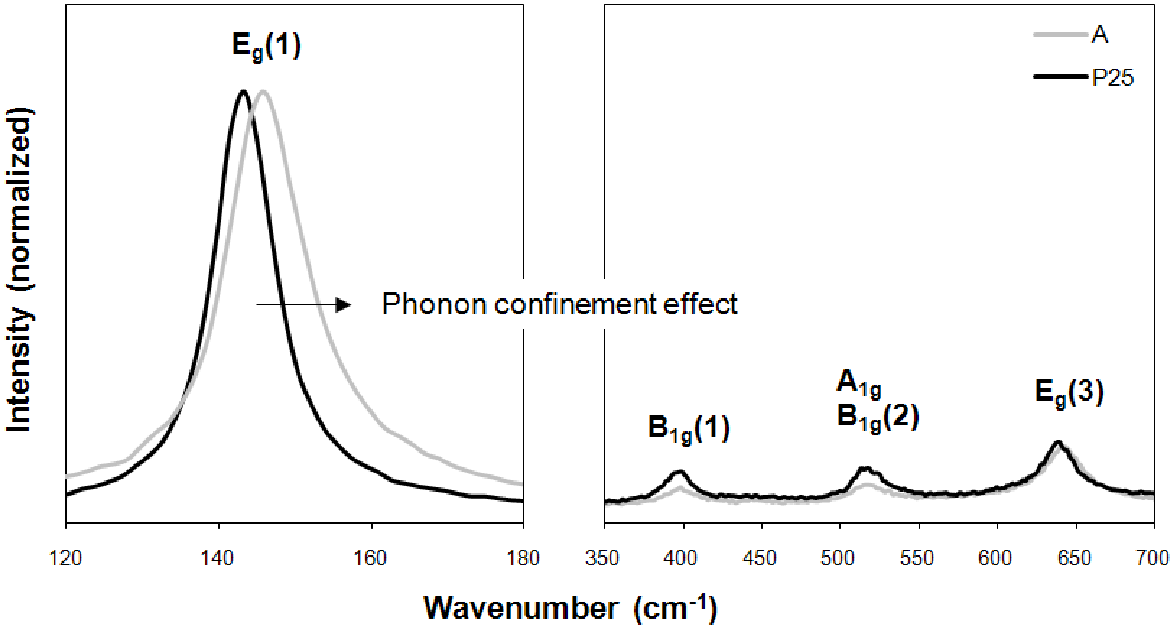

Figure 7.6. Micro-Raman spectra of films A and P25.

Chemical characterization of the films revealed that most of the impurities such as the adsorbed chlorides and ammonium chloride initially present in powders A and N were removed upon film annealing. This was exemplified by the absence of the Cl K_α peak on the EDS spectra of films A and N (Figure 7.7) and by the absence of the series of peaks previously attributed to ammonium chloride on the FT-IR spectrum of film N (Figure 7.8). According to the TGA weight loss curves of films A, N, and P25 in the temperature range T_{amb}-150 °C (Figure 7.9), the surface hydration of films A and N (2 and 2.7 wt. % loss) was found to be slightly higher than the surface hydration of film P25 (0.9 wt. % loss). This result originates from the larger surface area of films A and N. The weight loss observed in the temperature range 150–600 °C, 1.4, 1.4 and 0.2 wt. % for films A, N, and P25 respectively, is thought to correspond to the surface hydroxyl groups Ti-OH as described elsewhere [7].

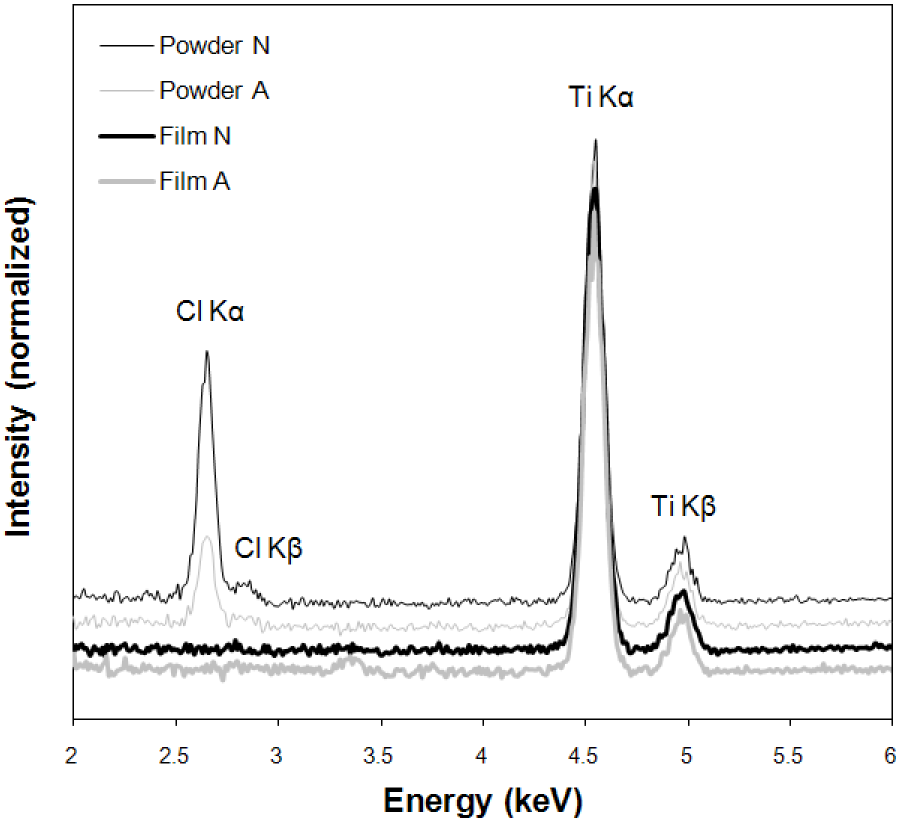

Figure 7.7. EDS spectra of powders and films A and N.

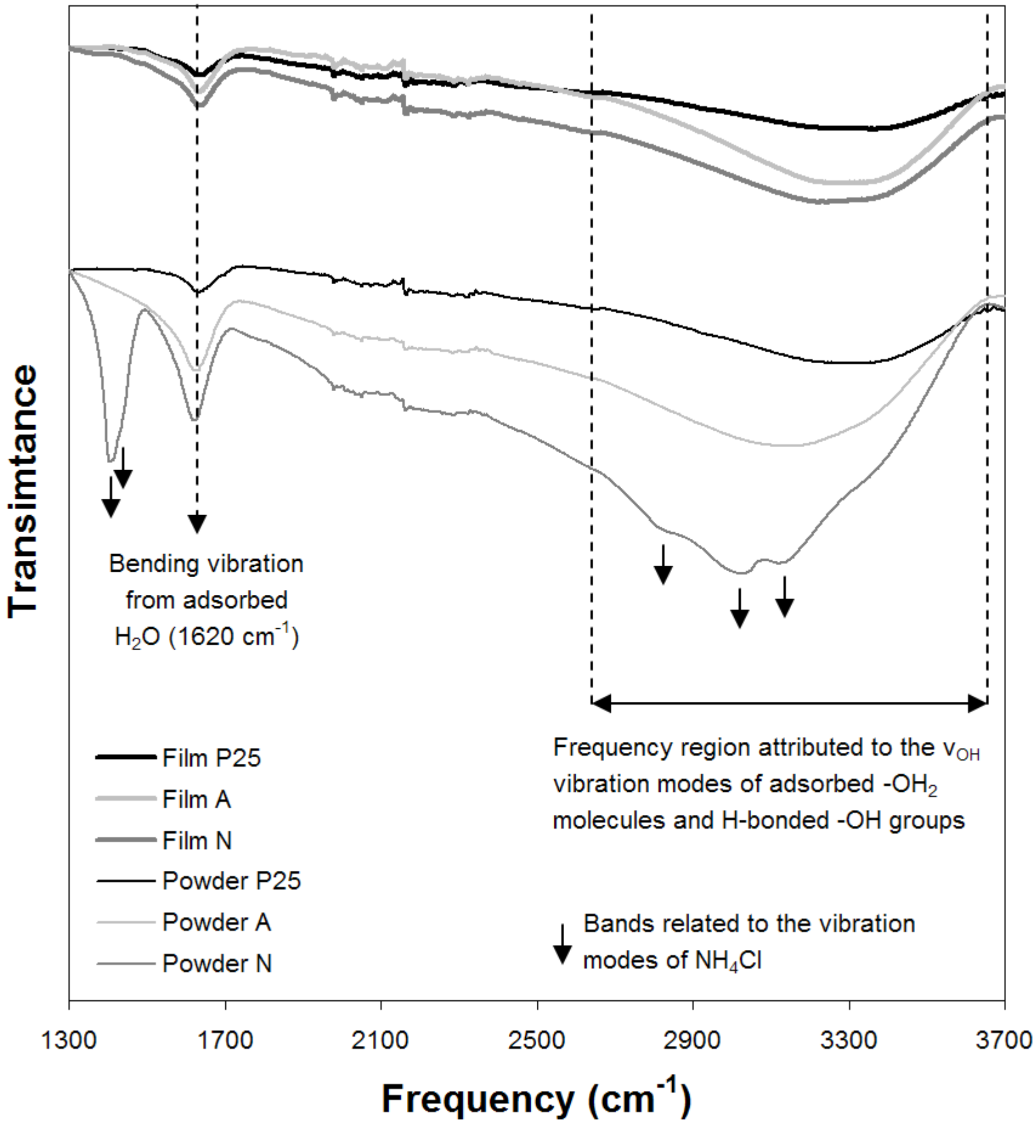

Figure 7.8. FT-IR spectra of powders and films A, N, and P25.

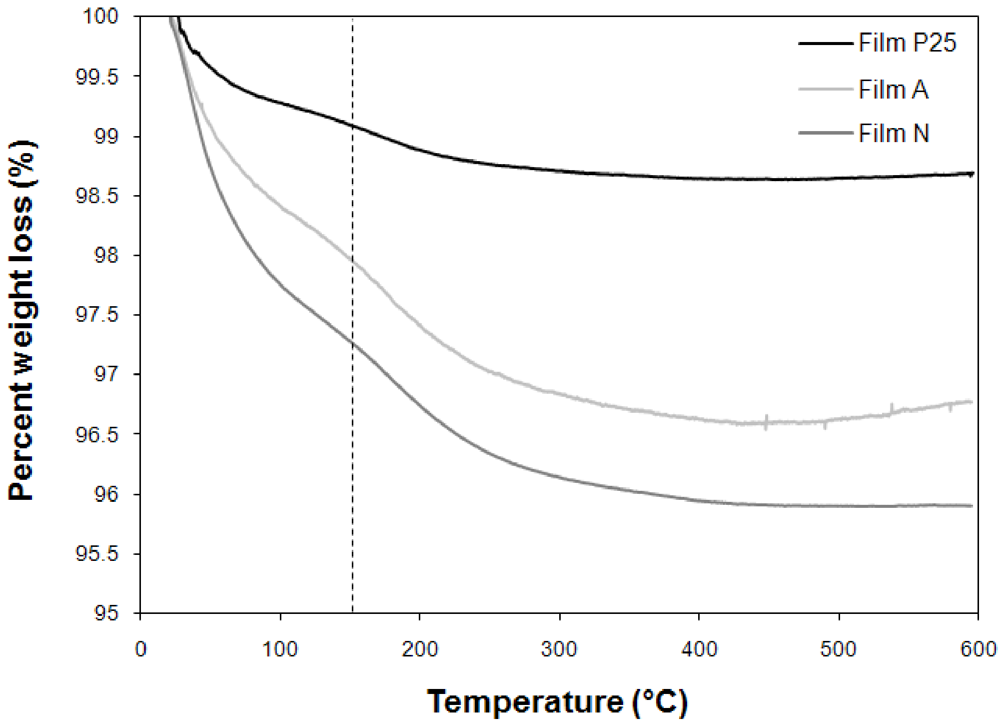

Figure 7.9. TGA curves of films A, N, and P25.

7.4. Cell performance

A series of photoanodes based on TiO_2 powders A, N and P25 were prepared with various film thicknesses and assembled into DSCs. The results of the photovoltaic measurements performed on these solar cells are provided in Table 7.3, and the corresponding I vs. V curves are shown in Figure 7.10.a.

From these data it can be seen that the DSC devices based on aqueous-synthesized powders A and N produced equivalent performance with the DSC based on the commercial powder P25. Film thickness and post-treatment by immersion into dilute aqueous $TiCl_4$ solution (Chapter 3, Figure 3.5.f) were found to influence cell performance in agreement with previous investigations [8-10]. The anodes which received the $TiCl_4$ treatment have much higher power conversion efficiency, η, and short circuit current density, I_{sc}. For example in the case of anodes prepared with equivalent thickness (~ 10-12 µm), η and I_{sc} were found to more than double for all three cells when using the $TiCl_4$ post-treatment. The respective numbers are (Table 7.3): from 0.89

to 2.40 % and 1.96 to 5.99 mA/cm^2 in the case of A films; from 1.32 to 2.70 % and 2.59 to 6.25 mA/cm^2 in the case of N films; and from 1.22 to 2.73 % and 3.07 to 6.22 mA/cm^2 in the case of the reference P25 films. According to a previous report [11] the beneficial effect of $TiCl_4$ treatment relates to improved electron transport and life time owing to the development of better chemical necking between the particles, here catalyzed by the enhanced surface hydration/hydroxylation of the nanocrystallites. Moreover, recent research suggests that this feature facilitates the binding of the dye molecules on the TiO_2 surface [7] that translates to enhanced cell performance [12,13].

The effect of film thickness on performance parameters for the two aqueous-synthesized anatase-based cells (A and N) is illustrated in Figure 7.10.b. The plotted results show that the efficiency and I_{sc} tend to increase whereas the open circuit voltage, V_{oc}, tends to decrease with the thickness of both TiO_2 films. The increase of the I_{sc} is thought to originate from the larger volume of TiO_2-anchored dye, hence higher density (per unit area) of electrons produced and transported. The tendency of the V_{oc} to decrease with the thickness of the film is thought to result from a combination of longer electron diffusion length and larger electrolyte resistance overpotential. However, the efficiency of a cell is known to depend more on its I_{sc} than on its V_{oc}. This explains why the efficiency of the A and N cells is observed to increase with the thickness of the TiO_2 film.

When comparing the performance characteristics of the two aqueous-synthesized nanocolloid-based cells (A and N), it can be observed that the N series had slightly better I_{sc} and efficiency than the A series. This result is thought to be caused by the presence of larger aggregates in the N film than in the A film, which may act as scattering particles, increasing the amount of light absorbed by the anode. At this point it is important to mention that the above comparative data refer to single transparent layer photoanodes without the inclusion of a scattering layer [14] that is a standard component of the so-called “double-layer” film structure [10]. Double-layer electrodes based on the A and P25 powders produced for example higher conversion efficiency outputs as described elsewhere, namely 5 and 4.1 % respectively [15].

Table 7.3. Characteristics and performance of the DSC devices fabricated with variable thickness photoanodes made from powders A, N and P25. The symbols identify data represented in Figure 7.10.

DSC	Thickness (µm)	$TiCl_4$ Treatment	I_{sc} (mA/cm^2)	V_{oc} (V)	FF	η (%)
A1	9.6		1.89	0.665	0.71	0.89
A2	10.2		1.96	0.655	0.69	0.89
A3	4.0	✓	4.43 △	0.685 ○	0.67	2.04 ◇
A4	8.0	✓	5.23 △	0.610 ○	0.64	2.04 ◇
A5	11.5	✓	5.45 △	0.605 ○	0.73	2.40 ◇
A6	12.0	✓	5.99 △	0.595 ○	0.67	2.40 ◇
N1	6.0		2.47	0.670	0.74	1.23
N2	12.4		2.59	0.660	0.77	1.32
N3	3.0	✓	3.94 ◬	0.655 ◍	0.72	1.86 ◈
N4	5.5	✓	5.45 ◬	0.605 ◍	0.71	2.34 ◈
N5	9.8	✓	5.51 ◬	0.625 ◍	0.72	2.48 ◈
N6	12.9	✓	6.25 ◬	0.620 ◍	0.70	2.70 ◈
P25-1	13.4		3.07	0.605	0.61	1.22
P25-2	10.6	✓	6.22 ▲	0.665 ●	0.69	2.73 ◆

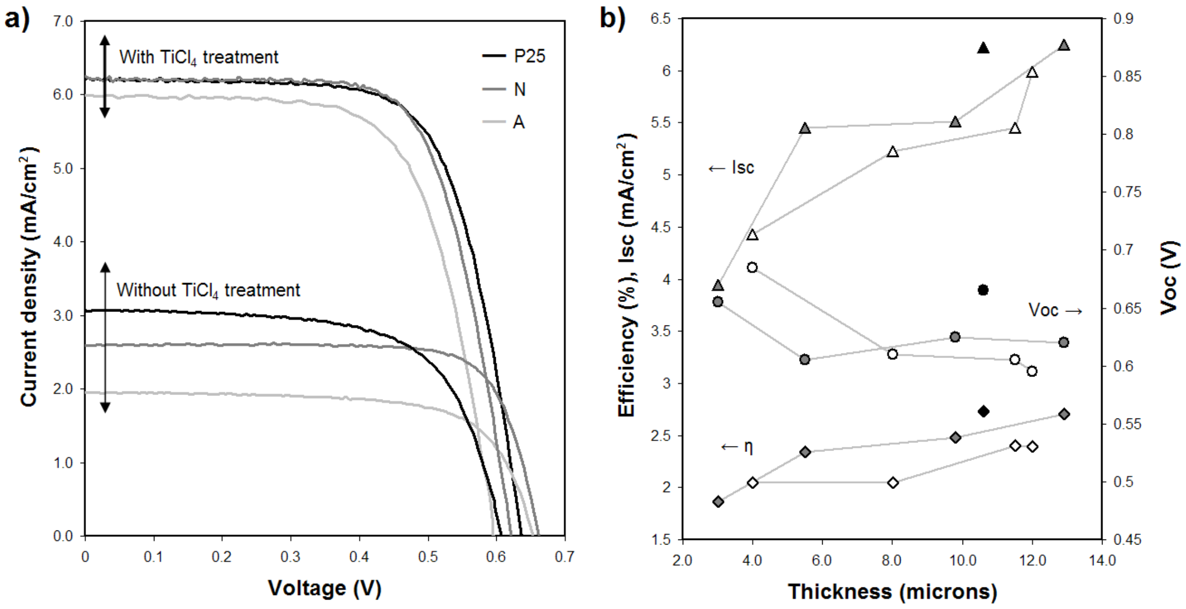

Figure 7.10. Photovoltaic measurements of a series of DSC devices based on photoanodes made from powders A, N and P25: I vs. V curves for the 12 µm thick film photoanodes with and without $TiCl_4$ treatment (a); effect of the film thickness (b) on the I_{SC} (triangles), V_{OC} (circles), and η (diamonds), of DSCs prepared with powder A (white), N (grey), and P25 (black).

7.5. Hybrid paste $H_{A/R}$

In view of the previous results and given the equivalent if not better performance of the aqueous-synthesized powder A to that of P25, it was further thought to use powder A for the formulation of a hybrid paste using mixed powders with complementary properties. Thus, a hybrid paste, labelled paste $H_{A/R}$, was prepared by using two constituted powders (A-nanocrystalline anatase and R-nanofibre structured rutile) both synthesized via the aqueous solution synthesis process described in Chapters 5 and 6. Single-layer films were fabricated and characterized with SEM imaging and DSC devices were assembled and tested.

7.5.1. Powder R

Powder R was obtained by isothermal treatment (80 °C, 2 hrs) of a 0.3 M $TiCl_4$ aqueous solution in the mechanically stirred reactor (1000 rpm). Solid/liquid separation, washing and drying of the synthesized powders were processed according to route A (Chapter 3, p. 59-60). The XRD pattern of powder R (Figure 7.11) shows rutile to be the major crystalline phase while small amounts of anatase can be detected by the appearance of a shoulder at 25.3° and a low intensity peak at 48.0°, attributed to the anatase (101) and (200) diffraction planes, respectively. SEM pictures of powder R are presented in Figure 7.12 from which the powder is observed to contain 200-400 nm particles characterized with an urchin-like structure. At the surface of the particles, small elongated triangular nanocrystals can be seen that grew in a radial direction providing the powders with a surface area of 112 m^2/g (Table 7.4). Hence, powder R simultaneously possesses the particle size distribution properties required for efficient light-scattering materials, and a high surface area, which is essential to the fabrication of efficient photoanodes. Moreover, the urchin-like structure characterizing the particles offers an ideal platform for hosting smaller anatase nanoparticles. The contribution of the light scattering and structural properties of powder R to the DSC performance was tested by assembling devices with single layer photoanodes made from the hybrid paste, namely paste $H_{A/R}$.

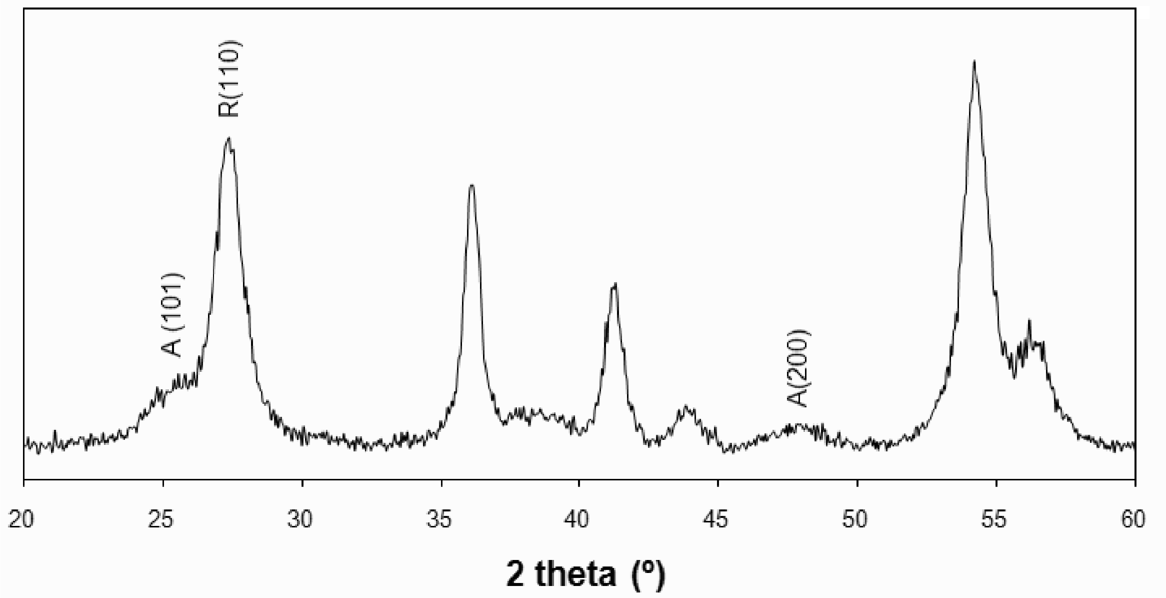

Figure 7.11. XRD pattern of powder R.

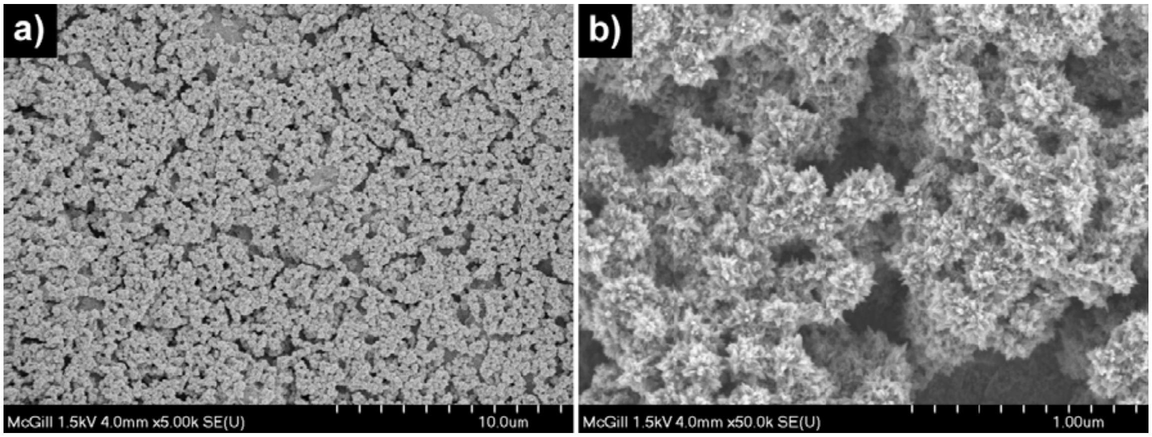

Figure 7.12. SEM pictures of powder R, produced via isothermal treatment (80 °C, 2 hrs) of a 0.3 M $TiCl_4$ solution.

7.5.2. Paste $H_{A/R}$

Paste $H_{A/R}$ was prepared starting with a mixed TiO_2 powder containing 50 wt. % of powder A and 50 wt. % powder R. The method followed to prepare this paste was identical to the one used for pastes A, N, and P25, as explained in Chapter 3.

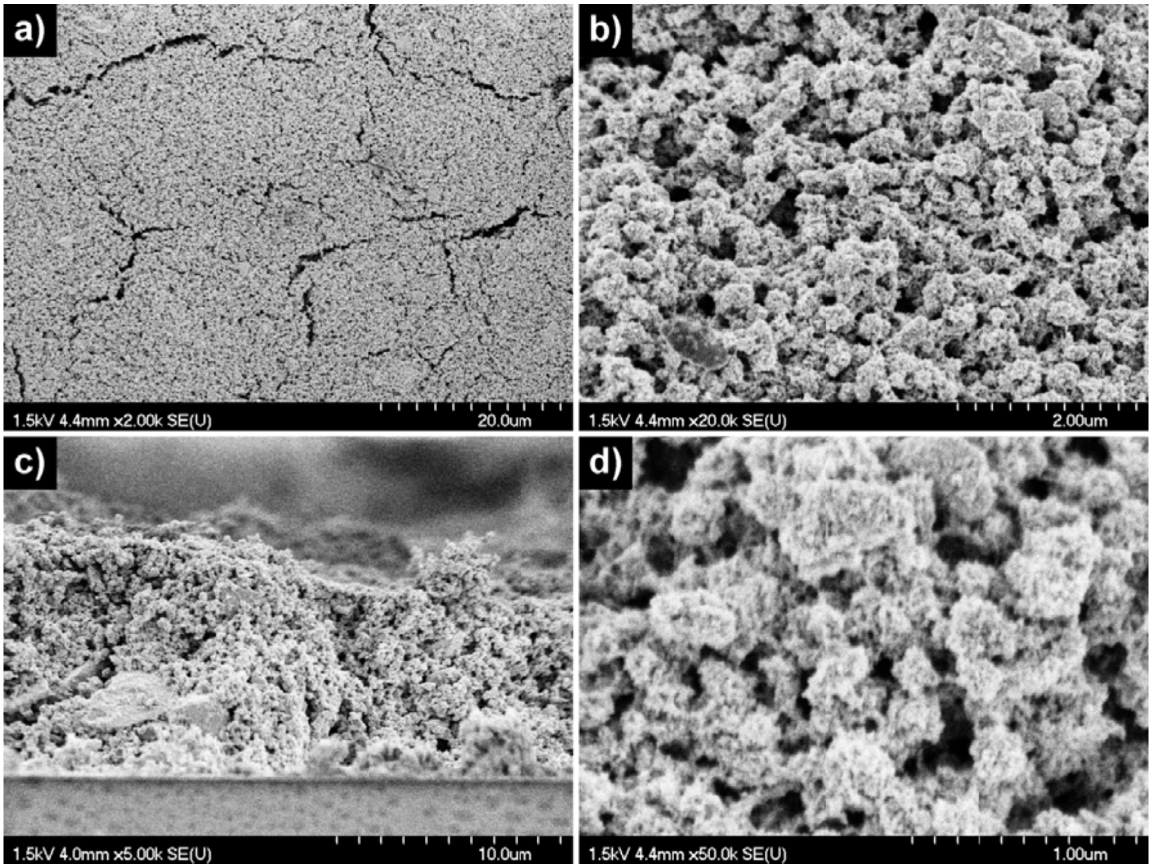

Figure 7.13. SEM pictures of a single layer thin film prepared with paste $H_{A/R}$; top views (a,b,d) and cross section (c).

Table 7.4. BET surface area and porosity analyses of powders A and R, and film $H_{A/R}$.

Sample	BET surface area ($m^2.g^{-1}$)	BET average pore size (Å)	d_{BET} (nm)
Powder A	362 (± 20)	27	4.3
Powder R	112	-	13.8
Film $H_{A/R}$	62	140	24.8

SEM pictures of a single layer TiO_2 thin film obtained by screen printing and annealing of paste $H_{A/R}$ on a microscopic glass slide are presented in Figure 7.13. At low magnification (Figure 7.13.a), a top view shows the film to bear some cracks and a few sub micron-size aggregates. These aggregates result from the strong aggregation of anatase nanoparticles characterizing powder A (Chapter 6) that could not be broken upon grinding during paste preparation. These aggregates are thought to be responsible for cracks generation within the film during annealing. During annealing, the film contracts mostly owing to the loss of the water adsorbed at the surface of the aqueous-synthesized TiO_2 particles and the destruction/removal of the organic ingredients of the paste. It is conceivable that the tension generated by contraction of the film, especially at the interface of the aggregates with the well dispersed particles, leads to the observed cracks. However, these cracks did not seem to affect the adhesion of the film to the glass substrate (Figure 7.13.c), a property of great importance for the good functioning of a DSC device. At higher magnification (Figures 7.13.c and 7.13.d), it is interesting to notice that the urchin-shaped rutile particles characterizing powder R were homogeneously covered by non-aggregated anatase nanoparticles from powder A. The resultant film structure is characterized with large voids (macropores) created by the arrangement of the 200-400 nm rutile particles from powder R, and smaller voids (mesopores) owing to the assembly of small 8-12 nm particles from powder A around the bigger rutile particles.

7.5.3. Cell performance

An 8 µm thick single layer film was prepared on FTO-coated glass with paste $H_{A/R}$ and the resultant photoanode was assembled into a DSC (post $TiCl_4$ treatment of the annealed film was applied). The I vs. V curve of this cell is shown and compared to the I vs. V curves of DSCs made with single powders A, N, and P25 in Figure 7.14. From this diagram, it is observed that the cell based of the hybrid paste $H_{A/R}$ registered higher short circuit current density and open circuit voltage, namely 8.96 mA/cm^2 and 0.71 V, than the other cells. These results translated in greatly improved light-to-current conversion efficiency, $\eta = 4.07$ %.

Such results may be explained on the basis of the properties of the mixed powder used to prepare the photoanode. First, the mixing of the small anatase nanoparticles characterizing powder A with the larger rutile particles apparently provides for a more uniform (fewer occurrences of aggregates) inter-particle network with larger pore size (140 Å average pore size, Table 7.4). As such, the resultant porous structure allows for easier infiltration of both the dye and the electrolyte within the film, hence for less diffusion resistance, resulting in a higher V_{OC}. Second, the larger particles introduced with the use of powder R are thought to act as scattering centres, so that the probability of photons travelling across the film without generating electrons is much lower than in the case of photoanodes prepared with powder A, N or P25 only. In standard DSCs, scattering particles are provided as a second layer (dual layer structure) on the top of the transparent film [16-18]. However, from a fabrication point of view, the deposition of a second layer makes the device building process much longer in manufacturing time and more costly since it requires more material (thicker films) and the application of a second annealing cycle.

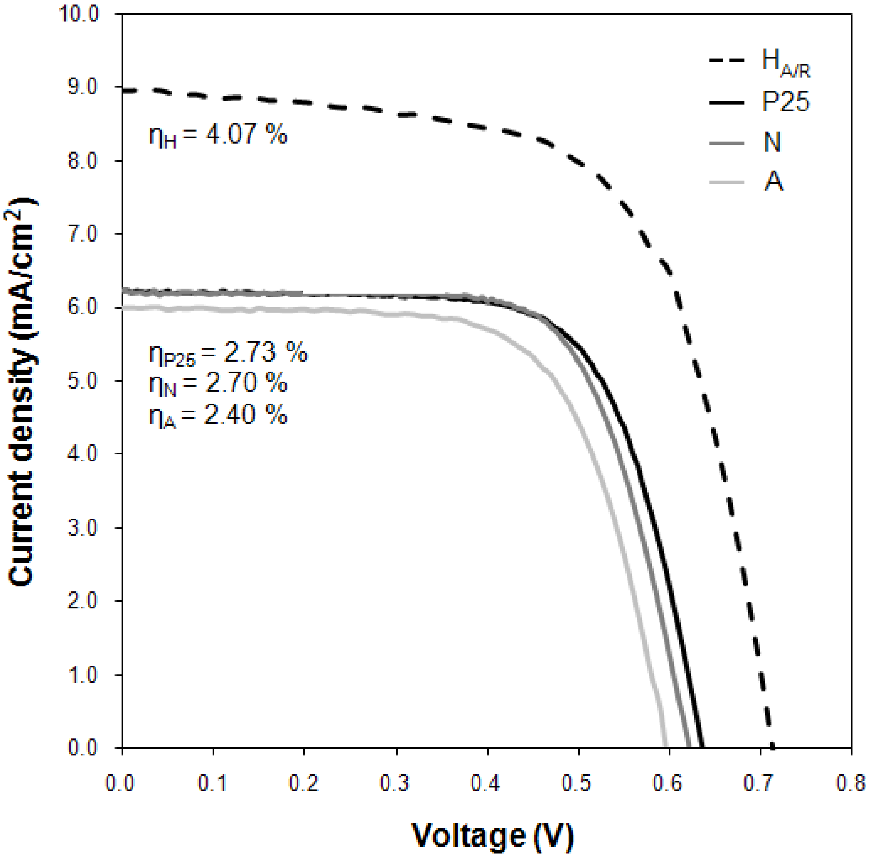

Figure 7.14. Photovoltaic measurements of DSC devices based on photoanodes made from powders A, N, P25 and $H_{A/R}$: I vs. V curves for the 12 μm thick film photoanodes A, N, and P25, and 8 μm thick film photoanode $H_{A/R}$ with $TiCl_4$ treatment.

It is interesting to mention here another study in which researchers reported on the "synergistic effect between anatase and rutile TiO_2 nanoparticles in dye-sensitized solar cells" [19] involving photoanode fabrication with an anatase-rutile nanocomposite powder. Similar to the present study, the authors in that study noticed an improvement in DSC performance when rutile was added up to 15 wt. % in anatase. That improvement was, however, attributed to interfacial transfer of electrons from rutile to anatase nanoparticles, similar to the beneficial effect of the $TiCl_4$ treatment, rather than due to scattering effect, as proposed here. Moreover in that study the performance of the nanocomposite was much lower than that of the P25 reference material (2.72 % vs. 4.59 % efficiency), which is exactly the opposite of what measured in the current study (4.07 % vs. 2.73 % efficiency). Hence, the hybrid paste formulation of the current work provides a superior alternative that deserves further development.

7.6. Alternative paste formulation protocols

In this section, alternative paste formulation methods were investigated in an effort to (i) improve the film properties hence the DSC performance and (ii) bring simplifications to the manufacturing process. For example, avoidance of the formation of large aggregates such as those observed in films prepared with pastes A and N could improve the uniformity and adhesion properties of the annealed films. On another front, the direct use of wet TiO_2 material as opposed to dry powders can significantly shorten and simplify the paste preparation procedure. In contrast to pastes made from dry powders, all pastes tested in this work were prepared starting with ethanolic or aqueous-based TiO_2 nanoparticle gels, namely gel N-Eth and gel A-Aq, which detailed preparations were described in Chapter 3 (Table 3.2).

7.6.1. Pastes N' and N'' based on "as is" ethanolic gel

7.6.1.1. Paste N'

A first attempt was made to simplify the paste preparation procedure and improve the dispersion of the particles by replacing powder N (dry) with the ethanolic gel N-Eth, without changing any other parameters of the paste formulation (when compared to paste N). The obtained paste, namely paste N’, was found to have good final rheological properties. However, after 2 days of storage in a closed glass vial, the paste was found to turn into a solid gel, probably due to the reaction of the ethyl cellulose with residual water. Hence with this method, very good dispersion of the anatase nanoparticles within the paste was achieved. However, the produced films proved very brittle as detailed in the following paragraphs.

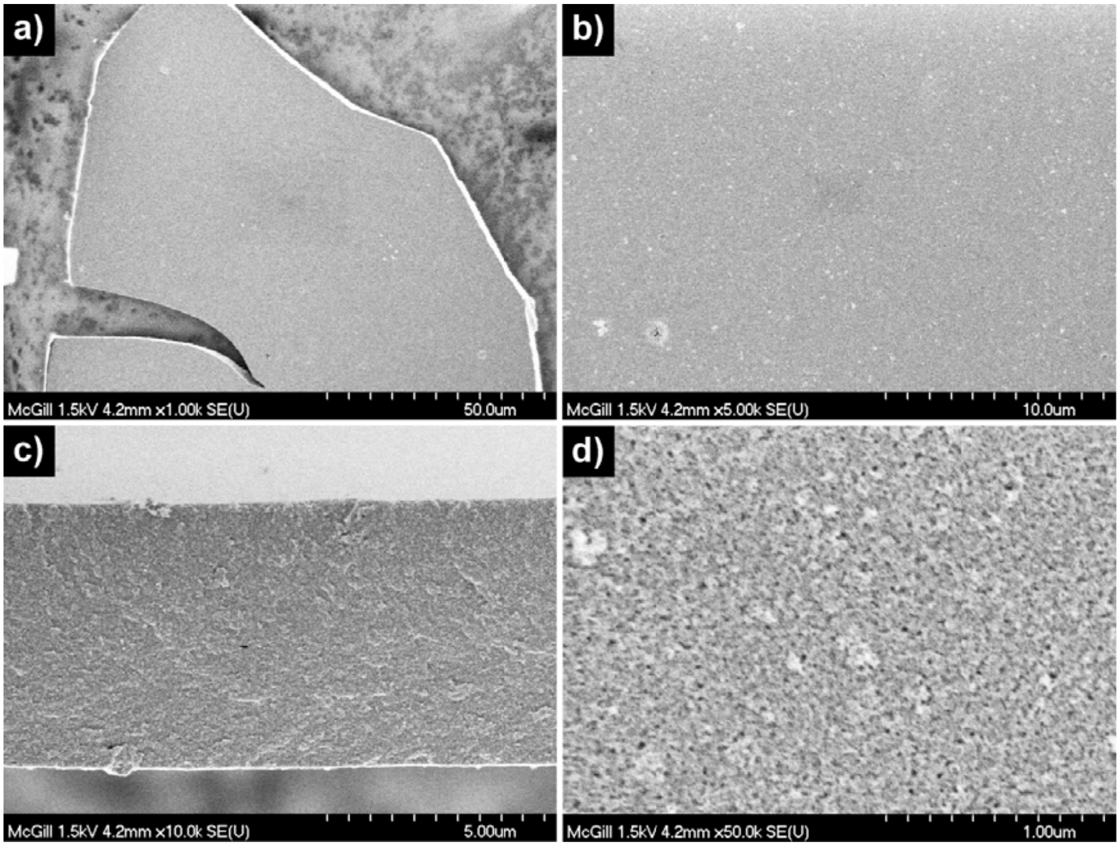

Figure 7.15. SEM pictures of plates from a TiO_2 single layer thin film prepared with paste N’: top views (a, b, and d); fracture surface (c).

Single layer TiO_2 thin films with different thicknesses (judging by the transparency of the screen-printed layer of paste) were prepared on regular glass slides by screen-printing and annealing of paste N’. During annealing, all films were found to crack and peel off the glass substrate. Figure 7.15 shows SEM pictures of plates collected from one of those films. The low magnification top views (Figures 7.15.a and 7.15.b) show the film to be characterized with a very uniform structure and low roughness. On Figure 7.15.a a crack is seen to propagate through the plate featuring clean edges, which are typical of a brittle fracture. The sharp and rather straight edges of the plate also reveal the brittle nature of the film. The flaking of the film, at all likelihood related to contraction induced as a result of water evaporation during annealing. From the cross sectional image in Figure 7.15.c, the thickness of the film, approximately 6 µm, appears to be constant and the internal structure of the film is seen to be rather homogenous. A high magnification top view image (Figure 7.15.d) makes it possible to distinguish uniformly distributed small pores of diameters < 50 nm.

7.6.1.2. Paste N''

In order to avoid the solidification of the paste upon storage at T_{amb}, ethyl cellulose was replaced by polyethylene glycol (PEG, 20,000 g/mol), a water soluble organic binder. The corresponding paste, namely paste N'', was prepared without adding any rheological agent like α-terpineol, as done in standard preparation protocols [20,21]. However, the resulting condensed paste was found to have poor rheological properties, essentially lacking elasticity that made it difficult to manually screen-print films with uniform thickness. In addition the film started to dry very fast at T_{amb} and the appearance of cracks at the surface of the film could be observed a few minutes only after the application of the paste on the glass substrate. During annealing, the cracks kept expanding and eventually led to flaking and peeling off of the film.

SEM images of the resultant plates are shown in Figure 7.16. These are found to bear similar characteristics to plates from film N' shown in Figure 7.15. In particular, the surface of the film is found to be very smooth and flat (Figure 7.16.a), while the internal structure of the film appears to be highly uniform and rather dense (Figure 7.16.b). In this case, packing of the particles is apparently so compact that no pores can be observed. Such film characteristics are not desired when fabricating photoanodes since a reasonable degree of film porosity, typically in the mesoporous range (pore diameters in the range 2-50 nm), is required for the good functioning of DSCs. Judging by the clean and straight fracture of the film, it appears again the latter to be brittle. Moreover, when looking at the fracture surface of the film (plate edges), hackle marks can be noticed that form symmetric patterns of chevron-like structure, revealing the direction of crack propagation (Figure 7.16.c, black lines), or concentric patterns initiated from a common origin in a plume structure (Figure 7.16.d, black lines). These features are typically encountered at the fracture surface of rocks and certain metals characterized with brittle mechanical properties [22]. The fracture of film N'' was most likely originated by its contraction upon drying and annealing. Moreover, it was experimentally noticed that an increasing film thickness may affect its mechanical and adhesion properties. In that sense, the large thickness of approximately 17 µm of the plates collected for film N'' might have contributed to weaken its mechanical and adhesion strength.

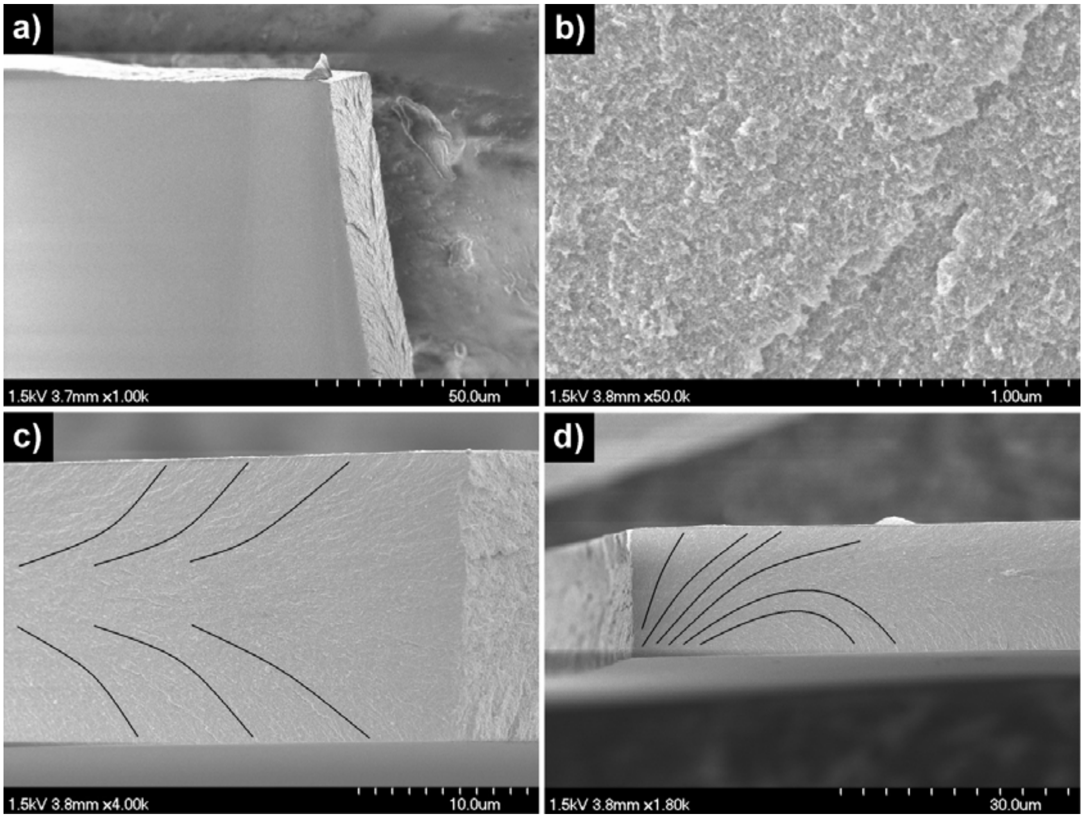

Figure 7.16. SEM pictures of plates from a TiO_2 single layer thin film prepared with paste N'': top views (a,b); fracture surface (c,d).

7.6.2. Pastes $H'_{N/P25}$ and $H'_{N/R}$ based on ethanolic gel blended with larger TiO_2 particle varieties

As detailed in the last section, the use of TiO_2 gels without prior drying and grinding proved successful in optimizing particle dispersion and avoiding the presence of undesirable aggregates within the paste and film. However, the resultant films were brittle and rather dense with low porosity not rendering them appropriate for DSC photoanode fabrication. In order to overcome the latter problem believed to stem from the very fine and narrow nanoparticles size distribution (4-8 nm) characterizing the aqueous-synthesized anatase, it was decided to blend it with larger average particle size TiO_2 varieties. Two TiO_2 varieties were used: the commercial P25 powder and the home-made rutile product, powder R. In both cases the hybrid pastes, $H'_{N/P25}$ and $H'_{N/R}$, were made with the N-Eth ethanolic anatase gel (Chapter 3, p. 62). $H'_{N/P25}$ was prepared starting with a mixture of gel N-Eth and dry powder P25 (50 wt. % powder N equivalent, 50 wt. % P25 powder), while $H'_{N/R}$ was prepared with a mixture of gel N-Eth and dry powder R (50 wt. % powder N, 50 wt. % powder R).

7.6.2.1. Paste $H'_{N/P25}$

The films prepared with paste $H'_{N/P25}$, were found to crack and peel off during annealing. However, the occurrence of cracks visually observed in the case of film $H'_{N/P25}$ was much lower than in the case of films N' and N'', a first indication of its improved mechanical properties. The better consistency of the film, vis-à-vis the simple N' film, may be deduced from the irregular trace of internal cracks (Figure 7.17.a) and from the small fragments of film partially detached at the fracture surface (Figure 7.17.c). Top view SEM images of a plate show that the film is characterized with higher roughness (Figure 7.17.b) and enhanced porosity (Figure 7.17.d), in comparison to film N', owing to the presence of larger particles (5-150 nm, 21 nm average particle size) introduced by the 50 wt. % of P25 powder. At low magnification the two TiO_2 materials appear to be quite homogeneously mixed (Figure 7.17.b). However, at higher magnification, it may be noticed that the particles from powder P25 (the brightest) are grouped into bundles encased in a denser structure formed by the aqueous-synthesized anatase nanoparticles (the darkest).

These bundles are responsible for the generation of pores in the approximate range 10-100 nm (Figure 7.17.d). From these observations, It may be advanced that the generated pores contribute to better film mechanical integrity by partially absorbing the tensions generated upon contraction of the film. Moreover, the presence of P25 particle bundles may be thought to counter the propagation of cracks within the film, as observed in Figure 7.17.a.

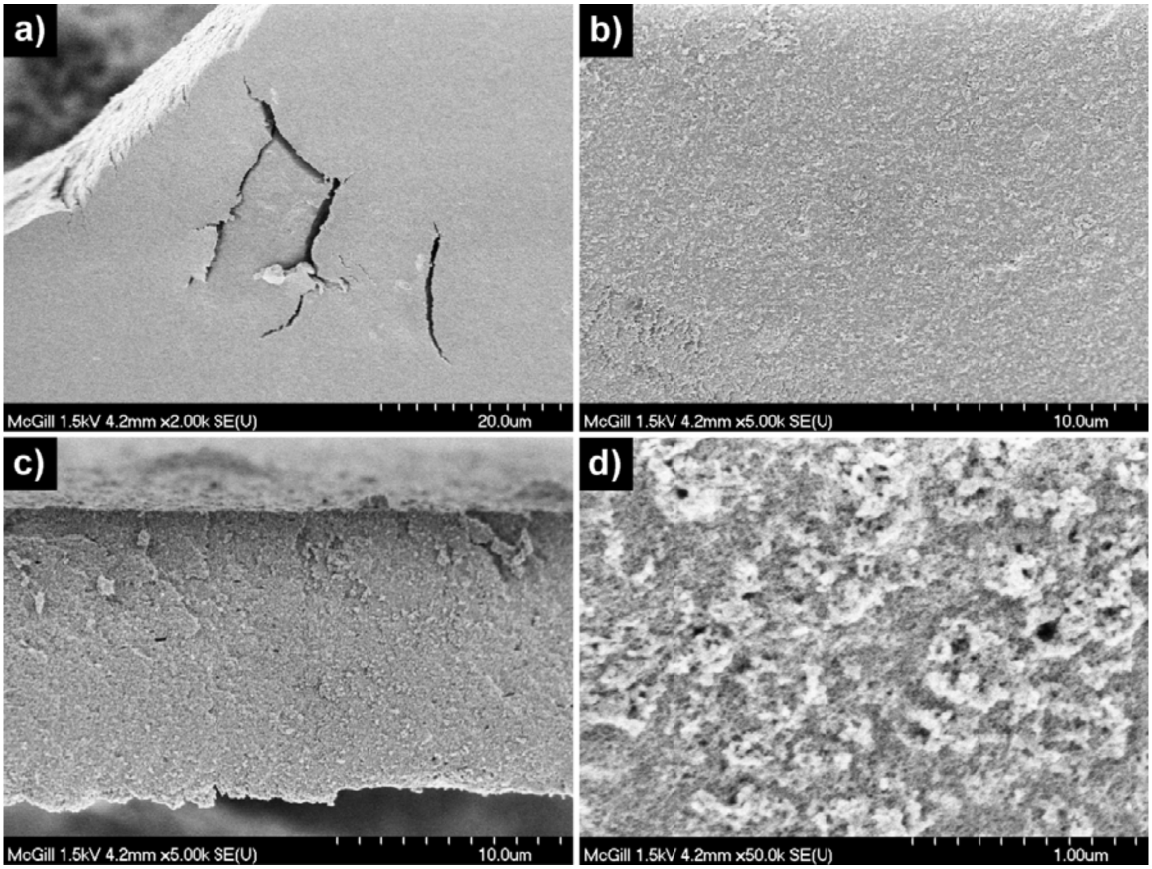

Figure 7.17. SEM pictures of plates from a TiO_2 single layer thin film prepared with paste $H'_{N/P25}$: top views (a,b, and d); fracture surface (c).

7.6.2.2. *Paste H'$_{N/R}$*[(a)]

Three films of different thicknesses were prepared by screen printing and annealing of paste H'$_{N/R}$. Among the three films, the two thicker ones were found to crack and peel off during annealing, but the thinnest one did not crack and showed good adhesion to the glass substrate. This result further illustrates the effect of the film thickness on its mechanical stability, as previously mentioned.

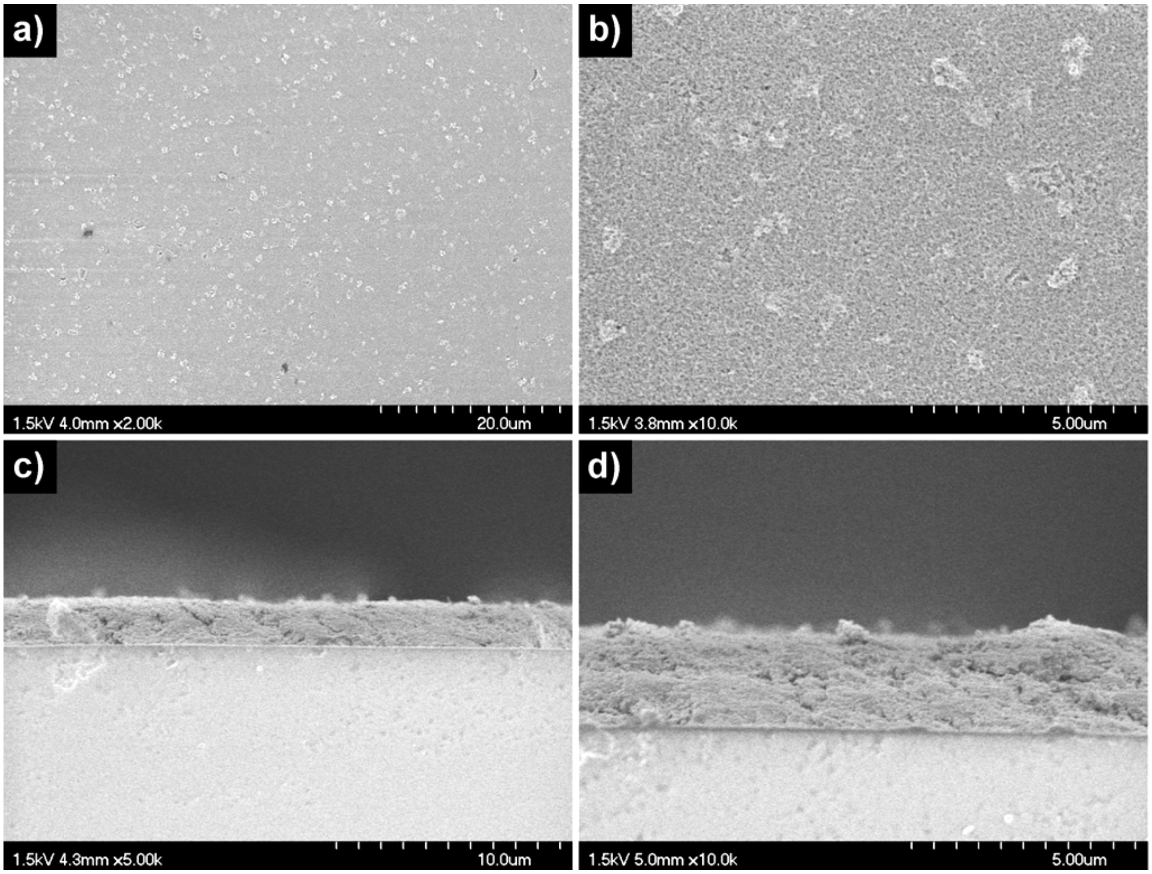

Figure 7.18. SEM pictures of plates from a TiO_2 single layer thin film (~ 2 µm) prepared with paste H'$_{N/R}$: top views (a,b); cross sections (c,d).

(a) Footnote: This blend is equivalent to the hybrid A/R mixture used in section 7.5 where the urchin-like rutile particles were used as scattering centres to enhance the DSC performance without resorting to double layer film structure. The difference between the work described in section 7.5 and the present one is the method of preparation of the paste. In the former case dry powders were used as starting ingredients while here a wet ethanolic gel is used.

Figure 7.18 presents SEM images of the surface (Figures 7.18.a and 7.18.b) and cross section of the thinnest of the three films (Figures 7.18.c and 7.18.d), as deposited on glass substrate. By comparing top views of film $H'_{N/R}$ (Figures 7.18.a and 7.18.b) and film N' (Figures 7.15.a and 7.15.b), it becomes evident that the addition of 50 wt. % 200-400 nm rutile particles to the paste formulation had a significant impact on the roughness of the film. In particular, the presence of uniformly distributed particle units of approximately 500 nm can be noticed at the surface of the film (Figure 7.18.b). No internal cracks such as previously observed in the case of film $H'_{N/P25}$ were found. By examining the cross sectional images of the film, it is confirmed that the latter has good adhesion properties since no voids can be observed between the film and the glass substrate. The film is characterized with a regular thickness of approximately 2 µm.

7.6.3. Paste N-Aq

Finally, a paste was prepared based on an aqueous gel (ethanol free) containing aqueous-synthesized anatase nanoparticles, namely paste N-Aq. This gel was mixed with PEG (the binder) and glycerol (the rheological agent), both soluble in water contrary to ethyl cellulose and α-terpineol. With this new paste formulation, solvent exchange from water to ethanol was eliminated, translating into further simplification of the paste preparation process.

After condensation, the paste was found to have good rheological properties and to be stable over time. Films of various thicknesses were prepared on regular glass slides. As the films were drying at ambient temperature, the appearance of small dots could be observed that were not removed upon annealing. Above a certain thickness, the films cracked during annealing. One film that did not visually appear to be cracked was used for further SEM imaging analysis (Figure 7.19).

Surprisingly, top views of this film show the latter to be composed of 20-50 µm size isolated fragments, separated from each other by a few microns wide gaps (Figures 7.19.a and 7.19.b). These fragments display typical features associated with brittle fracture. Side views of these fragments (Figures 7.19.c and 7.19.d) show the presence of large spherical cavities of a few microns in diameter that most likely resulted from the formation of trapped pockets of water vapour during annealing. Looking at the positioning of these cavities in the film, it is obvious that their formation was initiated in the interior of the film. The reason these pockets of high water vapour occurrence were observed may be thought to originate from an excess of glycerol, a highly hygroscopic compound.

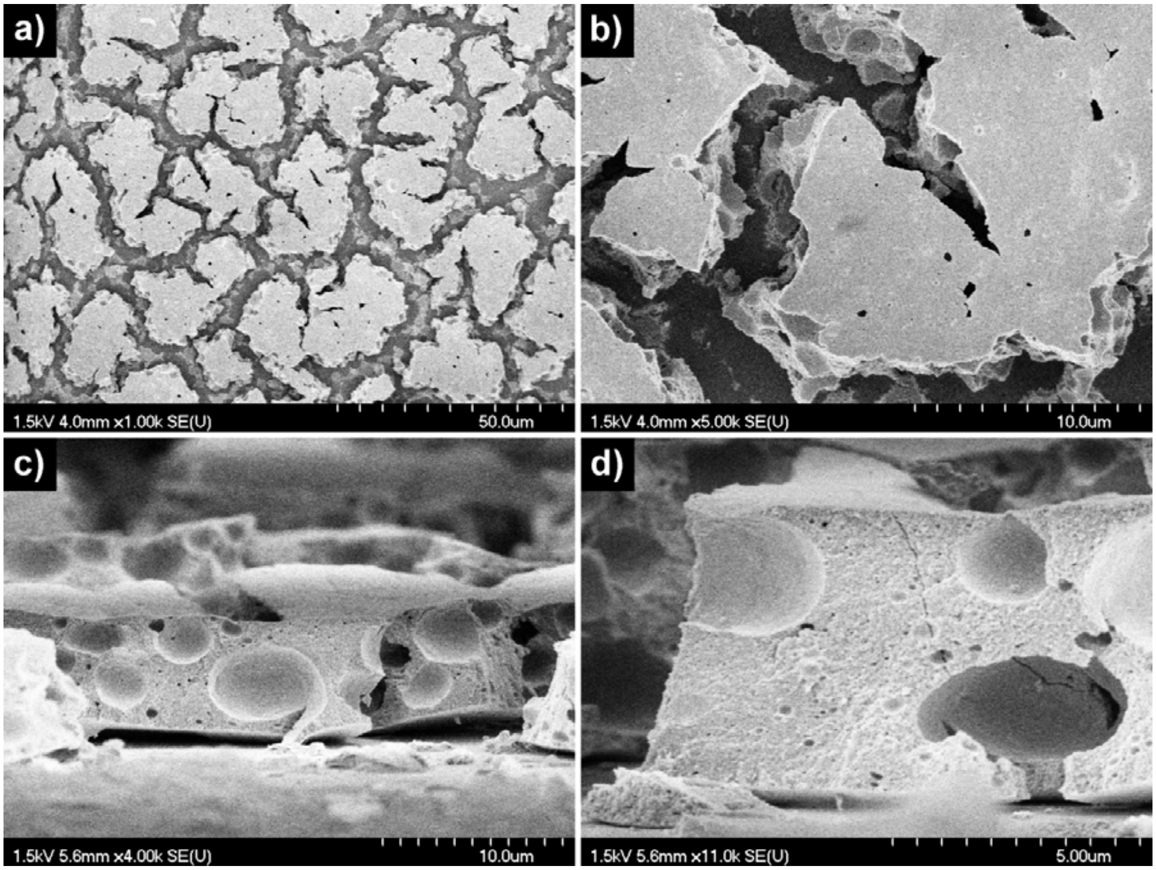

Figure 7.19. SEM pictures of plates from a TiO_2 single layer thin film prepared with paste N-Aq: top views (a,b); side views (c,d).

Improvement of the aqueous paste formulation is necessary before moving on to sensitization and DSC assembly and testing. This may be achieved first by using a water soluble rheological agent with higher volatility or equivalently lower boiling point than glycerol, namely 290 °C (against 214 °C for α-terpineol). For instance, propylene glycol, whose boiling point is 188 °C, is an organic compound often used in the food or cosmetics industry with the purpose of raising the viscosity of emulsions. Second, the incorporation of larger TiO_2 particles such as the 200-400 nm rutile particles of colloid R, may also be used for reducing the density of the particle network structure in the film, thus facilitating the evaporation/combustion of the binder and rheological agent.

7.7. Conclusions

The aqueous-synthesized powders A and N were successfully deposited as single-layer films and annealed into photoanodes. The fabricated films were found to have a specific surface area of ~ 130 m^2/g and the anatase nanocrystallites to have grown from 3-5 nm to ~ 12 nm upon annealing. The latter were also characterized with an enhanced band gap of 3.37 eV and to assume higher degree of crystallinity but still carrying ~ 1.5 wt. % surface OH groups. The pore size was determined to be ~ 8 nm. By comparison the film prepared with P25 nanoparticles had the following properties: 50 m^2/g, 30 nm, 3.15 eV, 0.2 % surface OH and 25 nm pore size. The films were optimized in terms of thickness and $TiCl_4$ post-treatment. The cells assembled with the aqueous-synthesized based TiO_2 photoanodes were found to match the performance of the cell assembled with the P25-based photoanode. The respective performance parameters (η, I_{sc}, V_{oc}, FF) were (N vs. P25): 2.70 %, 6.25 mA/cm^2, 0.620 V, 0.70 vs. 2.73 %, 6.22 mA/cm^2, 0.665 V, and 0.69.

Significant improvement of the cell performance was further achieved by using hybrid aqueous-synthesized TiO_2 powders, namely powder $H_{A/R}$ composed of 50 wt. % powder A and 50 wt. % powder R. The corresponding cell parameters (η, I_{sc}, V_{oc}, FF) were: 4.07 %, 8.96 mA/cm^2, 0.71 V, 0.64. These results were explained based on the improved porosity and structure of the film and scattering effect owing to the addition of 200-400 nm rutile particles to the paste formulation.

Finally, several attempts were made to simplify the paste and film preparation methods by making direct use of aqueous-synthesized TiO_2 gels as opposed to dried and ground powders. These efforts led to partially successful results. By far blending the anatase gel with larger TiO_2 particle varieties produced the most promising results in terms of mechanical integrity of the annealed films. However, further work is required to enable the building of thicker films via the optimization of gel-based paste formulation before moving on to cell assembly and testing.

7.8. References

[1] S. Ito, P. Chen, P. Comte, M. K. Nazeeruddin, P. Liska, P. Péchy, and M. Gratzel, *Prog. Photovolt.: Res. Appl.*, **15** (2007), 603.

[2] A. A. Christy, O. M. Kvalheim, R. A. Velapoldi, *Vib. Spec.*, **9** (1995)**,** 19.

[3] V. Nadtochenko, N. Denisov, A. Gorenberg, Y. Kozlov, P. Chubukov, J. A. Rengifo, C. Pulgarin, J. Kiwi, *Appl. Cat. B: Env.*, **91** (2009), 460.

[4] K. M. Reddy, S. V. Manorama and A. R. Reddy, *Mat. Chem. and Phys.*, **78** (2003), 239.

[5] A. K. Arora, M. Rajalakshmi, T. R. Ravindran and V. Sivasubramanian, *J. Raman Spectrosc.*, **38** (2007), 604.

[6] W. F. Zhang, Y. L. He, M. S. Zhang, Z. Yin, Q. Chen, *J. Phys. D: Appl. Phys.*, **33** (2000), 912.

[7] K. E. Lee, M. A. Gomez, S. Elouatik, and G. P. Demopoulos, *Langmuir*, **26** (2010), 9575.

[8] S. Chuangchote, T. Sagawa, and S. Yoshikawa, *ECS Trans.*, **16** (2009), 21.

[9] P. M. Sommeling, B. C. O'Regan, R. R. Haswell, H. J. P. Smit, N. J. Bakker, J. J. T. Smits, J. M. Kroon, and J. A. M. Van Roosmalen, *J. Phys. Chem. B*, **110** (2006), 19191.

[10] S. Ito, T.N. Murakami, P.Comte, P. Liska, C.Grätzel, M.K. Nazeeruddin, and M. Grätzel, *Thin Sol. Films*, **516** (2008), 4613.

[11] C. J. Barbe, F. Arendse, P. Compte, M. Jirousek, F. Lenzmann, V. Shklover, and M. Grätzel, *J. Am. Ceram. Soc.*, **80** (1997), 3157.

[12] F. Hirose, K. Kuribayashi, T. Suzuki, Y. Narita, Y. Kimura, and M. Niwano, *Electrochem. Solid- Stat. Lett.*, **11** (2008), A109.

[13] J. Wang and Z. Lin, *Chem. Mater.*, **22** (2010), 579.

[14] S. Hore, C. Vetter, Ra. Kern, H. Smit, and A. Hinsch, *Sol. Energy Mat. Sol. Cells*, **90** (2006), 1176.

[15] C. Charbonneau, K. E. Lee, G. B. Shan, M. A. Gomez, R. Gauvin and G. P. Demopoulos, *Electrochem. Solid-Stat. Lett.* **13** (2010), H257.

[16] S. Ito, T. N. Murakami, P. Comte, P. Liska, C. Graetzel, M. K. Nazeeruddin, M. Gratzel, *Thin Sol. Films*, **516** (2008), 4613.

[17] C.-Y. Huang, Y.-C. Hsu, J.-G. Chen, V. Suryanarayanan, K.-M. Lee, K.-C. Ho, *Sol. Energy Mater. Sol. Cells*, **90** (2006), 2391.

[18] H.-J. Koo, J. Park, B. Yoo, K. Yoo, K. Kim, N.-G. Park, *Inorg. Chim. Acta*, **361** (2008), 677.

[19] G. Li, C. P. Richter, R. L. Milot, L. Cai, C. A. Schmuttenmaer, R. H. Crabtree, G. W. Brudvig, V. S. Batista, *Dalton Trans.*, **45** (2009), 10078.

[20] K.-M. Lee, V. Suryanarayanan, K.-C. Ho, *J. Power Sources*, **188** (2009), 635.

[21] C. J. Barbe, F. Arendse, P. Comte, M. Jirousek, F. Lenzmann, V. Shklover, and M. Gratzel, *J. Am. Ceram. Soc.,* **80** (1997), 3157.

[22] P. J. Gash, *Tectonophysics*, **12** (1971), 349.

Chapter 8: Synopsis

Introduction

The specific findings of this work, presented in Chapters 4-7, have already been summarized in their respective conclusion sections at the end of each chapter. In this synopsis, global conclusions are drawn based on the whole body of the results presented and discussed, and the contributions to original knowledge are identified. Finally, this chapter also provides a list of suggestions for future work that may contribute to further understanding and control of $TiCl_4$ aqueous systems and advances in the field of TiO_2-based DSC devices.

Global conclusions

In this thesis, the synthesis of TiO_2 nanopowders via controlled forced hydrolysis of $TiCl_4$ aqueous solutions and the use of these materials for the fabrication of DSC thin film photoanodes were investigated in detail. The main conclusions arising from this work may be set out as follows:

- The speciation of Ti(IV) in Ti(IV)-Cl(-I)-H_2O solutions was deduced to be in the form of oxy- or hydroxy-chloro-Ti(IV) complexes of general formula $[TiO_x(Cl)_y]^{(4-2x-y)}$ and $[Ti(OH)_x(Cl)_y]^{(4-x-y)}$. The nature and ratio of these complexes strongly depend on the Ti(IV) concentration: as the concentration is decreased, partial hydrolysis occurs leading to the number of chloride ions coordinated to Ti(IV), y, to decrease while the number of hydroxyl/oxyl groups, x, increases. A new comprehensive hydrolysis reaction was suggested to describe this behavior:

$$a\, TiCl_4 + b\, H_2O = c\, [Ti(OH)_xCl_{z1}]^{4-(x+z1)} + d\, [TiO_yCl_{z2}]^{4-(2y+z2)} + (4a-cz_1-dz_2)\, Cl^- + (cx+2dy)\, H^+$$

- The kinetics of forced hydrolysis and TiO_2 nanoparticle formation was observed to depend on the type of agitation and mixing conditions. In contrast to previous studies, well reproducible results were obtained via a mechanically-stirred reactor in which controlled isothermal treatment (80 °C, P_{atm}) of $TiCl_4$ aqueous solutions could be undertaken.

- Nanoparticle product recovery, initially performed by using pressure filtration, was significantly improved in the case of anatase nanocolloids via the formation of reversible aggregates induced by partial neutralization to pH 3 with NH_4OH and subsequent centrifugation. In this way, the cumulative duration of S/L separation and washing was reduced from 3-4 days to approximately 1 hour, an essential improvement from a process implementation point of view.

- The kinetics of conversion of $TiCl_4(aq)$ into $TiO_2(s)$ was investigated under various experimental conditions of initial $TiCl_4$ concentration, temperature, and agitation. All these parameters were found to have a strong influence on $TiCl_4$ hydrolysis: an increase of the temperature or the agitation speed resulted in a faster kinetics of Ti(IV) conversion while an increase of the initial Ti(IV) concentration was found to be associated with a slower kinetics of Ti(IV) conversion. The latter phenomenon, rather counter intuitive, was related to the speciation of $TiCl_4$ solutions. For 0.2-1.5 M $TiCl_4$ solutions (isothermally treated at 70-90 °C), the kinetic curves of Ti(IV) conversion were characterized with an "S-shape", typical of the nucleation and growth Avrami model.

- Solutions with $TiCl_4$ concentration > 0.2 M yielded rutile upon isothermal treatment at 80 °C while those with ≤ 0.2 M gave anatase. This allows for proper selection of processing conditions to control the production of the desired nanostructured TiO_2 phase. Anatase is a metastable phase under these conditions that was detected upon solution ageing to undergo anatase-to-rutile phase transition via a dissolution-recrystallization mechanism.

- Controlled forced hydrolysis (80 °C, P_{atm}) of 0.3, 0.5, 1, and 1.5 M $TiCl_4$ aqueous solutions was found to lead to the formation of a unique nanostructured morphology of self-assembled rutile-nanofibre particles. The nanofibres were characterized with a diameter of 10-20 nm and their length was found to increase from approximately 100 nm (0.3 M $TiCl_4$) to 3 µm (1.5 M $TiCl_4$) with increasing concentration. The powders synthesized from 0.5-1.5 M $TiCl_4$ aqueous solutions had a surface area close to 80 m^2/g while the powder synthesized from the 0.3 M solution was characterized with a larger surface area of 112 m^2/g. This particular material, labelled as powder R, was further implemented to the fabrication of DSC photoanodes as light-scattering centres.

- Isothermal processing of a 0.2 M $TiCl_4$ solution in the custom-designed reactor (80 °C, P_{atm}, 30 min) led to the synthesis of semi-crystalline TiO_2 nanocolloids with anatase as the major crystalline phase (85 wt. %). The dry particles were found to consist of aggregated 4-8 nm nanocrystallites with a very high surface area (250-350 m^2/g) and enhanced band-gap (3.37 eV). The same material was found to bear important surface hydroxylation. In comparison, the reference powder P25 material is characterized with the following properties: 70 wt. % anatase/ 30 wt. % rutile, 20 nm average particle size, 50 m^2/g, 3.15 eV, very little -OH/-OH_2. Upon annealing at 450 °C for 30 min, the crystallinity of the powders was improved along with an increase of the crystal size to 10-12 nm, translating into lower but still high 130 m^2/g surface area but without any changes of the phase composition.

- A series of DSC devices was assembled using photoanodes based on single aqueous-synthesized anatase powders A (recovered by pressure filtration) and N (recovered following partial neutralization with NH_4OH and centrifugation). Typically, the photoanodes prepared with powder N led to better DSC performance than photoanodes prepared with powder A, probably due to the light scattering effect caused by the presence of aggregates induced by the partial neutralization treatment. The best cell performance, namely η = 2.70 %, I_{SC} = 6.25 mA/cm^2, V_{OC} =

0.620 V, and FF = 0.70, obtained for a photoanode prepared with the aqueous-synthesized TiO_2 powder N, was comparable to the performance of a cell prepared with a P25 TiO_2 thin film, namely η = 2.73 %, I_{SC} = 6.22 mA/cm^2, V_{OC} = 0.665 V, and FF = 0.69.

- In an effort to improve the performance of the aqueous-synthesized anatase nanophase, a hybrid powder containing 50 wt. % of powder A and 50 wt. % of powder R was used for the fabrication of a thin film mesoporous photoanode. This hybrid photoanode was characterized with a rather uniform mesoporous film structure (140 Å average) and surface area of 62 m^2/g. Such properties were found to translate into greatly improved cell performance: η = 4.07 %, I_{SC} = 8.96 mA/cm^2, and V_{OC} = 0.710 V, and FF =0.64. This observed improved performance was explained on the basis of a light scattering effect introduced by the presence of 200-400 nm size rutile particles (powder R), and the improved diffusion of both the dye and the electrolyte within the film hence lower diffusion resistance.

- Finally, a new TiO_2-based screen-printing paste preparation method was advanced that allows for the formulation of highly dispersed pastes (aggregate-free) by using directly wet ethanolic gels of aqueous-synthesized TiO_2 particles as a starting material instead of previously dried and manually ground powders. When using the aqueous-synthesized anatase as single TiO_2 powder, the resultant films were found to be characterized with a dense and highly homogeneous structure, but very brittle mechanical properties. However, the use of hybrid ethanolic gels containing TiO_2 particles with different size distributions showed to simultaneously allow for the creation of a mesoporous structure with improved adhesion and mechanical stability. A first attempt was made to further simplify the paste preparation by using water as a solvent (instead of ethanol), but further optimization of the paste formulation is needed before moving on to the assembly and testing of DSC devices.

Claims to originality

Several parts of this thesis can be considered as a contribution to original knowledge. Here are the most important ones:

- The use of Micro-Raman spectroscopy combined with OLI thermodynamic simulations to determine the speciation of 0-2 M $TiCl_4$ aqueous solutions was reported for the first time.

- The kinetics of Ti(IV) conversion into TiO_2(s) by isothermal treatment (70-90 °C, P_{atm}) of 0.2-1.5 M $TiCl_4$ solutions was determined for the first time. Similarly, the dependence of kinetics on agitation and mixing condition was observed for the first time.

- An entirely aqueous solution synthesis process was designed based on the isothermal treatment of $TiCl_4$ aqueous solutions (without resorting to the use of additives or pre-neutralization) in a stirrer-tank reactor (mechanically agitated and operated under P_{atm} condition) that allows the preferential synthesis of either anatase nanocolloids or self-assembled nanofibre rutile particles at low temperature (typically 80 °C).

- A new method was developed for the fast recovery of TiO_2 anatase nanocolloids that uses post-synthesis partial neutralization with NH_4OH and centrifugation.

- The formulation of screen printing pastes for the fabrication of DSC photoanodes based on the use of aqueous-synthesized hybrid TiO_2 gels is totally novel.

Suggestions for future work

- Chapter 4 of this thesis presents new Raman spectroscopy data and thermodynamic simulation of 0-2 M $TiCl_4$ aqueous solutions. It may be advised for future work to complete this part of the study with FT-IR analyses of the same solutions. These techniques may help to better define the speciation of $TiCl_4$ aqueous solutions, and more particularly elucidate the case of $TiOCl_2$, generally assumed to predominate in Ti(IV)-Cl(-I)-H_2O systems.

- At this point of the project and given the successful production of rutile nanostructured powders or anatase nanocolloids via controlled isothermal aqueous-synthesis, it would be interesting to study the possibility of scaling up the current production system (200 mL batch reactor), and further design a continuous process for industrial application.

- Chapter 7 reports the early results of TiO_2 photoanode thin films prepared based on the formulation of new hybrid aqueous-synthesized TiO_2 gels. Further development of these pastes is suggested that may greatly contribute to overcome the high production cost vs. light-to-current conversion efficiency issue currently faced by DSC technologies.

APPENDIX: Forced Hydrolysis of a 1 M $TiCl_4$ Aqueous Solution at 80 °C - Use of Additives

A.1. Sulfate additives

In this section, the effect of sulfate additives on forced hydrolysis of a 1 M $TiCl_4$ aqueous solution at 80 °C was investigated. This work was initiated with the objective of producing anatase nanoparticles from high concentration $TiCl_4$ solutions (> 0.2 M), hence increasing the reaction yield as well as modifying their morphology. Sulfate additives were chosen as they have been shown in literature (Chapter 2, section 2.4.3.2) to favor anatase formation. A variety of sulfate-based additives were tried such as sulfuric acid (concentrated H_2SO_4(l)), sodium sulfate anhydrous (Na_2SO_4(s)), magnesium sulfate hydrate ($MgSO_4 \cdot 5\ H_2O$ (s), and aluminium sulfate hydrate ($Al_2(SO_4)_3 \cdot 18\ H_2O$(s)). In all cases, the additives were mixed with the $TiCl_4$ solution at T_{amb} prior to processing in the reactor. When the additives were in the form of salts, they were first dissolved in deionized water and then mixed with the $TiCl_4$ solution. In the first part of this section, the kinetics of Ti(IV) conversion into TiO_2(s) for a 1 M $TiCl_4$ - x M H_2SO_4(aq) solution containing various concentrations, x, of H_2SO_4(aq) is presented. In the second part, the effect of the sulfate additives on the properties of TiO_2(s) material produced under various experimental conditions is investigated based on the results of XRD, FEG-SEM, EDS, and BET surface area analyses.

A.1.1. Kinetics

Two $TiCl_4$-H_2SO_4(aq) solutions were prepared by addition of 0.5 and 1.5 mL H_2SO_4(l) to 200 mL of a 1 M $TiCl_4$ aqueous solution, of final concentration 0.046 and 0.137 M in H_2SO_4. The solutions were hydrothermally treated at 80 °C in the mechanically agitated reactor (1000 rpm) and samples were regularly collected in order to monitor the evolution of Ti(IV) concentration with time. Figure A.1 compares the kinetics of Ti(IV) conversion, *x*, for 1 M $TiCl_4$, 1 M $TiCl_4$ – 0.046 M H_2SO_4, and 1 M $TiCl_4$ – 0.137 M H_2SO_4 aqueous solutions. The 1 M $TiCl_4$ and 1 M $TiCl_4$ – 0.046 M H_2SO_4 curves are both characterized with a typical "S-shape" associated to the kinetics of homogeneous nucleation and growth of particles (Chapter 5). The 1 M $TiCl_4$ – 0.137 M H_2SO_4 curve is associated with a much slower kinetics than the two previous cases. In particular, the induction period, which is approximately 50 min for the 1 M $TiCl_4$ and 1 M $TiCl_4$ – 0.046 M H_2SO_4 curves, increases up to 150 min for the 1 M $TiCl_4$ – 0.137 M H_2SO_4 curve. By comparing the 1 M $TiCl_4$ and 1 M $TiCl_4$ – 0.046 M H_2SO_4 curves it can also be noticed that Ti(IV) conversion after the induction period is slower in the case of the 1 M $TiCl_4$ – 0.046 M H_2SO_4 aqueous solution.

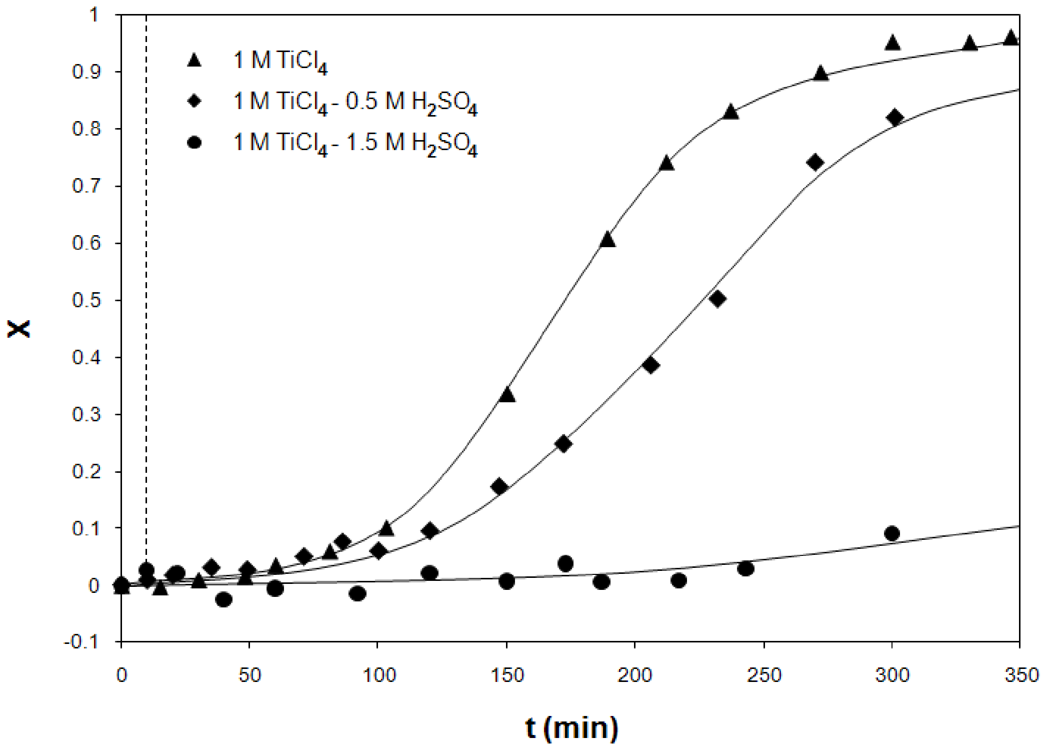

Figure A.1. Kinetics of Ti(IV) conversion for 1 M $TiCl_4$, 1 M $TiCl_4$ – 0.046 M H_2SO_4, and 1 M $TiCl_4$ – 0.137 M H_2SO_4 aqueous solutions processed at 80 °C in the mechanically agitated reactor (1000 rpm).

In conclusion, it can be deduced from this diagram that the addition of $H_2SO_4(l)$ to the initial 1 M $TiCl_4$ solution slows down the kinetics of Ti(IV) conversion. This may be attributed on one hand to the increased initial acidity of the medium owing to the additional protons H^+ brought by H_2SO_4(l) that hinders the precipitation of $TiCl_4$(aq) into TiO_2(s) according to Le Chatelier's principles. A similar phenomenon was observed and discussed for $TiCl_4$ solutions of increasing concentration and acidity (Chapter 5). On the other hand, the presence of sulfate ions may also be considered as a factor influencing the kinetics of $TiCl_4$ hydrolysis. In fact, it was suggested by *Zhang et al.* [1] that sulfate ions, which are larger and more negatively charged than chloride ions, tend to preferentially adsorb at the surface of the positively charged TiO_2 nuclei [2], thus hindering the hydrolysis reaction mechanism.

A.1.2. Characterization of the solid products

In this section, characterization of the solid products obtained via forced hydrolysis of 1 M $TiCl_4$ aqueous solution containing sulfate additives is provided. The effects of various experimental conditions are investigated, namely the nature and concentration of the sulfate additives on the phase composition and morphology of the solid products. In the case of sulfate salt additives, all the starting solutions were prepared so that the stoechiometric ratio of titanium to sulfate is kept constant, so that $[Ti(IV)]/[SO_4^{2-}] = 10$. All solid products were separated from their batch liquor and washed via the solid recovery route A (Chapter 3, p. 59-60).

A.1.2.1. Effect of H_2SO_4(aq)

Figure A.2 shows the XRD patterns of powders obtained via forced hydrolysis (80 °C, 5 hrs) of 1 M $TiCl_4$ – x M H_2SO_4 aqueous solutions with x = 0, 0.009, 0.046, 0.092, 0.137, and 0.183. The solutions were prepared by addition of 0, 0.1, 0.5, 1, 1.5, and 2 mL of concentrated H_2SO_4(l) to 200 mL of a 1 M $TiCl_4$ aqueous solution. All patterns are characterized with quite low intensity and broad peaks, which is indicative of the semi-crystalline character and small crystallite size of the powders. The powder produced by hydrothermal treatment of a 1 M $TiCl_4$ solution (Figure A.2.a) is characterized with the rutile phase, as previously discussed in Chapter 5. As the initial concentration of H_2SO_4(aq) in solution is increased, the appearance of peaks related to the anatase phase can be observed. In particular, the emergence of small peaks at 25.3° and 48.0° corresponding to the A(101) and A(200) atomic diffraction planes of the anatase crystalline phase of TiO_2 are evident on the pattern of the powder produced from the 1 M $TiCl_4$ – 0.046 M H_2SO_4 aqueous solution (Figure A.2.c). On the next patterns (Figure A.2.d-f), the phase composition of the powders is observed to bear an increasing amount of anatase, while the amount of rutile is inversely decreasing. These observations are in good correlation with other studies in literature that also report on the preferential crystallization of anatase TiO_2 when synthesized from aqueous solutions containing sulfate ions [1,3-5]. The main reason advanced to explain such phenomenon is the adsorption of sulfate ions at the surface of the TiO_2 nuclei. First, the adsorbed sulfate ions may prevent the mutual interaction of TiO_2 nuclei, thus preventing their aggregation, coalescence and further growth into rutile particles, as previously described in Chapter 6. Second, the limited growth of the nuclei, evident by the slow kinetics of Ti(IV) conversion observed for a 1 M $TiCl_4$ – 0.137 M H_2SO_4 aqueous solution (Figure A.1), may hinder the anatase-to-rutile phase transformation, which according to *Zhang and Banfield* [6] is expected to occur for TiO_2 crystals having an approximate diameter > 18 nm.

Figure A.3 shows TEM pictures and associated SAED pattern obtained for a powder synthesized by hydrothermal treatment of a 1 M $TiCl_4$ – 0.137 M H_2SO_4 aqueous solution at 80 °C (5 hrs). Figures A.3.a and A.3.b confirm the nanostructure of the powder expected from the corresponding XRD pattern (Figure A.2.e), with very small 3-5 nm crystallites aggregated into a particle of ~ 80 nm size (Figure A.3.a) and slightly bigger 5-30 nm crystallites aggregated into a particle of ~ 400 nm size (Figure A.3.b). The SAED pattern (Figure A.3.c) associated to the aggregate shown in Figure A.3.b displays broad rings which are characteristics of crystalline nanoparticles.

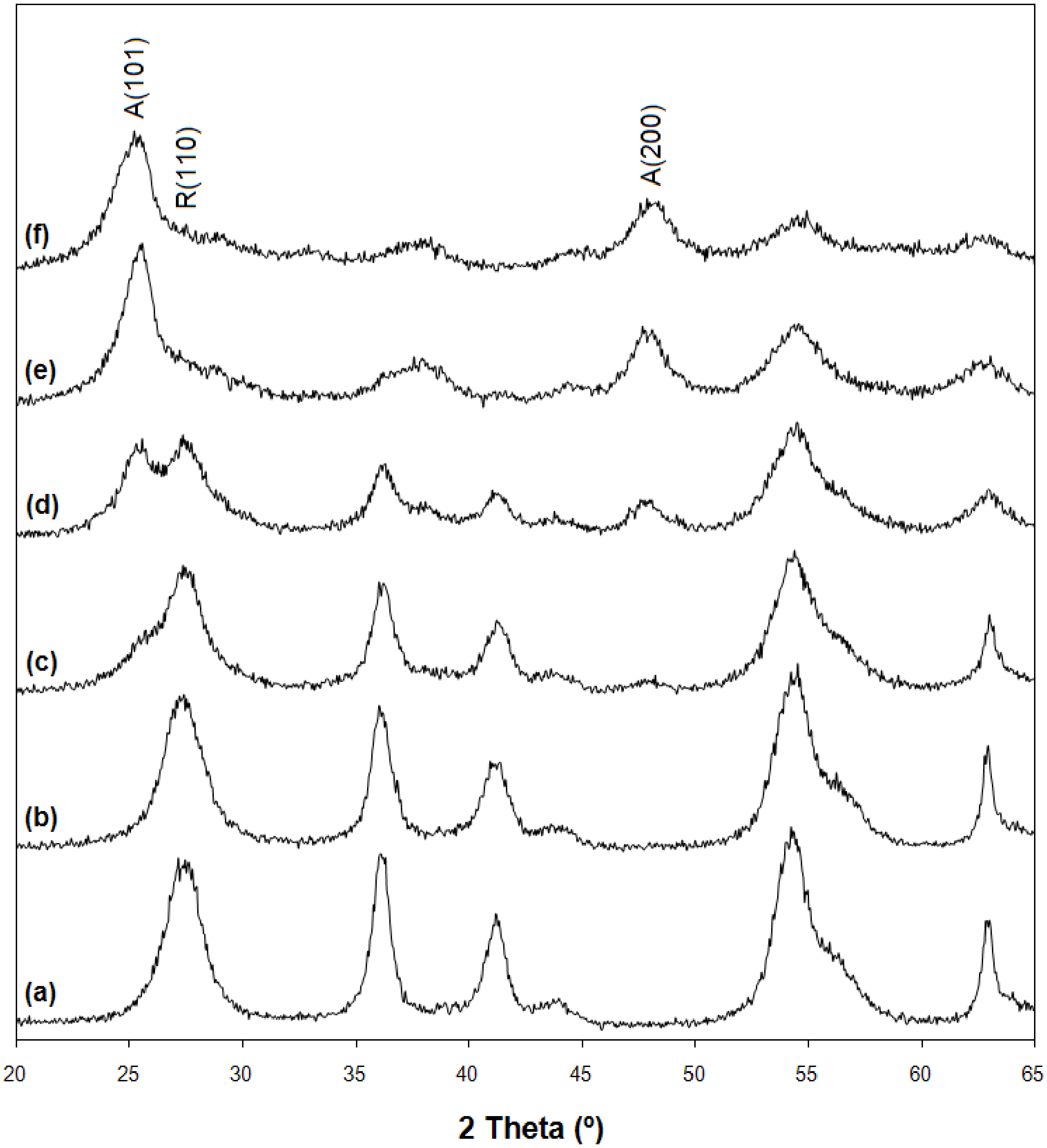

Figure A.2. XRD patterns of solid products obtained via forced hydrolysis of 1 M $TiCl_4$ – x M H_2SO_4 aqueous solutions, at 80 °C, for 5 hrs, with x = 0 (a), 0.009 (b), 0.046 (c), 0.092 (d), 0.137 (e), and 0.183 (f).

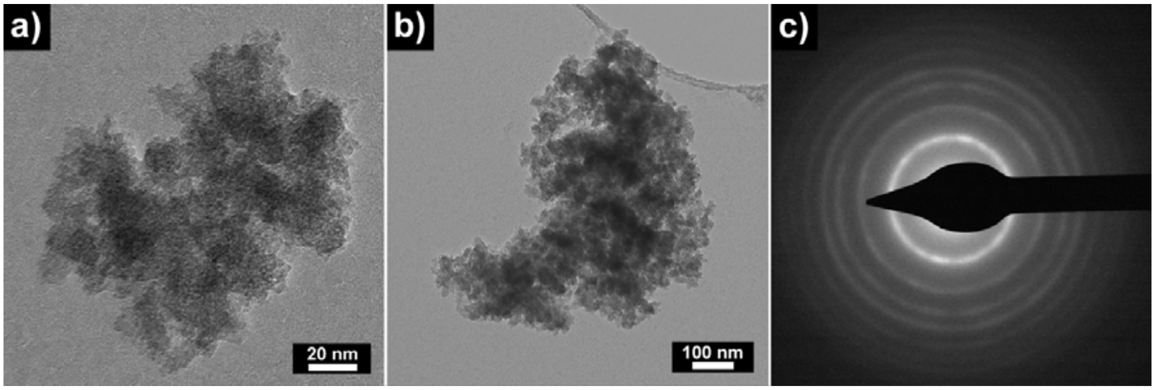

Figure A.3. TEM pictures of isolated particles from a powder synthesized by hydrothermal treatment of a 1 M $TiCl_4$ – 0.137 M H_2SO_4 aqueous solution at 80 °C, for 5 hrs (a,b); and SAED pattern associated to Figure A.3.b (c).

However, when examining the SEM pictures of the same powders (Figure A.4), these can be seen to consist of large aggregates in the size range 2-6 µm (Figure A.4.a), themselves composed of strongly aggregated particles in size range 50-200 nm (Figure A.4.b), such as the one observed on Figure A.3.b. BET surface area measurements performed on these powders confirmed the compact structure of the aggregates observed on Figure A.4.a with a surface area of 7 m^2/g (d_{BET} = 220 nm). Finally, the EDS spectrum of the same powder (Figure A.5) showed the presence of elemental sulfur whereas no trace of elemental chlorine was detected (Cl K_α is expected at 2.62 keV). This last result correlates the hypothesis of the preferential surface adsorption of sulfate ions as opposed to chloride ions. Moreover, this finding may indicate that sulfate ions participate in the aggregation of the nanocrystallites: with two oxygen atoms likely to engage chemical bounding (Figure A.6.a), it is possible that sulfate ions act as chemical bridges between adjacent TiO_2 crystallites, this way promoting strong aggregation of the nanocrystallites (Figure A.6.b).

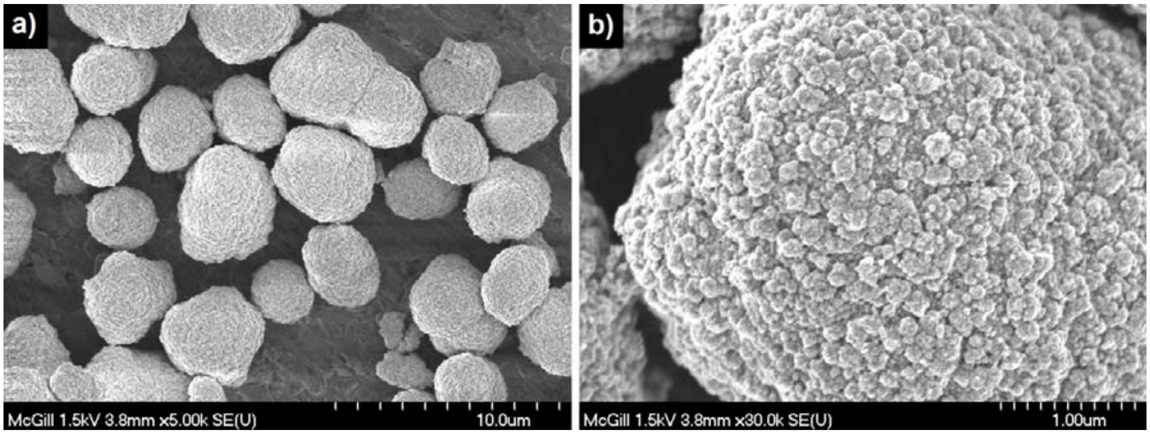

Figure A.4. SEM pictures a powder synthesized by hydrothermal treatment of a 1 M $TiCl_4$ – 0.137 M H_2SO_4 aqueous solution at 80 °C, for 5 hrs at low (a) and high (b) magnification.

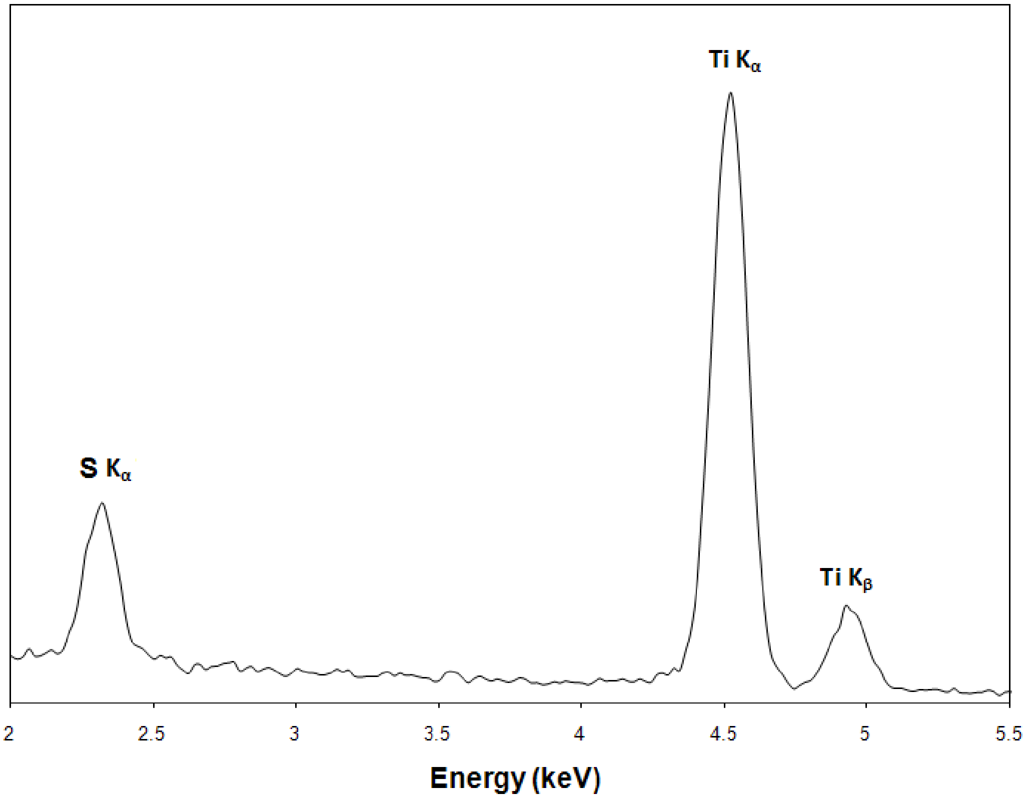

Figure A.5. EDS elemental analysis of a powder synthesized by hydrothermal treatment of a 1 M $TiCl_4$ – 0.137 M H_2SO_4 aqueous solution at 80 °C, for 5 hrs.

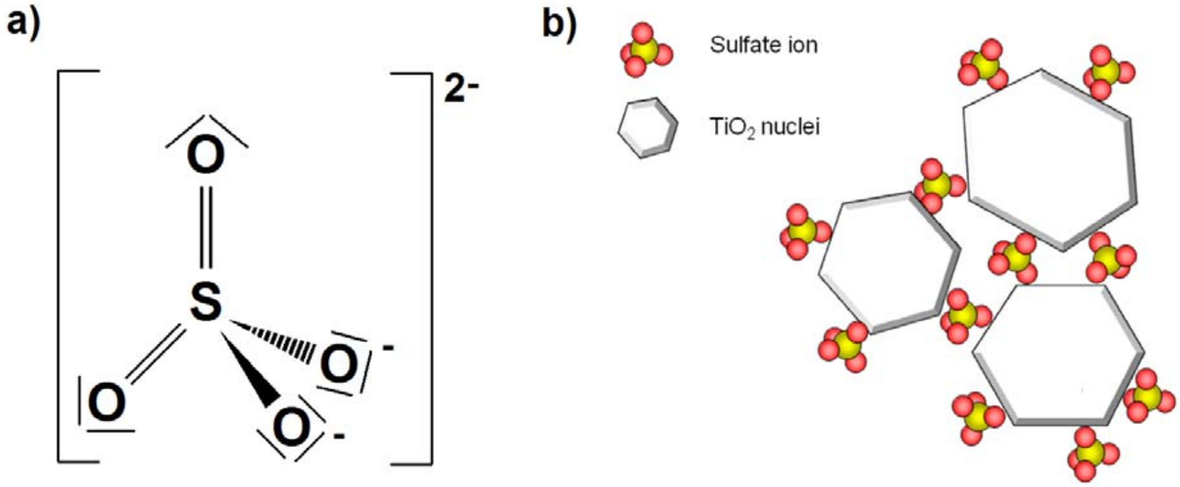

Figure A.6. Diagram representing the geometry of sulfate ions (a), and the adsorption of sulfate ions at the surface of TiO_2 nuclei (b).

A.1.2.2. Effect of sulfate salts

Figure A.7 shows the XRD patterns obtained for powders synthesized via forced hydrolysis (80 °C, 5 hrs) of a 1 M $TiCl_4$ aqueous solution prepared with sulfate salt additives ($[Ti(IV)]/[SO_4^{2-}] = 10$), namely $MgSO_4 \cdot 5\ H_2O(s)$, $Al_2(SO_4)_3 \cdot 18\ H_2O(s)$, and $Na_2SO_4(s)$. All XRD patterns are characterized with quite low intensity and broad peaks, indicative of the semi-crystalline character of the powders and small size of the synthesized crystallites. The three powders are found to contain both the anatase and rutile crystalline phases in different ratios. For the powder obtained by hydrothermal treatment of a 1 M $TiCl_4$ – 0.1 M Na_2SO_4 aqueous solution, anatase is the major crystalline phase whereas the two other powders contain approximately 50 wt. % of rutile and 50 wt. % of anatase, judging by the relative intensity of the A(101) and R(110) peaks. Such difference may be thought to arise from the different solubility properties of the three sulfate salt used as additives. Sodium sulfate is known for its high solubility properties in water, namely 43 g/L at 80 °C, as compared to 39.3 g/L and 35 g/L for magnesium sulfate and aluminium sulfate at 80 °C, respectively [7]. Also, the probability of sulfate ions to chemically interact with the surface of TiO_2 nuclei may be expected to increase when using sodium sulfate (or sulfuric acid) as compared to using magnesium or aluminium sulfate salt additives.

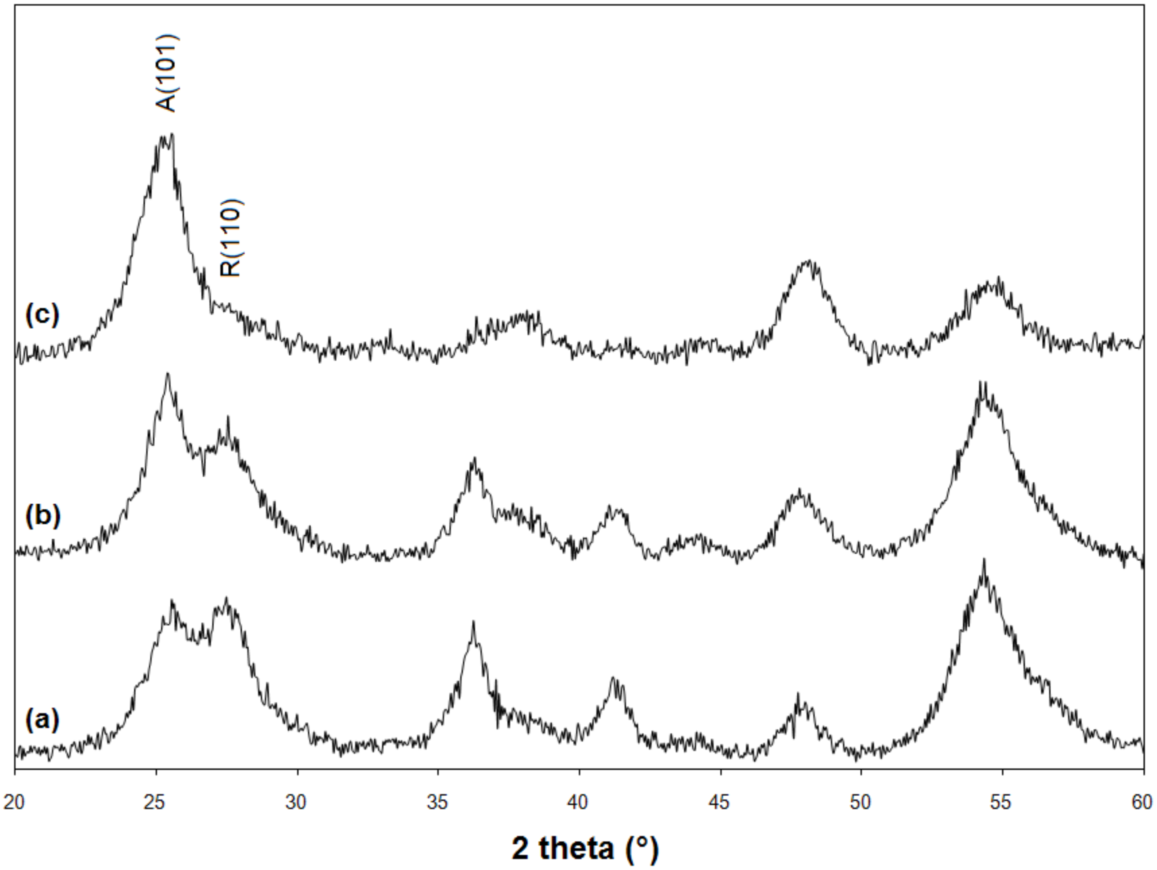

Figure A.7. XRD patterns of powders prepared by forced hydrolysis (80 °, 5 hrs) of 1 M $TiCl_4$ aqueous solutions prepared with 0.1 M of sulfate additive: $MgSO_4 \cdot 5\ H_2O$ (a), $Al_2(SO_4)_3 \cdot 18\ H_2O$ (b), and Na_2SO_4 (c).

The SEM pictures of the three powders (Figures A.8.a, A.8.c, and A.8.e) show that in all cases the synthesized TiO_2 material resulted in large aggregates in the size range 2-7 µm with compact structures. At higher magnification (Figures A.8.b, A.8.d, and A.8.f), the structure of the aggregates is found to vary slightly in correlation with the phase composition of the powder. The powder obtained by hydrothermal treatment of the 1 M $TiCl_4$ – 0.1 M Na_2SO_4 aqueous solution, is characterized with large aggregated particles composed of sub-units in the size range 50-200 nm. Such feature was already observed in the case of a powder issued from the 1 M $TiCl_4$ – 0.137 M H_2SO_4 aqueous solution (Figures A.4.b and A.8.b), which has a very similar phase composition (anatase being the major crystalline phase) as the powders produced from the 1 M $TiCl_4$ – 0.1 M Na_2SO_4 aqueous solution (Figures A.7.c and A.2.e). The other two powders, obtained by hydrothermal treatment of 1 M $TiCl_4$ – 0.1 M $MgSO_4 \cdot 5\ H_2O$ and 1 M $TiCl_4$ – 0.033 M $Al_2(SO_4)_3 \cdot 18\ H_2O$, respectively, are found to be characterized with particles in the form of cauliflower-shaped aggregates (Figures A.8.d and A.8.f). It may be advanced that this particular structure originates from the growth of self-assembled rutile nanofibres initiated at the surface of a core particle consisting of aggregated anatase nanocrystals.

The EDS spectra obtained for the three powders are compared in Figure A.9. All the spectra display a peak at 2.32 keV, which is attributed to the K_α line of elemental sulfur. In the case of the 1 M $TiCl_4$ – 0.1 M $MgSO_4 \cdot 5\ H_2O$ (Figure A.9.a) and 1 M $TiCl_4$ – 0.033 M $Al_2(SO_4)_3 \cdot 18\ H_2O$ (Figure A.9.b) starting aqueous solutions, the intensity of the S K_α is observed to be lower than in the case of the 1 M $TiCl_4$ – 0.1 M Na_2SO_4 aqueous solution (Figure A.9.c). This observation may be correlated to the particle structure observed for the three powders: in the first two cases the S K_α rays are most likely generated at the core of the particle and partially absorbed by the layer of rutile self-assembled nanofibres covering the particle core, whereas in the third case the same rays are generated directly at the surface of the particles, hence having a higher probability to reach the x-ray detector. No peaks were found that match the K_α line of sodium, magnesium or aluminium, expected at 0.95, 1.25, and 1.48 keV, respectively, and indication that the cations do not resort inside the TiO_2 particles during their formation.

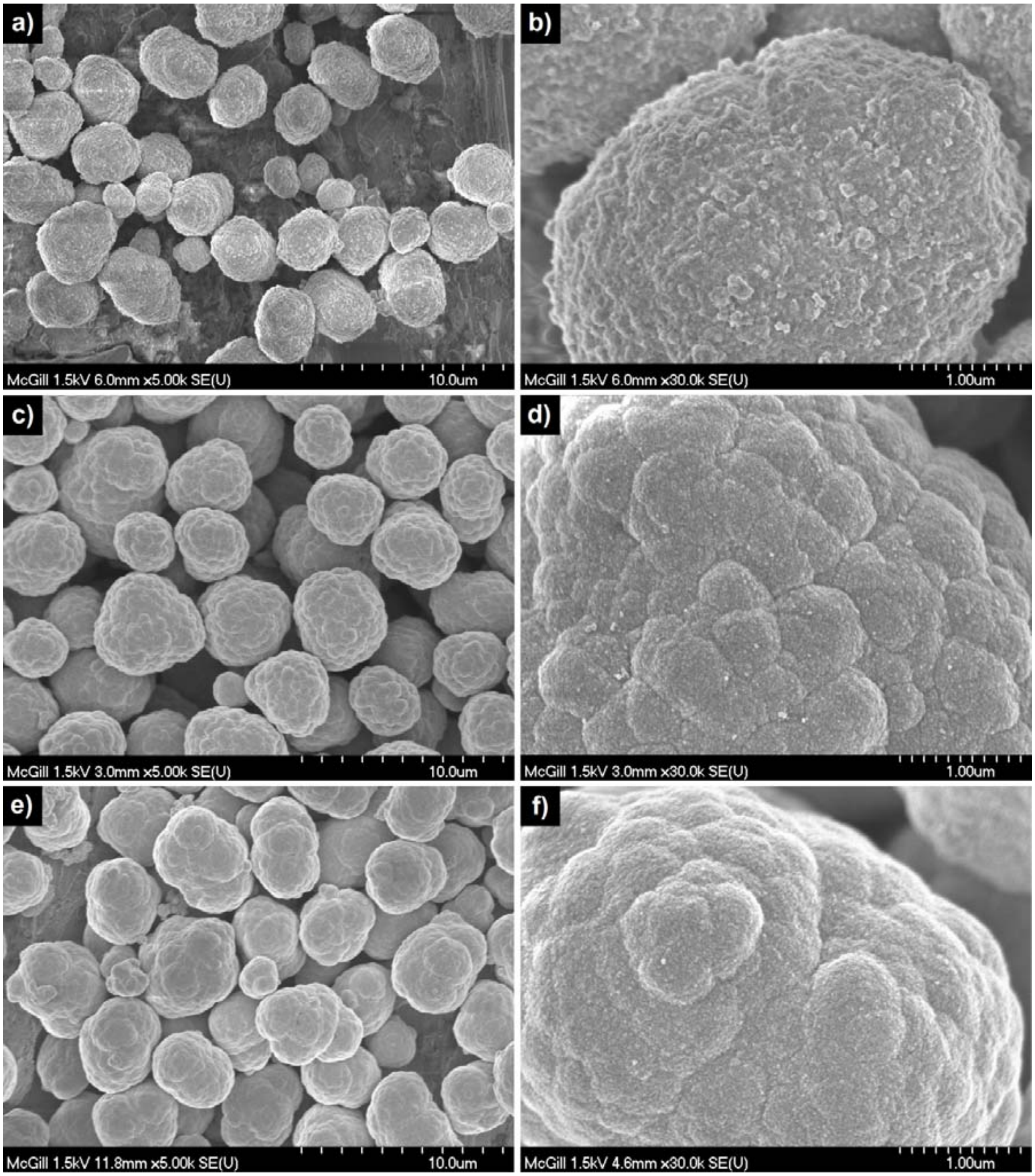

Figure A.8. SEM pictures of powders prepared by forced hydrolysis of 1 M $TiCl_4$ aqueous solution prepared with sulfate additives: Na_2SO_4 (a,b), $Al_2(SO_4)_3 \cdot 18\ H_2O$ (c,d), and $MgSO_4 \cdot 5\ H_2O$ (e,f).

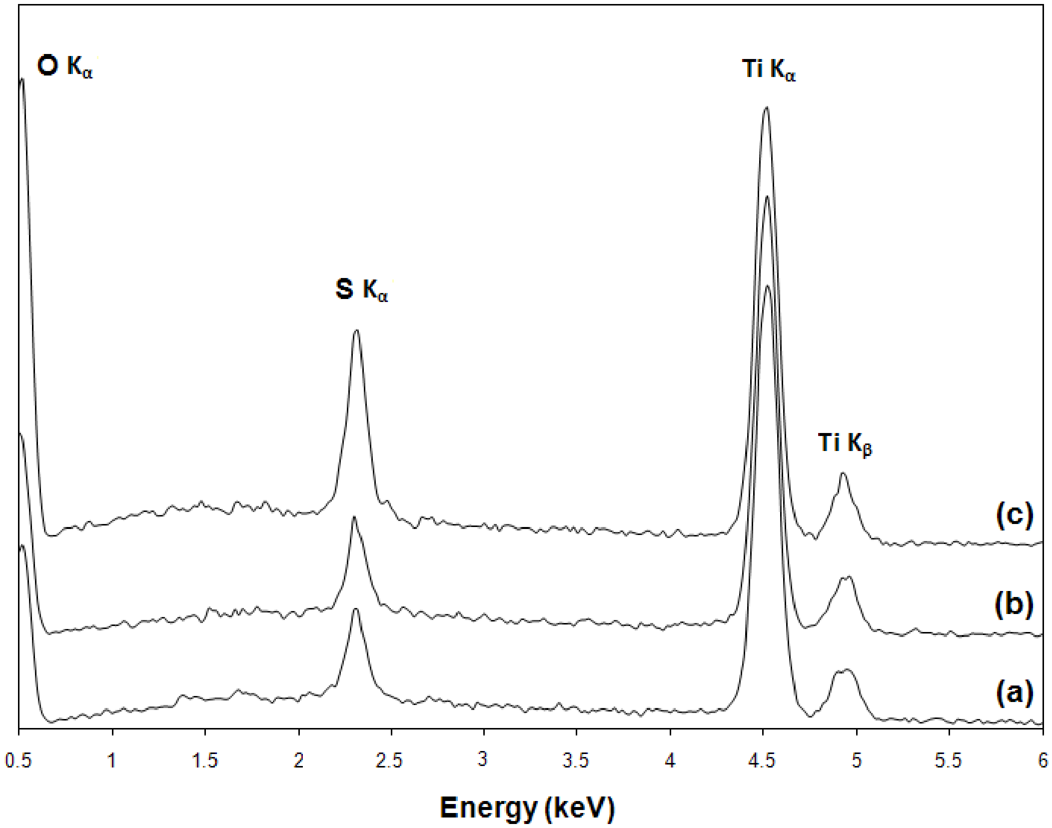

Figure A.9. EDS spectra of powders prepared by forced hydrolysis (80 °, 5 hrs) of 1 M $TiCl_4$ aqueous solution prepared with 0.1 M of sulfate additive: $MgSO_4 \cdot 5\ H_2O$ (a), $Al_2(SO_4)_3 \cdot 18\ H_2O$ (b), and Na_2SO_4 (c).

A.1.3. Conclusions

Hydrothermal treatment at 80 °C of a 1 M $TiCl_4$ solution containing sulfate additives in various forms was investigated. A kinetic study showed that the presence of sulfuric acid as additive in the initial chemical composition of the $TiCl_4$(aq) solution slowed down the kinetics of conversion of Ti(IV) into TiO_2(s). Although similar Ti(IV) conversion kinetics was previously found to lead to crystallization of TiO_2 with the rutile phase (Chapter 5), in this case the solid products were characterized with a mixed crystalline phase of anatase and rutile. More precisely, it was found that the higher the initial concentration in sulfate additives, the slower the kinetics of the hydrolysis reaction, and the larger the anatase content of the synthesized powders. This result, which is counter of other results presented in Chapters 5 and 6, may be attributed to preferential adsorption at the surface of the TiO_2 nuclei that stabilizes them as anatase. The presence of sulfate additives was also found to be responsible for the formation of aggregated particles in the micron size range, an attractive feature from the standpoint of product recovery (S/L separation). However, dense aggregation of the particles, apparently caused by chemical bridging of sulfate ions between adjacent TiO_2 nanocrystallites, was also found to be very detrimental to the surface area of the powders. Since the focus of this study is to synthesize TiO_2 nanopowders suitable for the fabrication of high surface area photoanodes for DSC applications, the use of sulfates ions was not further considered.

A.2. Neutralization

A.2.1. Introduction

In this section, the effect of neutralization of a $TiCl_4$ aqueous solution via base addition prior to hydrothermal processing is investigated. Neutralization was induced by mixing the 2 M $TiCl_4$ stock solution with a concentrated solution of sodium hydroxide (10 N) at T_{amb}. In all cases, the final concentration in $TiCl_4$ was 1 M and the concentration in NaOH was made to vary in the range 1-3 M. The solution was further processed at 80 °C in the mechanically agitated reactor (1000 rpm). In this section, the effect of pre-neutralization on the kinetics of Ti(IV) conversion and the properties of the synthesized TiO_2 powders is investigated.

A.2.2. Experimental observations

Neutralization was performed by addition of concentrated NaOH(l) to 100 mL of the 2 M $TiCl_4$ stock solution, previously diluted with an approximate volume of 50 mL of deionized water in a 200 mL conical flask. This procedure was performed under magnetic stirring at ambient temperature. Upon addition of the concentrated NaOH(l), a white cloud formed instantaneously inside the solution, and slowly disappeared. This is an important phenomenon to point out as the latter may be associated to partial hydrolysis leading to the transformation of Ti(IV)-chloro complexes into hydrated or hydroxylated Ti(IV) species. From the studies presented in Chapters 5 and 6, it is known that the speciation of Ti(IV) chloride solutions plays an important role in determining the kinetics of particle nucleation and growth as well as the properties of the resulting TiO_2 powders.

A.2.3. Kinetics

Figure A.10 shows the kinetic curves obtained for 1 M $TiCl_4$ aqueous solution, and two neutralized $TiCl_4$ aqueous solutions of initial chemical composition 1 M $TiCl_4$ - 1 and 2 M NaOH. All three curves follow the typical "S-shape" previously described the case of the forced hydrolysis of a 1 M $TiCl_4$ solution at 80 °C (Chapter 5). It can be noticed from this diagram that when neutralization is applied, the kinetics of Ti(IV) conversion is accelerated. In particular, the higher the degree of neutralization applied, the shorter the induction period, namely 5, 10, and 30 min for 1 M $TiCl_4$ - 2 M NaOH, 1 M $TiCl_4$ - 1 M NaOH, and 1 M $TiCl_4$ aqueous solutions. Neutralization is also found to be responsible for a faster growth of the particles, relatively to the increasing slope of the Ti(IV) conversion curves observed after the induction period.

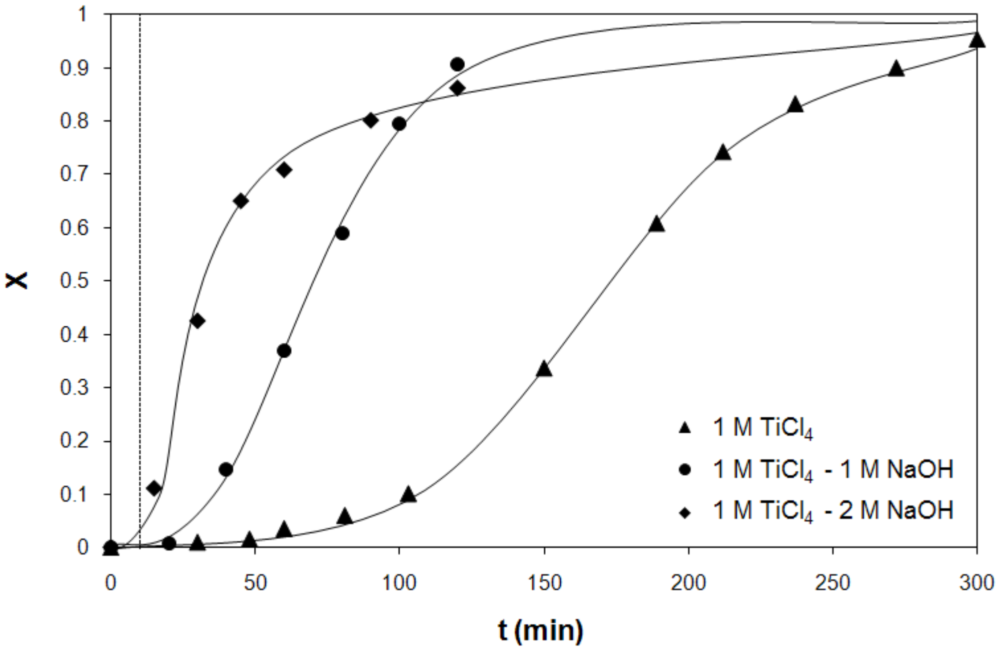

Figure A.10. Kinetics of Ti(IV) conversion for 1 M $TiCl_4$, 1 M $TiCl_4$ - 1 M NaOH, and 1 M $TiCl_4$ - 2 M NaOH aqueous solutions hydrothermally treated at 80 °C.

These observations may be associated to variations of the speciation of the solution, induced by neutralization. According to the study on the speciation of $TiCl_4$ aqueous solutions (Chapter 4), upon addition of sodium hydroxide, the chloro-Ti(IV) complexes found in the 2 M $TiCl_4$ solution are expected to transform into hydroxylated-Ti(IV) complexes. The replacement of chloride ions with hydroxyl, a first step towards the formation of TiO_2(s) nuclei by forced hydrolysis, explains the shorter induction period and accelerated particle growth observed when neutralization is applied.

A.2.4. Characterization of the solid products

All the powders characterized in this section were produced via neutralization at ambient temperature and forced hydrolysis (80 °C, 2 hrs) of 1 M $TiCl_4$ - x M NaOH aqueous solutions, with x = 1, 2, and 3. The recovery of the solids was carried out via route A (Chapter 3, p. 59-60).

Figure A.11 shows the effect of neutralization on the phase composition of powders synthesized via forced hydrolysis of a 1 M $TiCl_4$ aqueous solution. In all cases, rutile is found to be the major crystalline phase. In the case of the powder obtained from a 1 M $TiCl_4$ - 3 M NaOH solution, a small fraction of anatase can be detected by the appearance of a shoulder at 23.5° (Figure A.11.d). By comparing all four spectra from the lowest (x = 0) to the highest (x = 3) degree of neutralization, a narrowing of the peaks is observed along with a slight increase of the peak intensity. The appearance of a small peak at 39.1° and a medium peak at 56.1°, attributed to the rutile (200) and (220) crystal planes, can also be noticed on the spectra of powders produced from the 1 M $TiCl_4$ – 2 and 3 M NaOH aqueous solutions. These observations relate to an increased average crystallite size and improved crystallinity of the powders. This improvement may be thought, on a kinetics point of view, to originate from the shorter nucleation and growth period, hence the longer hydrothermal ageing of the powders (Figure A.10). The faster kinetics of Ti(IV) conversion observed with an increased degree of neutralization also justify the presence of small amounts of anatase. As previously discussed (Chapter 6), fast hydrolysis kinetics is usually favorable to the synthesis of TiO_2 nanocrystallites with the anatase phase.

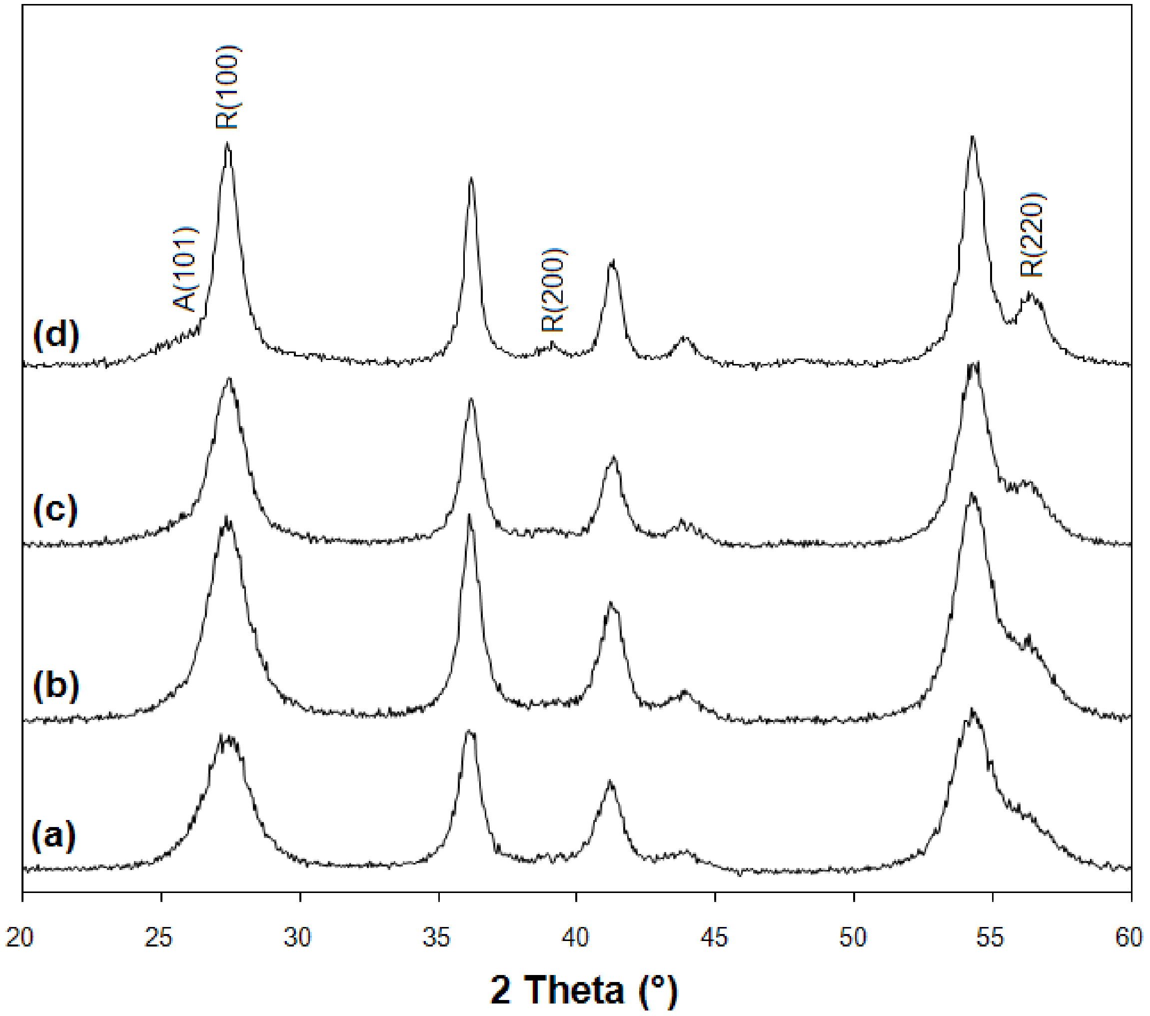

Figure A.11. XRD patterns of TiO_2 powders produced via isothermal treatment at 80 °C of pre-neutralized 1 M $TiCl_4$ aqueous solution: $[NaOH]_{initial}$ = 0 M (a), 1 M (b), 2 M (c), and 3 M (d).

SEM pictures of TiO_2 powders obtained via forced hydrolysis of a 1 M $TiCl_4$ aqueous solution after neutralization are shown in Figure A.12. On the left hand column, the particle size is observed to decrease with an increased degree of neutralization. Such phenomenon may be related to the faster hydrolysis kinetics, or more precisely to the faster nucleation of TiO_2 nuclei induced by neutralization (Figure A.10). Powders produced by forced hydrolysis of a 1 M $TiCl_4$ solution neutralized with 1 M NaOH are characterized with large particles of 1-5 µm average size, apparently composed of densely packed self-assembled rutile nanofibres, along which cracks are initiated (Figure A.12.a). Small nanoparticles in the size range 50-100 nm can also be observed at the surface of a large aggregate as well as a 200 nm size aggregate made of smaller nanoparticles (Figure A.12.a). The very thin and elongated but densely packed rutile nanofibres justify both the very high BET surface area of 249 m^2/g and the small average pore size of 26 Å measured for these powders. At a higher degree of neutralization, namely [Ti(IV)]/[NaOH] = 2, smaller 0.5 - 2 µm particles are formed, which structure resembles the one of sea urchins (Figures A.12.c and A.12.d). In this case, the assembly of the TiO_2 needles appears to be less dense and very few cracks can be observed. From the BET surface area analysis, the powders were found to have a surface area of 97 m^2/g and 41 Å average pore size. Finally, when the degree of neutralization is further increased to [Ti(IV)]/[NaOH] = 3, small crack-free nanostructured flower-like particles in the size range 0.3-0.5 µm are obtained (Figures A.12.e and A.12.f). These particles feature slightly elongated and self-assembled triangular-shaped crystallites pointing outwards in radial directions, which provide the powder with a surface area of 85 m^2/g and average pore size of 120 Å. From these results, it is observed that the surface area of the synthesized powders decreases when the degree of pre-neutralization is increased. This may be related to the decreasing particle size, or more precisely to the decreasing ratio of the length of the rutile nanofibres to the diameter of the particle core.

EDS elemental analysis of the three powders (Figure A.13) shows the presence of small but equivalent amounts of elemental chlorine in the chemical composition of the powders. Since the three powders are characterized with different shape and particle size, it may be deduced from this finding that chlorides resorts homogeneously in the structure of the particles, as opposed to being preferentially adsorbed at their surface. It may further be suggested that the presence of chloride impurities in TiO_2 powders formed via forced hydrolysis of $TiCl_4$ aqueous solutions mostly originates from the incomplete hydrolysis of Ti(IV)-chloro complexes upon isothermal processing.

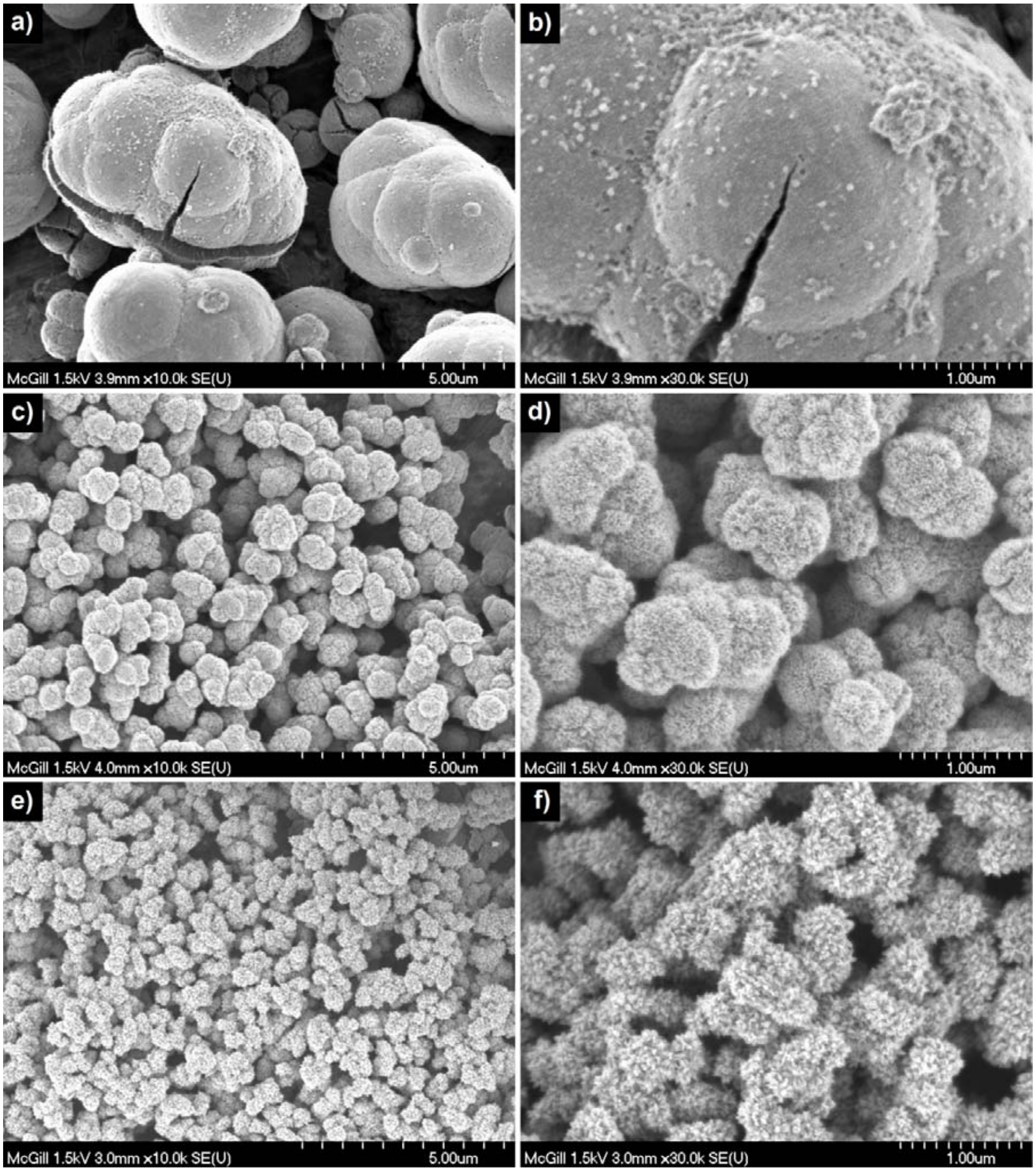

Figure A.12. SEM pictures of powders obtained via forced hydrolysis of pre-neutralized 1 M $TiCl_4$ - 1 M NaOH (a,b), 1 M $TiCl_4$ - 2 M NaOH (c,d), and 1 M $TiCl_4$ - 3 M NaOH (e,f) solutions.

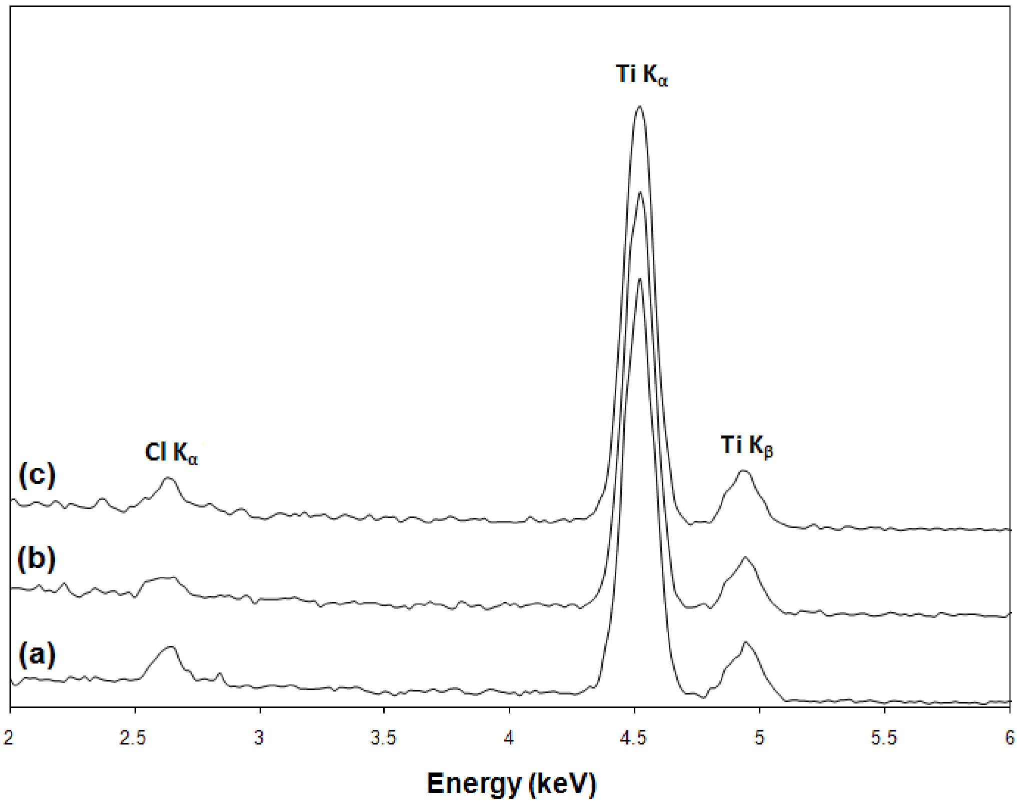

Figure A.13. EDS patterns of powders obtained via forced hydrolysis of 1 M $TiCl_4$ - 1 M NaOH (a), 1 M $TiCl_4$ - 2 M NaOH (b), and 1 M $TiCl_4$ - 3 M NaOH (c).

A.2.5. Conclusions

The use of neutralization via base addition at T_{amb} prior to hydrothermal treatment of a 1M $TiCl_4$ aqueous solution (80 °C, 2 hrs) was found to accelerate the kinetics of Ti(IV) conversion into TiO_2(s). This result was explained based on the modification of the speciation of the solution from Ti(IV)-chloro complexes to hydroxylated T(IV) complexes, which are more likely to form TiO_2 nuclei under forced hydrolysis. Control of the hydrolysis reaction kinetics via neutralization made it possible to synthesize rutile TiO_2 particles within a variety of sizes and shapes. In particular, flower-like nanostructured rutile particles with a high surface area of 85 m^2/g and good crystallinity were synthesized. Such material is endowed with a combination of properties (surface area, structure, and size) which may be very well suited as light scattering material in the fabrication of the of TiO_2-based photoanodes, as discussed in section 7.5 of Chapter 7.

A.3. References

[1] Q. Zhang, L. Gao, H. Xie, *Mater. Sci. Eng.*, **A343** (2003), 22.

[2] R. A. French, A. R. Jacobson, B. Kim, S. Isley, R. L. Penn, and P. C. Baveye, *Environ. Sci. Technol.*, **43** (2009), 1354.

[3] G. Lian, Z. Qinghong, *Mater. Trans.*, **42** (2001), 1676.

[4] Q. Zhang, L. Gao, J. Guo, *J. Eur. Ceram. Soc.*, **20** (2000), 2153.

[5] Q. H. Zhang, L. Gao, J. K. Guo, *Nanostruct. Mater.*, **11** (1999), 1293.

[6] H. Zhang, J. F. Banfield, *J. Phys. Chem. B*, **104** (2000), 3481.

[7] W.F. Linke, Solubilities : Inorganic and metal-organic compounds : A compilation of solubility data from the periodical literature, 4th edition, American Chemical Society, Washington, (1958-1965).